Measurements of differential *t*-channel single top-quark production cross-sections in proton–proton collisions at a centre-of-mass energy of 8 TeV with the ATLAS detector

Dissertation
zur
Erlangung des Doktorgrades (Dr. rer. nat.)
der
Mathematisch-Naturwissenschaftlichen Fakultät
der
Rheinischen Friedrich-Wilhelms-Universität Bonn

von
Pienpen Seema-Mergelmeyer
aus
Roi Et, Thailand

Bonn, 25.09.2017

Dieser Forschungsbericht wurde als Dissertation von der Mathematisch-Naturwissenschaftlichen Fakultät der Universität Bonn angenommen und ist auf dem Hochschulschriftenserver der ULB Bonn `http://hss.ulb.uni-bonn.de/diss_online` elektronisch publiziert.

1. Gutachter: Prof. Dr. Ian C. Brock
2. Gutachter: Prof. Dr. Klaus Desch

Tag der Promotion: 09.01.2018
Erscheinungsjahr: 2018

Contents

CHAPTER 1

Introduction

The theory describing the subatomic world is the Standard Model of particle physics. It successfully describes the fundamental particles and three of the four fundamental forces in the universe. Only gravity is unexplained by this model. One way of studying these fundamental particles and their interactions is that particles are accelerated to very high energies and collided. The Large Hadron Collider (LHC) at CERN is the most complex and powerful particle accelerator ever built. One of particle detectors of the LHC to record data from collisions is ATLAS. The goal of the ATLAS experiment is to investigate the widest possible range of the Standard Model particles and their interactions in the proton–proton collisions and search for new physics beyond the Standard Model.

The heaviest elementary particle in this model is the top quark with a mass of about 173 GeV/c^2. It was discovered in 1995 at the Tevatron, a proton–antiproton collider, by the CDF and D0 experiments. The top quark has several interesting properties, e.g. it is the only quark that decays before it forms hadrons. The top quarks are mainly produced in pairs via the strong interaction at both the LHC and the Tevatron. They can also be produced singly via the weak interaction, subdivided into three different production modes: t-channel, Wt-channel and s-channel. Studies of single top-quark production can probe the Standard Model in several ways, e.g. the direct measurement of the Cabibbo-Kobayashi-Maskawa (CKM) matrix element V_{tb}. New physics phenomena beyond the Standard Model may also be revealed through the singly produced top quarks.

The cross-section of the t-channel single top-quark production is of the same order of magnitude as the one of the top-quark-pair production at the LHC. It is large enough to make an extraction of the differential cross-section of this production process possible. Due to the parton distribution function (PDF) of the proton, singly produced top quarks (tq production) and top antiquarks ($\bar{t}q$ production) can have different kinematic properties. Separate measurements for tq and $\bar{t}q$ production are sensitive to the ratio of u-quarks and d-quarks in the proton. Moreover, studies of the transverse momentum and rapidity distributions of the top quark, the top antiquark and the light-quark jet can provide a good understanding of these production processes. Deviations from physics beyond the Standard Model may show up in the high transverse-momentum regime.

This thesis is dedicated to *the measurements of absolute and normalised t-channel single top-quark and top-antiquark differential cross-sections*. They are extracted as a function of the transverse momentum and the absolute value of the rapidity of the top (anti)quarks at both parton level and particle level. The parton-level measurements are based on top quarks over the full kinematic range. This makes comparisons to theoretical predictions straightforward. Alternatively, so-called pseudo-top-quarks are reconstructed from the stable particles in a fiducial phase space. Such particle-level differential cross-sections for single top-quark production are extracted for the first time. The benefit of the particle-level measurements is that the particle-level objects depend less on theoretical models, as the fiducial volume is defined to be as close as possible to the phase space of the measurement. Also, the differential cross-sections are extracted as a function of the transverse momentum and the absolute value of the rapidity of the light-quark jet in the t-channel exchange of a W boson.

The analysis presented in the thesis focuses on events whose experimental signature is given by one electron or muon, missing transverse momentum, and two jets, one of which is identified as originating from a b-quark. A sequence of selection cuts based on the measurements of the fiducial and total t-channel single top-quark and top-antiquark cross-sections, which is a topic of the thesis of a PhD student at the University of Wuppertal [1] is applied to discard background events. In the fiducial and total cross-section measurements, an artificial neural network is used to combine several kinematic variables into one powerful discriminant. The present analysis starts with imposing a cut on the final discriminant to achieve a good signal-to-background ratio. The differential cross-sections are extracted using an iterative Bayesian unfolding. All measurements use proton–proton collision data at a centre-of-mass energy of 8 TeV recorded with the ATLAS detector in 2012, corresponding to an integrated luminosity of 20.2 fb^{-1}. This analysis was published together with the fiducial and total cross-section measurements by the ATLAS collaboration [2].

This thesis is structured as follows: a summary of the Standard Model of particle physics including the properties of top quarks is given in Chapter 2. The ATLAS detector at the LHC is described in Chapter 3, followed by the reconstruction of physical objects from the collision data in Chapter 4. Chapter 5 is dedicated to the selection of the collision data as well as the modelling of the signal and background processes. It also describes the selection requirements applied to enhance signal events. Chapter 6 introduces the definition of parton and particle levels. This is followed by the discrimination of signal from background using the neural network and a summary of the fiducial and total cross-section measurements based on a binned maximum-likelihood fit in Chapter 7. The ingredients of the differential cross-section measurements is the subject of Chapter 8. It comprises an introduction of the high purity region where the unfolding is performed and the choice of the binning for each variable that is unfolded. In Chapter 9, a detailed description of the unfolding procedures with the iterative Bayesian method is presented. It consists of the definition of the parton-level, particle-level and normalised differential cross-sections, a brief overview of three different unfolding methods, and the ways to determine the number of iterations for the iterative Bayesian unfolding. Several tests of the unfolding method are explained at the end of this chapter, followed by the treatment of both statistical and systematic uncertainties through the unfolding in Chapter 10. The major sources of uncertainty contributing to the differential cross-section measurements are discussed at the end of this chapter. Finally, the unfolded differential cross-sections as a function of different variables at both parton and particle levels, compared to several predictions, are presented in Chapter 11. It includes a discussion of the results and comparisons among the measurements. A summary of the thesis is given in Chapter 12.

CHAPTER 2

Theoretical basis

This chapter summarises the theoretical basis of the analysis. An overview of the Standard Model of particle physics is presented in Section 2.1, followed by the phenomenology of proton-proton collisions in Section 2.2. As the top quark is the key for this analysis, its properties and its production at the LHC are described in Section 2.3. At the end of the chapter, more details on the single top quarks produced via the *t*-channel exchange of a *W* boson are addressed.

2.1 Standard Model of particle physics

All known matter in the universe is assumed to be made of fundamental point-like particles, governed by four fundamental interactions: the strong, the weak, the electromagnetic, and the gravitational force. The Standard Model of particle physics is our best description to explain how these particles and these forces, except the gravitational force, are related to each other. The Standard Model is a gauge field theory based on the symmetry group:

$$\mathrm{SU}(3)_C \times \mathrm{SU}(2)_{I_3} \times \mathrm{U}(1)_Y. \tag{2.1}$$

In this theory, quantum chromodynamics (QCD) is the theory of the strong interaction. It is based on the SU(3) symmetry group. The mediators of this interaction are massless gluons. In QCD, there are three basic states of colour charge, C, named red, green and blue. Gluons carry a mixture of a colour state and an anticolour state. There are nine possibilities to form gluons, but only eight gluons exist as one gluon is in singlet state. There are three different colour states for each quark. The weak interaction is based on the SU(2) symmetry group. Three massive bosons, the charged $W^\pm$ and the neutral Z carry the weak charge. Quantum electrodynamics (QED) describes the electromagnetic (EM) interaction based on the U(1) symmetry group. The massless photon is the mediator of this interaction. According to the Glashow-Salam-Weinberg (GSW) theory [3–5], the electromagnetic interaction and the weak interaction are unified into the electroweak interaction. This is a significant step towards the unification of all fundamental forces in nature. The electroweak interaction is based on the $\mathrm{SU}(2)_{I_3} \times \mathrm{U}(1)_Y$ symmetry group. Y is a quantum number called the weak hypercharge which is related to two other quantum numbers: electric charge, Q, and weak isospin, I_3, as $Y = 2(Q - I_3)$. This means that the Standard Model is the unified theory of strong, weak and electromagnetic interactions.

Besides the mediators of the interactions (also known as the gauge bosons with spin 1), fermions are also Standard Model particles with spin $\frac{1}{2}$. In addition, each Standard Model particle has a corresponding

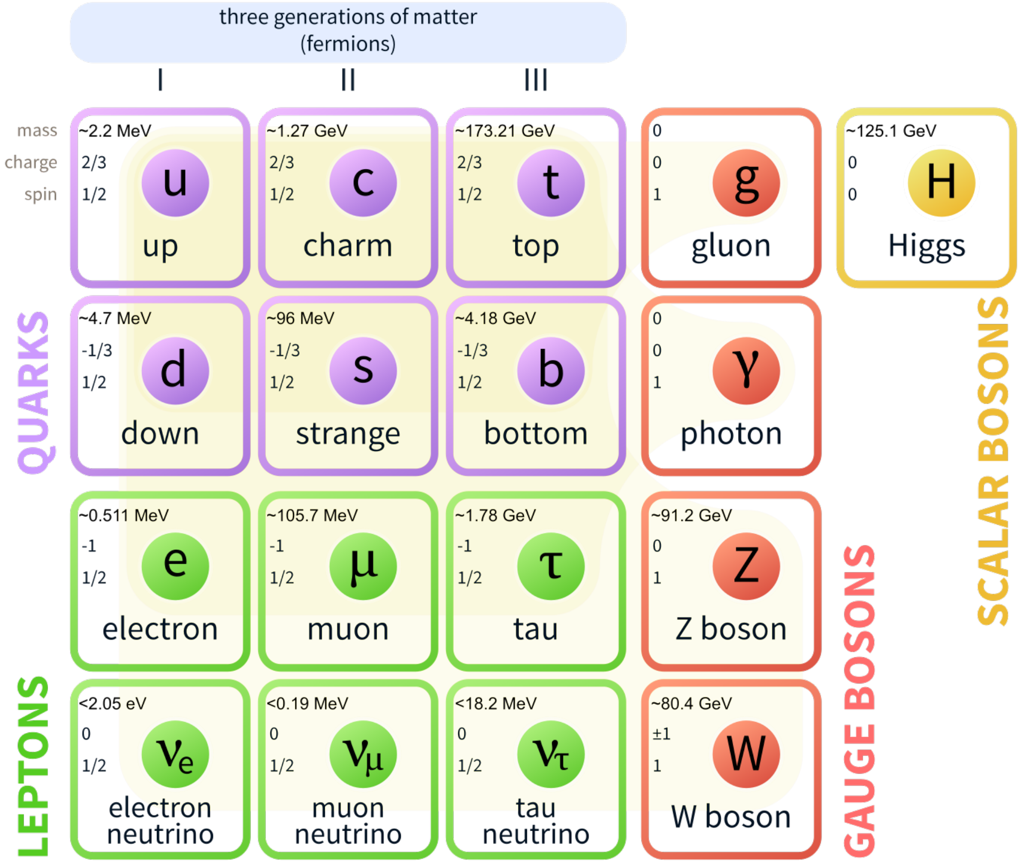

Figure 2.1: Overview of particles and interactions in the Standard Model picture [6, 7]. Mass, electric charge and spin of those are given. The masses are taken from the review of particle physics (2016) [7]. Neutrinos have non-zero masses from oscillations between different flavours. Quarks (in purple) are arranged in the upper doublets and leptons (in green) in the lower doublets (the actual doublets of leptons arrange neutrinos above charged leptons).

antiparticle except the Higgs boson (described later), Z boson and photon, which are their own antiparticle. The Standard Model antiparticles have the electric charge and other charges of opposite sign to their corresponding particles. Antiparticles have the same mass[1], lifetime and spin. Figure 2.1 summaries the Standard Model particles and interactions. The fermions are composed of six quarks and six leptons that are organised into doublets in three different generations. Quarks and leptons between different families differ by their flavour quantum numbers and mass. Each up-type quark carries $Q = +\frac{2}{3}e$, while each down-type quark carries $Q = -\frac{1}{3}e$. In case of leptons, each charged lepton (in the third row) carries $Q = -1e$, while all neutrinos are neutral. The up-type quarks and the neutral leptons have $I_3 = +\frac{1}{2}$, while the down-type quarks and the charged leptons have $I_3 = -\frac{1}{2}$. All those doublets are in left-handed states with a non-zero weak isospin, while the right-handed states only form singlets with $I_3 = 0$, which do not interact via the charged-current interaction[2]. In a higher generation, fermions are more massive.

As free particles observed in nature have a colour charge of zero, quarks cluster together to form colourless composite particles. They are held together by the strong interaction via gluon exchanges. The colourless particles are called hadrons. There are two classes of hadrons: baryons containing three quarks and mesons containing a quark and an antiquark. Baryons are half-integer-spin particles and mesons are integer-spin particles. Besides the strong interaction, quarks can interact with other fermions via both the electromagnetic and weak interactions. Leptons cannot interact via the strong interaction since they do not carry colour charge. The charged leptons interact via both electromagnetic and weak interactions, while the neutrinos interact only weakly.

The strength of each interaction is determined by a coupling constant. The coupling constant of the electromagnetic force, α, is about $\frac{1}{137}$. The massless photon which couples to the electric charge, Q, leads to the infinite range of this force. The weak force has a larger coupling constant and is short in range as its mediators are massive gauge bosons. The coupling of the strong interaction can be large (order of $O(1)$) at low energy, at which quarks and gluons are confined into hadrons, as mentioned above. At high energy, the coupling of the interaction becomes small and quarks can move freely inside the hadrons.

The weak interaction acts on all fermions via the $W^{\pm}$ and Z bosons. The charged $W^{\pm}$ bosons only act on left-handed particles and right-handed antiparticles, while the neutral Z boson also acts on right-handed particles[3], albeit with a different strength. The $W^{\pm}$ and Z gauge bosons obtain masses via electroweak symmetry breaking by the Higgs mechanism [8, 9]. The symmetry breaking happens only to the $\mathrm{SU}(2)_{I_3} \times \mathrm{U}(1)_Y$ group, while the $\mathrm{U}(1)_{\mathrm{EM}}$ group describing the electromagnetic force remains symmetric. Hence, the photon is massless and the electric charge is conserved. All fermions obtain their mass through Yukawa couplings between massless fermion fields and the scalar Higgs field. Furthermore, the mechanism predicts the so-called Higgs boson, which is an excitation of the Higgs field. The Higgs boson is massive and has no electric charge nor colour charge. It is unstable and decays almost immediately into other particles.

In the charged-current interaction, e.g. the $t \to Wb$ process, the flavour of a quark is not conserved. Transitions of quarks between the three generations are possible via the Cabibbo–Kobayashi–Maskawa (CKM) matrix introduced by Nicola Cabibbo, Makoto Kobayashi and Toshihide Maskawa. Theoretically, this means that the mass eigenstates of the quarks (d, s, b)[4] are different from their weak eigenstates (d',

---

[1] In particle physics, mass, momentum and energy are expressed in units of electronvolts, due to the use of the so-called natural units: $\hbar = c = 1$. One electronvolt (eV) is equal to 1.6×10^{-19} J.

[2] In the weak interaction, the charged-current interaction is mediated by the $W^{\pm}$ bosons. Another type of the interaction is the neutral-current interaction mediated by the Z boson.

[3] Only left-handed neutrinos exist in the Standard Model.

[4] The convention is to mix down-type quarks.

s', b'). They are connected to each other via the CKM matrix, V_{CKM}, as:

$$\begin{pmatrix} d' \\ s' \\ b' \end{pmatrix} = \begin{pmatrix} V_{ud} & V_{us} & V_{ub} \\ V_{cd} & V_{cs} & V_{cb} \\ V_{td} & V_{ts} & V_{tb} \end{pmatrix} \cdot \begin{pmatrix} d \\ s \\ b \end{pmatrix}.$$

The CKM matrix is a unitary matrix. Its elements describe the amplitude of a transition from one up-type quark, i, to another down-type quark, j, (or vice versa). The values of all nine CKM elements are estimated using results of all available experiments with theoretical constraints. The current magnitudes of the CKM matrix elements are [7]:

$$V_{\text{CKM}} = \begin{pmatrix} 0.97417 \pm 0.00021 & 0.2248 \pm 0.0006 & 0.00409 \pm 0.00039 \\ 0.220 \pm 0.005 & 0.995 \pm 0.016 & 0.0405 \pm 0.0015 \\ 0.0082 \pm 0.0006 & 0.040 \pm 0.0027 & 1.009 \pm 0.031 \end{pmatrix}.$$

The representation of the CKM matrix shows that the probability of the coupling within the same generation is close to one as seen on the diagonal. On the other hand, the off-diagonal terms, called the CKM suppressed terms, are rather small. This means that quarks mostly prefer to decay within the same generation. The second most probable transition is between the first and second generations, the third most probable transition is between the second and third generations. The transition between the first and third generations has the smallest probability.

To show particle interactions graphically, Feynman diagrams [10] are introduced. The diagrams are pictorial representations of probability amplitudes of a given process in perturbation theory. The Feynman diagrams are space-time diagrams. The time axis pointing to the right and the space axis pointing upward is commonly used in particle physics. Particles are represented by straight lines with arrows to the right, while the arrows of antiparticles point in the opposite direction. Wavy (or dashed) lines without any arrow represent the gauge bosons. Observable particles are shown by lines entering or leaving the diagram. The internal lines, which have the beginning and the ending in the diagram, represent virtual particles[5]. At each joining point called a vertex, all conservation laws corresponding to the interaction of each process have to be preserved. This implies that electric charge, baryon number[6] and lepton number[7] must be conserved at each vertex.

Figure 2.2 shows two examples of the Feynman diagrams for electron–positron scattering via the electromagnetic interaction at leading order. In Figure 2.2 (a), the diagram is interpreted as the e^+e^- annihilation process in which an electron and a positron annihilate into a virtual photon generating another e^+e^- pair. The two electrons are represented by the lines with arrows to the right and the two antielectrons, known as positrons, by the lines with arrows to the left. The photon is represented by the ended wavy line. The total electric charge of the initial-state system is $0e$; therefore, the final states are not only another electron–positron pair, but can also be $\mu^+\mu^-$ or another particle–antiparticle pair. Figure 2.2 (b) shows a different process by rotating the first diagram by 90°. An electron interacts with a positron by emitting a photon but they do not directly touch each other; hence, the final products remain the electron and the positron.

---

[5] Particles can be defined as virtual (or off-shell) particles by checking the magnitude of their four momentum which is not necessary equal to their rest mass.

[6] The baryon number (B) is an quantum number of a system defined as $B = \frac{1}{3}(n_q + n_{\bar{q}})$, where n_q and $n_{\bar{q}}$ are the number of quarks and the number of antiquarks, respectively.

[7] The lepton number (L) is another quantum number defined as $L = n_l - n_{\bar{l}}$, where n_l and $n_{\bar{l}}$ are the number of leptons and the number of antileptons, respectively.

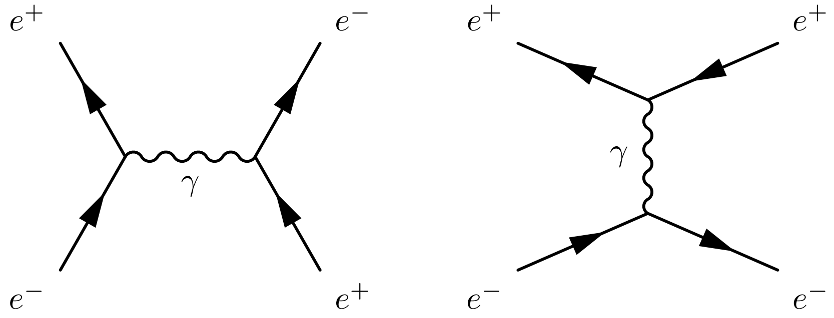

(a) (b)

Figure 2.2: Examples of Feynman diagrams at leading order in QCD for electron–positron scattering via the electromagnetic interaction.

2.2 Cross-sections in proton-proton collisions

To investigate interactions between subatomic particles experimentally, collisions of charged leptons or hadrons at high energy are required. At the LHC, two beams of protons are collided. Their interaction is the scattering process of the partons inside protons. Partons are the point-like constituents of hadrons, i.e. quarks, antiquarks and gluons. In the parton model proposed by Richard Feynman [11, 12], protons consist of two up quarks and one down quark (called valence quarks), as well as of quark–antiquark pairs from gluons (called sea quarks). The parton distribution functions (PDFs), $f_i(x_i, Q^2)$, describes the proton structure. They are defined as the probability of finding a parton of a certain flavour i with a certain longitudinal momentum fraction x_i at a certain energy scale Q^2, where $Q^2 = -q^2$, q is the four momentum of a produced mediator. The PDFs are usually determined based on parametrising and fitting to observed data from several experiments at the HERA[8], the Tevatron[9]and the LHC. Various sets of PDFs provided by different groups are generally used. Figure 2.3 shows the PDFs for u-, $\bar{u}$-, d-, $\bar{d}$-, c-, $\bar{c}$-, s-, $\bar{s}$-quark and gluon at $Q^2 = 10\,\text{GeV}^2$ provided by the MSTW 2008 group [13]. The momentum of a proton is carried mostly by valence quarks at large x and sea quarks at low x.

The probability to measure a certain production process X is described by the cross-section of the process. The cross-section corresponds to the effective area of a target hit by a probe. It is expressed in units of barn (b), $1\text{b} = 10^{-28}\ \text{m}^2$.

According to the factorisation theorem [14], the cross-section of the proton-proton scattering process $pp \to X$ can be calculated from two parts as:

$$\begin{aligned}
\sigma(p_1 p_2 \to X) &= \sum_{i,j} \int dx_i dx_j f_{i,p_1}(x_i, \mu_F^2) f_{j,p_2}(x_j, \mu_F^2) \cdot \hat{\sigma}_{ij\to X}(\hat{s}, \alpha_s(\mu_R), \mu_R, \mu_F)\,, \quad (2.2)\\
\hat{s} &= x_i x_j (p_1 + p_2)^2\,, \quad (2.3)
\end{aligned}$$

where $\hat{s}$ denotes the centre-of-mass energy squared of the colliding partons. The first part is the partonic cross-section ($\hat{\sigma}_{ij\to X}$), which comes from the hard scattering process between the incoming partons i and j at very short distance (high momentum transfer), where the strong coupling of the interaction is small. As a consequence, the partonic cross-section can be computed as a perturbative series in the strong

---

[8] The HERA was a hadron-electron ring accelerator at DESY.

[9] The Tevatron was a proton–antiproton collider at Fermilab.

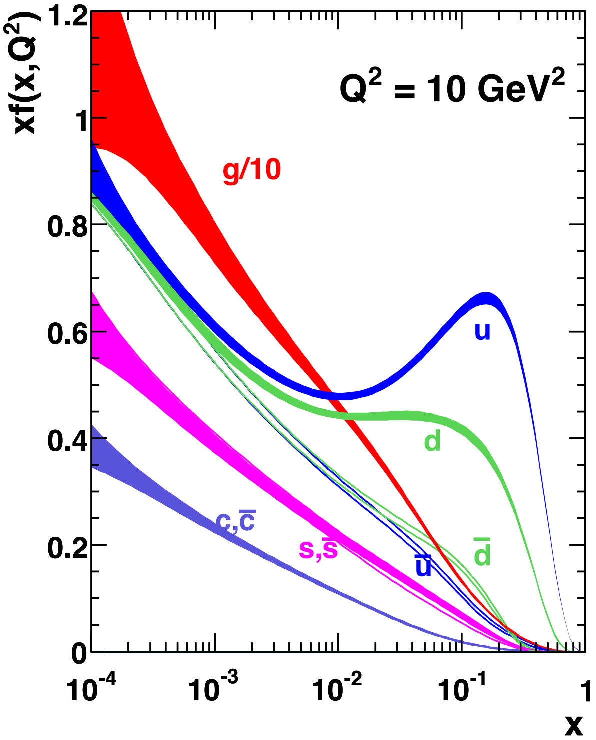

Figure 2.3: The NLO patron distribution functions as a function of the longitudinal momentum fraction of parton in proton at a scale of $Q^2 = 10\,\text{GeV}^2$ by the MSTW 2008 group [13]. The shaded areas show the uncertainties in the predicted values with one standard deviation.

coupling, α_s, at a reference scale called the renormalisation scale, μ_R. The second part is the probability of finding the partons i and j with the longitudinal momentum fractions x_i and x_j in the protons p_1 and p_2, $f_{i,p_1(j,p_2)}$. These two parts require a factorisation scale, μ_F, defining which partons are considered in the partonic cross-section and which partons are absorbed into the PDF. The factorisation scale and the renormalisation scale are arbitrary energy scales and they are often chosen to be $\mu_F = \mu_R = Q$.

2.3 Top-quark physics

The third generation of quarks was predicted by Makoto Kobayashi and Toshihide Maskawa in order to explain the observed CP violations in K meson decay in 1973 [15]. The top quark (sometimes called *truth* quark) is identified as the up-type quark of the third generation and its weak-isospin partner is the b-quark. The top quark is the heaviest elementary particle observed to date. Its mass is roughly 60,000 times the u-quark's mass and 40 times the b-quark's mass. The existence of the top quark was confirmed by the CDF and D0 experiments at the Tevatron in 1995 [16, 17]. After its discovery, various properties of the top quark have been explored by different experiments in order to understand the subatomic world. At the LHC, first top-quark measurements were accomplished in 2010 using proton–proton collision data at a centre-of-mass energy of 7 TeV. Single top-quark production via the weak interaction was first measured in 2011. The recent world average of the top-quark mass from measurements performed by the ATLAS, CDF, CMS and D0 collaborations is [18]:

$$m_t = 173.34 \pm 0.27(\text{stat}) \pm 0.71(\text{syst})\ \text{GeV}. \tag{2.4}$$

The top quark has a large decay width[10] of $\Gamma_t = 1.35\,\text{GeV}$ for $m_t = 173.3\,\text{GeV}$ [7]. Its corresponding lifetime is very short, $\tau_t \sim 5 \times 10^{-25}$ s. It decays before it forms any bound states.[11] Another consequence of the short lifetime is that the spin of the top quark can be inferred from the spin information of its decay products. According to the CKM matrix element $|V_{tb}| \gg |V_{ts}|$ and $|V_{td}|$, top quarks decay almost always into a b-quark and a W boson. In general, the decay modes of the top quark can be classified by the decay modes of the W boson. The W boson decays into a quark and an antiquark ($W \to q\bar{q}'$) with the branching ratio $\mathcal{B} = 68\%$ or into a lepton and its corresponding neutrino ($W \to \ell\nu$) with $\mathcal{B} = 32\%$. The first case is usually known as hadronic decay and the latter as leptonic decay.

2.3.1 Production of the top quark

At hadron colliders, top quarks are produced via two mechanisms. The production of top quark and top antiquark pairs ($t\bar{t}$) via the strong interaction is the dominant source of the top quarks at both the Tevatron and the LHC. Tens of thousands of $t\bar{t}$ were created at the Tevatron. Millions of $t\bar{t}$ were produced and studied at the LHC. Another top-quark production mechanism is single top-quark production via the weak interaction. The cross-section of single top-quark production is smaller than the cross-section of $t\bar{t}$ production, but this production mode is essential for investigating the electroweak theory.

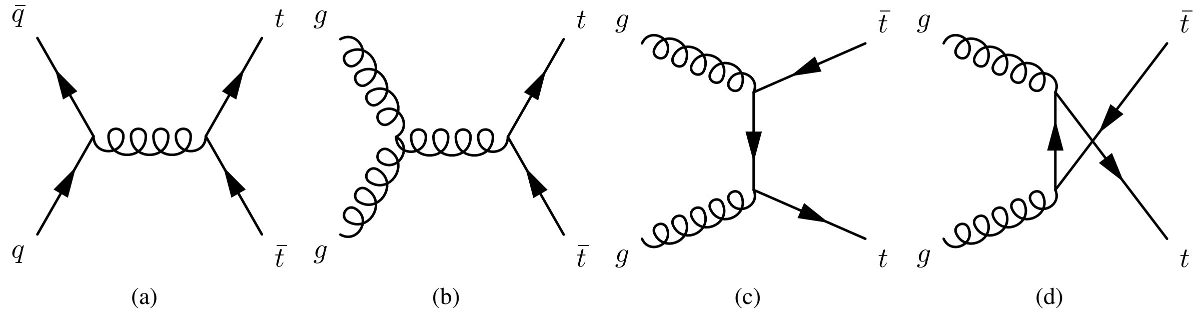

Figure 2.4: Examples of Feynman diagrams for $t\bar{t}$ production through the strong interaction at leading order via (a) quark-antiqaurk annihilation ($q\bar{q} \to t\bar{t}$) and (b-d) gluon fusion ($gg \to t\bar{t}$).

Top-quark pair production

At leading order in perturbative QCD calculations, the top-quark pairs are produced by quark–antiquark annihilation ($q\bar{q} \to t\bar{t}$), as depicted in Figure 2.4 (a) and by gluon-gluon fusion ($gg \to t\bar{t}$), as depicted in Figure 2.4 (b-c). As the minimal partonic energy is required to be $\sqrt{\hat{s}} \approx 2m_t$ for the production of top-quark pairs, a parton momentum fraction can be estimated from $x \approx 2m_t/\sqrt{s}$. This estimation is based on the fact that $\sqrt{\hat{s}} \approx x_i x_j s$, where s is the centre-of-mass energy squared of the collider and the momentum fraction of the partons i and j are assumed to be $x_i \approx x_j \approx x$. At the Tevatron at the centre-of-mass energy of $\sqrt{s} = 1.96\,\text{TeV}$, the value of the partonic momentum fraction is $x \approx 0.18$. Quark–antiquark annihilation contributes about 85% to the total cross-section there. In case of the LHC

---

[10] The decay width, Γ, is defined as the probability per unit time that any given particle will disintegrate. Often particles can decay in several ways called the partial decay widths, Γ_i. The sum of all partial decay widths is known as the total decay width, $\Gamma_{\text{tot}} = \sum \Gamma_i$. The mean lifetime of a particle, τ, is related to its total decay width as $\tau = \frac{1}{\Gamma_{\text{tot}}}$. Furthermore, one can determine the probability of a particle to decay into a particular decay mode in terms of the branching ratio, $\mathcal{B}$, which is defined as $\mathcal{B} = \frac{\Gamma_i}{\Gamma_{\text{tot}}}$.

[11] The typical time to form hadronic states is $\tau_{\text{had}} \sim 3 \times 10^{-24}$s.

at the centre-of-mass energy of $\sqrt{s} = 8\,\text{TeV}$, the corresponding partonic momentum fraction is $x \approx 0.04$. This means that the lower-x region becomes important. About 90% of the top-quark pairs are produced via the gluon fusion there. The total cross-section for the $pp \to t\bar{t}$ process at the centre-of-mass energy of $\sqrt{s} = 8\,\text{TeV}$ was calculated up to the next-to-next-to-leading order (NNLO) in QCD for $m_t = 172.5\,\text{GeV}$ using the MSTW2008, CT10 [19] and NNPDF [20] PDF sets. In these calculations, resummation of next-to-next-to-leading logarithmic (NNLL) soft gluons [21, 22] is included. The total cross-section is predicted to be:

$$\sigma(pp \to t\bar{t}) = 253^{+13}_{-15}\ \text{pb}. \tag{2.5}$$

The theoretical uncertainties are due to variations in the factorisation scale, the renormalisation scale, the PDFs and the strong coupling. The PDF and strong-coupling uncertainties are evaluated according to the PDF4LHC prescription [23]. The factorisation and renormalisation scales are varied independently by a factor of 2 and 0.5.

Experimentally, measurements of top-quark pair properties have been studied in different modes according to the decay products of the W bosons coming from the top quarks. The dilepton mode indicates the case where both of the W bosons decay leptonically. This mode contributes only 10.5%, but its final state is the cleanest. The second channel with a probability of 43.8% is called the semileptonic mode, where one of the W bosons decays hadronically and the other one decays leptonically. The hadronic mode is the case where both of the W bosons decay hadronically. This case happens with a chance of 45.7%, but it suffers strongly from large backgrounds caused by the production of jets[12]. Therefore, measurements of the cross-section for top-quark pair production have been performed mainly in the dilepton and semileptonic modes. Figure 2.5 shows the observed cross-section extracted by various measurements both at the Tevatron and the LHC. All measured cross-sections are in good agreement with the Standard Model predictions.

Single top-quark production

Single top quarks are produced via the electroweak interaction. There are three different production modes. They are distinguished according to the virtuality, $Q^2 = -q^2$, of the virtual W boson. Figure 2.6 depicts examples for Feynman diagrams for single top-quark production in the t-channel (a-b), the s-channel (c), and the Wt-channel (d-e). At the LHC at $\sqrt{s} = 8\,\text{TeV}$, the total cross-section of single top-quark production is predicted to be about 115.8 pb which is approximately 46% of the top-quark pair production cross-section. As the mass of the top quark is of the same order of magnitude as the scale of the electroweak symmetry breaking, single top-quark production is important as a probe to the electroweak theory.

t-channel production The t-channel is the dominant mode for single top-quark production at both the Tevatron (about 61%) and the LHC (about 76%). In the t-channel, a virtual space-like W boson ($q^2 \leq 0\,\text{GeV}^2$) fuses with a sea b-quark inside the proton to produce a top quark, as illustrated in Figure 2.6 (a). The final state of this production process can contain a second b-quark coming from a gluon which splits into a $b\bar{b}$ pair, as illustrated in Figure 2.6 (b). The $2 \to 3$ ($gq \to tbq'$) process is known as W-gluon fusion. In cross-section calculations, if the initial-state b-quark originates from the PDF of the proton, the $2 \to 2$ ($qb \to tq'$) process corresponds to the leading-order process. The b-quark is treated as massless in the matrix-element calculation. On the other hand, if the proton PDF contains no b-quark, the second b-quark is treated as massive and part of the matrix-element calculation. The

---

[12] A term "jet" is referred to as a hadron cluster produced by the hadronisation of a free quark or gluon.

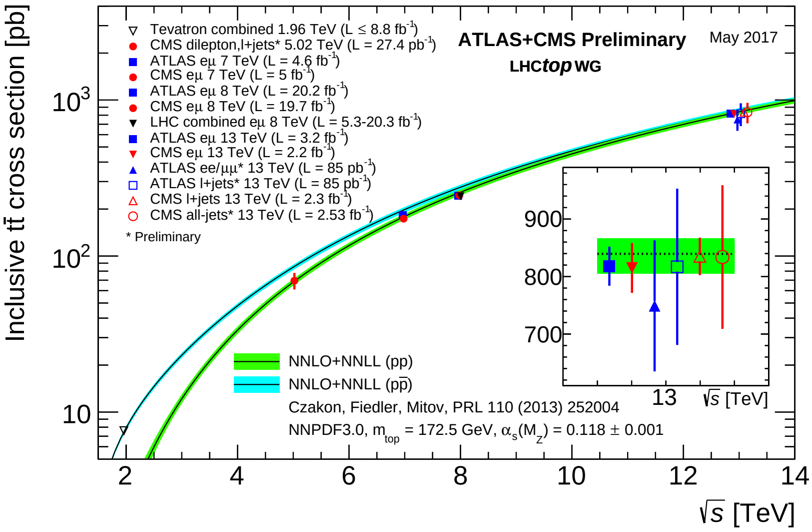

Figure 2.5: Observed and predicted cross-sections for top-quark pair production at the Tevatron and the LHC [24]. The measurements were preformed at $\sqrt{s}$ = 1.96 TeV by the CDF and D0 experiments, while at $\sqrt{s}$ = 7 TeV, 8 TeV and 14 TeV by the ATLAS and CMS experiments. The cross-sections are compared to the NNLO+NNLL predicted cross-section. The uncertainty band illustrates the theoretical uncertainties in the factorisation scale, the renormalisation scale, the parton distribution functions and the strong coupling.

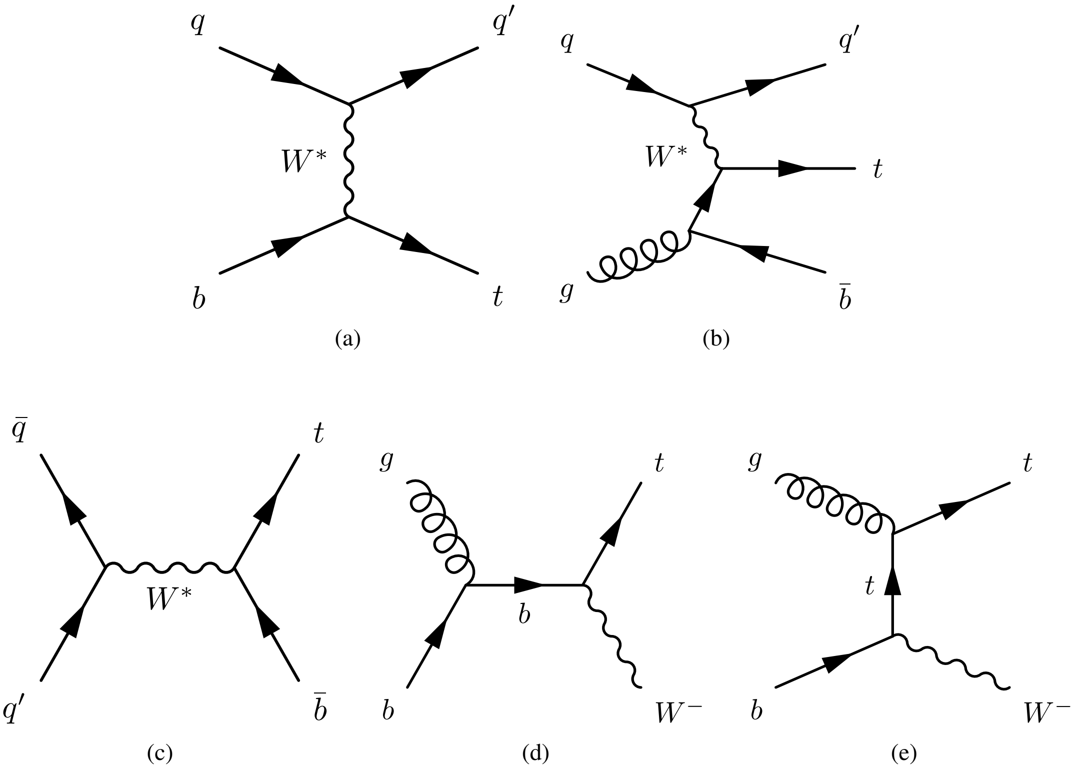

Figure 2.6: Examples of Feynman diagrams at leading order in QCD for single top-quark production through the weak interaction: (a) t-channel for the five-flavour scheme, (b) t-channel for the four-flavour scheme, (c) s-channel, and (d-e) Wt-channel.

$gq \to tbq'$ process corresponds to the leading-order process in the calculations. The first case is called five-flavour scheme (5FS), while the latter is called four-flavour scheme (4FS). The total cross-sections of top-quark and top-antiquark production in the t-channel (based on the $2 \to 3$ process) in pp collisions at a centre-of-mass energy of $\sqrt{s} = 8\,\text{TeV}$ for a top-quark mass of $m_t = 172.5\,\text{GeV}$ at NLO accuracy in QCD [25, 26] are calculated to be:

$$\sigma(tq) = 54.9^{+2.3}_{-1.9}\,\text{pb}\,, \tag{2.6a}$$

$$\sigma(\bar{t}q) = 29.7^{+1.7}_{-1.5}\,\text{pb}\,, \tag{2.6b}$$

where the MSTW2008, CT10 and NNPDF PDF sets are used. The theoretical uncertainties are calculated following the same prescription as used for the case of top-quark pair. More details about single top-quark production in the t-channel are given in Section 2.4.

s-channel production The cross-section for s-channel production is about 31% of the total cross-section for single top-quark production at the Tevatron, while it is only about 5% at the LHC at $\sqrt{s} = 8\,\text{TeV}$. In the s-channel, as shown in Figure 2.6 (c), a virtual time-like W boson ($q^2 \geq (m_t + m_b)^2$) is produced by the annihilation of a quark and an antiquark that belong to the same isospin doublet, mostly a u-quark and a d-antiquark. The W boson further decays into a single top quark and a b-antiquark. Some of the next-to-leading-order processes of the s-channel production as shown in Figure 2.7 (a) have the same initial and final states as the W-gluon fusion of the t-channel; however, one can distinguish them by their colour structure which does not allow them to interfere with each other [27]. The $t\bar{b}$ pair in the s-channel forms a colour singlet, since it comes from a virtual W boson, while the $t\bar{b}$ pair in the t-channel is a colour octet state since it comes from a gluon. The theoretical cross-section for s-channel production is predicted at NLO accuracy in QCD including the NNLL resummation of soft gluons using the MSTW2008 PDF set [28]. The total cross-section for pp collisions at $\sqrt{s} = 8\,\text{TeV}$ for $m_t = 172.5\,\text{GeV}$ is calculated to be:

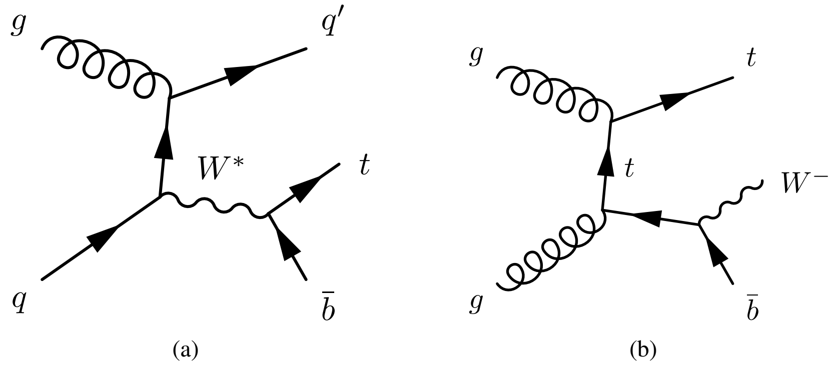

Figure 2.7: Example of Feynman diagrams at next-to-leading order for (a) s-channel production and (b) Wt-channel production.

$$\sigma(s) = 5.6 \pm 0.2\,\text{pb}\,. \tag{2.7}$$

Wt-channel production At the LHC, single top-quark production in the Wt-channel is the second largest production channel (about 19%), while its cross-section was too small to be observed at the Tevatron. A single top quark is produced in association with an on-shell (or close to on-shell) W boson ($q^2 = m_W^2$). At leading order, the W boson and the top quark are emitted from a virtual b-quark, as shown in Figure 2.6 (d) or t-channel-like as $bg \to Wt$ via a virtual top quark, as shown in Figure 2.6 (e). Considering the first case, but with an initial gg pair as shown in Figure 2.7 (b), this is an example of Wt-channel production at next-to-leading order. The final state corresponds to $t\bar{b}W$ which is the same as the final state of the production of top-quark pair (with the decay of one top quark) at leading order but with different kinematics. Predictions of the total cross-section of the Wt-channel production are available up to next-to-next-to-leading-order (NNLO) including soft-gluon resummation at NNLL [29]. For pp collisions at $\sqrt{s} = 8\,\mathrm{TeV}$, the theoretical total cross-section for Wt-channel production with $m_t = 172.5\,\mathrm{GeV}$ using the MSTW2008 PDF set is predicted to be:

$$\sigma(Wt) = 22.4 \pm 1.5\,\mathrm{pb}\,. \tag{2.8}$$

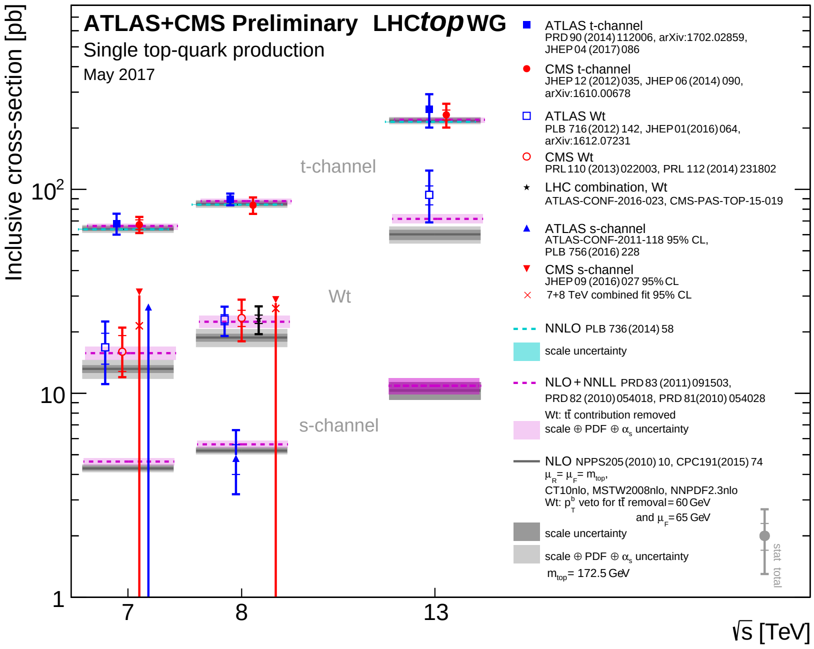

Figure 2.8: Observed and predicted cross-sections for single top-quark production at the LHC [24]. Various measurements were preformed at $\sqrt{s} = 7\,\mathrm{TeV}$, $8\,\mathrm{TeV}$ and $14\,\mathrm{TeV}$ by the ATLAS and CMS experiments. The cross-sections are compared to theoretical predictions at NLO in QCD including NNLL resummation for s- and Wt-channels, while at NNLO in QCD for t-channel.

Single top-quark production in the t-channel was observed at the Tevatron in 2009 using an integrated luminosity[13] of $\mathcal{L}_{\mathrm{int}} = 9.7\,\mathrm{fb}^{-1}$ of $p\bar{p}$-collision data at $\sqrt{s} = 1.96\,\mathrm{TeV}$ [30, 31]. It was discovered first due to its clean signature and sufficient statistics. Furthermore, several measurements of the t-channel production have been performed since 2011 at the LHC [32, 33]. For single top-quark production in the s-channel, it was first found in $p\bar{p}$ collisions at $\sqrt{s} = 1.96\,\mathrm{TeV}$ by the CDF and D0 experiments in 2014 [34]. The used dataset corresponds to $\mathcal{L}_{\mathrm{int}} = 9.7\,\mathrm{fb}^{-1}$. An evidence for the s-channel single top-quark production in pp collisions at $\sqrt{s} = 8\,\mathrm{TeV}$ corresponding to $\mathcal{L}_{\mathrm{int}} = 20.3\,\mathrm{fb}^{-1}$ was reported by the ATLAS experiment in 2015 [35]. The first observation of the Wt-channel single top-quark production was announced by the CMS experiment using pp-collision data at $\sqrt{s} = 8\,\mathrm{TeV}$ corresponding

---

[13] The (instantaneous) luminosity is defined as the number of particles produced in an interaction point per unit time. Integrating it over time, one obtains the so-called integrated luminosity. The determination of luminosity is given in detail in Section 3.3.

to $\mathcal{L}_{\text{int}} = 12.2\,\text{fb}^{-1}$ in 2014 [36]. Figure 2.8 summarises the cross-section measurements for single top-quark production by the ATLAS and CMS experiments. The results for all three production channels are in good agreement with the theoretical predictions and the other measurements. The most precise measurement is for the single top-quark production in the t-channel at $\sqrt{s} = 8\,\text{TeV}$ by the ATLAS experiment.

2.4 Single top-quark production in the t-channel

As mentioned previously, calculations of the cross-sections of t-channel single top-quark production can be done with two different approaches according to the number of flavours present in the PDF of the proton. In theory, the 5FS and 4FS should yield the same prediction if all orders of the perturbative QCD series are taken into account. In Ref. [25], the theoretical cross-sections as well as the resulting kinematic distributions of the 5FS and 4FS are compared. The 5FS has a smaller dependence on the choice of renormalisation and factorisation scales, as the scale dependence is mainly derived from the heavy-quark lines. The difference between the total cross-sections predicted at NLO accuracy in QCD in the two schemes is about 5%. The 4FS has a better description for all relevant differential distributions, in particular for the rapidity and the transverse momentum of the second b-quark.

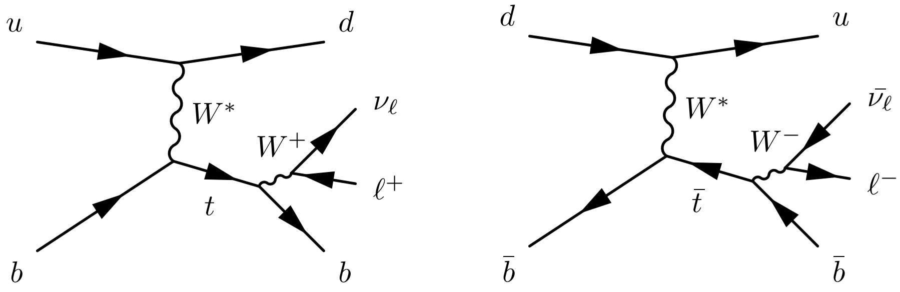

(a) (b)

Figure 2.9: Example of Feynman diagrams at leading order for (a) single top-quark and (b) top-antiquark t-channel production by the exchange of a virtual W^{*} boson, including the decay chain of the top quark and top antiquark, respectively.

In the t-channel at the LHC energies, the production cross-section of single top quarks is about twice the production cross-section of single top antiquarks as the scattered light quark in the t-channel exchange of a W boson mostly originates from one of valence quarks in the proton. As mentioned in Section 2.2, there are two valence u-quarks and one valence d-quark inside the proton. The valence u-quarks contribute to the production of single top quarks as illustrated in Figure 2.9 (a), while the valence d-quarks produce single top antiquarks as illustrated in Figure 2.9 (b). Therefore, one may extract the information of the PDFs of the u-quark and d-quark by performing separate measurements of these two production processes. The decay chain of single top (anti)quarks is also shown in the figure. As mentioned above, top (anti)quarks decay either hadronically or leptonically according to the decay modes of the produced W boson. The branching fraction of the hadronic decay mode is about twice as high as that of the leptonic decay mode, but large backgrounds mainly from multijet events can have the same final state as the hadronic decay mode. The leptonic decay mode can be isolated much better. As the charge of the lepton is inherited from the charge of the top quark, one can experimentally separate t-channel single top-quark and top-antiquark production according to the sign of the lepton charge. Therefore, the main focus in this thesis is the t-channel single top-quark and top-antiquark production in the leptonic decay mode.

CHAPTER 3

LHC and ATLAS experiment

The present analysis is performed using proton–proton collision data collected in the year 2012 by the ATLAS detector at the Large Hadron Collider (LHC). This chapter introduces the LHC and the ATLAS detector. The determination of the luminosity in ATLAS is briefly discussed at the end of the chapter.

3.1 Large Hadron Collider

The Large Hadron Collider (LHC) [37] is the most complex and powerful circular particle accelerator in the world. It is located at CERN, the European Organization for Nuclear Research, at the Switzerland-France border near Geneva. The LHC beam pipe has a circumference of approximately 27 km and lies about 100 m underground. Two beams made of bunches of hadrons are accelerated in opposite directions, then collided with each other. The LHC is expected to reach a centre-of-mass energy of $\sqrt{s} = 14$ TeV and a design luminosity of $\mathcal{L} = 10^{34}$ cm^{-2} s^{-1} in proton–proton collisions. By studying the particles produced in such collisions, the predictions of the Standard Model of particle physics can be verified, some of its parameters measured, and clarify several remaining puzzles about the universe. In addition, the LHC has a heavy-ion programme to study matters in the conditions that may exist in the very early universe according to the Big Bang theory.

Proton beams are prepared by several accelerators before entering the LHC ring. Figure 3.1 illustrates a schematic view of the CERN accelerator complex. Protons created by a hydrogen-gas source are accelerated by a radio-frequency (RF) cavity to 750 keV. They are then injected into the Linear Accelerator called LINAC2 to increase their energy to 50 MeV. The protons are sent to the Proton Synchrotron (PS) by the PS Booster. The protons leaving the PS with an energy of 25 GeV are injected into the Super Proton Synchrotron (SPS) to bring their energy up to 450 GeV. The two separate beams are injected into the LHC ring in opposite directions in order to be further accelerated to reach a maximal energy. The LHC ring contains dipole magnets that keep the proton beams on their circular path. For this purpose, the dipole magnets have to generate magnetic fields of 8.3 T. Quadrupole magnets are used for focusing the beams on four interaction points. In addition, multipole magnets are installed for small corrections of magmatic-field errors. The magnet system of the LHC is kept on its nominal operating temperature of 1.9 K using super-fluid helium.

The operation of the LHC at a proton–proton centre-of-mass energy of $\sqrt{s} = 7$ TeV was successful in 2010. In the year 2012, the centre-of-mass energy was increased up to $\sqrt{s} = 8$ TeV with around 1380 bunches per beam and about 1.7×10^{11} protons per bunch. A maximum instantaneous luminosity of 7.7×10^{33} cm^{-2} s^{-1} was reached. This corresponds to an event rate of 20 MHz. The full 2012

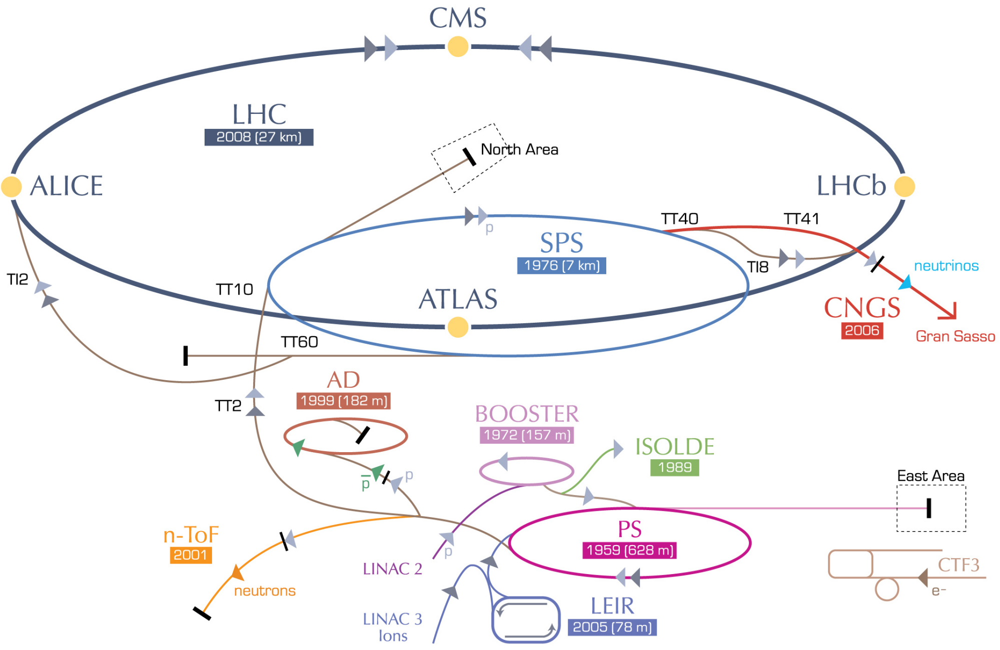

Figure 3.1: Sketch of the CERN accelerator chain [38].

proton–proton dataset was used in this present analysis. The operation of the LHC was continued in the year 2015 with proton–proton collisions at centre-of-mass energy of $\sqrt{s} = 13\,\text{TeV}$.

One of the biggest challenges at high instantaneous luminosity is multiple proton–proton collisions besides the collision of interest in each bunch crossing, called pile-up interactions. The presence of these interactions plays an important role in many analyses as a significant background. The number of pile-up events increases when raising the instantaneous luminosity. The average number of interactions was about 9 during 2011 and about 21 during 2012 [39]. It is expected to be more than 50 interactions per bunch crossing during Run 2 of the LHC [40].

There are four main detectors installed at the interaction points of the LHC. ATLAS and CMS are general-purpose detectors. Their aim is to investigate the widest possible range of particles and their interactions in the proton–proton collisions in order to test the Standard Model of particle physics and look for predicted phenomena beyond the Standard Model as well as completely new scenarios in physics. The ATLAS and CMS detectors were designed independently in order to cross-check each other. LHCb [41] is a medium-sized detector. Its goal is to contribute to understanding why the dominant substances in the visible universe are particles rather than their corresponding antiparticles using b-quarks. Another medium-sized detector is ALICE [42]. The ALICE experiment focuses on an understanding of heavy-ion collisions. These collisions are supposed to recreate a state of matter which existed shortly after the Big Bang, namely the quark-gluon plasma. Besides the four main detectors of the LHC, there are two more experiments, TOTEM [43] and LHCf [44], which are much smaller in size and weight. The TOTEM detector is placed near the CMS detector. The TOTEM experiment concentrates on the proton structure in detail as well as precise measurements of the proton–proton cross-section. The LHCf detector is located near the ATLAS detector. Cosmic rays have been studied in the laboratory conditions by the

LHCf experiment. A seventh experiment at the LHC, named as MoEDAL [45], is designed to search for magnetic monopoles as well as highly ionizing stable massive particles.

Kinematic variables

The standard coordinate system used at hadron colliders, e.g. at the LHC, is a right-handed (x, y, z) coordinate system. At the interaction point in the centre of a detector, the z-axis is parallel to the beam in the counter-clockwise direction. The x-axis points towards the centre of the LHC ring. The y-axis points upwards. In addition, cylindrical coordinates (r, θ, ϕ) are employed to describe particle positions. For a particle with a four momentum of (p_x, p_y, p_z, E), its transverse momentum, p_{T}, and its invariant mass, m, are defined as:

$$p_{\mathrm{T}} = \sqrt{p_x^2 + p_y^2}\,, \tag{3.1}$$

$$m = \sqrt{E^2 - p_x^2 - p_y^2 - p_z^2}\,. \tag{3.2}$$

The radial distance of the particle from the beam axis, r, is defined as:

$$r = \sqrt{x^2 + y^2}\,. \tag{3.3}$$

The polar angle, θ, is the angle between the particle direction and the beam axis. The azimuthal angle, ϕ, is the angle in the $x - y$ plane against the x-axis. It is common to use the rapidity, y, instead of the polar angle in particle physics. The definition of the rapidity is:

$$y = \frac{1}{2}\ln\left(\frac{E + p_{\mathrm{z}}}{E - p_{\mathrm{z}}}\right). \tag{3.4}$$

This parameter is useful since differences in the rapidity of two particles are invariant under Lorentz boosts along the beam axis. The pseudorapidity is another important quantity of a particle. It is simply used instead of the rapidity for highly relativistic particles, which are assumed to be massless or $E >> m$, since it depends upon only the polar angle θ as:

$$\eta = -\ln\left(\tan\frac{\theta}{2}\right). \tag{3.5}$$

The distance separation of two particles in the $\eta - \phi$ plane is given as:

$$\Delta R = \sqrt{(\Delta\eta)^2 + (\Delta\phi)^2}\,. \tag{3.6}$$

This quantity is invariant under Lorentz boosts along the beam axis if the involved particles are massless.

3.2 The ATLAS detector

ATLAS (A Toroidal LHC ApparatuS) is a multi-purpose particle detector. It has a symmetric cylindrical shape along the beam axis to explore the proton–proton collisions at the LHC. The ATLAS detector, with a size of about 44 m length, 25 m diameter and about 7 000 t weight, is the largest particle detector ever built. Many particle-physics experiments have been performed within the framework of the ATLAS collaboration. About 3000 physicists from 182 institutions in 38 countries around the world participate

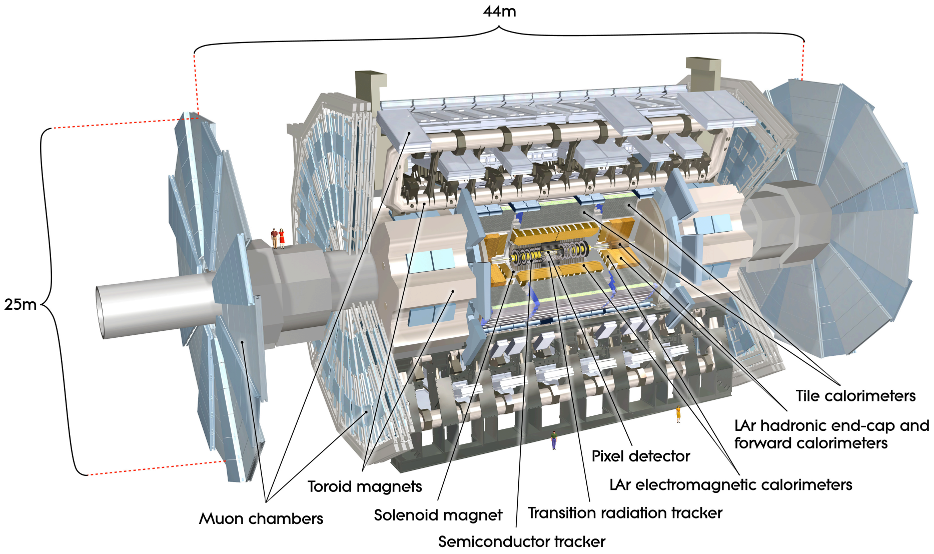

Figure 3.2: An overview of the ATLAS detector and its components [47].

in the project [46]. The ATLAS detector is structured in multiple layers of the individual components surrounding the interaction point as illustrated in Figure 3.2. Each component is built up from different materials in such a way that corresponding particles interact with the material and deposit their energies during interactions. The detector consists of three major components: the inner detector, the calorimeter and the muon spectrometer. In the following, an overview of the components of the ATLAS detector based on Ref. [47] is given.

3.2.1 Inner detector

The inner detector is the central tracking system of the ATLAS detector. It is placed around the interaction point of the ATLAS detector. The inner detector is designed to provide information about the point of origin called the vertex, momentum and charge of charged particles traversing the detector. The inner detector comprises three main sub-components, the pixel detector, the semiconductor tracker and the transition radiation tracker as illustrated in Figure 3.3. All sub-components are contained in a cylindrical envelope with 1.15 m diameter and 7.24 m length, surrounded by a solenoid magnet which provides a field of 2 T. The inner detector covers the pseudorapidity range of $|\eta| < 2.5$. The barrel region of each detector is arranged in concentric cylinders around the beam axis, while the end-cap regions are positioned on disks which are perpendicular to the beam axis.

The pixel detector is the innermost component with the inmost radial distance of just 50.5 mm away from the beam line. It consists of silicon pixel sensors with a pixel size of $50\,\mu\text{m} \times 400\,\mu\text{m}$. The pixel sensors are arranged in three concentric barrel layers and three end-cap disks on each side to cover a region up to $|\eta| < 2.5$. With about 80.4 million readout channels, the pixel detector is one of the most precise trackers of the ATLAS detector. A charged particle is expected to provide three hits per track in the pixel detector.

The semiconductor tracker (SCT) covers the intermediate radial distance from 299 mm to 560 mm. It

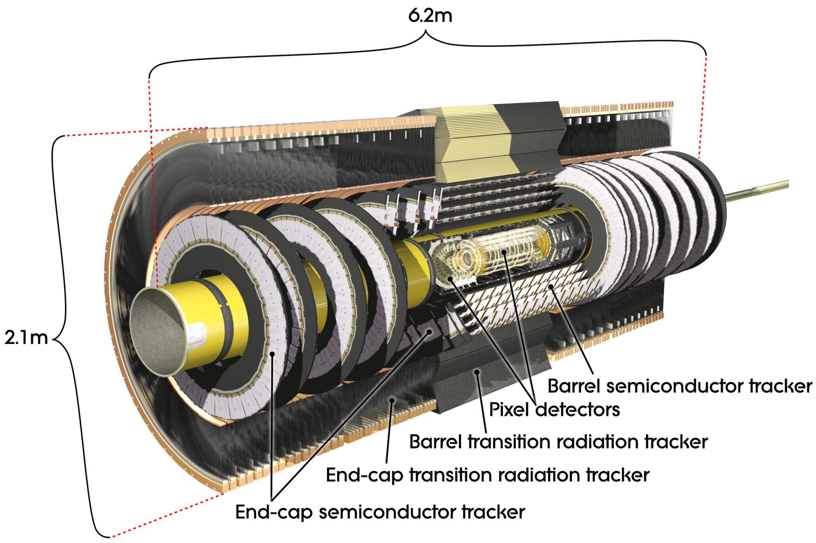

Figure 3.3: An overview of the ATLAS inner detector [47].

consists of silicon sensor modules that are arranged in four concentric layers in the barrel region as well as nine disks on each end-cap to cover the same η region as the pixel detector. Each module comprises two silicon strip sensors that are rotated by 40 mrad with respect to each other. Each of the silicon sensors consists of 768 strips of 120 mm long with a strip pitch of 80 µm. The strips are roughly parallel to the beam direction in the barrel region and radial in the forward regions. The total number of readout channels is about 6.3 million. The SCT is designed to provide four space points per track.

The transition radiation tracker (TRT) comprises straw tubes filled with a gas mixture of 70% Xe, 27% CO_2 and 3% O_2. Each straw tube of 4 mm diameter is enclosed by multi-layer films of 35 µm thickness. The barrel of the TRT is arranged into cylindrical layers covering the radial distance from 563 mm to 1 066 mm. In the barrel region, there are 73 layers of straws with a length of 144 cm each aligned parallel to the beam pipe. In the end-cap regions, 160 straw planes are arranged radially in wheels with a length of 37 cm. The total number of readout channels is about 351000. Between the straw layers (planes) are fibres (foils) providing transition radiation photons when charged particles, in particular electrons, traverse it. This is useful for electron identification. A stable particle with a transverse momentum of $p_{\mathrm{T}} > 0.5$ GeV and the pseudorapidity of $|\eta| < 2.0$ is expected to cross more than 36 straws. In the barrel-end-cap transition region ($0.8 < |\eta| < 1.0$), the expected number of crossed straws is reduced to a minimum of 22.

3.2.2 Calorimeter

The ATLAS calorimeter system is located outside the solenoid magnet surrounding the inner detector. The calorimeter system is designed to measure the energy of particles. In addition, it provides information about particle identification. It is divided into two sub-systems: the EM calorimeter and the hadron calorimeter as illustrated in Figure 3.4. The calorimeter system comprises absorber and active material. Incoming particles interact with absorber material and deposit their energy in the calorimeter which can

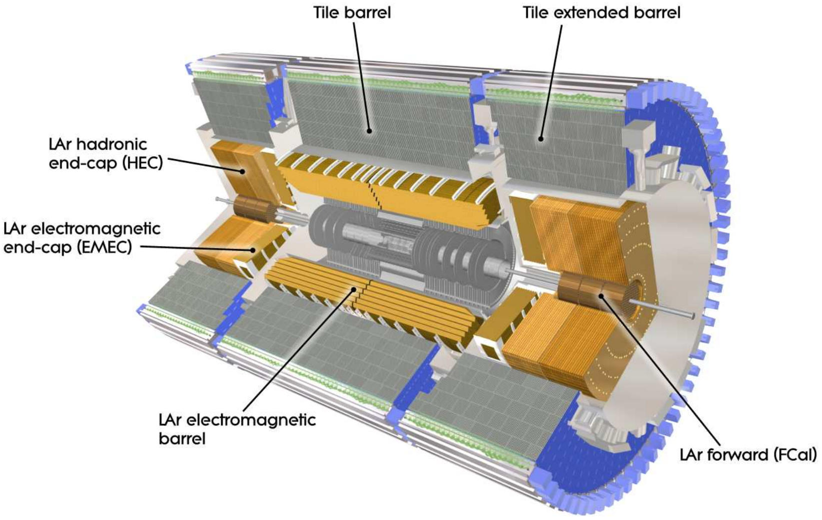

Figure 3.4: An overview of the ATLAS calorimeter system [47].

be further detected by active material. The EM calorimeter is designed to measure EM showers created by electrons and photons, while the hadron calorimeter measures hadronic showers created by jets.

The EM calorimeter is the closest part of the system to the beam pipe. It is divided into a barrel covering the pseudorapidity of $|\eta| < 1.475$ and two end-caps covering the pseudorapidity of $1.375 < |\eta| < 3.2$. Each of these three components is installed in their own cryostat. The EM calorimeter uses lead plates bent in an accordion shape as absorber material and liquid argon (LAr) as active material. Due to the accordion geometry, a complete ϕ range without any cracks in the azimuthal direction is covered. The EM calorimeter is divided in depth into three sections in the precision-measurement region of $|\eta| < 2.5$ and into two sections in the higher region of $2.5 < |\eta| < 3.2$. A presampler detector is used to measure the energy loss in front of the calorimeter in the region of $|\eta| < 1.8$. The EM calorimeter has a thickness of larger than 22 electromagnetic radiation lengths[1], X_0, in the barrel and larger than 24 X_0 in the end-caps. It has a cell granularity ranges from 0.003 to 0.1 in $\Delta\eta$ and from 0.025 to 0.1 in $\Delta\phi$.

The hadron calorimeter consists of the tile calorimeter, the LAr hadron end-cap calorimeters and the forward calorimeter. The tile calorimeter encloses the EM calorimeter. It has a central barrel part ($|\eta| < 1.0$) together with two extensions ($0.8 < |\eta| < 1.7$). Steel is used as absorber and scintillating tiles as active material. The tile calorimeter is subdivided into three layers with a granularity in $\Delta\eta \times \Delta\phi$ of 0.1×0.1 in the first two layers and of 0.2×0.1 in the last layer. The total thickness of the tile calorimeter is about 7.4 hadronic interaction lengths[2], λ. In the end-cap regions, the calorimeters comprise four layers covering the region of $1.5 < |\eta| < 3.2$. Copper plates are used as absorbers and LAr as active material. The cell granularity is 0.1×0.1 in the region of $|\eta| < 2.5$ and 0.2×0.2 for the other region. The

---

[1] The radiation length (X_0) is a property of a material indicating the energy loss of electromagnetic-interacting particles with the material. It is defined as the mean distance to reduce the energy of an electron by $\frac{1}{e}$ of its energy by bremsstrahlung or $\frac{7}{9}$ of the mean free path for pair production by a high-energy photon.

[2] The hadronic interaction length (λ) is defined as the mean free path of a hadron traversing a material to reduce its energy by a factor of $\frac{1}{e}$.

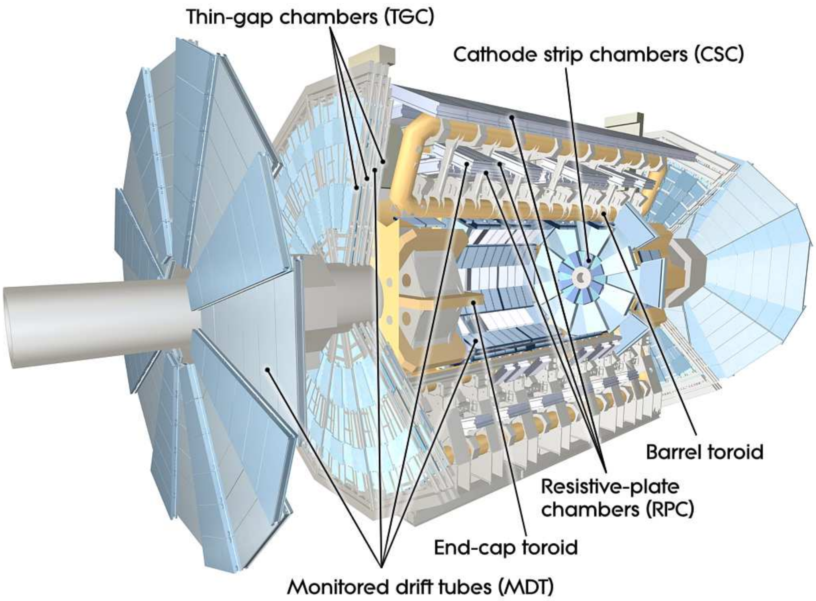

Figure 3.5: An overview of the ATLAS muon system [47].

forward calorimeter consists of three modules covering the region of $3.1 < |\eta| < 4.9$. The first module is made of copper plates as absorbers to measure EM showers, while the other modules are made of tungsten to measure hadron showers. LAr is utilised as active material. The forward calorimeter has a depth of about 10λ.

3.2.3 Muon spectrometer

The muon spectrometer is the outermost part and the largest tracking system of the ATLAS detector to measure muons, which cannot be identified by the calorimeter system. It is designed to measure muons with transverse momentum from 3 GeV to 1 TeV with a precision better than 10%. The muon spectrometer contains three large superconducting air-core toroids, precision tracking chambers and a trigger system. The three toroids generate a strong magnetic field in order to bend the muon tracks. The barrel toroid spreads over 25.3 m length with inner and outer diameters of 9.4 m and 20.1 m, respectively. There is an end-cap toroid at each end of the barrel toroid with a radius distance between 1.65 m to 10.7 m. The barrel toroid covering the region of $|\eta| < 1.4$ provides a bending power of 1.5 Tm to 5.5 Tm. The end-cap toroids covering the region of $1.6 < |\eta| < 2.7$ provide a bending power of 1 Tm to 7.5 Tm. The muon spectrometer consists of monitored drift tubes (MDTs), cathode strip chambers (CTCs), resistive plate chambers (RPCs) and thin gap chambers (TGCs) as shown in Figure 3.5.

Monitored drift tubes (MDTs) are used over most of the η-range to provide a precision momentum measurement of the tracks of muons. The MDTs with a diameter of 30 mm are filled with a Ar/CO_2 gas mixture. They are arranged into three layers in the barrel region and into four layers in the end-caps. The MDTs aim to reach a resolution of 60 μm − 80 μm. Cathode strip chambers (CSCs) are used instead of the MDTs for the innermost layer of the end-caps in the range of $2.0 < |\eta| < 2.7$ to deal with high flux rate in this forward region. The CSCs are multi-wire proportional chambers. The CSCs reach a resolution of 40 μm in the bending plane and a resolution of 5 mm in the transverse plane.

The trigger system of the muon spectrometer covers a region of $|\eta| < 2.4$ and consists of resistive plate chambers (RPCs) in the barrel ($|\eta| < 1.05$) as well as thin gap chambers (TGCs) in the end-caps ($1.05 < |\eta| < 2.4$). The RPCs consist two parallel electrode plates with a gas mixture of $C_2H_2F_4$, Iso-C_4H_{10} and SF_6. The TGCs are multi-wire proportional chambers filled with a gas mixture of CO_2 and n-C_5H_{12}. The trigger system identifies bunch crossings and provides p_T thresholds together with coordinate information in the direction orthogonal to that provided by the precision-tracking system.

3.2.4 Trigger and data acquisition system

During the 2012 run of the LHC, bunches of protons were collided in the centre of the ATLAS detector at a rate of 20 million bunch crossings per second. At the design luminosity, there will be 40 million bunch crossings per second. Each event requires a data volume of approximately 1.3 MB; therefore, it is impossible to record every collision event. Moreover, not all events are of interest. With the help of the ATLAS trigger and data acquisition system, interesting physics events can be selected. This implies that the total amount of data is reduced; for example, the event rate was reduced from 20 MHz to 400 Hz during 2012 [48]. The trigger system consists of three levels of event selection: Level 1 (L1), Level 2 (L2) and Event Filter (EF). The L1 trigger is hardware-based, while the L2 and EF triggers are software-based.

The L1 trigger uses information from the calorimeter and muon spectrometer detectors to search for signatures of high-p_T muons, electrons, photons, tau leptons decaying hadronically, jets, and events with large total transverse energy or large missing transverse energy. The L1 trigger takes a decision to keep an event in about 2.5 μs. It reduces the event rate to 65 kHz. For each event that passes the L1 trigger, regions that satisfy trigger requirements are marked as regions-of-interest (RoI) in η and ϕ within the detector. The RoI information is subsequently used by the L2 trigger. The L2 uses information from all detector components, including the inner detector, which is not available at L1. The L2 trigger reduces the event rate to about 5.5 kHz and each event has a processing time of roughly 40 ms. The events selected by the L2 trigger are passed on to the EF trigger, which reconstructs them using object reconstruction algorithms that are also utilised in physics analyses. The processing time of the EF trigger to keep or reject an event is about 1 s. The EF trigger decision reduces the event rate to roughly 400 Hz. The events in this stage are classified into ATLAS physics data streams e.g. the Egamma stream containing events passing the electron or photon triggers and the Muon stream containing events passing muon triggers.

3.3 Luminosity determination

The instantaneous luminosity ($\mathcal{L}$) is a measure of the rate at which collisions happen in an interaction point. The luminosity is usually expressed in $\mathrm{cm}^{-2}\mathrm{s}^{-1}$. The number of produced events per unit time in the interaction point can be written as:

$$\dot{N} = \sigma \mathcal{L}, \tag{3.7}$$

where σ is the cross-section of the interested process. It can be seen from Equation 3.7 that the number of produced events increases with more luminosity. As a consequence, statistical uncertainty is reduced.

In the following, a short description on the luminosity determination for the ATLAS detector based on Refs. [49, 50] is given. The LUCID detector and the Beam Conditions Monitor (BCM) are employed for the luminosity measurement for each bunch in ATLAS. The LUCID detector is a Cerenkov detector placed at a position of 17 m on each side of the interaction point. It consists of sixteen aluminium tubes filled with C_4F_{10} to measure the visible inelastic proton–proton scatterings in the forward direction covering the pseudorapidity range of $5.6 < |\eta| < 6.0$. The BCM detector comprises four diamond sensors located at a distance of 1.84 m on each side of the interaction point. It measures the visible inelastic proton–proton collisions at the pseudorapidity range of $|\eta| = 4.2$.

The number of visible (observed) interactions per bunch crossing, μ_{vis}, measured by LUCID and BCM is related to the luminosity as:

$$\mathcal{L} = \frac{n_b f_r \mu_{\text{vis}}}{\sigma_{\text{vis}}}, \tag{3.8}$$

where n_b is the number of bunches per beam, f_r is the revolution frequency in the collider and σ_{vis} is the visible cross-section. To obtain the luminosity, the visible cross-section has to be calibrated using beam-separation scans, known as van-der-Meer scans [51, 52]. The instantaneous luminosity can then be expressed in terms of the parameters of the colliding beams as:

$$\mathcal{L} = \frac{n_b f_r n_1 n_2}{2\pi \sigma_x \sigma_y}, \tag{3.9}$$

where n_1 and n_2 are the number of protons per bunch of each of the two beams, and σ_x and σ_y are the horizontal and vertical widths of the overlap of the two beams. The beam widths are measured in van-der-Meer scans during several special runs.

In addition, the integrated luminosity is commonly used as a measure of the total amount of data taken over a particular time. It is usually given in units of pb^{-1} or fb^{-1}.

CHAPTER 4

Particle reconstruction

As several different particle types can be produced in each collision event, it is necessary to reconstruct them before any physics analyses can be performed. The ATLAS combined performance working groups develop algorithms for the reconstruction of electrons, photons, muons, τ leptons, and jets [53]. For this analysis, the final state of the signal events is characterised by one electron or muon, one neutrino, and two jets, one of them is identified as originating from a b-quark. The reconstruction of neutrinos can be done based on the missing transverse momentum as they are not measured directly by the detector.

In this chapter, a short description of the algorithms used to reconstruct and identify the final-state particles which are relevant for the present analysis is given. Furthermore, the reconstruction of the W boson and the top quark in t-channel single top-quark production is addressed.

4.1 Tracks and vertices

The trajectory of a charged particle through the magnetic field of the tracking detectors can be approximated by a helix, which is described by five parameters $(d_0, z_0, \theta, \phi_0, q/p)$. These parameters are defined at the perigee point of the track, which is the point of closest approach of the track to a reference point (e.g. the origin) as depicted in Figure 4.1. The parameters d_0 and z_0 are the transverse and longitudinal distances of the perigee from the origin, θ is the polar angle, ϕ_0 is the azimuthal angle at the perigee, and q/p is the ratio of the electric charge to the momentum.

In the following, the two strategies employed in ATLAS to reconstruct the tracks of charged particles in the inner detector based on Refs. [55, 56] are briefly discussed. The reconstruction of charged particle tracks starts from finding hits in the tracking detectors that belong to one track using the inside-out algorithm. Three space points from the hits in the silicon detectors (pixel and SCT) are formed to determine a preliminary direction of the track. Further hits are added to the candidate track using a Kalman filter [57, 58]. After adding each hit, the trajectory of the track is refitted with a χ^2 fit to select only the hits that improve the track fit. After the inside-out strategy, the outside-out procedure is performed to complement the track reconstruction. This approach starts from searching for unassigned track segments in the TRT using a Kalman filter and matches them back to the remaining hits in the silicon detectors.

The origin of a set of reconstructed tracks is called a vertex. The primary vertex is the point where a pp collision presumably occurred. At high instantaneous luminosity, several primary vertices are found in an event due to pile-up interactions. The primary vertex of the hard interaction is identified as the one that has the largest quadratic sum of the transverse momenta of its associated tracks. The primary

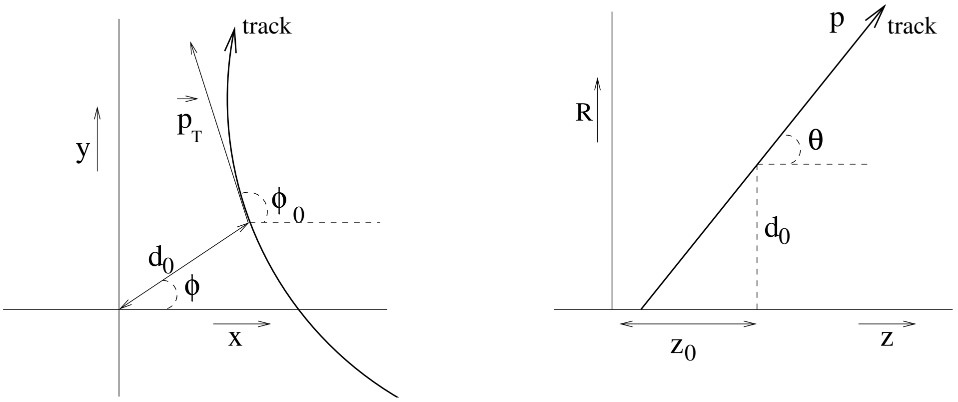

Figure 4.1: Illustration of the track parameters at the perigee point depicted in the $x - y$ plane (left) and in the $R - z$ plane (right) [54].

vertex is reconstructed from the selected tracks using an iterative procedure [59]. A vertex candidate is found by searching for the global maximum in the distribution of z component of the tracks. A χ^2 fit is performed using the vertex candidate and its associated tracks. Incompatible tracks are removed from the vertex candidate. These incompatible tracks are used to seed another vertex and the fitting procedure is repeated until no additional vertices are found in the event. In addition, vertices originating from particle decays, photon conversions and hadronic interactions are called secondary vertices. The reconstruction of secondary vertices is important for the identification of objects such as b-jets, which is mentioned in Section 4.2.1.

4.2 Jets

Quarks and gluons originating from the hard interactions cannot be observed as isolated particles in the detector, but they (except the top quarks) hadronise to produce a collimated spray of particles that may decay or interact with the detector material. The sprays of particles are jets that are accessible as energy deposits in the calorimeters. This allows one to deduce the momentum of the original particles.

The jet reconstruction starts with forming topological clusters from energy deposits in the calorimeters [60]. Calorimeter cells with an energy deposit above some noise threshold are used as seeds. Neighbouring cells are included to build a cluster if their energy deposit is larger than a certain threshold. At the end, all adjacent cells to the previous set are added. If there are more than one energy maxima found inside one cluster, it is split accordingly. The topological-cluster energies are calibrated with the local cluster weighting method [61] in order to cope with the non-compensating nature of the ATLAS calorimeters and signal losses due to clustering as well as due to energy lost in non-instrumented regions. In this step, each topological cluster is classified as an electromagnetic or a hadronic shower based on properties of the cluster such as the energy density and the shower shape.

The anti-k_T algorithm [62] is used to merge these calibrated topological clusters into jets. This algorithm first calculates the distance measure between two clusters (i, j):

$$d_{ij} = \min\left(\frac{1}{p_{\mathrm{T}i}^2}, \frac{1}{p_{\mathrm{T}j}^2}\right)\frac{(\Delta_{ij})^2}{R^2}, \tag{4.1}$$

and the distance between the cluster i and the beam axis:

$$d_{iB} = \frac{1}{p_{\mathrm{T}i}^2}. \tag{4.2}$$

Here, $p_{\mathrm{T}i(j)}$ is the transverse momentum of the cluster $i(j)$. Δ_{ij}^2 is the distance between clusters i and j in the $y - \phi$ plane defined as $\Delta_{ij}^2 = (y_i - y_j)^2 + (\phi_i - \phi_j)^2$. The parameter R denotes the algorithm resolution and defines the cone size of each jet. In this analysis, the parameter R is set to 0.4. For every cluster i, all distances d_{ij} and d_{iB} are computed. The jet finding starts from this list of clusters. If the smallest distance is d_{ij}, the clusters i and j are merged and the list of clusters is updated. If the smallest distance is d_{iB}, the cluster i is defined as a final jet and removed from the list of clusters. The procedure is repeated until no cluster remains in the event. The four momentum of a jet is computed by adding the four momenta of its constituent clusters.

There are several steps to calibrate the kinematic properties of the reconstructed jets. In a first step, the average additional energy due to pile-up interactions is subtracted from the energy measured by the calorimeters using the pile-up correction. This correction is determined by *in-situ* measurements. Secondly, the jet direction is adjusted by the vertex correction to ensure that the jet originates from the primary interaction vertex. The energy of the jet is brought to the particle level using calibration corrections derived from simulation data. In a last step, each jet in observed data are calibrated using the residual correction to account for differences between observed and simulated events. This final correction is determined using *in-situ* balance techniques described in the following. The average p_{T} of the jets in the forward region are calibrated to the jets in the central region by exploiting the p_{T} balance of central and forward jets in dijet events. Using Z+jet and γ+jet events, a correction for the energy scale of jets in the central region is determined by balancing p_{T} of the jet against the Z boson and the photon. The p_{T} balance of low-p_{T} jets against high-p_{T} jets is employed to calibrate jets in the TeV region. The total jet-energy uncertainty is typically below 1% for jets in the central region and increases to 3.5% for jets with low transverse momentum at high absolute pseudorapidity [63].

The algorithms reconstruct not only jets from quarks or gluons, but also jets from background sources caused by e.g. electronic noise, beam-induced interactions and cosmic rays. These jets are flagged as "bad" jets and events containing a bad jet are discarded [64].

Furthermore, if a reconstructed jet is found to be within a cone of $\Delta R = 0.2$ of the selected electron, the jet is rejected as the jet and the electron most likely come from the same physical object.

Jets originating from pile-up interactions are suppressed by imposing a cut on a variable called jet vertex fraction (JVF) [65]. This variable is defined as the fraction between the $\sum p_{\mathrm{T}}$ of all tracks within the jet originating from the primary vertex and the $\sum p_{\mathrm{T}}$ of all tracks associated to the jet. This cut is applied only to jets inside the inner detector acceptance of $|\eta| < 2.4$. Jets with p_{T} below 50 GeV are rejected if their |JVF| value is below 0.5 as pile-up jets typically have low transverse momentum.

4.2.1 *b*-tagged jets

One important ingredient of all physics analyses involving top quarks is the identification of jets originating from b-quarks. This is a way to reduce large backgrounds that do not contain a b-quark jet in the final state. There are several so-called b-tagging algorithms that are used to distinguish b-quark jets from light-flavour jets and c-quark jets at ATLAS.

After b-quarks are produced, they hadronise into b-hadrons. The weakly decaying b-hadrons can travel a few millimetres with respect to the pp interaction vertex due to their relatively long lifetime ($\sim$ 1.5 ps) and their typically large momenta. The tracks of charged particles produced in the hard process

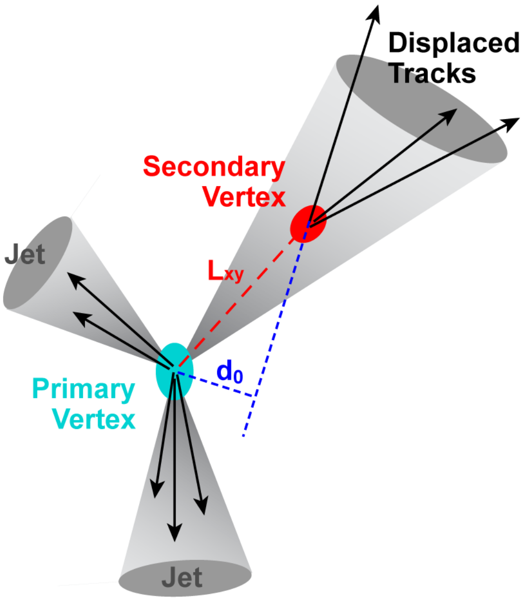

Figure 4.2: Sketch of the decay of a b-hadron causing a secondary vertex [66]. The parameter L_{xy} is the distance between the secondary vertex and the primary vertex. d_0 is the transverse impact parameter of one of the tracks originating from the secondary vertex.

often point to the primary vertex, while the tracks of charged particles produced in the b-hadron decay point to a secondary vertex at a significant distance from the origin that can be resolved by the inner trackers. Figure 4.2 illustrates the decay of a b-hadron causing a secondary vertex displaced from the interaction point with a certain distance. All b-tagging algorithms have been developed using the features related to the decay of the b-hadrons. For instance, a b-hadron can be identified using the transverse d_0 and longitudinal z_0 impact parameters of the tracks at this displaced vertex and by reconstructing the secondary vertex explicitly.

The MV1c b-tagging algorithm is used in this analysis. This algorithm is based on a neural network that combines the information from three other b-tagging algorithms JetFitterCombNN, IP3D and SV1. A detailed description of these three algorithms can be found in Refs. [67, 68]. The MV1c algorithm is an improved version of the MV1 algorithm [69] with a higher rejection of c-quark jets. The input variables to the neural network are the output weights of the three algorithms as well as the transverse momentum and pseudorapidity of the jet [70]. The neural network trains b-quark jets against c-quark jets and a mixture of light-flavour jets. A cut on the output of the neural network (weight ranging from zero to one) is applied in order to identify the jet being either b-tagged or b-untagged, reflecting the efficiency of tagging a b-quark jet of each b-tagging working point. In the same way, one can determine the probability of mistakenly tagging a c-quark jet or a light-flavour jet.

The performance of the b-tagging algorithms can be different between simulation and real data. All algorithms must be calibrated to match the b-tagging efficiency measured in simulation to that measured in collision data. Different methods are used to measure the b-tagging efficiency in data. Scale factors defined as the ratio of the efficiency in data to that in simulation are derived. In addition, the calibration is done for c-quark jets and light-flavour jets separately. These scale factors are further applied to the jets in simulated events in the present analysis.

4.3 Electrons

In this analysis, electrons in the central region of $|\eta| < 2.47$, excluding the transition region of $1.37 < |\eta| < 1.52$, are reconstructed using the standard electron reconstruction algorithm [71]. The reconstruction of electrons starts with energy clusters in the electromagnetic calorimeter. A sliding window algorithm [72] is employed to search for clusters with $E_\mathrm{T} > 2.5$ GeV and with 3×5 cells in $\eta - \phi$ space, corresponding to the granularity of the middle layer of the calorimeter, to be used as seeds. For each cluster, the algorithm further looks for a track in the inner detector with $p_\mathrm{T} > 400$ MeV that matches to the cluster. The track is matched to the cluster if the distance between them satisfies $\Delta\eta < 0.05$ and $\Delta\phi < 0.05$. Bremsstrahlung losses are taken into account by enlarging $\Delta\phi$ in the bending direction of the track up to 0.1. If multiple tracks are matched to the cluster, the track with the closest distance in ΔR is chosen. The cluster size is enlarged to 3×7 cells in the barrel and to 5×5 cells in the end-caps to account for overall possible energy deposits in the calorimeter. Simulation-based corrections are then applied to the cluster energy to obtain the electron energy. The directions and energies of electrons are measured precisely from the inner detector trackers and from the calorimeter. The transverse energy of the electron candidate is then usually calculated from this combination as:

$$E_\mathrm{T} = \frac{E(\text{cluster})}{\cosh \eta(\text{track})}. \tag{4.3}$$

The algorithms reconstruct not only electrons associated with the W-boson and Z-boson decays, but also fake electrons from hadronic jets and electrons from photon conventions. The background electrons can be suppressed by applying identification criteria referred to as *"loose", "medium", "tight"* ordered according to their background rejection power [71, 72]. These criteria are defined inclusively, such that looser selection is a subset of tighter one. *Loose* selection is applied on shower shape variables of the EM second layer as well as on the hadronic leakage. *Medium* selection requires a cut on shower shape variables of the EM first layer. To increase fake-electron rejection, requirements on electron-track quality and track-cluster matching are used. *Tight* selection requires additional cuts on election-track quality and the track-cluster matching. A cut on the ratio of the cluster energy and the track momentum (E/p) is used to isolate electrons from charged pions. Some information from the TRT is employed for particle identification. Electrons from photon conversions are suppressed by requiring a hit in the innermost layer of the pixel detector. Electron candidates that are matched to a reconstructed photon are rejected. As isolated electrons are essential for the analysis, the *tight* identification is employed here.

Apart from the electron identification criteria, additional isolation criteria based on calorimeter and track isolations are imposed on the electron candidates to further improve the signal purity [73]. The calorimeter isolation requires a cut on the scalar sum of the transverse energy measured by the EM calorimeter cells in a cone of $\Delta R = 0.2$ around the electron. Similarly, the track isolation is done by defining a cut on the scalar sum of the transverse momenta of the tracks in a cone of $\Delta R = 0.3$ around the electron. The isolation cuts are chosen such that the selection efficiency of 90% is achieved in the full range of electron p_T and η. After applying the overlap between jets and electrons as discussed in Section 4.2, electrons are further discarded if they are within a cone of $\Delta R = 0.4$ around a jet with $p_\mathrm{T} > 25\,\mathrm{GeV}$ satisfying the JVF requirement.

The reconstruction efficiency and the identification efficiency are measured using $Z \to ee$ events. Scale factors are derived from the differences in the efficiencies between data and simulation and further used to correct simulation to match data in this analysis. The derived scale factors are close to one with an uncertainty of a few percent in low$-E_\mathrm{T}$ and high$-\eta$ regions [74]. $Z \to ee$ events are used to calibrate the electron energy scale and resolution. $J/\psi \to ee$ events are exploited to validate the calibrated electron energy scale. The derived scale factors are further applied to simulation to match data. Uncertainties in the calibration of the energy scale vary from 0.03% to 2.25%, while the uncertainty in the calibration of the energy resolution is about 10% [75].

4.4 Muons

As muons travel through the ATLAS calorimeter system by depositing a very small amount of their energy, the muon candidates used in the present analysis are reconstructed using a combination of tracks in the muon spectrometer that match to tracks in the inner detector, discussed in Section 4.1. A detailed description of the muon reconstruction is given in Ref. [76]. The reconstruction of muon tracks in the muon spectrometer starts from building track segments from hits in each chamber. These segments are combined into a track by performing a fit. The full track in the muon spectrometer is extrapolated back to the point of closest approach to the beam axis. The energy loss of the muon in the calorimeters is taken into account in this step. A track in the inner detector compatible with the extrapolated track is searched for. A global refit is then performed to combine the two tracks into a single track for each muon candidate. As a consequence, only the candidates within the geometric acceptance of the inner detector up to $|\eta| = 2.5$ are reconstructed.

In addition, the resulting muon track has to have the impact parameter $z_0 \leq 2$ mm in order to suppress tracks from pile-up interactions. The so-called mini-isolation requirement [77] is further applied to suppress background events originating from heavy-flavour decays. The muon candidates are accepted if they fulfil the following cut:

$$\frac{I_{\text{mini}}}{p_{\text{T}}(\mu)} < 0.05\,, \tag{4.4}$$

where I_{mini} is called the mini-isolation variable defined as the scalar sum of the transverse momenta with p_{T} above 1 GeV of all tracks, except the track that is matched to the muon itself. Those tracks need to satisfy:

$$\Delta R(\text{track}, \mu) < \frac{10\,\text{GeV}}{p_{\text{T}}(\mu)}\,. \tag{4.5}$$

Furthermore, muons within a cone of $\Delta R = 0.4$ around a jet with $p_{\text{T}} > 25\,\text{GeV}$ satisfying the JVF requirement are discarded. Events are removed if a selected electron and a muon candidate share the same track in the inner detector.

The reconstruction and identification efficiencies are measured using muons from Z decays or J/ψ decays. The efficiencies are above 99% with permille precision. The efficiencies are reduced for $\eta \sim 0$ as this region is used to support services for the inner detector and calorimeters. Another inefficient region is $1.1 < \eta < 1.3$ since some of muon chambers were not yet installed. Scale factors are applied in the present analysis to correct for small differences between data and simulation. The momentum scale and resolution are estimated using $J/\psi \to \mu\mu$, $\Upsilon \to \mu\mu$ and $Z \to \mu\mu$ events. Scale factors are derived by performing a fit to the distributions of the di-muon mass separately for the inner detector and the muon spectrometer. The resulting scale factors of the order of 0.1% are further used in the analysis.

4.5 Missing transverse momentum

Neutrinos are the only stable particles that interact very weakly such that they escape the detector undetected. Only indirect measurements of them can be made using energy-momentum conservation in the transverse plane. As the transverse momenta of the incoming particles in this plane are known to be negligible, the vector sum of the reconstructed transverse momenta of the final-state particles must be zero. If an imbalance in the transverse momentum is present in an event, this must be from unseen particles such as neutrinos. This means that the so-called missing transverse momentum, $E_{\mathrm{T}}^{\mathrm{miss}}$, is in principle equal to the negative vector sum of all transverse momenta of the reconstructed particles in the event.

The calculation of missing transverse momentum makes use of information from the energy deposits in the calorimeters and the muon momentum from the muon spectrometer [78]. The $E_{\mathrm{T}}^{\mathrm{miss}}$ is computed using the calibrated physics objects. Calorimeter cells that are not associated to any of the calibrated physics objects are also taken into account. The $E_{\mathrm{T}}^{\mathrm{miss}}$ used in this present analysis follows the prescriptions for top-quark analyses [73] as:

$$E_{x,y}^{\mathrm{miss}} = E_{x,y}^{\mathrm{RefElec}} + E_{x,y}^{\mathrm{RefJet}} + E_{x,y}^{\mathrm{RefSoftJet}} + E_{x,y}^{\mathrm{RefMuon}} + E_{x,y}^{\mathrm{CellOut}} . \tag{4.6}$$

Each term on the right side of the equation is the negative sum of the calibrated cell energies, E_{i}, of the corresponding physics objects projected onto either the x or y direction as:

$$E_x^{\mathrm{miss}} = -\sum_i^{n_{\mathrm{cell}}} E_i \sin\theta_i \cos\phi_i , \tag{4.7}$$

$$E_y^{\mathrm{miss}} = -\sum_i^{n_{\mathrm{cell}}} E_i \sin\theta_i \sin\phi_i . \tag{4.8}$$

The $E_{x,y}^{\mathrm{RefElec}}$ term refers to electrons with $p_{\mathrm{T}} > 10\,\mathrm{GeV}$ that satisfy the *tight* electron identification cuts. The $E_{x,y}^{\mathrm{RefJet}}$ term denotes topological clusters belonging to jets with $p_{\mathrm{T}} > 20\,\mathrm{GeV}$ over the full pseudorapidity range of $|\eta| < 4.9$. The $E_{x,y}^{\mathrm{RefSoftJet}}$ term includes clusters belonging to jets with lower p_{T} between 7 GeV and 20 GeV. The $E_{x,y}^{\mathrm{RefMuon}}$ term is computed from the transverse momenta of reconstructed muons with $|\eta| < 2.7$. Isolated muons are determined from the combined measurement of the inner detector and the muon spectrometer. In case of non-isolated muons satisfying $\Delta R(\mu, \mathrm{jet}) < 0.3$, only the muon momentum after the energy loss in the calorimeter measured in the muon spectrometer enters the muon term. If there is the energy loss of the non-isolated muons in the calorimeter, it is then added in the calculation. The $E_{x,y}^{\mathrm{CellOut}}$ term includes all clusters not associated with any physics objects. The magnitude of the $E_{\mathrm{T}}^{\mathrm{miss}}$ is expressed from the x and y components as:

$$E_{\mathrm{T}}^{\mathrm{miss}} = \sqrt{(E_x^{\mathrm{miss}})^2 + (E_y^{\mathrm{miss}})^2} . \tag{4.9}$$

4.6 Top quarks

In this analysis, t-channel single top-quark events where only the W boson originating from the top quark decays into a charged lepton and a neutrino are considered. The W boson can then be reconstructed from its decay products: the charged lepton and the neutrino. The reconstruction of the top quark is achieved by combining the W boson with the b-tagged jet from the top-quark decay.

The reconstruction of the charged lepton being either an electron or a muon is discussed in Sections 4.3 and 4.4. By assuming that the main contribution to the $E_{\mathrm{T}}^{\mathrm{miss}}$ comes from the neutrino, the x and y components of the neutrino are known. The z component of the neutrino momentum, $p_{z,\nu}$, can be derived from the energy-momentum conservation of the W-boson system using the mass of the W boson as a constraint, following the description presented in Refs. [79, 80]. The $p_{z,\nu}$ can be written in a quadratic equation as:

$$p_{z,\nu}^2 - 2 \cdot \frac{\mu \cdot p_{z,\ell}}{p_{T,\ell}^2} \cdot p_{z,\nu} + \frac{p_\ell^2 \cdot p_{\mathrm{T},\nu}^2 - \mu^2}{p_{T,\ell}^2} = 0\,, \tag{4.10}$$

with

$$\mu = \frac{m_W^2}{2} + p_{\mathrm{T},\ell} \cdot p_{\mathrm{T},\nu} \cdot \cos\Delta\phi\,, \tag{4.11}$$

where m_W is the W-boson mass set to 80.4 GeV and $\Delta\phi$ is the azimuthal angle difference between the charged lepton and the $E_{\mathrm{T}}^{\mathrm{miss}}$. The quadratic equation has two solutions as:

$$p_{z,\nu} = \frac{\mu \cdot p_{z,\ell}}{p_{\mathrm{T},\ell}^2} \pm \sqrt{\frac{\mu^2 \cdot p_{z,\ell}^2}{p_{\mathrm{T},\ell}^4} - \frac{p_\ell^2 \cdot p_{\mathrm{T},\nu}^2 - \mu^2}{p_{\mathrm{T},\ell}^2}}\,. \tag{4.12}$$

If the two solutions are real, the one with smaller $|p_{z,\nu}|$ is picked. According to a study with simulated events shown in Ref. [79], the smaller real solution reproduces the correct W boson in most of the cases. The case of two real solutions occurs in about 70% of all events. The solutions can be complex if the transverse mass of the W boson reconstructed from the lepton and the $E_{\mathrm{T}}^{\mathrm{miss}}$ defined as:

$$m_{\mathrm{T}}\left(\ell, E_{\mathrm{T}}^{\mathrm{miss}}\right) = \sqrt{2 p_{\mathrm{T}}(\ell) \cdot E_{\mathrm{T}}^{\mathrm{miss}} \left[1 - \cos\left(\Delta\phi\right)\right]} \tag{4.13}$$

is larger than m_W. This can happen due to poor resolution in the reconstructed $E_{\mathrm{T}}^{\mathrm{miss}}$. A real solution can be obtained by modifying the value of the $p_{\mathrm{T},\nu}$ by constraining the value of $m_{\mathrm{T}}\left(\ell, E_{\mathrm{T}}^{\mathrm{miss}}\right)$ to m_W with the restriction that Equation 4.10 is still valid. The procedure starts by setting the square-root part of Equation 4.12 to zero. This leads to a quadratic equation between the $p_{x,\nu}$ and $p_{y,\nu}$ components. To obtain a real solution for the quadratic equation, the distance between the modified value and the measured value is minimised by a fit. In order to keep the modified transverse momentum close to the measured one, the smaller solution is chosen to compute the $p_{z,\nu}$ component. The four momentum of the W boson can then be reconstructed from the four momenta of the reconstructed charged lepton and the reconstructed neutrino.

The four momentum of the top quark is finally obtained by adding the four momenta of the reconstructed W boson and the b-tagged jet. The reconstruction of the b-tagged jet is given in Section 4.2.1.

CHAPTER 5

Dataset and event selection

Several physics processes can have a similar final state to the signal process. To be able to extract the cross-sections of t-channel single top-quark production from observed data collected by the ATLAS detector, a good understanding of the contributing physics processes is important. This can be revealed by modelling these physics processes based on their theoretical predictions. To further select the candidate events for the analysis, a sequence of selection requirements following the decay topology of the signal process are applied on both observed and modelled data.

This chapter presents the observed data and Monte Carlo simulation samples entering the analysis. Section 5.1 describes the analysed collision data, followed by the modelling of the signal and background processes in Section 5.2. The selection criteria to discard a large amount of background events without losing too much of the signal fraction are summarised in Section 5.3.

5.1 Collision data

The present analysis is performed based on proton–proton collision data at a centre-of-mass energy of 8 TeV collected by the ATLAS detector at the LHC in 2012. The data used in this thesis require the LHC beams to be stable and all detector components to be fully operational. This condition is necessary due to the fact that the reconstruction of all physics objects involving top-quark decays demands all detector components to be successfully functional. As this analysis focuses on top-quark decays involving electrons or muons, the data events are selected using unprescaled single-electron and single-muon triggers with the lowest p_{T} thresholds [81, 82]. They are filtered using a good-runs list [83] to obtain only the data that are good for any physics analysis. Figure 5.1 illustrates the integrated luminosity recorded by the ATLAS detector versus the day in the year 2012. The total amount of integrated luminosity used in this thesis is 20.2 fb^{-1} with an uncertainty of 1.9%.

5.2 Signal and background modelling

To understand the composition of the collision data, theoretical calculations are used. All relevant physics processes, except for the multijet background, are simulated using Monte Carlo generators. In general, the simulation process consists of three steps: generation of the events originating from hard pp interactions to the stable final-state particles, simulation of the detector response, and conversion into detector signals that have the same format as the real data. Multijet-background events are derived by

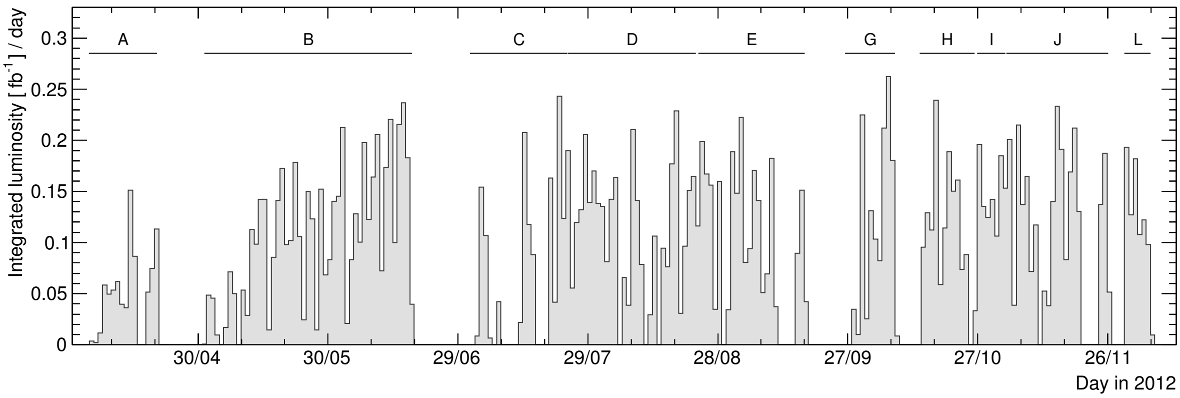

Figure 5.1: Integrated luminosity versus time collected by ATLAS for pp collisions at $\sqrt{s} = 8$ TeV in 2012. Only data utilised in this thesis are shown. There are ten data-taking periods indicated using letters A-L. The small stops between individual runs as well as the short pauses for special runs are also depicted. The long breaks in April, June and September were related to the technical stops. [84]

data-driven methods described in Section 5.2.3. All simulated samples used in this analysis are listed in tables in Appendix A with their predicted cross-section and the number of generated events.

5.2.1 Monte Carlo simulation

The event generation with Monte Carlo generators is done in several steps as illustrated in Figure 5.2. First, the hard process is simulated using fixed-order perturbative QCD calculations. This is followed by the modelling of the parton-shower evolution. During this stage, quarks, antiquarks and gluons are created. The next step is called hadronisation, where colourless hadrons are formed from those quarks and antiquarks using phenomenological models. Unstable particles further decay into stable particles. In addition, the underlying event is generated. The underlying-event component consists of all processes from the interactions of the beam remnants plus initial-state and final-state radiation.

After that, the generated events are passed through the simulation of the ATLAS detector performed using the Geant4 framework [86] in order to model the detector response. All relevant information of the detector geometry and the detector material is included. The effect of pile-up simulated with Pythia 8 [87] is also added. The full simulation of particles traversing the ATLAS calorimeter and electromagnetic particles is time-consuming. The fast simulation with Atlfast-II can be alternatively used. The approach is to use pre-simulated showers instead of low energy electromagnetic particles to reduce computing time. At the end, the hits of the energies deposited in the detector from the simulation are converted into detector responses to have the same format as the real data. Therefore, the same trigger and reconstruction algorithms can be applied to both simulated and collision data. Details on the ATLAS simulation infrastructure are given in Ref. [88].

5.2.2 Signal modelling

The generators Powheg-Box (revision 2556) [89] and MadGraph5_aMC@NLO (version 2.2.2) [90] are employed to generate t-channel single top-quark events using the NLO QCD calculations in the four-flavour scheme ($qg \rightarrow q' t\bar{b}$). More details about t-channel single top-quark production are given in Section 2.3.1. With these generators, the top quark is assumed to decay exclusively into a W boson and a b-quark, and its mass is set to 172.5 GeV. For every event, the renormalisation and factorisation

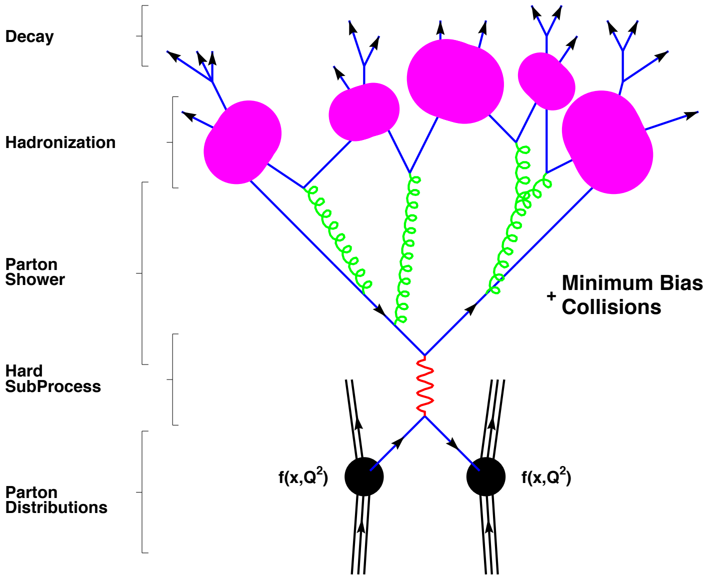

Figure 5.2: Typical structure of a hadron collision event simulated by an event generator. [85]

scales are calculated using $\mu_{R(F)} = 4 \cdot \sqrt{m_b^2 + p_{\mathrm{T},b}^2}$, where m_b are $p_{\mathrm{T},b}$ are the mass and the transverse momentum of the b-quark from the initial-state gluon splitting. The b-quark mass is set to 4.75 GeV. The NLO CT10 set [19] of PDFs is used.

Another generator to produce the signal events at LO accuracy is AcerMC (version 3.9) [91] with the LO CTEQ6L1 set [92] of PDFs. Both four-flavour and five-flavour ($qg \rightarrow q't$) schemes are implemented in the AcerMC generator. Using the ACOT method [93], the two processes are combined into one sample without kinematic overlaps. A scale of $\mu = 115$ GeV is used, as it leads to agreement with the predictions from the NLO generators (see Ref. [94]).

The simulation of the parton shower and the hadronisation can be done with Pythia 6 (version 6.428) [95] or Herwig (version 6.5.20) [90]. The underlying event is simulated using the Pythia generator itself or Jimmy (version 4.31) [96] for the Herwig generator. The Perugia 2012(2011C) tune [97] is used to set the parameters for the Pythia generator (in case of Pythia for AcerMC), while the ATLAS AUET2 tune [98] is for the Herwig + Jimmy generators (for simplicity, later only Herwig will be written for Herwig +Jimmy).

The nominal signal sample for this analysis is generated using Powheg-Box interfaced to Pythia 6. Alternative signal samples simulated using different generators are used for estimating systematic effects from different generators as well as generator-parameter configurations. Details of the alternative signal samples are given in Section 7.2.

5.2.3 Background modelling

Different production processes can contribute events that have the same signature as the signal process. Furthermore, if the acceptance for such events after the event selection is not negligible, they have to be considered in the analysis. The background contributions for this present analysis come from top-quark pair ($t\bar{t}$) production, the other two single top-quark production processes (Wt- and s-channel), W+jets production, Z+jets production, diboson production and multijet production. The theoretical definition of the production of top-quark background processes is detailed in Section 2.3.1. Here, the other relevant background processes are introduced. A description of the modelling of each background production is given. All MC-driven backgrounds are normalised to a theoretical cross-section that is computed at a fixed-order in QCD calculation given in tables in Appendix A.

Top-quark background

The nominal samples of $t\bar{t}$ as well as single top-quark in the Wt-channel and s-channel events are generated with Powheg-Box coupled to Pythia 6 using the Perugia 2011C tune. The NLO CT10 set of PDFs is used. For $t\bar{t}$ events, the model parameter h_{damp}, which controls the high-p_{T} radiation in Powheg-Box, is set to the top-quark mass (m_t). Alternative samples of these processes are simulated with Powheg-Box (using $h_{\text{damp}} = \infty$ for $t\bar{t}$)+ Pythia 6, Powheg-Box + Herwig or MC@NLO [99] + Herwig.

Production of a W boson in association with jets

The production of a real W boson in association with jets is one of the two main backgrounds for this analysis due to its large cross-section. In addition, this background can easily have a similar final state to the signal process when the W boson decays leptonically into a charged lepton and a neutrino. The accompanying jets coming from a gluon are a pair of light-flavour quarks shown in Figure 5.3 (a) or a pair of heavy-flavour quarks (b or c) shown in Figure 5.3 (b).

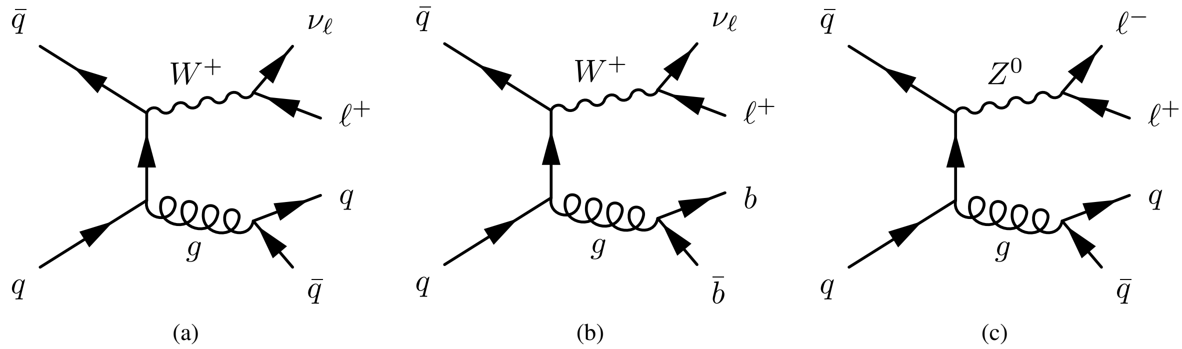

Figure 5.3: Examples for Feynman diagrams of the production of a real V boson in association with jets: (a) production of a W boson with two additional jets, (b) production of a W boson and two heavy-flavour jets, and (c) production of a Z boson with two additional jets.

The W+jets events are simulated using the LO generator Sherpa (version 1.4.1) [100] with the CT10 PDF set and its own tune. The hard process, the parton shower, the hadronisation and the underlying event all are modelled by the Sherpa generator. The b-quark and c-quark are treated as massive quarks in the matrix elements and the parton showers. Flavour filters are used to divide the events as follows. The b-filtered samples include only events where there is a b-hadron within $|\eta| < 4.0$. The c-filtered samples contain only events where there is a c-hadron with $p_{\text{T}} > 15\,\text{GeV}$ within $|\eta| < 3.0$ and no such b-hadron. Both filters are not applied for the samples of W+light-flavour jets.

The inclusive cross-sections of W-boson production are calculated to NNLO precision with FEWZ [101, 102]. To estimate the uncertainty on the W+jets process generated with Sherpa, parameters in the generation of the events are varied. A normalisation uncertainty of 21% is assigned for the modelling of the production of W boson in association with two jets.

Production of a Z boson in association with jets

Z+jets production contributes as a minor background to this analysis since the events are strongly suppressed by the event selection. Figure 5.3 (c) illustrates an example for a Feynman diagram of this process where the Z boson decays into two charged leptons with two additional jets. Only events where one of the leptons is mis-reconstructed as a jet or out of the detector acceptance may pass the event selection.

The Z+jets events are simulated with Sherpa using the same settings as for the W+jets process. Based on the same strategy as for the case of W+jets background, a normalisation uncertainty of 21% is also assigned for the modelling of the production of Z boson in association with two jets.

Production of WW, ZZ and WZ

Another minor background arises from the production of two vector bosons denoted as VV. WW and WZ production can have a similar final state to W+jets as depicted in Figure 5.4 (a) and (c). In case of ZZ production, its final state can be similar to Z+jets as depicted in Figure 5.4 (b). Therefore, with the same reasons as mentioned above, the production of WW, ZZ and WZ processes can pass the event selection.

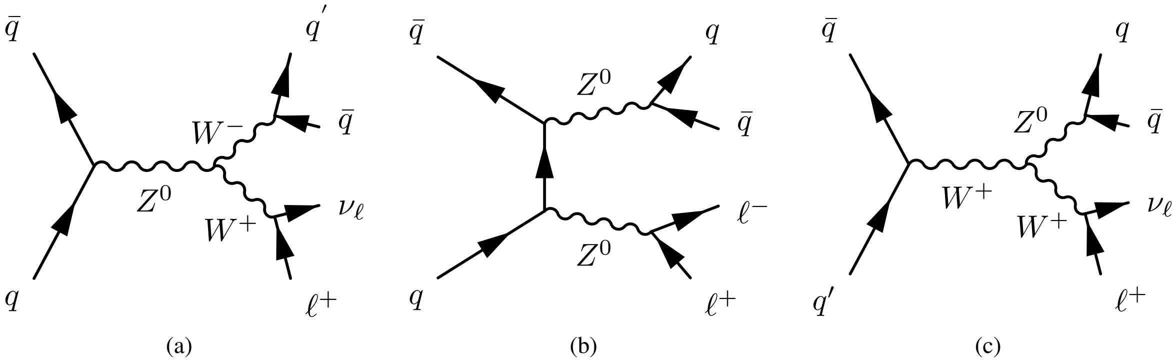

(a) (b) (c)

Figure 5.4: Examples for Feynman diagrams of the diboson production: (a) WW, (b) ZZ and (c) WZ production.

The Sherpa generator is also used to simulate the production of two vector bosons with the same settings as for the production of one vector boson in association with jets. Only events where one of the two bosons decays leptonically and the other decays hadronically are taken into account. The NLO cross-section of the diboson production is predicted using MCFM [103]. The uncertainty in the inclusive cross-section is calculated to be 5%.

Multijet background

The last background for this analysis comes from multijet events. Figure 5.5 (a) shows an example of a multijet event originated from $b\bar{b}$ production. One of the b-hadrons decays semileptonically into a non-prompt lepton[1], a neutrino and a jet. Similarly, a semileptonic decay of a heavy-flavour c-hadron can also lead to a non-prompt lepton. This production is an important source of multijet events with

---

[1] Leptons arising from decays of hadronic jets

non-prompt muons. Another scenario is the misidentification of a jet as a lepton (normally as an electron) shown in Figure 5.5 (b). Such multijet events can play a role in the analysis. Fortunately, the large amount of the multijet background is reduced in the first place by applying the event selection; however, this contribution cannot be fully suppressed since its cross-section is several orders of magnitude larger than the other background production.

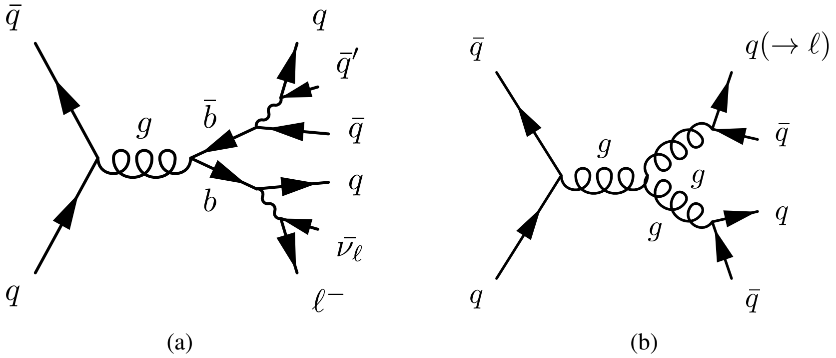

Figure 5.5: Examples for Feynman diagrams of the multijet production (a) with a lepton coming from $b\bar{b}$ production and (b) with a misidentified jet as lepton.

Using Monte Carlo approach to directly generate a sample of multijet background with feasible statistics is difficult. Different approaches are used to produce these fake-lepton events. The jet-lepton model is employed to model events having a fake electron and the anti-muon method is used to model events having a non-prompt muon. These two different methods are employed here in order to have the best possible modelling of kinematic distributions in the validation regions described later in Section 5.3.

The jet-lepton model As mentioned in Section 4.3, hadronic jets can be misidentified as electron candidates if their kinematic properties are similar to the electron definition. The multijet background in the electron channel is modelled using the jet-lepton model by selecting events with an electron-like jet. This model is applied to a so-called JF17 dijet sample simulated with Pythia 8. This sample is filtered to have at least one jet with $p_{\mathrm{T}} > 17\,\mathrm{GeV}$ and $|\eta| < 2.7$. To form multijet events with a fake electron, the following cuts are applied to all jets present in each event of the dijet sample. A candidate jet has to have the same kinematic properties as a real electron: $p_{\mathrm{T}} > 25\,\mathrm{GeV}$ and $|\eta| < 2.47$ excluding the crack region. An energy deposit of the jet in the electromagnetic calorimeter must be between 80% and 95% of its total energy. At least four tracks have to be found in the jet to reduce the contribution from converted photons. This jet is then used as an electron and called the "jet-lepton". The event is rejected if it contains another lepton. The candidate events are further selected using the standard event selection except for the electron selection.

The anti-muon method The anti-muon method is used to model multijet events in the muon channel from collision data. Some of the muon identification requirements are relaxed or inverted in order to obtain a non-isolated muon that most likely originates from a jet. This muon is called "anti-muon". The changed requirements are given in the following. A candidate anti-muon must have the energy loss in the calorimeter less than 6 GeV. It has to have the transverse energy in a cone of $\Delta R = 0.2$ around itself to be greater than 0.03 times its own p_{T}. The isolation cut (see Equation 4.4) is relaxed to be less than 0.10. No cut on the impact parameter z_0 is applied. Afterwards, the standard muon selection explained in Section 5.3 is required.

5.3 Event selection

A sequence of harder cuts is applied on both collision and simulated data in order to discard undesired events without losing too many of the signal events. In the first part of this section, the series of event-selection cuts is discussed. This is followed by the multijet-background estimation. At the end, the expected and observed event yields are given. Detailed studies of the event selection and the multijet-background estimation are given in the thesis [1].

5.3.1 Event-selection cuts

Basic requirements of the event selection are following the final state of t-channel signal top-quark production where the W boson stemming from the top quark decays into an electron or a muon. Events where the W boson decays into a τ lepton are also taken into account if the τ lepton subsequently decays into an electron or a muon. Thus, the signal event signature contains one charged lepton (either e or μ), exactly two quark jets, one of the two jets being a b-tagged jet, and missing transverse momentum. One special characteristic of the t-channel topology is that the light-quark jet tends to be scattered in the forward direction. The full pseudorapidity range of the detector is required for its reconstruction. The sequence of selection cuts is explained in the following:

- The single-electron or single-muon trigger is needed to be fired and all collision data are required to pass the good-runs list.
- Each event must have at least one primary vertex reconstructed from at least 5 associated tracks with $p_{\mathrm{T}} > 400\,\mathrm{MeV}$. Events containing jets with $p_{\mathrm{T}} > 20\,\mathrm{GeV}$ failing the jet quality selection criteria [61] are vetoed.
- Exactly one isolated electron or muon with $p_{\mathrm{T}} > 25\,\mathrm{GeV}$ being only in the central region of the detector is required. This electron or muon has to satisfy the overlap removal criteria described in Section 4.
- Each event must have missing transverse momentum of $E_{\mathrm{T}}^{\mathrm{miss}} > 30\,\mathrm{GeV}$.
- Exactly two jets with $p_{\mathrm{T}} > 30\,\mathrm{GeV}$ and $|\eta| < 4.5$ are considered. Jets in the transition region between the end-cap and forward calorimeters ($2.7 < |\eta| < 3.5$) are required to have $p_{\mathrm{T}} > 35\,\mathrm{GeV}$. One of the two jets is required to be a b-tagged jet.
- Unlike signal events, fake-lepton events usually contribute softer $E_{\mathrm{T}}^{\mathrm{miss}}$. As a result, these events also have low transverse mass of the lepton-$E_{\mathrm{T}}^{\mathrm{miss}}$ system, $m_{\mathrm{T}}\left(\ell, E_{\mathrm{T}}^{\mathrm{miss}}\right)$. A cut is imposed on $m_{\mathrm{T}}\left(\ell, E_{\mathrm{T}}^{\mathrm{miss}}\right) > 50\,\mathrm{GeV}$ to reduce this multijet-background contribution. This transverse mass is defined as in Equation 4.13.
- The multijet-background events can be further suppressed by placing a cut on a low-p_{T} lepton which is back-to-back with the highest-p_{T} jet, j_1, in the event. This additional requirement is defined as:

$$p_{\mathrm{T}}(\ell) > \max\left(25\,\mathrm{GeV}, 40\,\mathrm{GeV} \cdot \left(1 - \frac{\pi - |\Delta\phi(j_1, \ell)|}{\pi - 1}\right)\right). \tag{5.1}$$

- $t\bar{t}$ dilepton and Z+jets backgrounds can be reduced by using a veto on a secondary lepton in an event. Unlike the primary leptons, the secondary leptons do not need to pass the isolation requirement. They are required to have the opposite charge to the primary leptons as well as

$p_T > 10\,\mathrm{GeV}$. The pseudorapidity range of $|\eta| < 4.9$ is considered for secondary electrons, while $|\eta| < 2.5$ for secondary muons. Electrons in the region of $2.5 < |\eta| < 4.9$ are identified using the information from the calorimeters only [72].

Events with a secondary lepton are vetoed if the secondary and primary leptons have the same flavour, if the invariant mass of the secondary and primary leptons is between 80-100 GeV and if the secondary lepton is not within $\Delta R = 0.4$ of the selected b-tagged jet.

- A cut on the invariant mass of the selected lepton and b-tagged jet, $m(\ell b)$, is applied to discard events in the region of $m(\ell b) > 160\,\mathrm{GeV}$, as they are not well modelled [2].
- The sign of the lepton charge is used to divide the selected events into two parts, named as the ℓ^+ channel and the ℓ^- channel. This is because the measurements are performed separately for tq and $\bar{t}q$ production.

There are three different regions defined in this analysis. All three regions use the same selection as mentioned above, except the b-tagged requirement. The signal region is used to extract the tq and $\bar{t}q$ cross-sections. In this region, one of the two jets is tagged by the MV1c b-tagging algorithm with MV1c weight > 0.9195, corresponding to 50% efficiency. Two validation regions are introduced in order to check the kinematic modelling of the two dominant backgrounds: W+jets and $t\bar{t}$. In the W+jets validation region, a looser b-tagged criterion is utilised. One of the two jets is required to be tagged with the MV1c algorithm with 0.4051 < MV1c weight < 0.8349. This corresponds to a b-tagging efficiency between 80% and 60%. This implies that all events in the signal region are excluded. As there are two b-quark jets present in the final state of the $t\bar{t}$ topology, the $t\bar{t}$ validation region is specified by requiring two jets to be tagged with MV1c weight > 0.9195.

5.3.2 Multijet-background estimation

As described in Section 5.2, the multijet production has the largest cross-section among the other background processes. The data-driven methods are exploited in order to estimate it. The jet-lepton model is used to create events for the election channel and the anti-muon model is for the muon channel. The procedure to extract the multijet-background normalisation is summarised as follows. First, all event-selection cuts except the E_T^{miss} requirement are applied to these events. A binned maximum-likelihood fit on the E_T^{miss} distribution is performed. Fits are done for the electron and muon channels separately, but for the ℓ^+ and ℓ^- channels simultaneously as the multijet production is charge symmetric. The electron channel is sub-divided into two sets where fits are also performed separately. One set is referred to electrons in the barrel region ($\eta < 1.37$) and another is referred to electrons in the end-cap region ($\eta > 1.52$). In the fit, all W+jets processes, all top-quark processes, as well as Z+jets and diboson processes are grouped into one template each. As the contributions from Z+jets and diboson backgrounds are small, their normalisation is fixed in the fitting procedure.

Table 5.1 gives the multijet-background estimates for $E_T^{\mathrm{miss}} > 30\,\mathrm{GeV}$ for all channels in the signal region. Figure 5.6 illustrates the E_T^{miss} distributions normalised to the fit results for the barrel e^+ and the μ^+ channels in the signal region. An uncertainty of 15% is assigned on the multijet-background normalisation by comparing to the multijet-background normalisation estimated using an alternative method called the matrix method [104].

5.3.3 Event yield

Event yields after event selection in the signal region for each process are listed in Table 5.2. The event yields are given for the ℓ^+ and ℓ^- channels separately. All processes except the multijet background, are

Channel	barrel $e^{\pm}$	end-cap $e^{\pm}$	$\mu^{\pm}$
Number of events	850 ± 199	720 ± 90	2950 ± 280

Table 5.1: Expected numbers of multijet-background events for $E_{\mathrm{T}}^{\mathrm{miss}} > 30\,\mathrm{GeV}$ for all channels in the signal region. The given uncertainty is the fit uncertainty taking only statistical uncertainties into account.

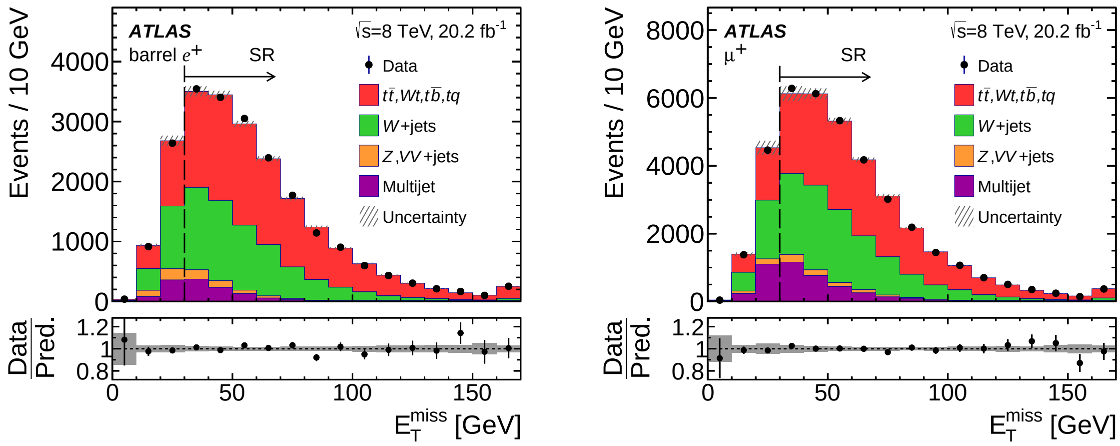

(a)

(b)

Figure 5.6: Observed distributions of the missing transverse momentum, $E_{\mathrm{T}}^{\mathrm{miss}}$, in the signal region (SR), including events with $E_{\mathrm{T}}^{\mathrm{miss}} < 30\,\mathrm{GeV}$, for (a) events in the e^{+} channel with an electron in the barrel region and for (b) events in the μ^{+} , compared to the model obtained from simulated events. The normalisation is obtained from a binned maximum-likelihood fit to the full $E_{\mathrm{T}}^{\mathrm{miss}}$ distributions, and applied to the SR. The hatched uncertainty band represents the MC statistical uncertainty and the normalisation of the multijet background. The ratio of observed (Data) to predicted (Pred.) number of events in each bin is shown in the lower panel. Events beyond the x-axis range are included in the last bin. [2]

normalised to their theoretical cross-sections computed at (N)NLO precision in QCD (see Appendix A). The number of multijet-background events is estimated by performing a binned maximum-likelihood fit to the $E_{\mathrm{T}}^{\mathrm{miss}}$ distribution. The uncertainties corresponding to the theoretical cross-section uncertainties for top-quark processes and the normalisation uncertainties for the other processes, are summarised in Section 7.2. The total number of all simulated events is in good agreement with the total number of data events for both channels. The signal-to-background ratio is 21% for the ℓ^{+} channel and 14% for the ℓ^{-} channel, as background compositions in each channel are different. Furthermore, there are a small number of tq events in the ℓ^{-} channel and $\bar{t}q$ events in the ℓ^{+} channel due to misidentification of lepton charge.

Process	ℓ^+ SR	ℓ^- SR
tq	$11\,400 \pm 470$	17 ± 1
$\bar{t}q$	10 ± 1	$6\,290 \pm 350$
$t\bar{t}, Wt, t\bar{b}/\bar{t}b$	$18\,400 \pm 1\,100$	$18\,000 \pm 1\,100$
W^+ + jets	$18\,700 \pm 3\,700$	47 ± 10
W^- + jets	25 ± 5	$14\,000 \pm 2\,800$
Z, VV + jets	$1\,290 \pm 260$	$1\,190 \pm 240$
Multijet	$4\,520 \pm 710$	$4\,520 \pm 660$
Total expected	$54\,300 \pm 4\,000$	$44\,100 \pm 3\,100$
Data	55 800	44 687

Table 5.2: Predicted and observed event yields for the signal region (SR). The multijet-background prediction is obtained from a binned maximum-likelihood fit to the $E_{\mathrm{T}}^{\mathrm{miss}}$ distribution. All the other predictions are derived using theoretical cross-sections. The uncertainties are the theoretical cross-section uncertainties for top-quark processes and the normalisation uncertainties for the other processes. [2]

CHAPTER 6

Measurement definitions

The present chapter is dedicated to the definition of parton-level top quarks and particle-level objects. The parton-level measurements usually refer to the measurements in the full kinematic range, while the particle-level ones are performed within a so-called fiducial phase space that is defined to be as close as possible to the phase space covered by the detector. With this approach, some of the theoretical-model dependencies, that are introduced by the extrapolation to full phase space, can be avoided in the particle-level measurements.

6.1 Parton-level top quarks

The parton-level top quark is defined as the top quark before its decay but after gluon radiation. Technically, this means that the top quark with status code 3 is searched for in the event record[1] for PYTHIA 6, while this corresponds to status code 155 for HERWIG. In this analysis, the t-channel single-top quark events simulated with POWHEG-BOX + PYTHIA 6 are utilised to extract the nominal generator-level distributions, which are needed as an input for the unfolding procedure. The other simulated signal samples are used for comparison and systematic evaluation.

The differential cross-sections are measured as a function of the p_{T} and $|y|$ of the top quarks and the top antiquarks at parton level in the full phase space (no event-selection cuts are applied). This makes the predictions of the differential cross-sections straightforward. Some examples of the predicted differential cross-sections calculated at NLO precision using MCFM with several PDF sets are presented in Figure 6.1. It can be seen that there are small differences between the different PDF sets and large ones at large $\pm y$.

6.2 Particle-level objects

The parton-level cross-section measurements are model-dependent, as their final results have a large amount of MC simulation involved, containing events that are outside the detector acceptance. To reduce such model dependencies, the particle-level cross-section measurements are needed. These measurements are performed in a fiducial phase space, which is designed to be close to the reconstruction-level phase space.

---

[1] An event record contains relevant information of every step in a simulation.

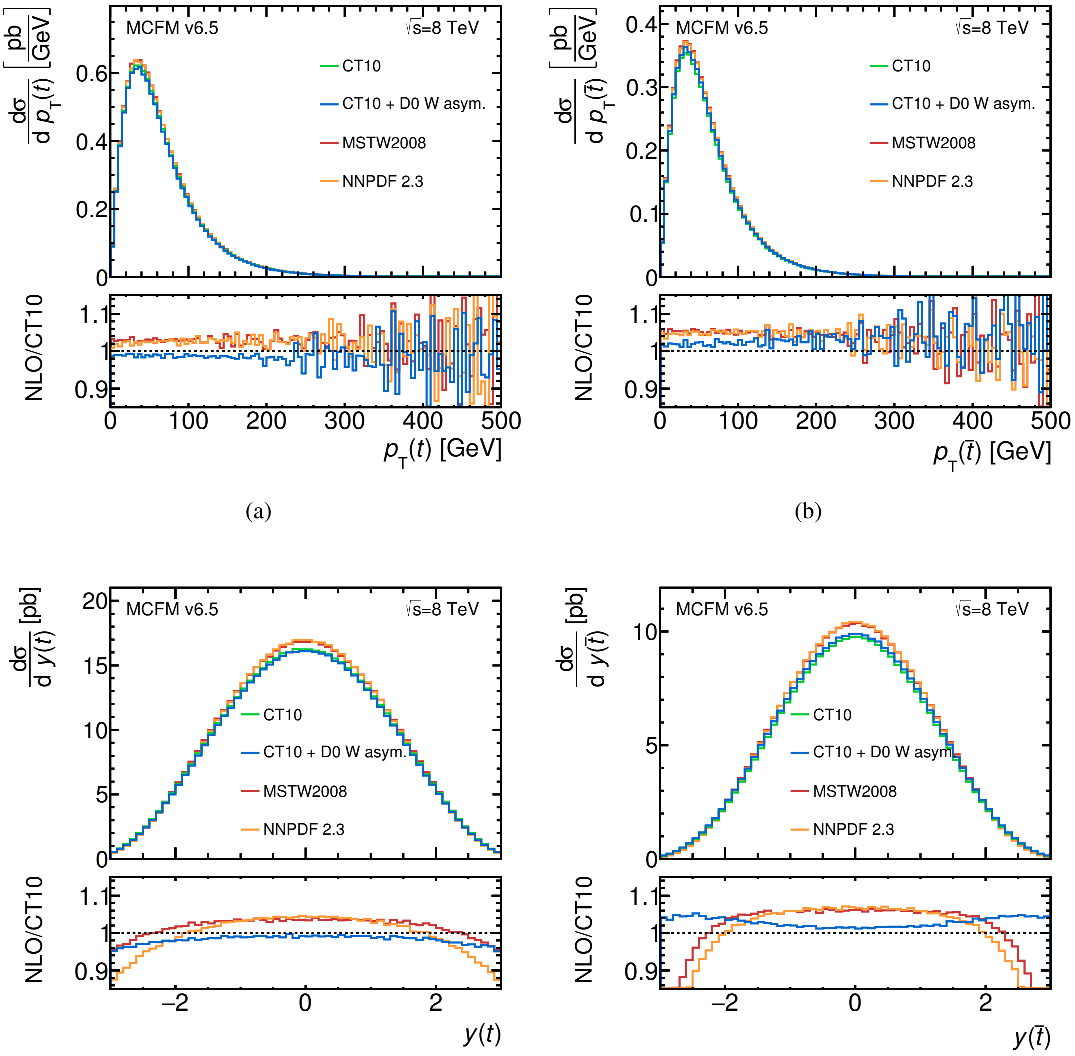

(a) (b)

(c) (d)

Figure 6.1: Differential cross-sections as a function of (a) $p_{\mathrm{T}}^{tq}(t)$, (b) $p_{\mathrm{T}}^{\bar{t}q}(t)$, (c) $|y^{tq}(t)|$ and (d) $|y^{\bar{t}q}(t)|$ at parton level using various PDF sets. In the bottom plot, the ratio is calculated with respect to the differential cross-section with the CT10 PDF set.

The definition of the particle-level objects follows the LHCTop-working-group recommendations [105]. The particle-level objects are constructed from stable particles, coming from the hard scattering of the proton–proton collisions. There is no simulation of these particles interacting with the detector components involved. The stable particles are defined as having a mean lifetime greater than 0.3×10^{-10} s. The particle-level objects are defined as close as possible to the physics objects that are reconstructed in the detector level. In the following, how these objects are formed is described.

- **Leptons**: all considered electrons or muons must not come from hadronic decays either directly or via a hadronic τ decay. This requirement is needed to make sure that the leptons emerge from an electroweak decay. In this analysis, exactly one electron or muon is present in each t-channel single top-quark event. The four momenta of all photons within a cone of $\Delta R = 0.1$ around the direction of the selected lepton are added to the four momentum of the lepton, to take into account that leptons can radiate photons.

- **Neutrinos:** Particle-level neutrinos are selected in the same way as the particle-level leptons. Neutrinos from hadronic decays either directly or via a hadronic τ decay are discarded.
- **Jets:** All stable particles, except the selected lepton, the photons associated with the lepton and the selected neutrinos are used to reconstruct particle-level jets. These particles are clustered into jets using the anti-k_t algorithm with a radius parameter of $R = 0.4$.
- ***b*-jets:** A particle-level jet is identified as a b-jet if there is any b-hadron found within the given jet using the ghost matching algorithm [106]. The algorithm starts from b-hadrons with $p_\mathrm{T} > 5\,\mathrm{GeV}$. The four momentum of the b-hadrons are rescaled to have a very small energy and then added to the list with other stable particles for jet-clustering, explained above. This means that the b-hadrons cannot change the four momentum of the jet. A jet having a b-hadron within its cone is a b-jet.
- **Overlap removal:** Events where a selected particle-level lepton is within a cone of $\Delta R = 0.4$ around a selected particle-level jet are discarded.

6.2.1 Particle-level selection

In this analysis, the particle-level event selection requires exactly one particle-level electron or muon with $p_\mathrm{T} > 25\,\mathrm{GeV}$ and $|\eta| < 2.5$. Exactly two particle-level jets with $p_\mathrm{T} > 30\,\mathrm{GeV}$ and $|\eta| < 4.5$ have to be found in the events. One of the two jets with $|\eta| < 2.5$ must be b-jet. The cut on $m(\ell b) < 160\,\mathrm{GeV}$ is also applied to exclude the off-shell region.

6.2.2 Pseudo-top-quarks

The term "pseudo-top-quark" is used to refer to a top quark reconstructed from the stable particles at particle level in a fiducial phase space. This nomenclature is first mentioned in [107]. The pseudo-top-quark is reconstructed from its decay products, i.e., the W boson and the b-jet. As the analysis is performed in the lepton+jets topology, the W boson is reconstructed from a charged lepton and a neutrino at particle level. In order to be close to the reconstruction-level objects, the W-boson mass is used as a constraint in the same way as explained in Section 4.6 to compute the z component of the neutrino momentum. In the quadratic equation, it is possible to have two real solutions, the one with smaller absolute value is always chosen. For particle level, there is a 90% chance to have 2 solutions. It is higher than for reconstruction level because there is no detector and there is rare mis-measurement of the $E_\mathrm{T}^\mathrm{miss}$ at this level. It is not 100% because there might be some off-shell W bosons plus some rounding effects. It is also possible that the solutions are complex. In this case, the value of the $E_\mathrm{T}^\mathrm{miss}$ is modified in order to have a real solution. In each considered event, there are always two jets and exactly one b-jet. Therefore, the four momentum of the pseudo-top-quark is obtained by adding the four momenta of the W boson and the b-jet.

In addition to the measurement as a function of the p_T and $|y|$ of the pseudo-top-quarks and the pseudo-top-antiquarks, it is possible to measure the differential cross-sections as a function of the p_T and $|y|$ of the untagged jets at particle level, since the untagged jets are well defined at this level. This untagged jet is assumed to emerge from the light quark in the t-channel exchange of a W boson. In this thesis, the pseudo-top-quark is written as $\hat{t}$, while the untagged jet is denoted as $\hat{j}$.

The definition of the pseudo-top-quark is not only close to the definition of the reconstruction-level top quark, but also close to the definition of the parton-level top quark. A strong correlation between parton-level top-quark and pseudo-top-quark observables can be seen in Figure 6.2.

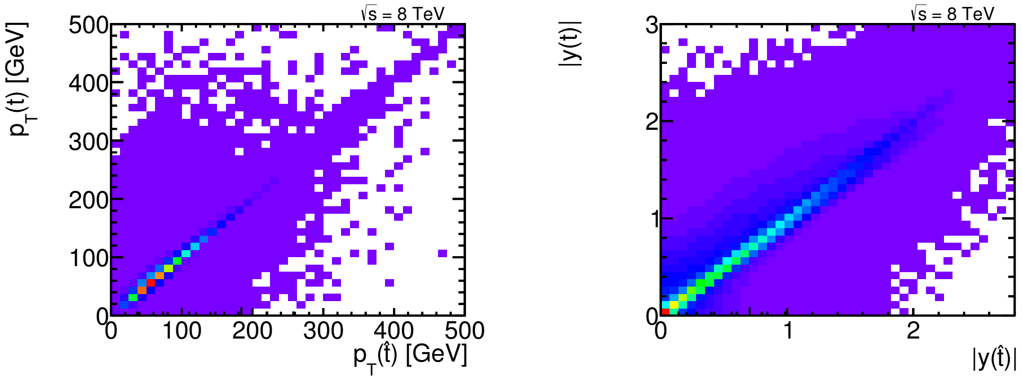

(a)

(b)

Figure 6.2: The correlation between parton-level top-quark and pseudo-top-quark observables: (a) $p_{\mathrm{T}}(t)$ vs. $p_{\mathrm{T}}(\hat{t})$ and (b) $y(t)$ vs. $y(\hat{t})$ in the fiducial phase space. The distributions are shown for tq and $\bar{t}q$ events combined. The Powheg-Box + Pythia 6 signal sample is used.

CHAPTER 7

Signal discrimination and extraction

This chapter summarises the measurements of the fiducial and total single top-quark t-channel production cross-sections at $\sqrt{s} = 8$ TeV with the ATLAS detector. This work is done by a PhD student at the University of Wuppertal [1]. The measurements focus on the final state of t-channel single top-quark events, which consist of one electron or muon, missing transverse momentum, and two jets, one of which must be a b-tagged jet. After applying the event-selection cuts described in Section 5.3, the backgrounds are highly suppressed but not completely removed. An artificial neural network based on the NeuroBayes software is exploited to combine several kinematic variables into one final discriminant, that provides good separation of the signal events from the background events. A binned maximum-likelihood fit is applied to the final discriminant to extract the fiducial cross-sections and determine the impact of statistical and systematic uncertainties on the measurements. The fiducial results are then extrapolated to the full kinematic range to obtain the total cross-sections.

7.1 Signal discrimination

A fraction of background events can be rejected by applying the event selection as mentioned in Section 5.3. However, the background events – mainly from top-quark pair production and W+jets production – still contribute dominantly over the t-channel signal events. Also, finding one single variable that shows large differences in shape between the signal events and the background events for the statistical analysis is not easy. In this section, a neural network technique is introduced. It is used to separate the signal events from the background events by constructing a powerful discriminant from several input variables. At the end, the construction of the input variables and the final neural network *utilised as the default neural network for the analysis* is discussed.

7.1.1 Multivariate analysis with NeuroBayes

Multivariate techniques are commonly employed in high energy physics analyses in order to combine several input variables into one powerful discriminant. An artificial neural network provided by the NeuroBayes package is exploited in this analysis. NeuroBayes is composed of a complex robust preprocessing of the input variables and a feed-forward neural network for learning to distinguish the signal from the background. In the following, a description of the preprocessing and the neural network implemented within NeuroBayes [108, 109] is briefly explained.

Preprocessing

Before going through the neural network algorithms, the input variables are preprocessed to find a better starting point for neural network training. This is a big achievement of the NeuroBayes package. There are three steps to obtain a set of the most significant input variables with the NeuroBayes preprocessing.

In a first step, each distribution of all input variables is binned such that the number of signal and background events combined is equally distributed over all bins. The signal purity in each bin of the flatted distribution is then calculated to form a purity distribution. A spline [110] is fitted to the resulting distribution in order to reduce the influence of statistical outliers. The values of the fitted purity are transformed to a Gaussian with a mean of zero and a width of one to establish optimal learning environment for the neural network training [111]. With this procedure, the input variables have the same scales and can be compared.

After that, the input variables are ranked according to their significance as follows. The correlation matrix of the transformed input variables is first computed. The total correlation to the target of all input variables is then calculated using the correlation matrix. One variable after the other is removed from the set of input variables and the total correlation to the target of the remaining input variables is recomputed. With this, the loss in total correlation to the target can be determined for each variable. Only input variables with a loss in correlation above a threshold cut, that can be defined by a user, are kept for the neural network training.

At the end, the chosen input variables are decorrelated. This is done by diagonalising the covariance matrix of the transformed input variables with iterative Jacobi rotations.

Neural networks

Artificial neural networks are inspired by how neurons in central nervous systems of animals work. The neural network implemented with the NeuroBayes package is a feed-forward neural network with nodes arranged in three layers. This means that the nodes are arranged into serial layers: an input layer, a hidden layer and an output layer. The connections of these layers are only in one direction (from the input layer to the output layer).

A graphical representation of a feed-forward neural network is shown in Figure 7.1. The values of the input variables, chosen in the preprocessing step, are passed to the nodes in the input layer. This layer consists of one input node for each input variable and one bias node. The internal nodes in the hidden layer receive the output of the input nodes. The analyser can adjust the number of internal nodes in a reasonable range, where the network training results are stable. In this analysis, 15 internal nodes are used. Information from the hidden layer is transferred to the output layer to form one discriminant variable.

Each internal node j is connected to each input node i via the weight w_{ij}. The value of each internal node is the weighted sum of all input values. To map the value of the output a to the interval $[-1, 1]$, a symmetric Sigmoid function S is employed. It is defined as:

$$S(a) = \frac{2}{1 + e^{-a}} - 1 \, . \tag{7.1}$$

Similarly, the output node is connected to each internal node via the weight w_j. The response of the neural network can then be expressed as:

$$o = S\left[\sum_{j=1}^{m} w_j S\left(\sum_{i=1}^{n} w_{ij} x_i + w_{0j}\right)\right] , \tag{7.2}$$

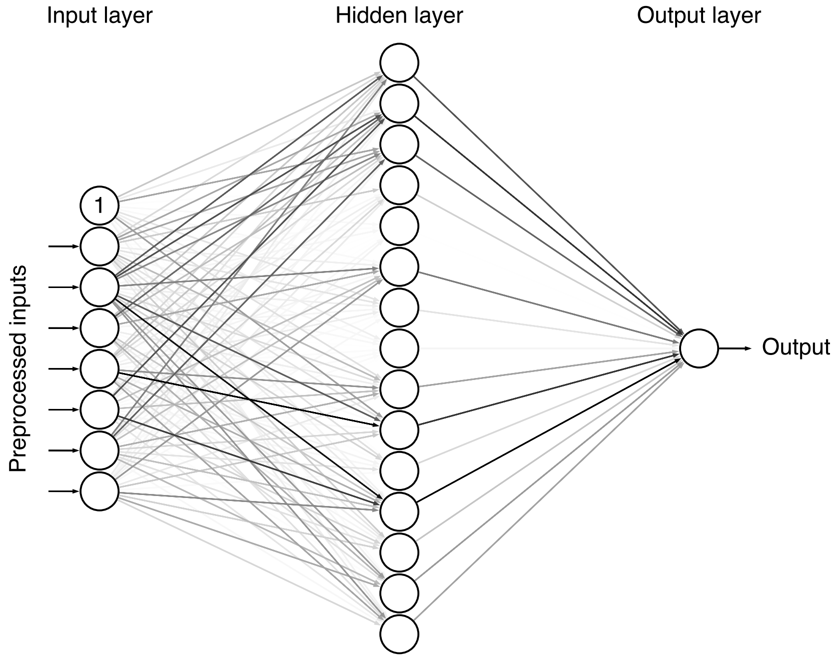

Figure 7.1: Representation of a feed-forward neural network with seven input variables, fifteen internal nodes in the hidden layer and one output node in the output layer. The darkness of the connecting line corresponds to the significance of the weight between the nodes. This configuration is used as the default neural network to separate the t-channel signal from the backgrounds in this analysis.

where m is the number of internal nodes, n is the number of input variables, x_i is the value of the i^{th} input variable and w_{0j} is the weight between the j^{th} internal node and the bias node. Looking at Equation 7.1, this activation function is sensitive in a small region near $a = 0$ and reaches saturation for large $\pm a$. The weight w_{0j} is needed in order to shift the value of the activation function to its sensitive region.

To form a final output of the neural network, the weights w_{ij} and w_j have to be evaluated. In the network training, a training sample is usually from simulation. Therefore, the actual target value t is known for each event: $t = 1$ for a signal event, $t = -1$ for a background event. The weights are adjusted using the backpropagation algorithm [112] such that they describe the actual target values best. This minimisation is done with the entropy loss function:

$$E = \sum_{i}^{n} \log\left(\frac{1}{2}(1 + t_i \cdot o_i + \epsilon)\right) , \tag{7.3}$$

where n is the number of training events. ϵ is a regularisation constant decreased with each training iteration and became zero after a few iterations. It is introduced to avoid numerical problems for untrained networks.

During the network training, it is possible that the network has learned to distinguish the signal from the background based on statistical fluctuations instead of actual structure in the data. To avoid this, NeuroBayes uses Bayesian regularisation techniques. With this procedure, insignificant connections which have large weights are removed. More details can be found in [108].

7.1.2 Input variables and final discriminant

Potential input variables are required in order to discriminate t-channel signal events from background events. In principle, these input variables should show significant differences in shape for the signal compared to the backgrounds. In this analysis, the input variables are obtained from the kinematics of the particles in $1\ell + 2$ jets final state. All kinematic variables of the reconstructed W boson and the reconstructed top quark are also included. In addition, one can construct the input variables from the kinematic differences between the objects, the angular correlation variables, the invariant mass of each objects, the $E_{\mathrm{T}}^{\mathrm{miss}}$, the lepton charge, and the sum of the transverse momenta of several objects, H_{T}.

Here, the simulated events for the t-channel process is considered as the signal, while the simulated events for the other processes are treated as the background. The signal and background contributions are used to construct a training sample. Different backgrounds are first reweighted according to their number of expected events. A fraction of 50% signal events and 50% background events is chosen.

The choice of neural network variables was optimised based on the total uncertainty. Details are given in Refs. [1, 2]. Table 7.1 lists seven input variables to the default neural network ordered by their discriminating power. Figure 7.2 shows the resulting output distributions normalised to unit area for the signal and the two main backgrounds: top-quark background and W+jets background. It can be seen that a very good separation of the signal against these two main backgrounds is achieved. Before ensuring that this discriminating variable can be further used in the analysis, the modelling of all processes compared to the collision data of all input variables is needed to be checked in the two validation regions. Good agreement between simulated and observed data is achieved in all input distributions (see Ref. [1]).

Variable	Definition
$m(jb)$	The invariant mass of the untagged jet and the b-tagged jet.
$\lvert\eta(j)\rvert$	The absolute value of the pseudorapidity of the untagged jet.
$m(\ell\nu b)$	The invariant mass of the reconstructed top quark.
$m_{\mathrm{T}}(\ell, E_{\mathrm{T}}^{\mathrm{miss}})$	The transverse mass of the lepton–$E_{\mathrm{T}}^{\mathrm{miss}}$ system.
$\lvert\Delta\eta(\ell\nu, b)\rvert$	The absolute value of the difference in pseudorapidity of the reconstructed W boson and the b-tagged jet.
$m(\ell b)$	The invariant mass of the charged lepton and the b-tagged jet.
$\cos\theta^{*}(\ell, j)$	The cosine of the angle, θ^{*}, between the charged lepton and the untagged jet in the rest frame of the reconstructed top quark.

Table 7.1: The seven input variables to the default neural network ordered by their discriminating power. [2]

7.2 Sources of systematic uncertainties

Various sources of systematic uncertainties affect the fiducial, total and differential cross-section measurements of t-channel single top-quark production. Each systematic uncertainty can have an impact on the shape of the discriminant distributions as well as on the normalisation of all contributions. In the following, the sources of considered systematic uncertainties are described shortly. They are split into the different groups: reconstruction uncertainties, multijet-background shape, generator uncertainties, parton-distribution-function uncertainties, background normalisation, simulation statistics and luminosity.

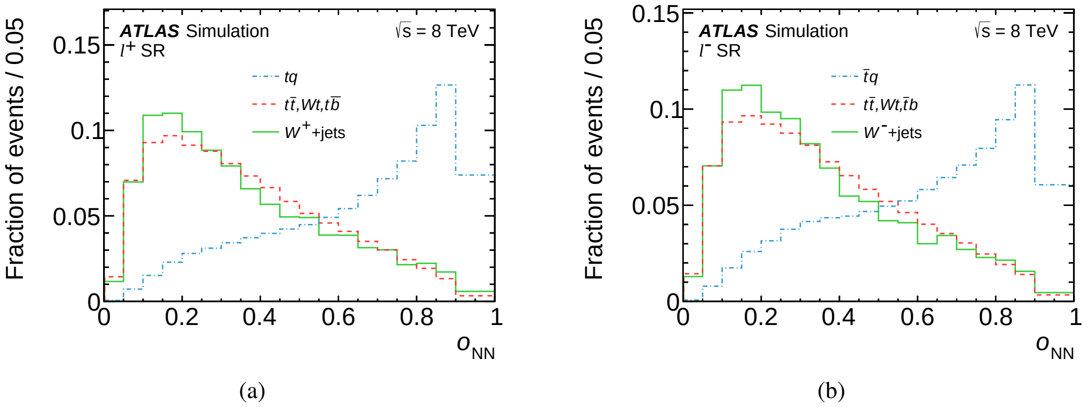

(a)

(b)

Figure 7.2: Probability densities of the NN discriminants in the signal region (SR) for the tq and $\bar{t}q$ signal processes, the W+jets background and the top-quark background: (a) in the ℓ^+ channel and (b) in the ℓ^- channel. [2]

Reconstruction uncertainties

The reconstruction of physics objects with the ATLAS detector was described in Chapter 4. Here, systematic uncertainties related to residual differences between observed data and simulation of those reconstructed objects are given.

- **Jet energy scale (JES):** The p_T and η of the reconstructed jet are used in the evaluation of the uncertainty due to the jet energy scale. The jet energy scale uncertainty consists of several components. They are classified into different groups named as detector, physics modelling, mixed detector and modelling, statistical, η intercalibration, single particle, flavour and punch-through. Additional components are due to the pile-up modelling. The last contribution is the uncertainty on the energy scale of the b-quark jets. Overall, there are 26 contributions that are considered in this analysis. A description of all components is given in detail in Ref. [113]. To estimate the impact of each contribution, the energy of each jet is rescaled up and down by one standard deviation before applying the event selection.

- **Jet energy resolution (JER):** The effect of the uncertainty due to the jet energy resolution is evaluated by smearing the jet energy in the simulated samples by a Gaussian with width dependent on the p_T and η of the jet to match the jet energy resolution in data. The difference between the nominal and smeared MC samples is symmetrised and then assigned as the final JER uncertainty.

- **Jet reconstruction efficiency:** The jet reconstruction efficiency is determined using minimum bias and QCD dijet events [114]. The reconstruction is found to be fully efficient for jets with $p_T > 30$ GeV. Its uncertainty is estimated by randomly dropping jets from simulated events. For this analysis, the impact of the jet reconstruction efficiency is expected to be very small because only jets with $p_T > 30$ GeV are selected.

- **Jet vertex fraction:** The uncertainty associated with the cut on the jet vertex fraction (JVF) is determined by varying the cut value. The cut value is changed from $|\mathrm{JVF}| > 0.5$ for the nominal case to $|\mathrm{JVF}| > 0.53$ for the up variation and to $|\mathrm{JVF}| > 0.47$ for the down variation.

- **Lepton energy scale and resolution:** The uncertainties related to the lepton energy scale and resolution were derived using $Z \to \ell\ell$ and $J/\psi \to \ell\ell$ events [75, 76]. The impact of lepton energy scale uncertainties is determined by varying the lepton momentum up and down by one standard deviation before applying the event selection. For the uncertainties due to lepton energy resolution, the lepton momentum smeared using a Gaussian is applied before the event selection. The uncertainties in the muon energy resolution are separated into two parts: inner detector and spectrometer, as the information from these two components is used to reconstruct muons.

- **Lepton reconstruction:** Scale factors are applied to the simulated lepton trigger, identification and reconstruction efficiencies to match the ones observed in data. The uncertainties due to these scale factors are estimated by varying the scale factors up and down by one standard deviation before applying the event selection.
- **Flavour-tagging efficiency:** The uncertainties related to the tagging efficiencies of b-quark, c-quark and light-flavour jets are taken into account. To evaluate these uncertainties, the efficiency correction factors derived from data are varied up and down by one standard deviation and then applied to all simulated jets before event selection. The uncertainties in the b-tagging, c-tagging and mistag[1] efficiencies are treated independently. In this analysis, the uncertainties are broken down according to their kinematic range into nine sub-components for the b-tagging efficiency, four sub-components for the c-tagging efficiency and twelve sub-components for the mistag efficiency.
- **$b\bar{b}$ efficiency:** The uncertainty due to the difference between the b-tagging efficiency for tagging a jet originated from a b-quark and a b-antiquark is taken into account. The simulated signal samples with Powheg-Box + Pythia 6 are used to calculate the efficiencies. The difference is determined to be 0.94% and assigned as an acceptance uncertainty.
- **Missing transverse momentum:** The uncertainties from the reconstruction of leptons and jets are propagated into the calculation of the missing transverse momentum. Remaining uncertainties to the $E_{\mathrm{T}}^{\mathrm{miss}}$ calculation arise from calorimeter cells that are not associated to any jets, and soft jets that are jets within a p_{T} range of 7 GeV $< p_{\mathrm{T}} <$ 20 GeV. The uncertainties due to the energy scale and resolution of this contribution are varied separately.

Multijet-background shape

A multijet-background sample is constructed using the jet-lepton model for the electron channel and the anti-muon model for the muon channel. Afterwards, the number of expected events is determined by fitting the $E_{\mathrm{T}}^{\mathrm{miss}}$ distribution to the data (see Section 5.3.2). To derive the uncertainty due to the multijet-background estimation, an alternative multijet method is used to estimate this background. The uncertainty in the shape of the multijet background is evaluated by comparing the distribution obtained with the default models to the one obtained with the matrix method [104].

Generator uncertainties

Systematic effects from the Monte Carlo modelling for all top-quark processes are considered in the analysis. The uncertainties are determined by either comparing different generators or varying parameters in the generation of events. Details of the simulated samples with different generators are given in Section 5.2.

- **NLO matching:** For the $t\bar{t}$, s-channel and Wt-channel single top-quark production, the modelling uncertainty related to the matching of the matrix-element calculation is estimated by comparing

---

[1] The term mistag is often used to refer to the efficiency for tagging light-flavour jets.

the MC@NLO + Herwig to the Powheg-Box ($h_{\text{damp}} = \infty$) + Herwig samples. The uncertainty associated to the t-channel signal is determined by comparing the MadGraph5_aMC@NLO + Herwig to the Powheg-Box + Herwig samples.

- **Parton shower:** The uncertainty related to the modelling of the parton shower and the hadronisation is estimated from the comparison between the Powheg-Box + Pythia and Powheg-Box + Herwig samples. Both cases are with an assumption of $h_{\text{damp}} = \infty$.
- **Scale variations:** The uncertainty related to the choice of the factorisation and the renormalisation scales is evaluated by changing these parameters in the event generation done with the Powheg-Box generator. The scale in the Pythia parton shower that is used to evaluate the amount of QCD radiation is tuned to the varied renomalisation scales accordingly. Here, the factorisation and the renormalisation scales are varied by a factor of 0.5 for more radiation and 2.0 for less radiation.
- ***W*+jets shape modelling:** The shape uncertainty associated to the modelling of W+jets background produced with Sherpa is not taken into account in the analysis, since it is found to be negligible (see Ref. [1]).

Parton-distribution-function uncertainties

The uncertainties related to the PDF of the initial-state protons are determined for all processes, except for the Z+jets, diboson and multijet processes. The Z+jets and diboson contributions are not considered because of their low statistics. The PDF uncertainties are evaluated using the PDF4LHC15_NLO combined PDF set with 15 eigenvectors. The evaluation procedure follows the PDF4LHC recommendation [115]. To build a set of varied systematic samples, the events in simulated samples are reweighted according to the central value and eigenvectors of the PDF4LHC15_NLO PDF set. The final PDF uncertainty includes the difference between each eigenvector and the central value of the PDF4LHC15_NLO prediction. The difference between the central value of the PDF4LHC15_NLO PDF set and the central value of the CT10 PDF set is also taken into account, as the uncertainty obtained with the PDF4LHC15_NLO PDF set does not cover the CT10 PDF set. The uncertainties are estimated using the AcerMC +Pythia sample for t-channel signal, the MC@NLO +Herwig samples for top-quark backgrounds and the Sherpa samples for W+jets.

Background normalisation

Uncertainties in the theoretical cross-sections are used for evaluating the uncertainties due to background normalisation for the top-quark background processes. The uncertainties of 6.0%, 7.6% and 4.2% are for $t\bar{t}$, Wt-channel and s-channel background processes, respectively. As the production of $t\bar{t}$, Wt-channel and s-channel backgrounds is combined in the statistical analysis, a combined uncertainty of 6.6% is assigned. This combined uncertainty is calculated by adding the theoretical uncertainties according to their relative fractions.

A normalisation uncertainty of 21% is applied for the combined W+jets and the Z+jets grouped with dibosons backgrounds. This uncertainty is derived by changing the factorisation, renormalisation and resummation scales in the event generation with Sherpa.

Similar to the shape uncertainty for the multijet background, the normalisation uncertainty for this process is estimated by comparing the yield obtained with the jet-lepton and the anti-muon models to the one obtained with the matrix method. The uncertainty is determined to be 15%.

Simulation statistics

The uncertainty due to the limited size of simulated samples for all processes is included. The simulated templates for each process are randomised using a Gaussian with a width corresponding to the statistical error in the number of simulated events in each bin.

Luminosity

The luminosity is determined based on dedicated *van der Meer* scans [50]. The relative uncertainty in the integrated luminosity for 2012 data is evaluated to be 1.9%.

7.3 Signal extraction

This section gives an overview of the fiducial and total cross-section measurements of the t-channel single top-quark production at 8 TeV with the ATLAS detector based on Refs. [1, 2]. A statistical tool exploited to estimate the normalisation of the signal and background contributions is introduced in the first part of this section. After that, the final results of the fiducial and total cross-sections are briefly discussed.

7.3.1 Binned maximum-likelihood fit

The number of observed signal events is estimated by a binned maximum-likelihood fit of the simulated events to the collision data. The entire range of the neural network output distributions in the ℓ^+ and ℓ^- channels discussed in Section 7.1.2 is fit simultaneously. The following technical description is based on Ref. [80]. The likelihood function is built from the product of the Poisson likelihoods of the content in each histogram bin and the product of Gaussian functions to constrain the background normalisation. The function is defined as:

$$L(\beta^s_{tq}, \beta^s_{\bar{t}q}; \beta^b_j) = \prod_{k=1}^{M} P(n_k; \mu_k) \cdot \prod_{j=1}^{B} G(\beta^b_j; 1.0, \Delta_j)\,, \tag{7.4}$$

where the parameters β^s_{tq} and $\beta^s_{\bar{t}q}$ are the scale factors for the two signal processes, and β^b_j are the scale factors for each background process j. The scale factors are defined as a ratio of the estimated cross-section to the expected cross-section. M is the number of bins of the neural network output distribution and B is the number of background processes.

The Poisson term describing the probability to observe n_k events in the bin k is defined as:

$$P(n_k; \mu_k) = \frac{e^{-\mu_k} \cdot \mu_k^{n_k}}{n_k!}\,, \tag{7.5}$$

where μ_k is the number of expected events in bin k given by the sum of the number of expected signal events $\mu^s_{tq,k}$ and $\mu^s_{\bar{t}q,k}$ and the number of expected background events μ^b_{jk}:

$$\mu_k = \mu^s_{tq,k} + \mu^s_{\bar{t}q,k} + \sum_{j=1}^{B} \mu^b_{j,k} \quad \text{where} \quad \mu^s_{t(\bar{t})q,k} = \beta^s_{t(\bar{t})q} \cdot \tilde{\nu}^s_{t(\bar{t})q} \cdot \alpha^s_{t(\bar{t})q,k} \text{ and } \mu^b_{jk} = \beta^b_j \cdot \tilde{\nu}^b_j \cdot \alpha^b_{jk}\,.$$

$\tilde{\nu}$ denotes the number of predicted events. α_k is the fraction of events in each bin k of the histogram. For each process, the α_k must be normalised such that $\sum_{k=1}^{M} \alpha_k = 1$.

A Gaussian is used to constrain the normalisation of each background process. The function has a mean of one and a width corresponding to the relative normalisation uncertainty of each background process.

Instead of maximisation of the likelihood function, minimisation of the negative logarithm of the likelihood function is employed. This is because it is numerically more stable. The minimisation is done using Minuit [116].

7.3.2 Fiducial and total cross-section measurements

As described in Section 7.3.1, the simultaneous binned maximum-likelihood fit to the neural network output distributions in the ℓ^+ and ℓ^- channels is performed to extract the numbers of signal events $\hat{\nu}(tq)$ and $\hat{\nu}(\bar{t}q)$. In the fit, all W^++jets processes, all W^-+jets processes, all top-quark background processes, as well as Z+jets and diboson processes are grouped into one template each. The event yields of the tq production, the $\bar{t}q$ production, the top-quark background, the W^++jets background and the W^-+jets background are fitted simultaneously. The event yields of the other background processes are fixed to the predicted numbers given in Table 5.2. After the fit, the event yields for the different processes are given in Table 7.2. In Figure 7.3, the neural network output distributions in the signal region for ℓ^+ and ℓ^- channels are shown. Figure 7.4 illustrates a representative set of the distributions of the input variables in the signal region for the ℓ^+ and ℓ^- channels. The simulated distributions of all processes are normalised to the event numbers obtained from the final fit to these discriminants given in Table 7.2. Good agreement between the modelling and the collision data is obtained for all cases.

Process	$\hat{\nu}(\ell^+)$	$\hat{\nu}(\ell^-)$
tq	11 800 ± 200	17 ± 1
$\bar{t}q$	11 ± 1	6 920 ± 170
$t\bar{t}, Wt, t\bar{b}/\bar{t}b$	19 300 ± 740	18 900 ± 730
W^++ jets	18 800 ± 780	48 ± 2
W^-+ jets	23 ± 1	13 100 ± 740
Z, VV + jets	1 290	1 190
Multijet	4 520	4 520
Total estimated	55 800 ± 1 100	44 700 ± 1 100
Data	55 800	44 687

Table 7.2: Event yields for the different processes estimated after the fit to the neural network distribution compared to the numbers of observed events. Only the statistical uncertainties are quoted. The Z+jets and VV contributions and the multijet background are fixed in the fit; therefore no uncertainty is quoted for these processes. [2]

To avoid the large model dependencies, the cross-sections are measured in the fiducial phase space as discussed in Section 6.2. The definition of the fiducial cross-section, σ_{fid}, is defined as:

$$\sigma_{\text{fid}} = \frac{N_{\text{fid}}}{N_{\text{sel}}} \cdot \frac{\hat{\nu}}{\mathcal{L}_{\text{int}}}, \tag{7.6}$$

where N_{fid} is the number of simulated signal events after applying the cuts of particle-level selection, N_{sel} is the number of simulated signal events after applying the cuts of reconstruction-level selection, and $\mathcal{L}_{\text{int}}$

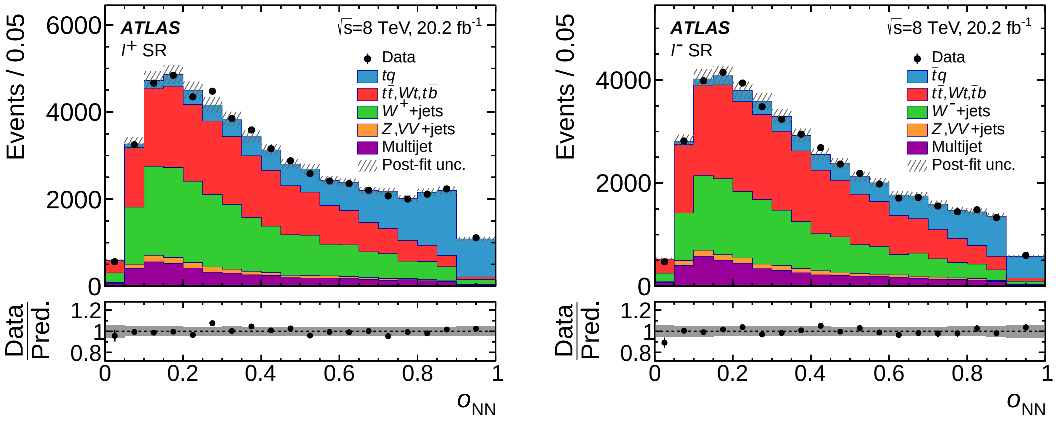

(a) (b)

Figure 7.3: Observed distributions of the NN discriminants in the SR for (a) the ℓ^+ channel and (b) the ℓ^- channel compared to the model obtained from simulated events. The simulated distributions are normalised to the event rates obtained by the fit to the discriminants. The hatched uncertainty band represents the total uncertainty in the rates of all processes after the fit and the bin-by-bin MC statistical uncertainty, added in quadrature. The lower panels show the ratio of the observed to the expected number of events in each bin to illustrate the goodness-of-fit. [2]

is the integrated luminosity. The fiducial cross-sections are measured to be [2]

$$\begin{aligned}\sigma_{\text{fid}}(tq) &= 9.78 \pm 0.16\,(\text{stat.}) \pm 0.52\,(\text{syst.}) \pm 0.19\,(\text{lumi.})\text{ pb} \\ &= 9.78 \pm 0.57\text{ pb}\end{aligned} \tag{7.7}$$

and

$$\begin{aligned}\sigma_{\text{fid}}(\bar{t}q) &= 5.77 \pm 0.14\,(\text{stat.}) \pm 0.41\,(\text{syst.}) \pm 0.11\,(\text{lumi.})\text{ pb} \\ &= 5.77 \pm 0.45\text{ pb.}\end{aligned} \tag{7.8}$$

Pseudo experiments are exploited to determine the uncertainties in the number of signal events $\hat{\nu}(tq)$ and $\hat{\nu}(\bar{t}q)$. The procedure of the uncertainty evaluation is given in detail in Ref. [117]. The uncertainties are then propagated to the measured results. Table 7.3 shows the breakdown of the uncertainties for the fiducial cross-section measurements. The total uncertainties are determined to be ±5.8% for σ_{fid} (tq) and ±7.8% for σ_{fid} $(\bar{t}q)$. Figure 7.5 illustrates the measured fiducial cross-sections compared to the predictions from the NLO event generators Powheg-Box and MadGraph5_aMC@NLO in both four-flavour and five-flavour schemes. The parton shower, the hadronisation and the underlying event are simulated with either Pythia 6, Pythia 8 (version 8.2) [87], Herwig or Herwig 7 (version 7.0.1) [118]. Good agreement between the predictions is found. The measured cross-sections are described by all predictions.

The fiducial cross-sections can be extrapolated to the full phase space by applying a fiducial acceptance correction. It is defined as the ratio of the number of simulated signal events after applying the cuts of particle-level selection to the total number of simulated signal events before applying any selection cuts. The total cross-sections for different MC generators are shown in Figure 7.6. All extrapolated total cross-sections agree with each other. In case of the default generator Powheg-Box + Pythia 6, the total

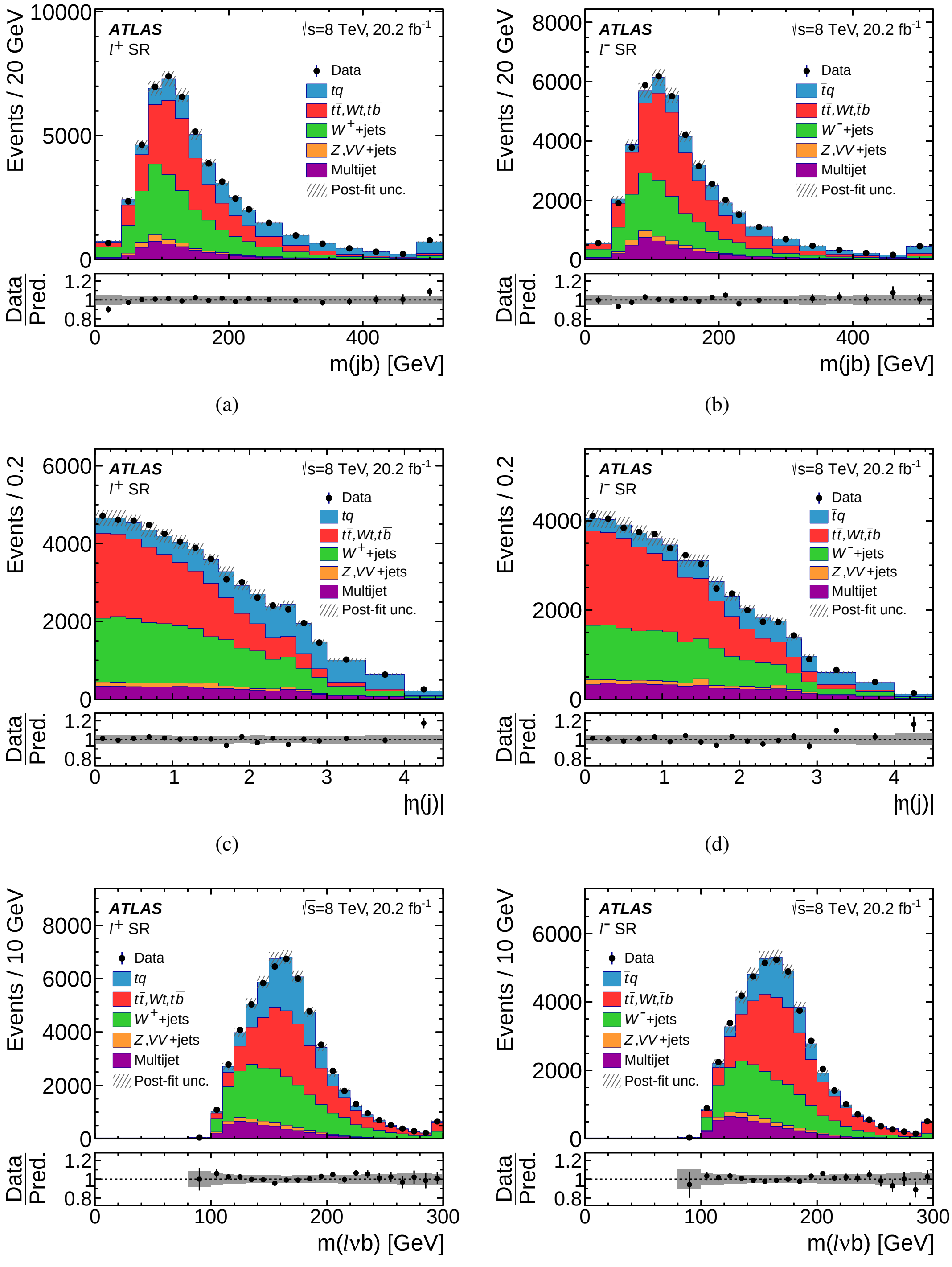

(a) (b) (c) (d) (e) (f)

Figure 7.4: Observed distributions of the three most important input variables to the NN in the signal region (SR) compared to the model obtained with simulated events. The definitions of the variables can be found in Table 7.1. The simulated distributions are normalised to the event rates obtained by the maximum-likelihood fit to the NN discriminants. The hatched uncertainty band represents the total uncertainty in the rates of all processes after the fit and the bin-by-bin MC statistical uncertainty, added in quadrature. The lower panels show the ratio of the observed to the expected number of events in each bin to illustrate the goodness-of-fit. Events beyond the x-axis range in (a), (b), (e) and (f) are included in the last bin. [2]

Source	$\Delta\sigma_{\text{fid}}(tq)$ / $\sigma_{\text{fid}}(tq)$ [%]	$\Delta\sigma_{\text{fid}}(\bar{t}q)$ / $\sigma_{\text{fid}}(\bar{t}q)$ [%]
Data statistics	± 1.7	± 2.5
Monte Carlo statistics	± 1.0	± 1.4
Background normalisation	< 0.5	< 0.5
Background modelling	± 1.0	± 1.6
Lepton reconstruction	± 2.1	± 2.5
Jet reconstruction	± 1.2	± 1.5
Jet energy scale	± 3.1	± 3.6
Flavour tagging	± 1.5	± 1.8
$E_{\text{T}}^{\text{miss}}$ modelling	± 1.1	± 1.6
$b/\bar{b}$ tagging efficiency	± 0.9	± 0.9
PDF	± 1.3	± 2.2
tq ($\bar{t}q$) NLO matching	± 0.5	< 0.5
tq ($\bar{t}q$) parton shower	± 1.1	± 0.8
tq ($\bar{t}q$) scale variations	± 2.0	± 1.7
$t\bar{t}$ NLO matching	± 2.1	± 4.3
$t\bar{t}$ parton shower	± 0.8	± 2.5
$t\bar{t}$ scale variations	< 0.5	< 0.5
Luminosity	± 1.9	± 1.9
Total systematic	± 5.6	± 7.3
Total (stat. + syst.)	± 5.8	± 7.8

Table 7.3: Detailed list of the contribution from each source of uncertainty to the total uncertainty in the measured values of $\sigma_{\text{fid}}(tq)$ and $\sigma_{\text{fid}}(\bar{t}q)$. The estimation of the systematic uncertainties has a statistical uncertainty of 0.3 %. Uncertainties contributing less than 0.5 % are marked with "< 0.5". [2]

cross-sections are [2]

$$\begin{aligned}\sigma_{\text{total}}(tq) &= 56.7 \pm 0.9\,(\text{stat.}) \pm 2.7\,(\text{exp.})\,^{+2.7}_{-1.7}\,(\text{scale}) \pm 0.4\,(\text{PDF}) \\ &\quad \pm 1.0\,(\text{NLO-matching method}) \ \pm 1.1\,(\text{parton shower}) \pm 1.1\,(\text{lumi.})\ \text{pb} \\ &= 56.7^{+4.3}_{-3.8}\ \text{pb}\end{aligned} \tag{7.9}$$

and

$$\begin{aligned}\sigma_{\text{total}}(\bar{t}q) &= 32.9 \pm 0.8\,(\text{stat.}) \pm 2.3\,(\text{exp.})\,^{+1.4}_{-0.8}\,(\text{scale}) \pm 0.3\,(\text{PDF}) \\ &\quad ^{+0.7}_{-0.6}\,(\text{NLO-matching method}) \ \pm 0.6\,(\text{parton shower}) \pm 0.6\,(\text{lumi.})\ \text{pb} \\ &= 32.9^{+3.0}_{-2.7}\ \text{pb}\,.\end{aligned} \tag{7.10}$$

The total uncertainties are $^{+7.6}_{-6.7}$% for σ_{total} (tq) and $^{+9.1}_{-8.4}$% for σ_{total} ($\bar{t}q$).

It can be seen that the total uncertainties in the fiducial cross-sections are smaller. This is due to the reduction of the uncertainties related to signal MC generators, as the differences in the signal acceptance is in the fiducial phase space only. Complete details on the fiducial and total cross-section measurements of the t-channel single top-quark production can be found in Refs. [1, 2].

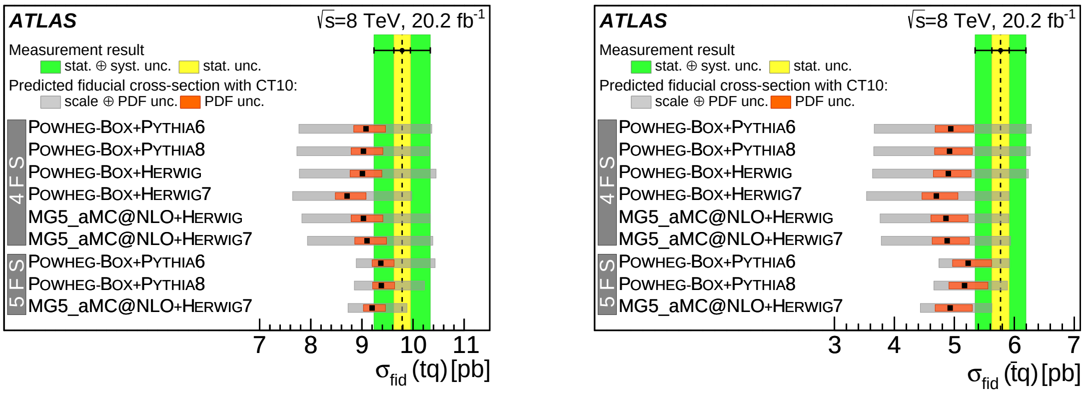

(a) (b)

Figure 7.5: Measured *t*-channel (a) single-top-quark and (b) single-top-antiquark fiducial cross-sections compared to predictions by the NLO MC generators POWHEG-BOX and MADGRAPH5_aMC@NLO in the four-flavour scheme (4FS) and five-flavour scheme (5FS) combined with different parton-shower models. The uncertainties in the predictions include the uncertainty due to the scale choice using the method of independent restricted scale variations and the intra-PDF uncertainty in the CT10 PDF set. [2]

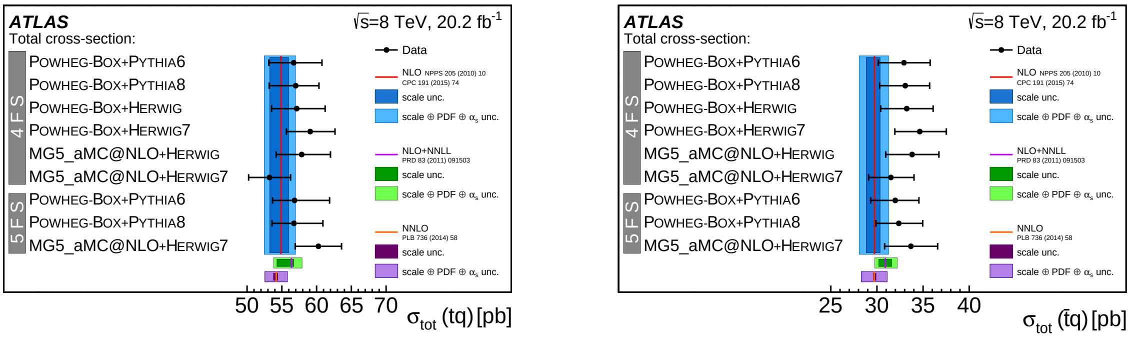

(a) (b)

Figure 7.6: Extrapolated *t*-channel (a) single-top-quark and (b) single-top-antiquark production cross-sections for different MC-generator setups compared to fixed-order NLO calculations. For the three calculations, the uncertainty from the renormalisation and factorisation scales are indicated in darker shading, and the total uncertainties, including the renormalisation and factorisation scale as well as the PDF+α_S uncertainties, are indicated in lighter shading. For the NNLO prediction, only the renormalisation and factorisation scale uncertainty is provided in Ref. [119]. For comparison, the PDF+α_S uncertainties from the NLO prediction [26] are added to the NNLO renormalisation and factorisation scale uncertainty reflected in the lighter shaded uncertainty band. For this comparison, the uncertainty in the extrapolation does not include the contribution from the NLO-matching method and from the choice of parton-shower model. [2]

CHAPTER 8

Ingredients of differential cross-section measurements

The differential cross-section measurements are performed in a high purity region, which is obtained by imposing a cut on the neural network discriminant, in order to achieve a good signal-to-background ratio. As a consequence, the effect of systematic uncertainties on the background can be decreased, while the statistical uncertainties are at an acceptable level. The same O_{NN} discriminant as employed to extract the fiducial and total t-channel cross-sections is used, except for the $|y(\hat{j})|$ measurement, where a second neural network (O_{NN2}) is trained without the variable $|\eta(j)|$.

This chapter starts with a description of the high purity region. The strategy to decide a suitable binning of p_{T} and $|y|$ for top (anti)quarks, pseudo-top-(anti)quarks and untagged jets is discussed in the second part of the chapter.

8.1 Enriched signal region

A large purity of the signal candidate events is necessary for a differential cross-section measurement because it keeps the uncertainties due to background normalisation at bay. This can be reached by placing a cut on the O_{NN} discriminant. A sufficient cut is chosen by looking at the signal-over-background ratio, S/B, distribution of the O_{NN} discriminant. Figure 8.1 shows the S/B distribution of the default O_{NN} discriminant for the ℓ^+ and ℓ^- channels. A cut of $O_{\mathrm{NN}} > 0.8$ is chosen. This gives an $S/B \sim 2$ for the ℓ^+ channel and an $S/B \sim 1.2$ for the ℓ^- channel. The optimisation of the $O_{\mathrm{NN}} > 0.8$ cut is detailed in Appendix B.

The event yields of the ℓ^+ and ℓ^- channels after the selection cuts together with the $O_{\mathrm{NN}} > 0.8$ cut applied are listed in Table 8.1. The fraction of multijet background is estimated using a fit to the full $E_{\mathrm{T}}^{\mathrm{miss}}$ distribution. The other processes are normalised with the fractions that are evaluated from the binned maximum-likelihood fit for the total cross-section measurement. The uncertainties are the normalisation uncertainty after the fit. Figure 8.2 shows distributions of the first three input variables to the default O_{NN} discriminant after the $O_{\mathrm{NN}} > 0.8$ cut for both ℓ^+ and ℓ^- channels. The expected number of events for each process is normalised to its estimate given in Table 8.1. The uncertainties are the normalisation uncertainty after the fit and bin-by-bin MC statistical uncertainty. Overall, good agreement between collision data and modelling is observed for all kinematic variables. Each variable shows that its distributions are similar between the ℓ^+ and ℓ^- channels. It can be seen in Figure 8.2 (a-b) that the signal distribution peaks at $m(jb) \sim 200\,\mathrm{GeV}$. Some deviations are found in a region of

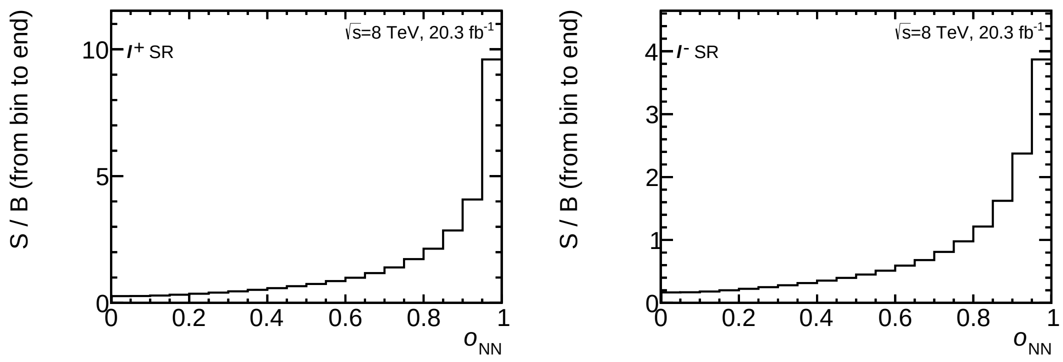

(a) ℓ^+ channel

(b) ℓ^- channel

Figure 8.1: Signal-over-background ratio distribution of the default neural network for (a) the ℓ^+ and (b) ℓ^- channels.

$|\eta(j)| < 1.0$ and of $|\eta(j)| > 4.0$, as shown in Figure 8.2 (c-d). t-channel signal events populate mostly around $150\,\text{GeV} < m(\ell\nu b) < 180\,\text{GeV}$, as shown in Figure 8.2 (e-f).

Process	ℓ^+ SR ($O_{\text{NN}} > 0.8$)	ℓ^- SR ($O_{\text{NN}} > 0.8$)
tq	$4\,470 \pm 180$	5 ± 0
$\bar{t}q$	3 ± 0	$2\,270 \pm 130$
$t\bar{t}, Wt, t\bar{b}/\bar{t}b$	754 ± 45	753 ± 45
$W^+ +$jets	960 ± 190	1 ± 0
$W^- +$jets	1 ± 0	610 ± 120
$Z, VV +$jets	52 ± 10	60 ± 12
Multijet	291 ± 46	267 ± 39
Total estimated	$6\,540 \pm 270$	$3\,960 \pm 190$
Data	6 567	4 007

Table 8.1: Predicted (post-fit) and observed event yields for the signal region (SR), after the requirement on the default neural network discriminant, $O_{\text{NN}} > 0.8$. The multijet-background prediction is obtained from the fit to the $E_{\text{T}}^{\text{miss}}$ distribution, while all the other predictions and uncertainties are derived from the total cross-section measurement. An uncertainty of 0 means that the value is < 0.5. [2]

8.1.1 Untagged jet distribution

Placing a cut on the default neural network shows a considerable deficit for small pseudorapidity values of the untagged jets shown in Figure 8.3 (a) and (b). This is because the absolute value of the pseudorapidity of the untagged jet is the second most important variable to this neural network. Such a distortion of the distribution due to a cut on the O_{NN} discriminant leads to very large and rapidly changing correction factors, $C_k^{\text{ptcl!reco}}$, illustrated in Figure 8.4 (a) and (b). This makes the extraction of a reliable unfolded distribution difficult. The correction factors, $C_k^{\text{ptcl!reco}}$, are defined in Equation 9.7.

To resolve this problem, a second network is trained omitting the $|\eta(j)|$ from the list of variables of the default neural network. Distributions of the neural network discriminant of this second network, O_{NN2},

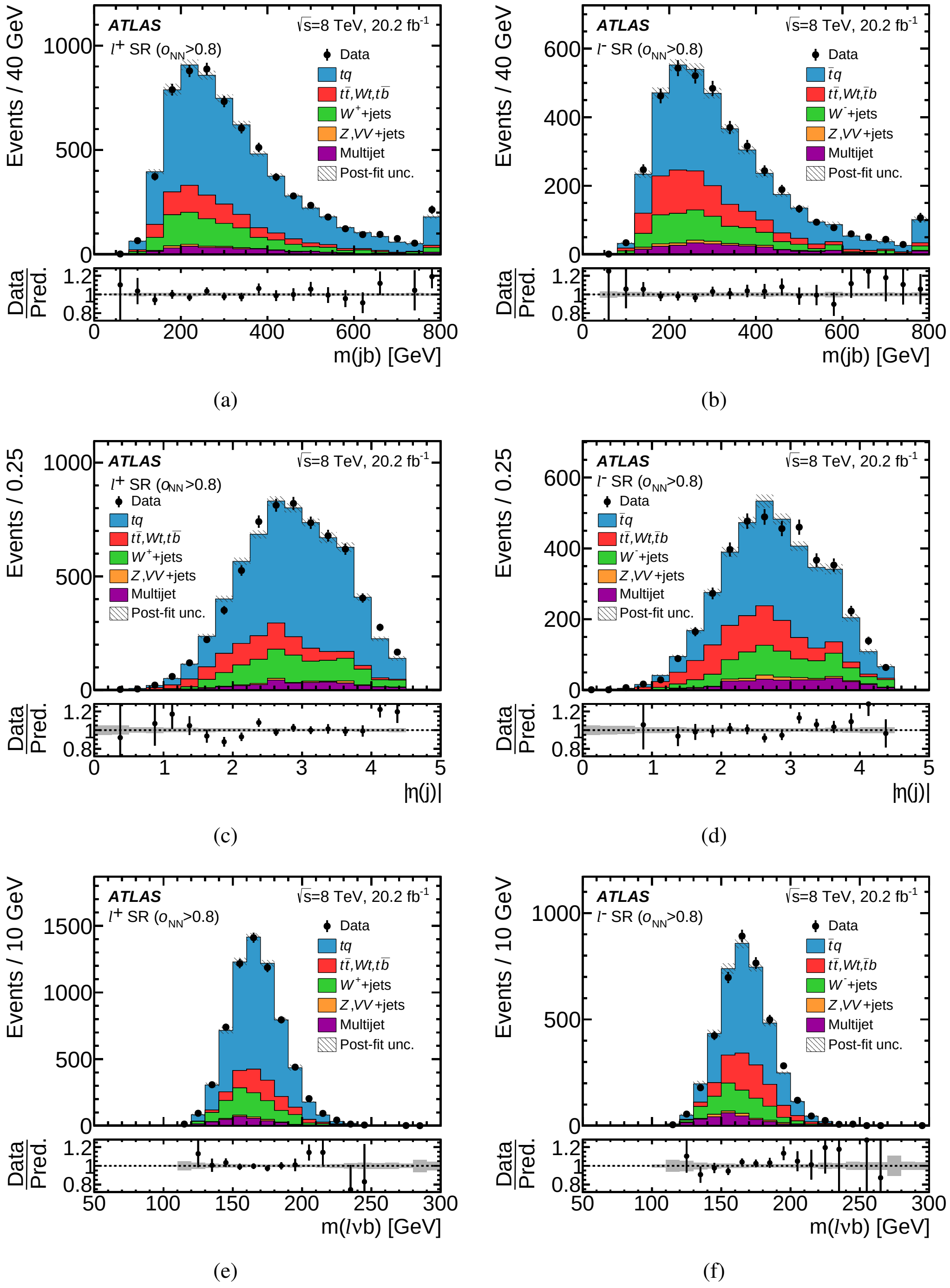

(a) (b)

(c) (d)

(e) (f)

Figure 8.2: Observed distributions of the first three input variables to the default neural network in the signal region (SR), after a cut of $O_{\mathrm{NN}} > 0.8$ on the network output. The distributions are compared to the model obtained from simulated events. The simulated distributions are normalised to the event rates obtained by the fit to the discriminants. The definitions of the variables can be found in Table 7.1. The hatched uncertainty band represents the total uncertainty in the rates of all processes after the fit and the bin-by-bin MC statistical uncertainty, added in quadrature. Events beyond the x-axis range in (a) and (b) are included in the last bin. The lower panels show the ratio of the observed to the expected number of events in each bin to illustrate the goodness-of-fit. [2]

normalised to the fit results of the default network are shown in Figure 8.5. The fit results of the default network are used as the primary estimate through the analysis. A good separation of t-channel signal from the backgrounds is achieved. With this second network, the changes in the $|y(\hat{j})|$ when applying a cut on the network discriminant are much reduced, as illustrated in Figure 8.3 (c) and (d). The correction factors are also much reduced and, more importantly, are much flatter as a function of $|y(\hat{j})|$, as can be seen in Figure 8.4 (c) and (d).

Process	ℓ^+ SR ($O_{\mathrm{NN2}} > 0.8$)	ℓ^- SR ($O_{\mathrm{NN2}} > 0.8$)
tq	$3\,440 \pm 140$	3 ± 0
$\bar{t}q$	2 ± 0	$1\,860 \pm 100$
$t\bar{t}, Wt, t\bar{b}/\bar{t}b$	$1\,072 \pm 64$	$1\,057 \pm 63$
$W^+ +$ jets	770 ± 150	0 ± 0
$W^- +$ jets	0 ± 0	494 ± 99
$Z, VV +$ jets	43 ± 9	48 ± 10
Multijet	192 ± 30	186 ± 27
Total estimated	$5\,520 \pm 220$	$3\,650 \pm 160$
Data	$5\,546$	$3\,647$

Table 8.2: Predicted (post-fit) and observed event yields for the signal region (SR), after the requirement on the neural network discriminant without $|\eta(j)|$, $O_{\mathrm{NN2}} > 0.8$. The multijet-background prediction is obtained from the fit to the $E_{\mathrm{T}}^{\mathrm{miss}}$ distribution, while all the other predictions and uncertainties are taken from the total cross-section measurement. An uncertainty of 0 means that the value is < 0.5. [2]

Figure 8.6 shows the signal-over-background ratio for the ℓ^+ and ℓ^- channels for the neural network without $|\eta(j)|$. By placing the same cut of 0.8 on this O_{NN2} discriminant, an $S/B \sim 1.6$ is achieved for the ℓ^+ channel and an $S/B \sim 0.9$ for the ℓ^- channel. Even though the signal-over-background ratio with the network without $|\eta(j)|$ is smaller, the separation is still good. This neural network is then used for the measurement of the $|y(\hat{j})|$ distribution. Table 8.2 shows the event yields of the ℓ^+ and ℓ^- channels after event selection as well as the $O_{\mathrm{NN2}} > 0.8$ cut applied. Figure C.1 in Appendix C shows distributions of the input variables after cutting on this O_{NN2} discriminant. The data is overall well described by the predictions.

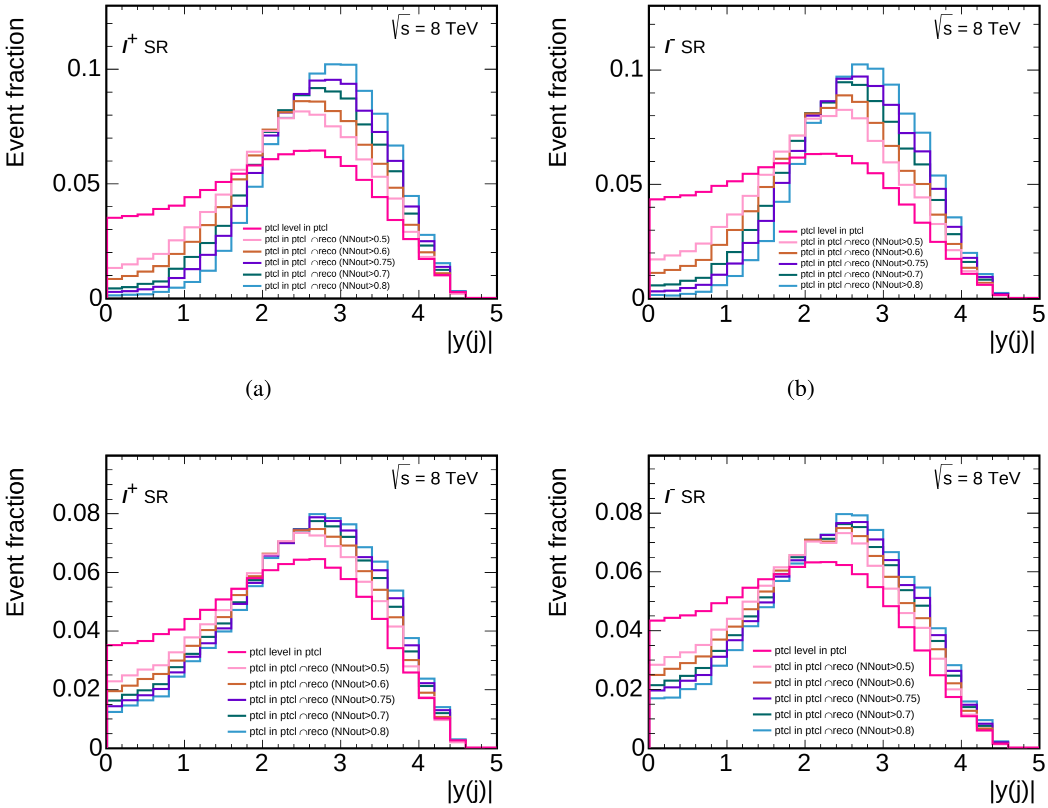

(a) (b)

(c) (d)

Figure 8.3: Distribution of $|y(\hat{j})|$ in (a) the ℓ^+ channel and (b) the ℓ^- channel with the default neural network. Distributions of $|y(\hat{j})|$ in (c) the ℓ^+ channel and (d) the ℓ^- channel with the neural network without $|\eta(j)|$. The particle-level untagged jets in the particle-level phase space is in dark pink. The other colours represent the particle-level untagged jets in the overlap region between the particle-level phase space and the reconstruction-level phase space with different O_{NN} cuts.

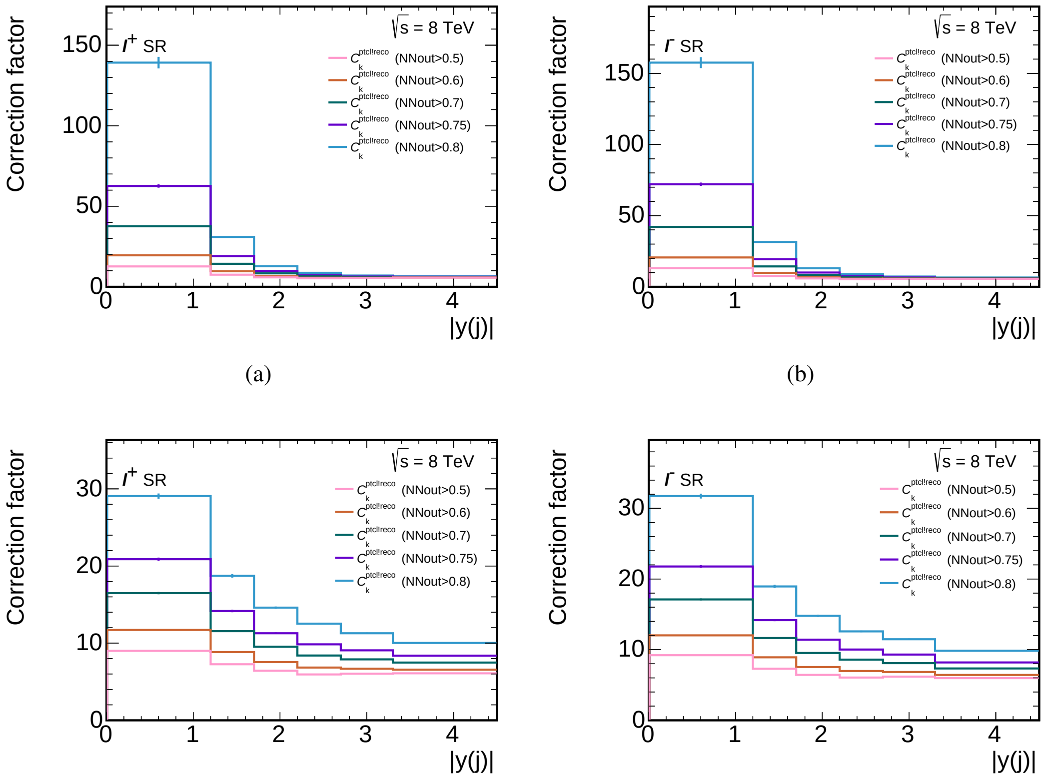

(a) (b)

(c) (d)

Figure 8.4: $C_k^{\text{ptcl!reco}}$ of $|y(\hat{j})|$ with different O_{NN} cuts for the ℓ^+ channel and the ℓ^- channel (a, b) with the default neural network training and (c, d) with the neural network training without $|\eta(j)|$.

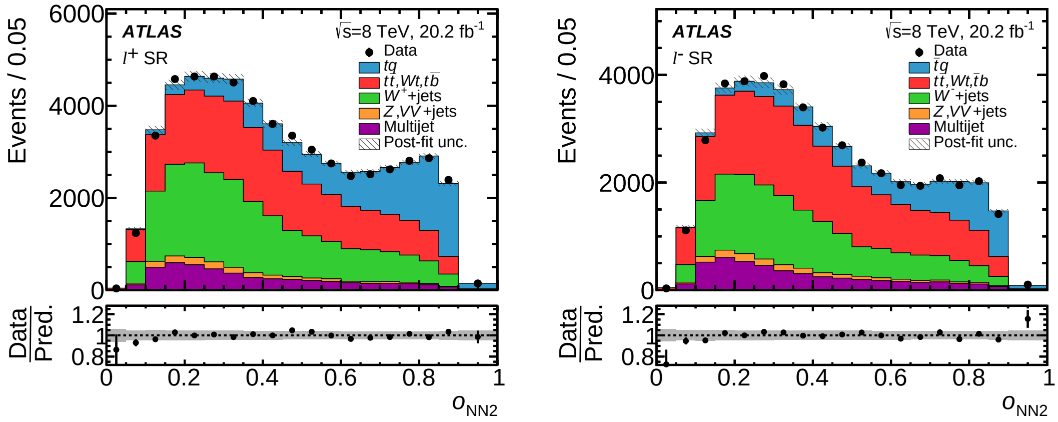

(a)

(b)

Figure 8.5: Neural network output distribution (O_{NN2}) of the neural network without $|\eta(j)|$ normalised to the fit results of the default network for (a) the ℓ^+ and (b) the ℓ^- signal region (SR). The distributions are compared to the model obtained from simulated events. The simulated distributions are normalised to the event rates obtained by the fit to the discriminants. The hatched uncertainty band represents the total uncertainty in the rates of all processes after the fit and the bin-by-bin MC statistical uncertainty, added in quadrature. The lower panels show the ratio of the observed to the expected number of events in each bin. [2]

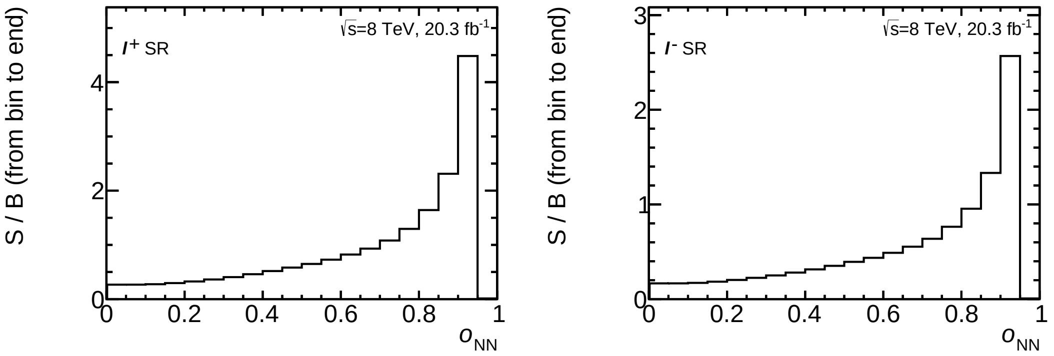

(a) ℓ^+ channel

(b) ℓ^- channel

Figure 8.6: Signal-over-background ratio distribution of the neural network without $|\eta(j)|$ for (a) the ℓ^+ channel and (b) the ℓ^- channel.

8.2 Binning of measured observables

The binning of the distributions for the differential cross-section measurement is chosen taking into account a reasonable range for the measurement, the experimental resolution of the variable, the data statistics in each bin and the migration matrix of the binned variable. The procedure of finding the binning for each variable is described as follows:

- An upper limit for each variable is set in order to have a reasonable range for doing the measurement.
- The experimental resolution of the variable is evaluated to set the minimal bin size. The resolution is defined as the width of a Gaussian fit to its residual distribution.
- The tails of the distributions are checked according to the data statistics in a bin of the data histogram before subtracting the backgrounds. A maximal uncertainty due to data statistics of the tail bin of around 10 % is required. In this way, mainly the size of the last bin of the distribution is fixed.
- The remaining variable range is scanned in steps of the size of the resolution. For each binning the migration matrices are built. A binning is preferred where at least 60 % of the events are in each of the diagonal bins, as this leads to the stability of the unfolding procedure.
- Except for the highest p_{T} bins, the same binning for the top-quark and top-antiquark distributions are used.

The binning of $p_{\mathrm{T}}^{tq}(t)$ and $p_{\mathrm{T}}^{\bar{t}q}(t)$ used when unfolding to parton level is discussed in detail along with the explanation of the strategy. The chosen binning of all unfolded variables is summarised in Section 8.2.1 and Section 8.2.2.

8.2.1 Binning of observables unfolded to parton level

$p_{\mathrm{T}}(t)$ distributions

For the $p_{\mathrm{T}}(t)$ distributions, an upper limit at 300 GeV is set because the statistics are poor above this value. For the inclusive generator-level distribution, the events in the overflow bins correspond to 0.55 % for the $p_{\mathrm{T}}^{tq}(t)$ and 0.37 % for the $p_{\mathrm{T}}^{\bar{t}q}(t)$ of the complete cross-section. This leads to a use of a migration matrix with overflow bins in the unfolding procedure. The average resolution (RMS of a Gaussian fitted in its residual distribution) is found to be 17 GeV. Thus, the minimal bin size of this variable is 17 GeV. Distributions of selection efficiency and resolution of each variable can be seen in Appendix D.

In order to have a sufficient number of data events in the last bin, a range of $[200, 300]$ GeV for the $p_{\mathrm{T}}^{tq}(t)$ and of $[150, 300]$ GeV for the $p_{\mathrm{T}}^{\bar{t}q}(t)$ are defined as the last bin of this distribution. The data statistical uncertainty of the last bin is 8.5 % for the $p_{\mathrm{T}}^{tq}(t)$ and 6.6 % for the $p_{\mathrm{T}}^{\bar{t}q}(t)$. For the remaining region, the parton-level p_{T} distributions with/without event selection are first investigated as shown in Figure 8.7. It can be seen that peak position of the selected top-(anti)quarks is clearly shifted due to the selection cuts. The remaining bin sizes of p_{T} are therefore chosen such that the peak structure is less pronounced, as sudden changes in a distribution lead to unstable unfolding.

The binning in steps of 5 GeV is scanned, requiring a minimal bin size of 17 GeV. The corresponding migration matrices are then built. Each diagonal entry of the matrix should be larger than 60 %. The first bin fulfils this condition at a minimal bin size of $[0, 50]$ GeV. The remaining region between 50 GeV and 200 GeV is divided in such a way that as many bins as possible are built with the > 60 % requirement along the diagonal of the matrix. The final p_{T} binning is set to $[0, 50, 100, 150, 200, 300]$ GeV for the $p_{\mathrm{T}}^{tq}(t)$ and to $[0, 50, 100, 150, 300]$ GeV for the $p_{\mathrm{T}}^{\bar{t}q}(t)$.

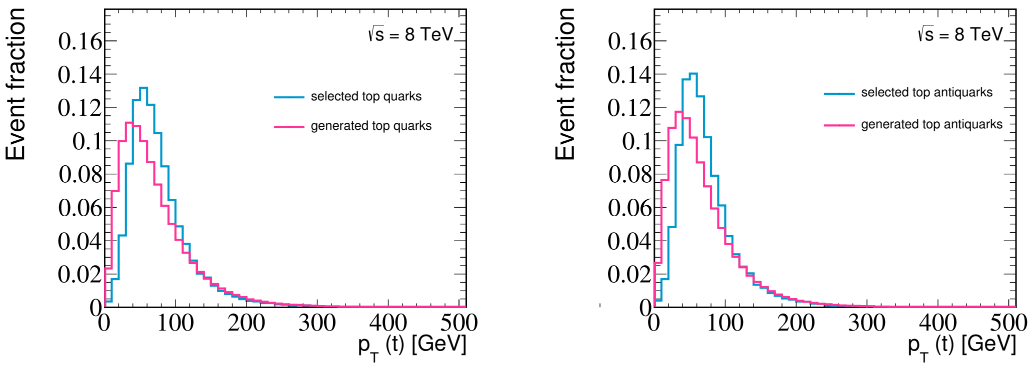

(a) (b)

Figure 8.7: Parton-level (a) $p_{\mathrm{T}}^{tq}(t)$ and (b) $p_{\mathrm{T}}^{\bar{t}q}(t)$ distributions with and without event-selection cuts applied.

$|y(t)|$ distributions

The selection efficiency for $|y^{tq}(t)|$ and $|y^{\bar{t}q}(t)|$ distributions drops very fast for $|y(t)| \gtrsim 1.8$. Large fluctuations are also observed in a region $|y(t)| > 2.5$, due to low statistics. To extend the range of the measurement as much as possible, the upper limit for this variable is set to $|y(t)| = 2.2$, where the efficiency is about a factor of 3–4 lower than at $|y(t)| = 0$ and the unreliable region is ignored. The events in the overflow bins correspond to 3.0 % for the $|y^{tq}(t)|$ and 1.9 % for the $|y^{\bar{t}q}(t)|$ of the complete cross-section.

In the region $|y(t)| < 2.2$, the average resolution is found to be 0.3. The last bin is set as [1.3,2.2] to fulfil the requirement on data statistics. The data statistical uncertainty of the last bin is 3.0 % for the $|y^{tq}(t)|$ and 4.1 % for the $|y^{\bar{t}q}(t)|$. The binning for the top-(anti)quark $|y(t)|$ distribution is then chosen to be $[0, 0.3, 0.7, 1.3, 2.2]$.

8.2.2 Binning of observables unfolded to particle level

$p_{\mathrm{T}}(\hat{t})$ distributions

The same strategy is used to find an appropriate binning of the pseudo-top-(anti)quark $p_{\mathrm{T}}(\hat{t})$ distributions. A range of $[0, 300]$ GeV is used for the measurement of $p_{\mathrm{T}}(\hat{t})$ distributions at particle level, due to large statistical uncertainty above 300 GeV. For the inclusive generator-level distribution, the events in the overflow bins correspond to 0.38 % for the $p_{\mathrm{T}}^{tq}(\hat{t})$ and 0.23 % for the $p_{\mathrm{T}}^{\bar{t}q}(\hat{t})$ of the complete cross-section in the fiducial phase space. The average resolution is found to be 9 GeV for this variable. The final binning is chosen to be $[0, 35, 50, 75, 100, 150, 200, 300]$ GeV for the $p_{\mathrm{T}}^{tq}(\hat{t})$ and $[0, 35, 50, 75, 100, 150, 300]$ GeV for the $p_{\mathrm{T}}^{\bar{t}q}(\hat{t})$. The bin sizes of the distributions are generally narrower than the distributions unfolded to parton level. This is due to better resolution of the pseudo-top-(anti)quark.

$|y(\hat{t})|$ distributions

For the same reasons as for the $|y(t)|$ distributions, an upper limit at 2.2 is also chosen for the $|y(\hat{t})|$ distributions. The selection efficiency drops very fast after 1.8. This yields the simulated events in the overflow bins of 0.22 % for the pseudo-top-quark $|y(\hat{t})|$ and 0.20 % for the pseudo-top-antiquark $|y(\hat{t})|$ of the complete cross-section in the fiducial phase space. The average resolution is found to be 0.03 for the $|y(\hat{t})|$ distributions. The final binning of $[0, 0.15, 0.3, 0.45, 0.7, 1.0, 1.3, 2.2]$ is chosen for both event sets.

$p_{\mathrm{T}}(\hat{j})$ distributions

In case of the $p_{\mathrm{T}}(\hat{j})$ distributions, the measurement is performed in a range of $[0, 300]$ GeV, due to high statistical fluctuation above 300 GeV. The number of particle-level events in the overflow bins corresponds to 0.37 % for the $p_{\mathrm{T}}^{tq}(\hat{j})$ and 0.23 % for the $p_{\mathrm{T}}^{\bar{t}q}(\hat{j})$ of the complete cross-section in the fiducial phase space. The average resolution is found to be 7 GeV for both $p_{\mathrm{T}}^{tq}(\hat{j})$ and $p_{\mathrm{T}}^{\bar{t}q}(\hat{j})$. A final binning of $[30, 45, 60, 75, 100, 150, 300]$ GeV is chosen. The data statistical uncertainty of the last bin is 5.0 % for $p_{\mathrm{T}}(\hat{j})$ of the top quark and 7.1 % for $p_{\mathrm{T}}(\hat{j})$ of the top antiquark.

$|y(\hat{j})|$ distributions

The range of the $|y(\hat{j})|$ distributions goes from 0 to 4.5. This range includes all reconstruction-level and generator-level events before and after selection. The average resolution is found to be 0.02 for both $|y^{tq}(\hat{j})|$ and $|y^{\bar{t}q}(\hat{j})|$. A binning of $[0, 1.2, 1.7, 2.2, 2.7, 3.3, 4.5]$ is chosen. The data statistical uncertainty of the last bin is 3.0 % for $|y^{tq}(\hat{j})|$ and 4.3 % for $|y^{\bar{t}q}(\hat{j})|$.

The measured differential distributions are shown in Figures 8.8 and 8.9. It can be seen that data is slightly softer than the model in the last bin of the $p_{\mathrm{T}}(\ell\nu b)$ distributions, but it is slightly higher than the model in the low-p_{T} region of the distribution for the ℓ^- channel. A small discrepancy between data and the model is found in the low-$|y|$ region of the $|y(\ell\nu b)|$ distribution for the ℓ^- channel. For the $p_{\mathrm{T}}(j)$ distributions, data are slightly higher than the model in the low-p_{T} region, but softer in the high-p_{T} region. There is a discrepancy between data and the model in the third bin of the $|y(j)|$ distribution for the ℓ^+ channel. This was studied in detail by varying the cut on the O_{NN2} discriminant in steps of 0.1. The distributions for electron and muon events were checked separately. In conclusion, it is most likely just a statistical fluctuation in the muon events.

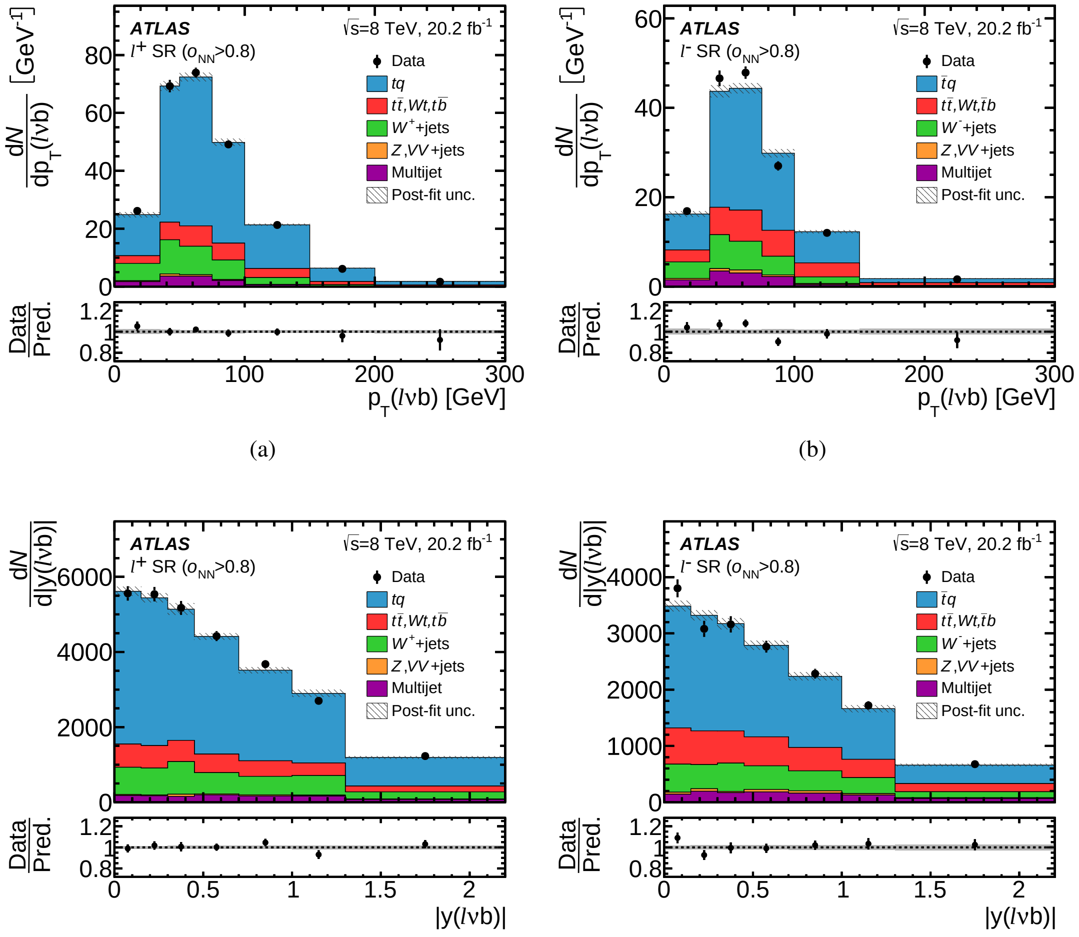

(a)

(b)

(c)

(d)

Figure 8.8: Measured distribution of (a,b) $\boldsymbol{p_\mathrm{T}(\ell\nu b)}$ and (c,d) $\boldsymbol{|y(\ell\nu b)|}$ for (a,c) ℓ^+ and (b,d) ℓ^- events in the signal region (SR) after a cut of $\boldsymbol{O_\mathrm{NN} > 0.8}$. The distributions are compared to the model obtained from simulated events. The simulated distributions are normalised to the event rates obtained by the fit to the discriminants. The hatched uncertainty band represents the total uncertainty in the rates of all processes after the fit and the bin-by-bin MC statistical uncertainty, added in quadrature. The lower panels show the ratio of the observed to the expected number of events in each bin to illustrate the goodness-of-fit. [2]

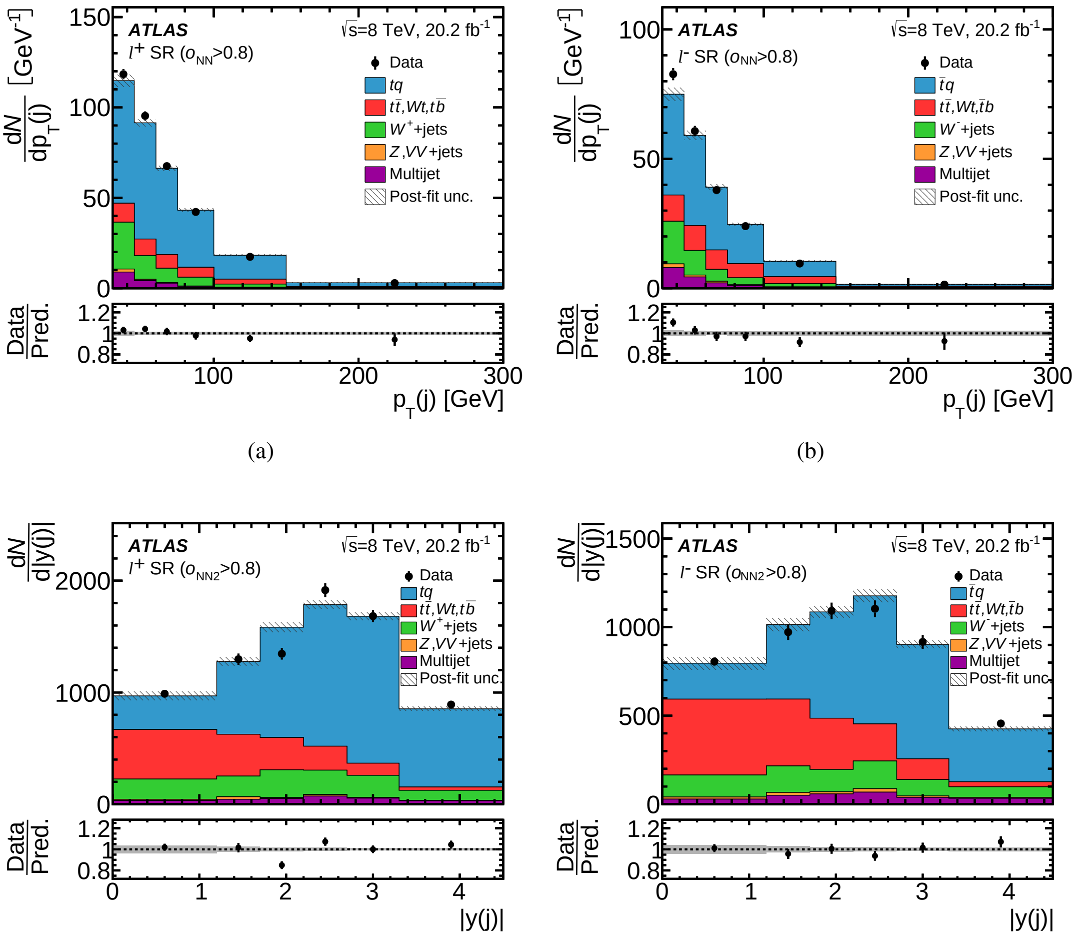

(a) (b)

(c) (d)

Figure 8.9: Measured distribution of (a,b) $p_{\mathrm{T}}(j)$ and (c,d) $|y(j)|$ for (a,c) ℓ^+ and (b,d) ℓ^- events in the signal region (SR) after a cut of $O_{\mathrm{NN}}(O_{\mathrm{NN2}}) > 0.8$. The distributions are compared to the model obtained from simulated events. The simulated distributions are normalised to the event rates obtained by the fit to the discriminants. The hatched uncertainty band represents the total uncertainty in the rates of all processes after the fit and the bin-by-bin MC statistical uncertainty, added in quadrature. The lower panels show the ratio of the observed to the expected number of events in each bin to illustrate the goodness-of-fit. [2]

CHAPTER 9

Differential cross-section extraction

After defining the high purity region described in Chapter 8, the measured distributions are unfolded using D'Agostini's iterative approach and corrected for the loss in selection efficiency to recover their underlying parton/particle-level distribution. Both absolute and normalised differential cross-sections are extracted in bins of $p_\mathrm{T}(t)$ and $|y(t)|$ at parton level in the full phase space as well as of $p_\mathrm{T}(\hat{t})$, $|y(\hat{t})|$, $p_\mathrm{T}(\hat{j})$ and $|y(\hat{j})|$ at particle level in the fiducial volume discussed in Section 6.2.

The first three sections of this chapter focus on describing the unfolding procedures to extract the absolute and normalised differential cross-sections. An overview of three different unfolding methods used in this analysis is given in Section 9.4. The ways to determine the number of iterations for the iterative Bayesian approach are discussed in Section 9.5. At the end of the chapter, various tests are presented in order to validate the unfolding procedure.

9.1 Parton-level differential cross-sections

Reconstructed measured distributions are distorted by detector effects and selection efficiency. In order to undo these effects, an unfolding technique is employed. At parton level, the relation between the observed (reconstruction-level) distribution and the generator-level distribution can be illustrated as:

$$N_j^\mathrm{data} = \sum_k M_{jk} \epsilon_k \mathcal{L}_\mathrm{int} \cdot \mathrm{d}\hat{\sigma}_k + \hat{B}_j \,, \tag{9.1}$$

where N_j^data is the number of measured data events in bin j, $\hat{B}_j$ the sum of all estimated background processes, $\mathrm{d}\hat{\sigma}_k$ the estimated parton-level cross-section in each bin k, $\mathcal{L}_\mathrm{int}$ the integrated luminosity of the data sample, ϵ_k the selection efficiency and M_{jk} the migration matrix.

Each estimated number of background events, $\tilde{\nu}_j^b$, is computed from the binned maximum-likelihood fit of the total cross-section measurements. $\hat{B}_j$ can be expressed as:

$$\hat{B}_j = \sum_{b \in \text{all backgrounds}} \tilde{\nu}_j^b \,. \tag{9.2}$$

The matrix M_{jk} describes the probability of finding an event that falls into parton-level bin k in bin j of the measured/observed distribution due to the detector resolution (assuming that the event is reconstructed at all). The migration matrices used in the unfolding for the $p_\mathrm{T}(t)$ and $|y(t)|$ at parton level are shown in Figure 9.1. The migration matrices and efficiencies were determined with the simulated t-channel sample using Powheg-Box + Pythia 6. It can be seen that the migration matrices of the top quark and top antiquark are similar and the diagonal elements are dominant.

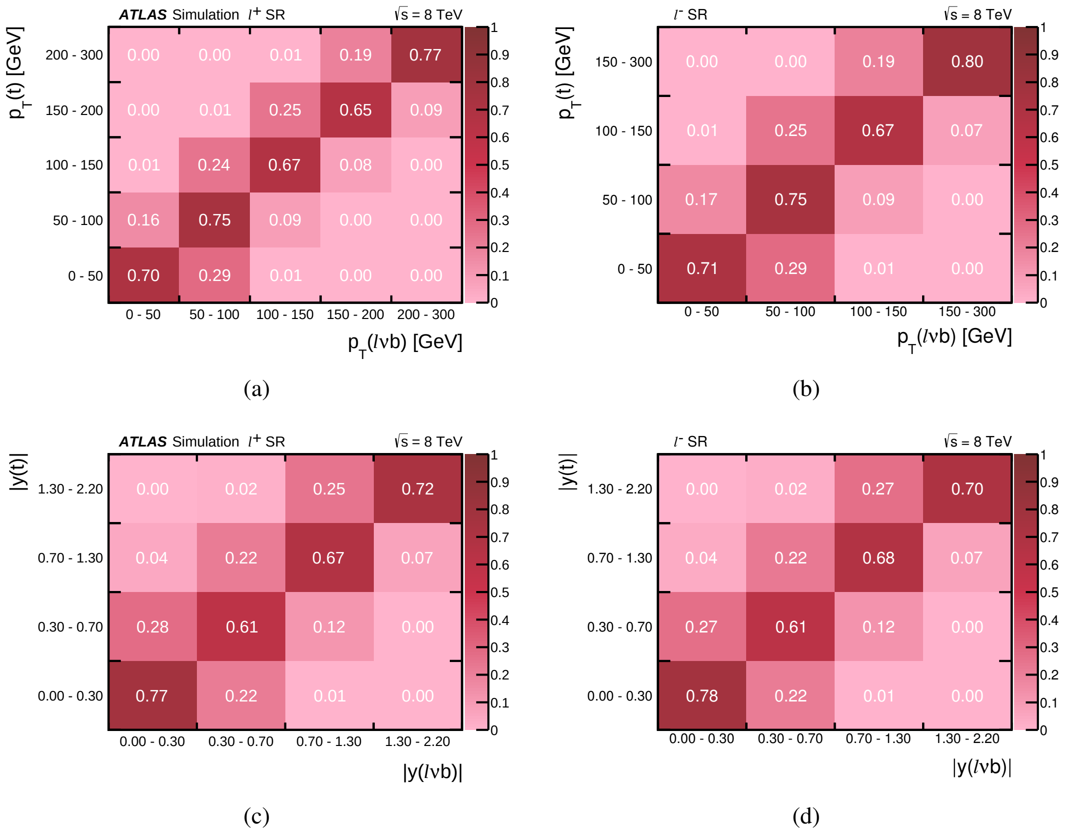

p_T(t) [GeV] \ p_T(lνb) [GeV]	0 - 50	50 - 100	100 - 150	150 - 200	200 - 300
200 - 300	0.00	0.00	0.01	0.19	0.77
150 - 200	0.00	0.01	0.25	0.65	0.09
100 - 150	0.01	0.24	0.67	0.08	0.00
50 - 100	0.16	0.75	0.09	0.00	0.00
0 - 50	0.70	0.29	0.01	0.00	0.00

(a)

p_T(t) [GeV] \ p_T(lνb) [GeV]	0 - 50	50 - 100	100 - 150	150 - 300
150 - 300	0.00	0.00	0.19	0.80
100 - 150	0.01	0.25	0.67	0.07
50 - 100	0.17	0.75	0.09	0.00
0 - 50	0.71	0.29	0.01	0.00

(b)

|y(t)| \ |y(lνb)|	0.00 - 0.30	0.30 - 0.70	0.70 - 1.30	1.30 - 2.20
1.30 - 2.20	0.00	0.02	0.25	0.72
0.70 - 1.30	0.04	0.22	0.67	0.07
0.30 - 0.70	0.28	0.61	0.12	0.00
0.00 - 0.30	0.77	0.22	0.01	0.00

(c)

|y(t)| \ |y(lνb)|	0.00 - 0.30	0.30 - 0.70	0.70 - 1.30	1.30 - 2.20
1.30 - 2.20	0.00	0.02	0.27	0.70
0.70 - 1.30	0.04	0.22	0.68	0.07
0.30 - 0.70	0.27	0.61	0.12	0.00
0.00 - 0.30	0.78	0.22	0.01	0.00

(d)

Figure 9.1: Migration matrices for (a) $p_{\mathrm{T}}^{tq}(t)$, (b) $p_{\mathrm{T}}^{\bar{t}q}(t)$, (c) $|y^{tq}(t)|$ and (d) $|y^{\bar{t}q}(t)|$ for parton level. The parton-level top quark is shown on the y-axis and the reconstruction-level variable is shown on the x-axis. The figures with ATLAS are published in Ref. [2].

The ϵ_k includes detector efficiencies due to e.g. trigger, b-tagging, a cut on the neural network output, as well as the probability for a t-channel event to pass the kinematic selection criteria. It is defined as:

$$\epsilon_k = \frac{S_k^{\mathrm{sel,MC}}}{S_k^{\mathrm{prod,MC}}}, \tag{9.3}$$

where $S_k^{\mathrm{prod,MC}}$ is the number of generated MC events in bin k, and $S_k^{\mathrm{sel,MC}}$ is the number of selected MC events after all cuts are applied in bin k. In Figure 9.2, it can be observed that the efficiency of top quark and top antiquark are similar. They are in a range of 0.7-1.5 %.

The estimated differential cross-section as a function of variable X in each bin k can then be written as:

$$\frac{\mathrm{d}\hat{\sigma}_k}{\mathrm{d}X_k} = \frac{1}{\Delta X_k} \cdot \frac{\sum_j M_{jk}^{-1}(N_j^{\mathrm{data}} - \hat{B}_j)}{\epsilon_k \cdot \mathcal{L}_{\mathrm{int}}}, \tag{9.4}$$

where ΔX_k is the width of bin k of variable X.

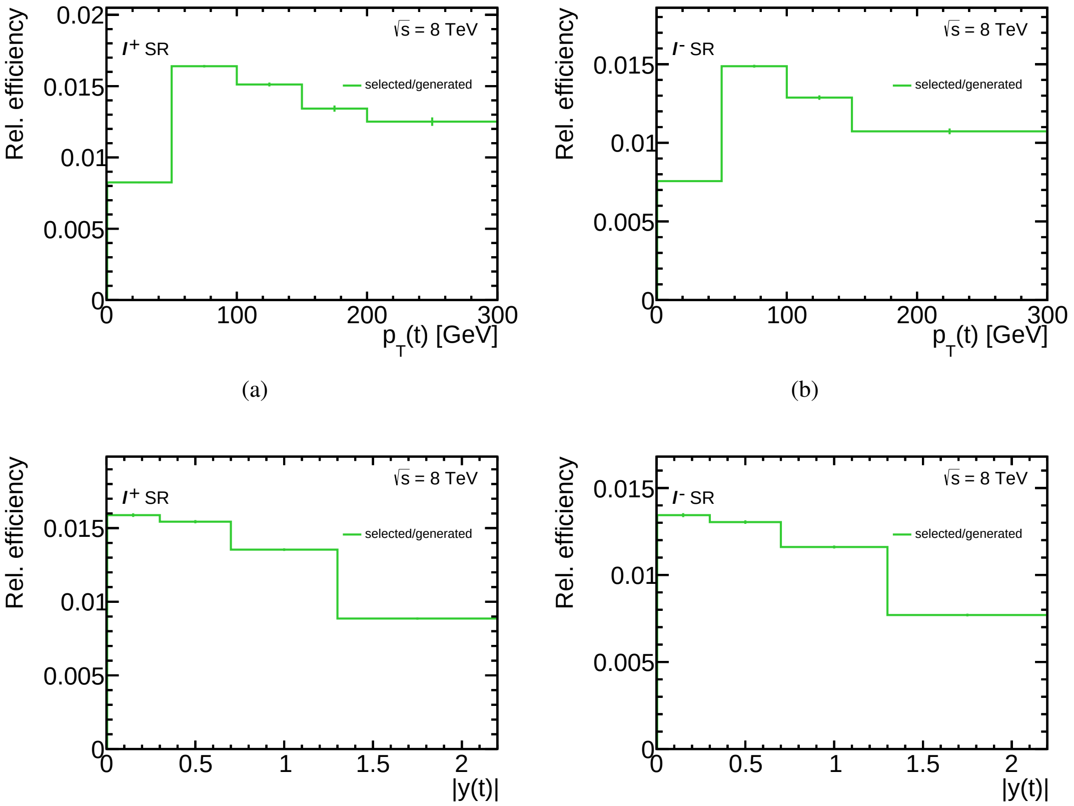

(a)

(b)

(c)

(d)

Figure 9.2: Selection efficiencies of (a) $p_{\mathrm{T}}^{tq}(t)$, (b) $p_{\mathrm{T}}^{\bar{t}q}(t)$, (c) $|y^{tq}(t)|$ and (d) $|y^{\bar{t}q}(t)|$ for parton level.

9.2 Particle-level differential cross-sections

The measured kinematic properties of the pseudo-top-quarks, pseudo-top-antiquarks and untagged jets are unfolded to the particle level within the fiducial phase space. The estimated number of signal events at particle level in bin k of the fiducial volume can be written as:

$$\hat{\nu}_k^{\text{ptcl}} = C_k^{\text{ptcl!reco}} \cdot \sum_j M_{jk}^{-1} \cdot C_j^{\text{reco!ptcl}} \cdot (N_j^{\text{data}} - \hat{B}_j)\,, \tag{9.5}$$

where M_{jk}^{-1} represents the Bayesian unfolding procedure described in Section 9.4.1, and $C_j^{\text{reco!ptcl}}$ and $C_k^{\text{ptcl!reco}}$ are correction factors. The migration matrix, M_{jk}, is constructed from events that pass both reconstruction-level and particle-level event selections.

Figure 9.3 shows the migration matrices for $p_{\mathrm{T}}(\hat{t})$, $|y(\hat{t})|$, $p_{\mathrm{T}}(\hat{j})$ and $|y(\hat{j})|$ for tq events at particle level. The migration matrices for $\bar{t}q$ events are shown in Figure E.1. Comparing to the parton-level migration matrices, the particle-level migration matrices have much smaller off-diagonal terms due to better resolution of the pseudo-top-(anti)quark. Strong correlation between the particle-level untagged jets and the reconstruction-level untagged jets are also seen in those figures (c,d).

The correction factor $C_j^{\text{reco!ptcl}}$ accounts for signal events that pass the reconstruction-level event

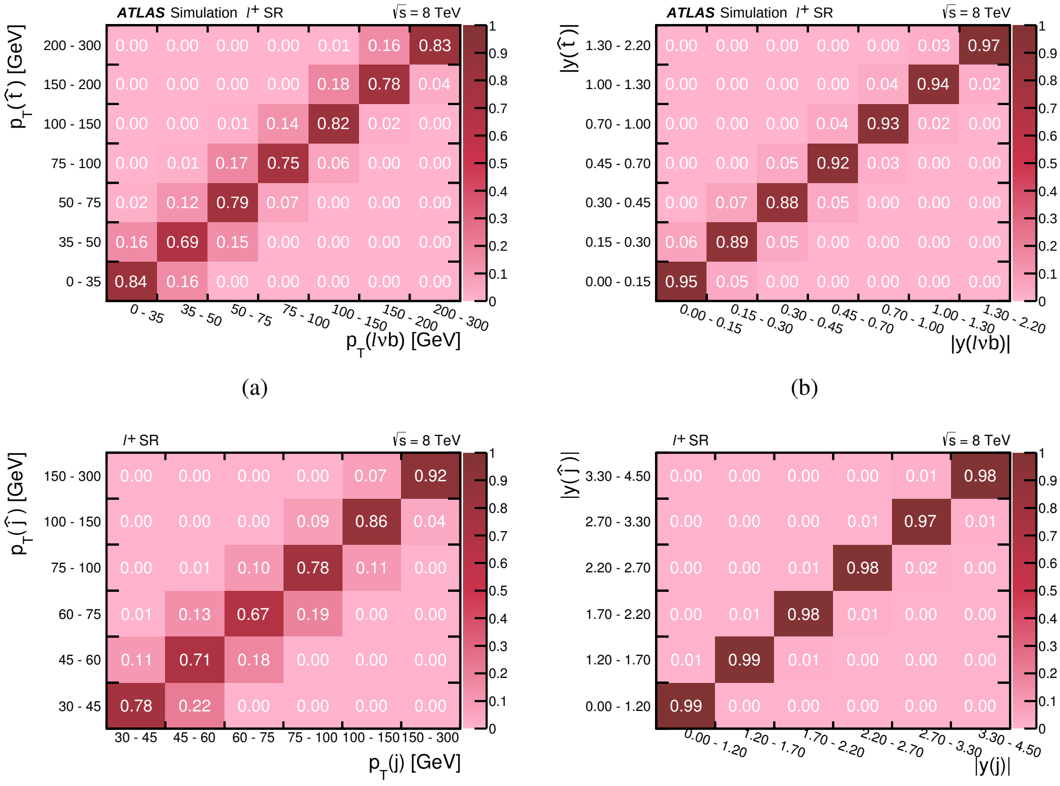

$p_T(\hat{t})$ [GeV] \ $p_T(l\nu b)$ [GeV]	0 - 35	35 - 50	50 - 75	75 - 100	100 - 150	150 - 200	200 - 300
200 - 300	0.00	0.00	0.00	0.00	0.01	0.16	0.83
150 - 200	0.00	0.00	0.00	0.00	0.18	0.78	0.04
100 - 150	0.00	0.00	0.01	0.14	0.82	0.02	0.00
75 - 100	0.00	0.01	0.17	0.75	0.06	0.00	0.00
50 - 75	0.02	0.12	0.79	0.07	0.00	0.00	0.00
35 - 50	0.16	0.69	0.15	0.00	0.00	0.00	0.00
0 - 35	0.84	0.16	0.00	0.00	0.00	0.00	0.00

(a)

$\lvert y(\hat{t})\rvert$ \ $\lvert y(l\nu b)\rvert$	0.00 - 0.15	0.15 - 0.30	0.30 - 0.45	0.45 - 0.70	0.70 - 1.00	1.00 - 1.30	1.30 - 2.20
1.30 - 2.20	0.00	0.00	0.00	0.00	0.00	0.03	0.97
1.00 - 1.30	0.00	0.00	0.00	0.00	0.04	0.94	0.02
0.70 - 1.00	0.00	0.00	0.00	0.04	0.93	0.02	0.00
0.45 - 0.70	0.00	0.00	0.05	0.92	0.03	0.00	0.00
0.30 - 0.45	0.00	0.07	0.88	0.05	0.00	0.00	0.00
0.15 - 0.30	0.06	0.89	0.05	0.00	0.00	0.00	0.00
0.00 - 0.15	0.95	0.05	0.00	0.00	0.00	0.00	0.00

(b)

$p_T(\hat{j})$ [GeV] \ $p_T(j)$ [GeV]	30 - 45	45 - 60	60 - 75	75 - 100	100 - 150	150 - 300
150 - 300	0.00	0.00	0.00	0.00	0.07	0.92
100 - 150	0.00	0.00	0.00	0.09	0.86	0.04
75 - 100	0.00	0.01	0.10	0.78	0.11	0.00
60 - 75	0.01	0.13	0.67	0.19	0.00	0.00
45 - 60	0.11	0.71	0.18	0.00	0.00	0.00
30 - 45	0.78	0.22	0.00	0.00	0.00	0.00

(c)

$\lvert y(\hat{j})\rvert$ \ $\lvert y(j)\rvert$	0.00 - 1.20	1.20 - 1.70	1.70 - 2.20	2.20 - 2.70	2.70 - 3.30	3.30 - 4.50
3.30 - 4.50	0.00	0.00	0.00	0.00	0.01	0.98
2.70 - 3.30	0.00	0.00	0.00	0.01	0.97	0.01
2.20 - 2.70	0.00	0.00	0.01	0.98	0.02	0.00
1.70 - 2.20	0.00	0.01	0.98	0.01	0.00	0.00
1.20 - 1.70	0.01	0.99	0.01	0.00	0.00	0.00
0.00 - 1.20	0.99	0.00	0.00	0.00	0.00	0.00

(d)

Figure 9.3: Migration matrix for (a) $p_{\mathrm{T}}^{tq}(\hat{t})$, (b) $|y^{tq}(\hat{t})|$ (c) $p_{\mathrm{T}}^{tq}(\hat{j})$ and (d) $|y^{tq}(\hat{j})|$ for particle level. The particle-level variable is shown on the y-axis and the reconstruction-level variable is shown on the x-axis. The figures with ATLAS are published in Ref. [2].

selection but not the particle-level event selection. It is expressed as:

$$C_j^{\text{reco!ptcl}} = \frac{S_j^{\text{reco}} - S_j^{\text{reco!ptcl}}}{S_j^{\text{reco}}}\,, \tag{9.6}$$

where S_j^{reco} is the number of reconstructed signal events in bin j and $S_j^{\text{reco!ptcl}}$ is the number of signal events that pass the reconstruction-level selection but not the particle-level selection. For each variable, the correction-factor distribution is typically flat over all bins as shown in Figure 9.4 for tq events. The distributions for $\bar{t}q$ events are shown in Figure E.2. The value is about 1 for the p_{T} distributions and about 0.9 for the $|y|$ distributions.

The correction factor $C_k^{\text{ptcl!reco}}$ accounts for signal events that pass the particle-level selection but not the reconstruction-level selection:

$$C_k^{\text{ptcl!reco}} = \frac{S_k^{\text{ptcl}}}{S_k^{\text{ptcl}} - S_k^{\text{ptcl!reco}}}\,, \tag{9.7}$$

where S_k^{ptcl} is the number of signal events at particle level and $S_k^{\text{ptcl!reco}}$ is the number of signal events that pass the particle-level selection but not the reconstruction-level selection. Figure 9.5 shows the correction

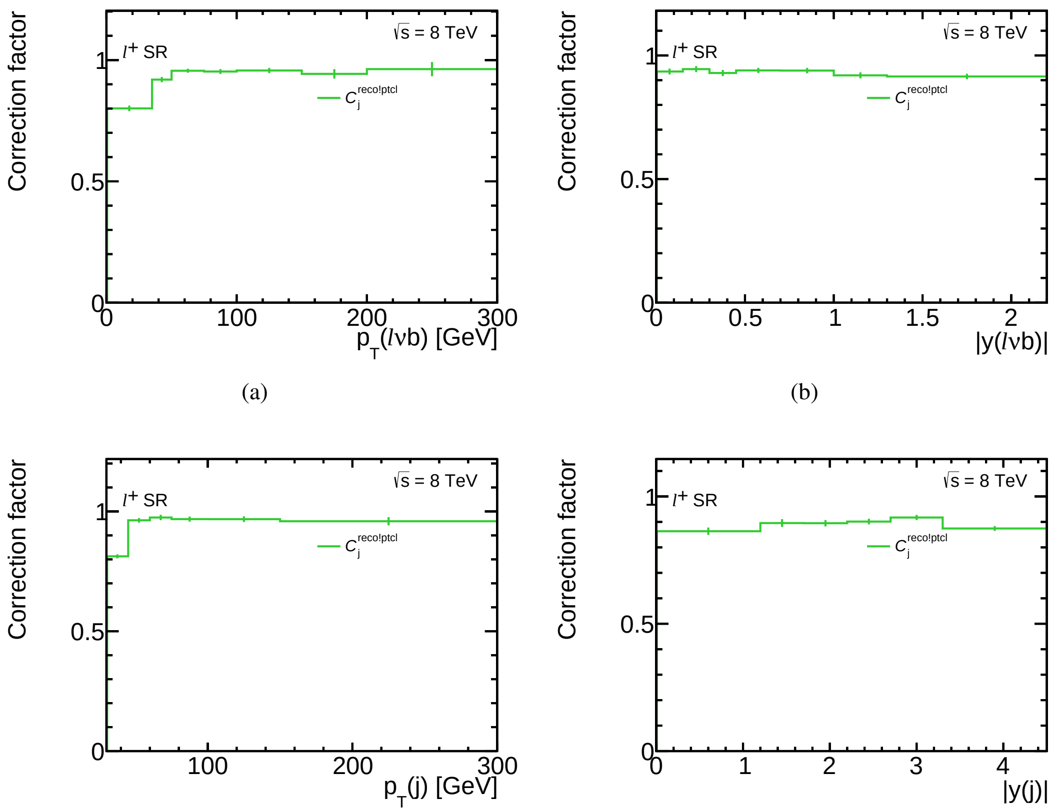

(a)

(b)

(c)

(d)

Figure 9.4: Correction factor $C_j^{\text{reco!ptcl}}$ for (a) $p_{\text{T}}(\ell\nu b)$, (b) $|y(\ell\nu b)|$, (c) $p_{\text{T}}(j)$ and (d) $|y(j)|$ at reconstruction level for tq events.

factor $C_k^{\text{ptcl!reco}}$ in the different bins of $p_{\text{T}}(\hat{t})$, $|y(\hat{t})|$, $p_{\text{T}}(\hat{j})$ and $|y(\hat{j})|$ for tq events. The distributions for $\bar{t}q$ events are shown in Figure E.3. The correction factors are in a range of 11-19 for the p_{T} distributions. The correction factors of the $|y(\hat{t})|$ are relatively flat. The correction factors are in a range of 12-32 for the $|y(\hat{j})|$. The large correction factors are found for all variables due to the event-selection requirements at reconstruction level and the cut on the neutral network discriminant. Sequential cutflows for the reconstruction-level and particle-level selections are shown in Appendix F. For the $|y(\hat{j})|$ distributions, the correction factor for the first bin is a factor of three larger than the one for the last bin.

The fiducial differential cross-section in bin k can be extracted from:

$$\frac{\mathrm{d}\hat{\sigma}_k}{\mathrm{d}X_k} = \frac{1}{\Delta X_k} \cdot \frac{\hat{\nu}_k^{\text{ptcl}}}{\mathcal{L}_{\text{int}}} . \tag{9.8}$$

9.3 Normalised differential cross-sections

The measurement of normalised different cross-sections is introduced because it leads to a reduction/cancellation of many systematic uncertainties. For a given variable, dividing the observed cross-section of each bin by the sum of the observed cross-sections in all bins yields normalised differential cross-sections. The uncertainty in the normalised cross-section in each bin is determined from the

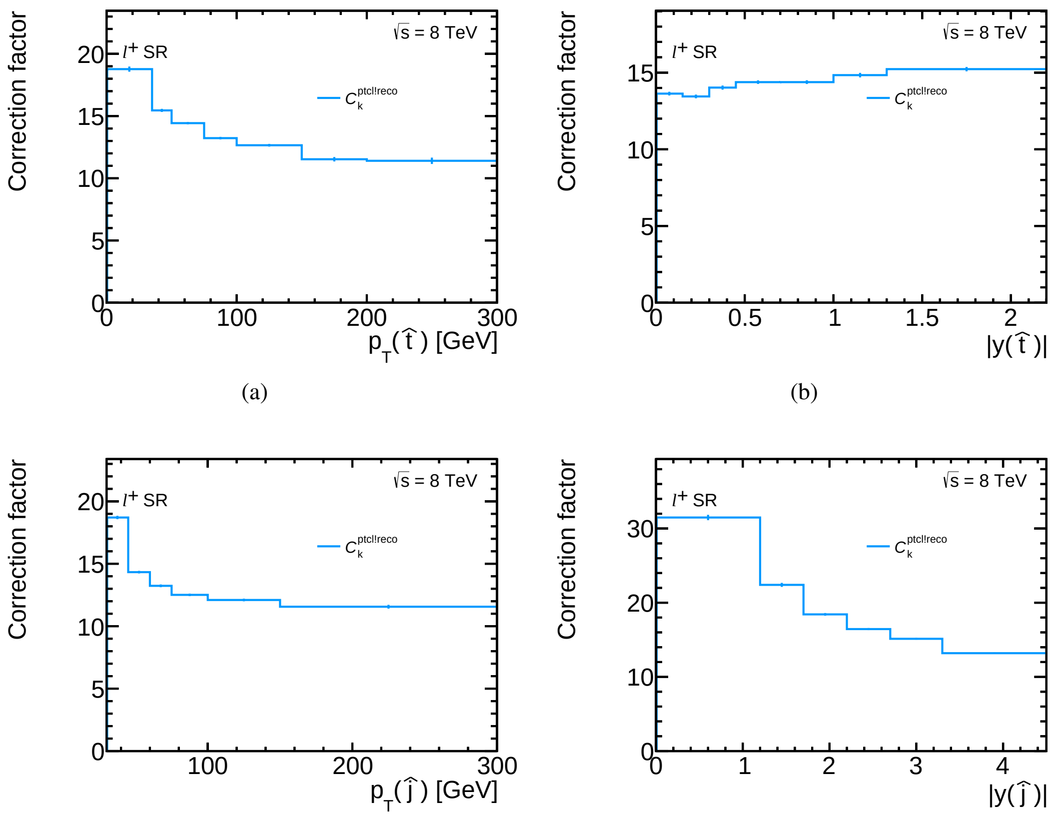

(a)

(b)

(c)

(d)

Figure 9.5: Correction factor $C_k^{\text{ptcl!reco}}$ for (a) $p_{\text{T}}(\hat{t})$, (b) $|y(\hat{t})|$, (c) $p_{\text{T}}(\hat{j})$ and (d) $|y(\hat{j})|$ for tq events.

coherent variation of the cross-section in that bin and the total cross-section when a variation reflecting a systematic uncertainty is applied.

9.4 Unfolding methods

9.4.1 Iterative Bayesian unfolding

The iterative Bayesian unfolding introduced by D'Agostini [120], implemented in RooUnfold framework [121], is employed as the default method in this thesis. The method can be described using a picture of an effect, E, and a cause, C. Each cause can generate various effects ($E_j, j = 1, 2, ..., n_E$), on the other hand the precise cause is unknown for a particular effect. Knowing the migration matrix, and the measurement efficiency and resolution, one can estimate the probability for an effect to come from a defined cause $P(E_j|C_k)$. This knowledge is usually obtained from Monte Carlo simulation. Using Bayes theorem [120] in terms of many independent causes ($C_k, k = 1, 2, ..., n_c$), the probability $P(C_k|E_j)$ for a cause C_k given the observation E_j can be expressed as:

$$P(C_k|E_j) = \frac{P(E_j|C_k) \cdot P_0(C_k)}{\sum_{l=1}^{n_c} P(E_j|C_l) \cdot P_0(C_l)}, \tag{9.9}$$

and the number of estimated events of cause C_k as:

$$N(C_k) = \frac{1}{\epsilon_k} \sum_{j=1}^{n_E} P(C_k|E_j) \cdot N(E_j)\,. \tag{9.10}$$

$P_0(C_k)$ is an initial distribution for the generator-level distribution, $P(E_j|C_k)$ corresponds to the migration matrix, as it describes the probability for effect E_j to originate from cause C_k, ϵ_k is the efficiency for events to be selected in bin k and $N(E_j)$ is the number of observed events. $N(C_k)$ is derived in an iterative way starting from the initial distribution $P_0(C_k)$.

In this analysis, the reconstructed measured t-channel single top (anti-)quark events in bin j, N_j^{reco}, are the effect, E_j. Thus, the expected number of produced t-channel events in bin k, corresponding to the cause, C_k, at parton level can be written as:

$$N(C_k) = \frac{1}{\epsilon_k} \sum_{j=1}^{n_E} P(C_k|E_j) \cdot N^{\text{reco}}(E_j)\,. \tag{9.11}$$

For the particle-level unfolding, the $N(C_k)$ can be expressed as:

$$N(C_k) = C_k^{\text{ptcl!reco}} \cdot \sum_{j=1}^{N} P(C_k|E_j) \cdot C_j^{\text{reco!ptcl}} \cdot N^{\text{reco}}(E_j)\,, \tag{9.12}$$

where $C_k^{\text{ptcl!reco}}$ and $C_j^{\text{reco!ptcl}}$ are the correction factors as described in Equation 9.6 and Equation 9.7, respectively.

In the iterative Bayesian unfolding, the solution can be regularised by iterative repeating the unfolding process as mentioned above until the result is stable. Criteria used to determine the optimal number of iterations can be found in detail in Section 9.5.

9.4.2 Singular value decomposition

Another method for unfolding is based on a singular value decomposition (SVD) of a migration matrix [122]. This method is regularised by a parameter, τ. In this thesis, the SVD method is used as a cross-check and the parameter τ is always set to the number of bins in the distribution.

9.4.3 Bin-by-bin correction factor

A bin-by-bin correction factor is used as a cross-check in this thesis. It uses the ratio of the reconstructed simulation to the theoretical predictions and extracts correction factors for each bin in the distribution. This method is meaningful when the measured values are very near to the predicted values, but in the case of large migrations or poor resolution, more complex unfolding methods are warranted. This is because off-diagonal elements are simply ignored when making the matrix inversion.

9.5 Choice of number of iterations

The number of iterations corresponding to the regularisation parameter of the iterative Bayesian unfolding is determined to ensure that the unfolding converges. To serve this purpose, three different criteria are investigated.

χ^2/N_{bin}

The solution from the current and previous iterations are compared using a χ^2 calculation after each iteration. The uncertainty is taken as the Poisson error on the number of events. The χ^2 is therefore a measure of the change of the unfolded distribution after each iteration. The iterations are stopped when the value of χ^2 divided by the number of bins smaller than 0.1. This criterion results in 2 iterations for $p_{\mathrm{T}}(t)$ for the parton-level cross-sections and 1 iteration for the other distributions.

Change of bin content

The absolute change in each bin content after each iteration, i, is evaluated. As a stopping criterion, the change in each bin respected to the bin content, N_k, is required to be less than 1 %:

$$\frac{|N_k(n_{\text{iter}} = i) - N_k(n_{\text{iter}} = i + 1)|}{N_k(n_{\text{iter}} = i + 1)} < 1\,\%\,, \tag{9.13}$$

where n_{iter} is the number of iterations. A Poisson distribution of the bin content in the background-subtracted data is employed to create 10000 pseudo experiments used in this investigation. The number of iterations is determined to be 4 for $p_{\mathrm{T}}(t)$ as well as for $|y^{tq}(t)|$ and 6 iterations for $|y^{\bar{t}q}(t)|$ for the parton-level cross-sections. It is estimated to be 3 for $p_{\mathrm{T}}^{tq}(\hat{t})$, 6 for $p_{\mathrm{T}}^{\bar{t}q}(\hat{t})$, 2 for $|y(\hat{t})|$, 3 for $p_{\mathrm{T}}^{tq}(\hat{j})$, 5 for $p_{\mathrm{T}}^{\bar{t}q}(\hat{j})$ and 2 for $|y(\hat{j})|$ for the particle-level cross-sections. This criterion is more stringent than the previous one because this method requires every bin to converge rather than imposing a global criterion.

Bias of the unfolded cross-section as a function of number of iterations

The bias of the unfolded cross-section after each iteration is checked for all differential cross-sections. The bias is determined from the difference between the unfolded result using the MadGraph5_aMC@NLO + Herwig signal sample as an alternative input for unfolding and its generator-level distribution. Its distribution is unfolded with the migration matrix and the efficiencies created from the simulated signal sample using Powheg-Box + Pythia 6. Here, the different simulated samples are used to calculate the bias because it can tell how well the unfolding process with alternative ingredients can recover its true distribution.

This criterion requires the bias to be smaller than 1 % in all bins. The change of the bias after each iteration for the differential cross-sections for tq events is shown in Figure 9.6. The distributions for $\bar{t}q$ events are shown in Figure E.4. It can be seen that the change of the bias for tq and $\bar{t}q$ events is similar for all variables, except for $p_{\mathrm{T}}(\hat{j})$. The number of iterations is determined to be 8 for $p_{\mathrm{T}}(t)$ and for $|y(t)|$ for the parton-level cross-sections. It is evaluated to be 8 for $p_{\mathrm{T}}(\hat{t})$, 4 for $|y(\hat{t})|$, 5 for $p_{\mathrm{T}}^{tq}(\hat{j})$, 9 for $p_{\mathrm{T}}^{\bar{t}q}(\hat{j})$ and 3 for $|y(\hat{j})|$ for the particle-level cross-sections.

Overall, the convergence depends on the shape of the measured distribution as well as the resolution of the variable. The $|y|$ distributions normally need a few iterations before convergence. On the other hand, the largest number of iterations is required for the p_{T} since the distribution has a peak at low-p_{T} region. The bias of the unfolded cross-section is the most stringent criterion and is the one that is finally adopted.

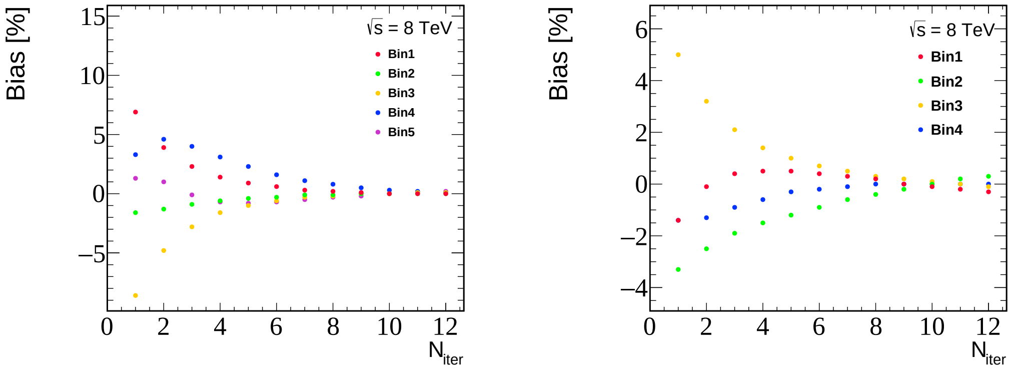

(a) $p_{\mathrm{T}}^{tq}(t)$ (b) $|y^{tq}(t)|$

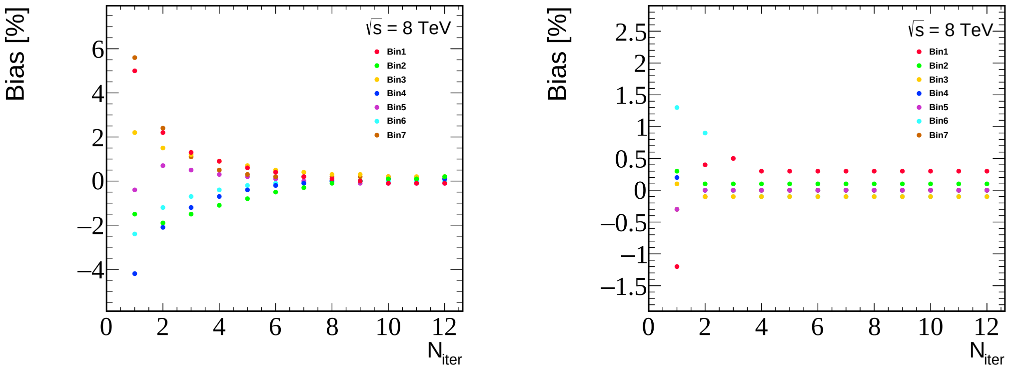

(c) $p_{\mathrm{T}}^{tq}(\hat{t})$ (d) $|y^{tq}(\hat{t})|$

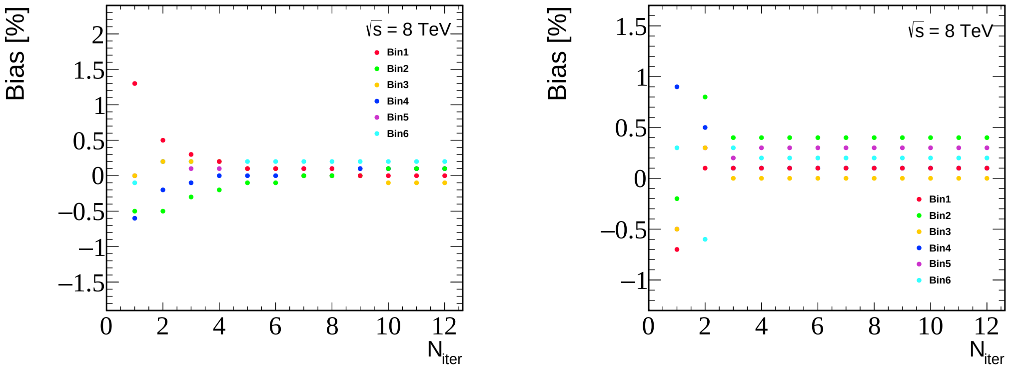

(e) $p_{\mathrm{T}}^{tq}(\hat{j})$ (f) $|y^{tq}(\hat{j})|$

Figure 9.6: Bias of the unfolded cross-section after each iteration for each bin in %, scanning the number of iterations from 1 to 12 for (a) $p_{\mathrm{T}}^{tq}(t)$, (b) $|y^{tq}(t)|$, (c) $p_{\mathrm{T}}^{tq}(\hat{t})$, (d) $|y^{tq}(\hat{t})|$, (e) $p_{\mathrm{T}}^{tq}(\hat{j})$ and (f) $|y^{tq}(\hat{j})|$.

9.6 Tests of the unfolding procedure

In the following, several tests are presented in order to validate the unfolding procedure. Comparison of the results with different unfolding methods is also discussed. Distributions for tq events are shown in the main text, while distributions for $\bar{t}q$ events are in Appendix E.3.

9.6.1 Closure of the simulation

For the closure test of the simulation, the signal sample simulated with Powheg + Pythia 6 is split into statistically comparable and independent halves. One half (`half1`) is used as the measured distribution, while the other half (`half2`) is used to build the migration matrix and efficiency. The measured distribution of `half1` is unfolded with the unfolding ingredients from `half2`. The unfolded distribution is then compared to the generator-level distribution of `half1`. Figure 9.7 shows the comparison for all distributions for tq events. It can be seen that good agreement between the unfolded and generator-level distributions within the uncertainty due to the size of the signal MC sample is achieved for all variables.

9.6.2 Stress test for the unfolding

A stress test for all variables for particle-level unfolding is performed, in order to verify that the unfolding procedure does not bias the result due to the Monte Carlo shape used for the migration matrix and efficiency. The particle-level unfolding is investigated for the normalised differential cross-sections only, because the difference in shape can be seen better with the normalised cross-sections. Each generator-level distribution created from the simulated signal sample with Powheg + Pythia 6 is reweighted bin-by-bin with [20 %, 10 %, 10 %, 0 %, −10 %, −10 %, −20 %] for a 7-bins case and [20 %, 10 %, 10 %, −10 %, −10 %, −20 %] for a 6-bins case. Clear differences between the observed data and the simulation with these reweighted reconstruction-level distributions are created. This demonstrates that the reweighted distributions are a good test of whether the unfolding can compensate for such a level of disagreement.

Each corresponding reconstruction-level reweighted distributions is then unfolded with the nominal migration matrix and efficiency. The unfolded reweighted distribution is compared to the reweighted generator-level and the nominal generator-level distribution. Figure 9.8 shows the stress test for $p_{\mathrm{T}}^{tq}(\hat{t})$, $|y^{tq}(\hat{t})|$, $p_{\mathrm{T}}^{tq}(\hat{j})$ and $|y^{tq}(\hat{j})|$. It can be seen that each unfolded reweighted distribution follows its reweighted generator-level distribution for all variables. The differences in shape between the unfolded reweighted distribution and the nominal generator-level distribution can also be found. From the results, the chosen unfolding method performs well and gives no significant bias.

9.6.3 Pull distributions

To ensure that the statistical error from the unfolding procedure is evaluated correctly, the pull distributions for each bin of the unfolding distribution are investigated. 2000 pseudo experiments from drawing a random number from a Poisson distribution whose mean is equal to the bin content in the simulated t-channel sample with aMC@NLO + Herwig are used for this check. The pseudo data from each experiment is unfolded using the nominal migration matrix and efficiency. Each pull is computed. It is defined as:

$$\mathrm{pull}_i = \frac{N_i^{\mathrm{unfold}} - N^{\mathrm{truth}}}{\sigma_i^{\mathrm{unfold}}}, \tag{9.14}$$

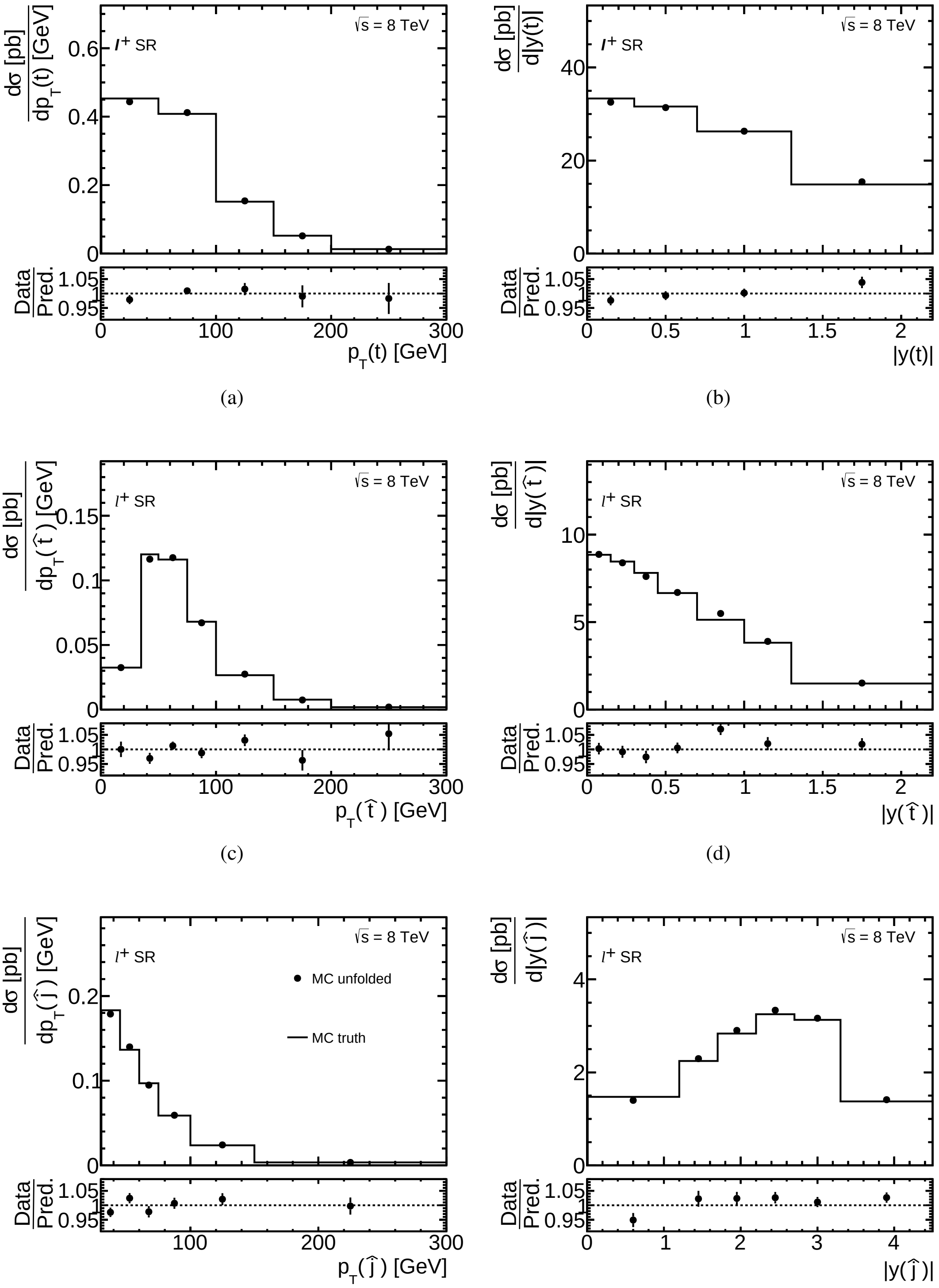

(a)

(b)

(c)

(d)

(e)

(f)

Figure 9.7: Closure of the unfolding procedure by unfolding one half of the signal MC sample with the migration matrix and efficiency built with the other half. Closure is shown for (a) $p_{\mathrm{T}}^{tq}(t)$, (b) $|y^{tq}(t)|$, (c) $p_{\mathrm{T}}^{tq}(\hat{j})$, (d) $|y^{tq}(\hat{t})|$, (e) $p_{\mathrm{T}}^{tq}(\hat{j})$ and (f) $|y^{tq}(\hat{j})|$. The error bar represents the uncertainty due to the size of the signal MC sample. The ratio is the unfolded distribution over the generated distribution shown in the bottom plot.

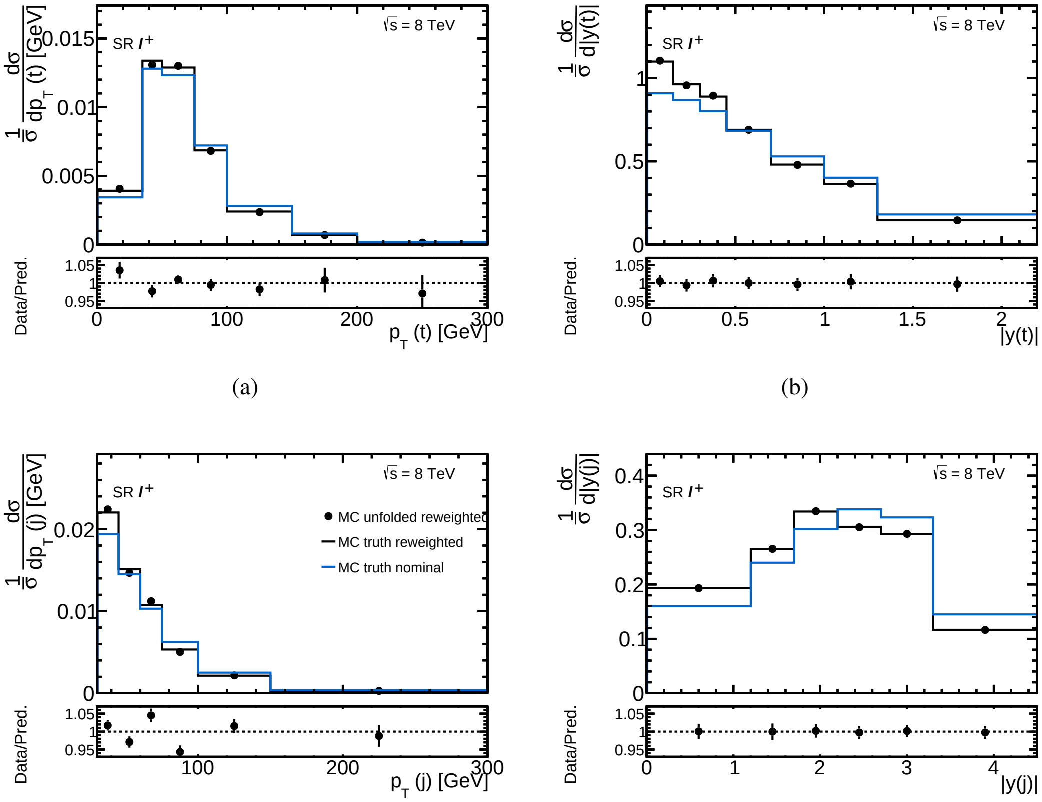

(a) (b)

(c) (d)

Figure 9.8: Unfolded distribution of reweighted sample for (a) $p_{\mathrm{T}}^{tq}(\hat{t})$, (b) $|y^{tq}(\hat{t})|$, (c) $p_{\mathrm{T}}^{tq}(\hat{j})$ and (d) $|y^{tq}(\hat{j})|$. The unfolded reweighted distribution (black dots) is compared to the reweighted generator-level (black line) and the nominal generator-level (blue line) distribution. The error bar represents the uncertainty due to the size of the signal MC sample. The ratio of the unfolded reweighted distribution to the reweighted generator-level distribution is shown in the bottom plot.

where i is the number of the pseudo experiment, N_i^{unfold} is the number of unfolded events, σ_i^{unfold} is the statistical error of the number of unfolded events, given by $\sqrt{N_i^{\text{unfold}}}$, and N^{truth} is the number of generator-level events.

The pull distributions for $p_{\mathrm{T}}^{tq}(t)$ and $|y^{tq}(t)|$ for parton-level unfolding are shown in Figure 9.9 and Figure 9.10. For particle-level unfolding, the pull distributions for $p_{\mathrm{T}}^{tq}(\hat{t})$ are shown in Figure 9.11, for $|y^{tq}(\hat{t})|$ in Figure 9.12, for $p_{\mathrm{T}}^{tq}(\hat{j})$ in Figure 9.13 and for $|y^{tq}(\hat{j})|$ in Figure 9.14. Each distribution is fitted in a range of $[-2, 2]$ to exclude its tails using a Gaussian. A mean of close to 0.0 and width close to 1.0 are obtained for all pull distributions. There are some cases where the pull width is a little bit off (close to 0.9), but those bins have low statistics, where maybe some non-Gaussian effects come in. Therefore, this test indicates that the statistical uncertainties are determined correctly and no significant bias in the unfolding procedure is found.

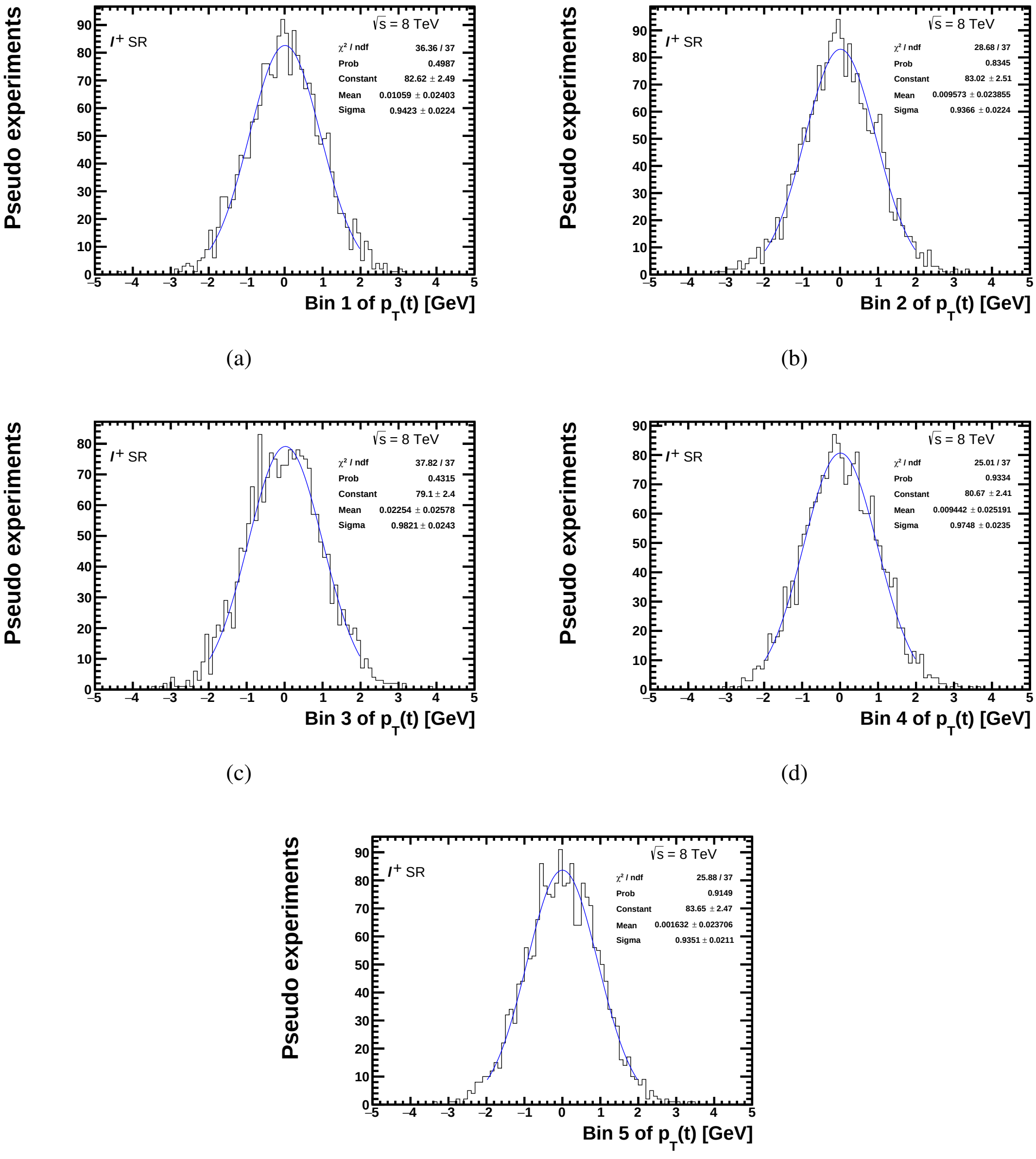

(a)

(b)

(c)

(d)

(e)

Figure 9.9: Pull distributions of 2000 pseudo experiments for all bins of the $p_{\mathrm{T}}^{tq}(t)$ variable used to unfold to parton level.

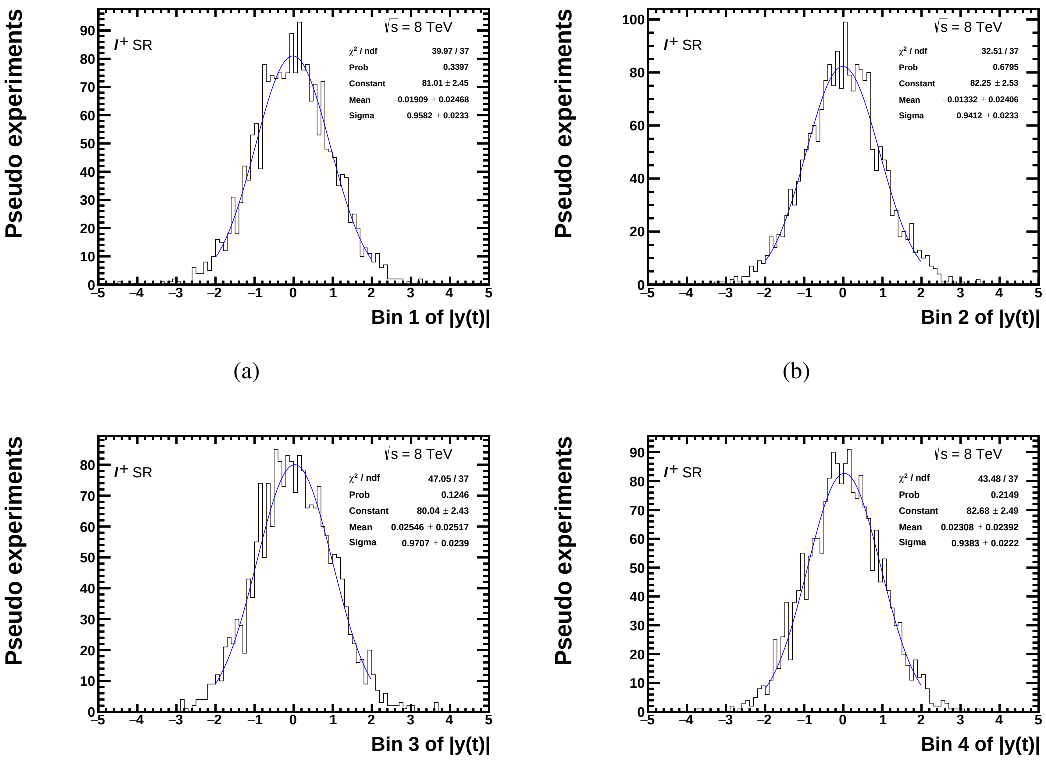

(a) (b)

(c) (d)

Figure 9.10: Pull distributions of 2000 pseudo experiments for all bins of the $|y^{tq}(t)|$ variable used to unfold to parton level.

9.6.4 Unfolding with different methods

The unfolded results with the iterative Bayesian method are cross-checked with the bin-by-bin method and the SVD method. There is no optimisation done in case of unfolding with the bin-by-bin method and the SVD method. The uncertainty due to data statistics in each method is determined using 10 000 pseudo experiments. The results are compared in Figure 9.15. All methods are compatible within the data statistical uncertainty. This test shows that reliable results are obtained from the iterative Bayesian unfolding.

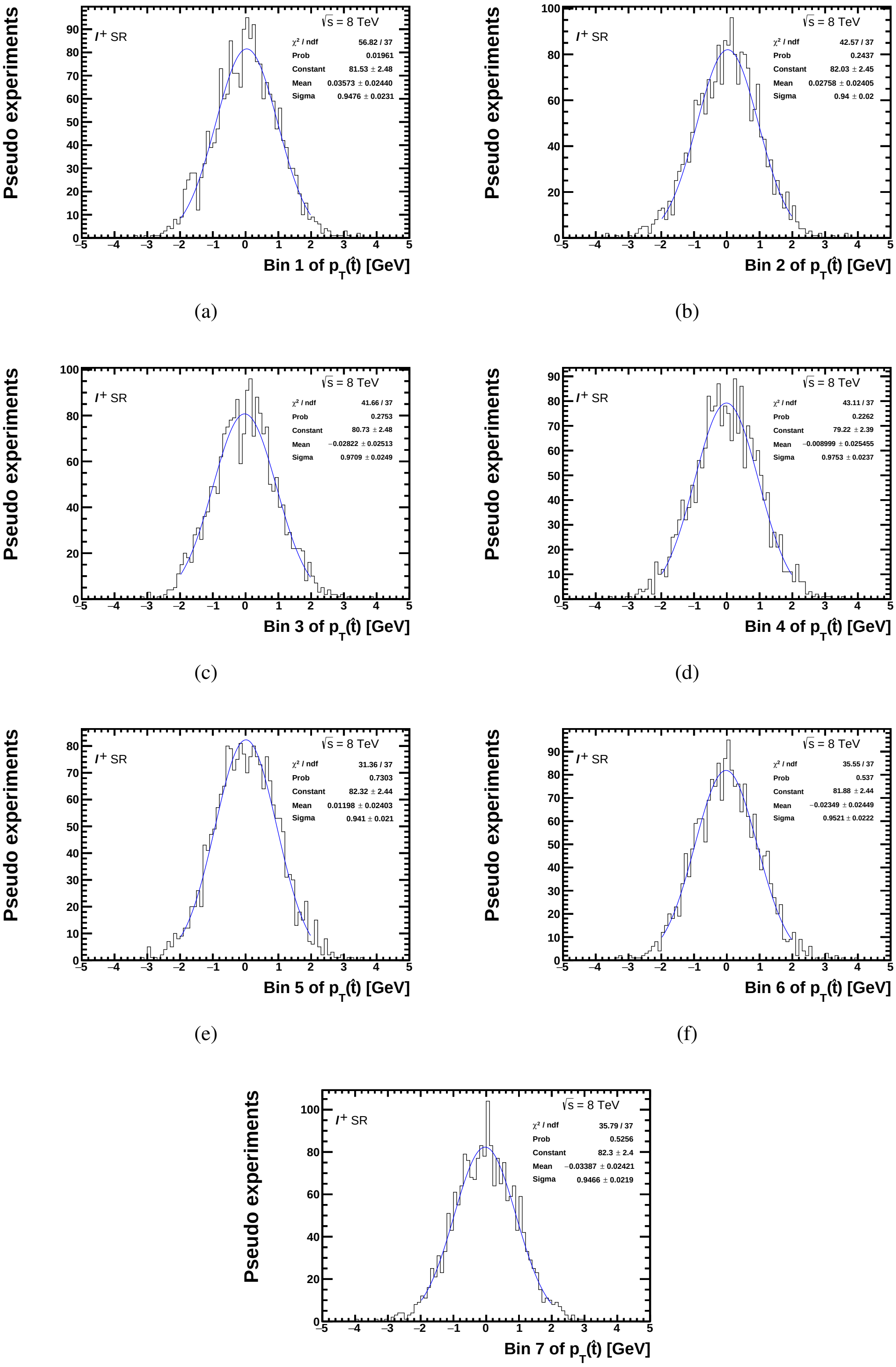

(a) (b) (c) (d) (e) (f) (g)

Figure 9.11: Pull distributions of 2000 pseudo experiments for all bins of the $p_{\mathrm{T}}^{tq}(\hat{t})$ variable used to unfold to particle level.

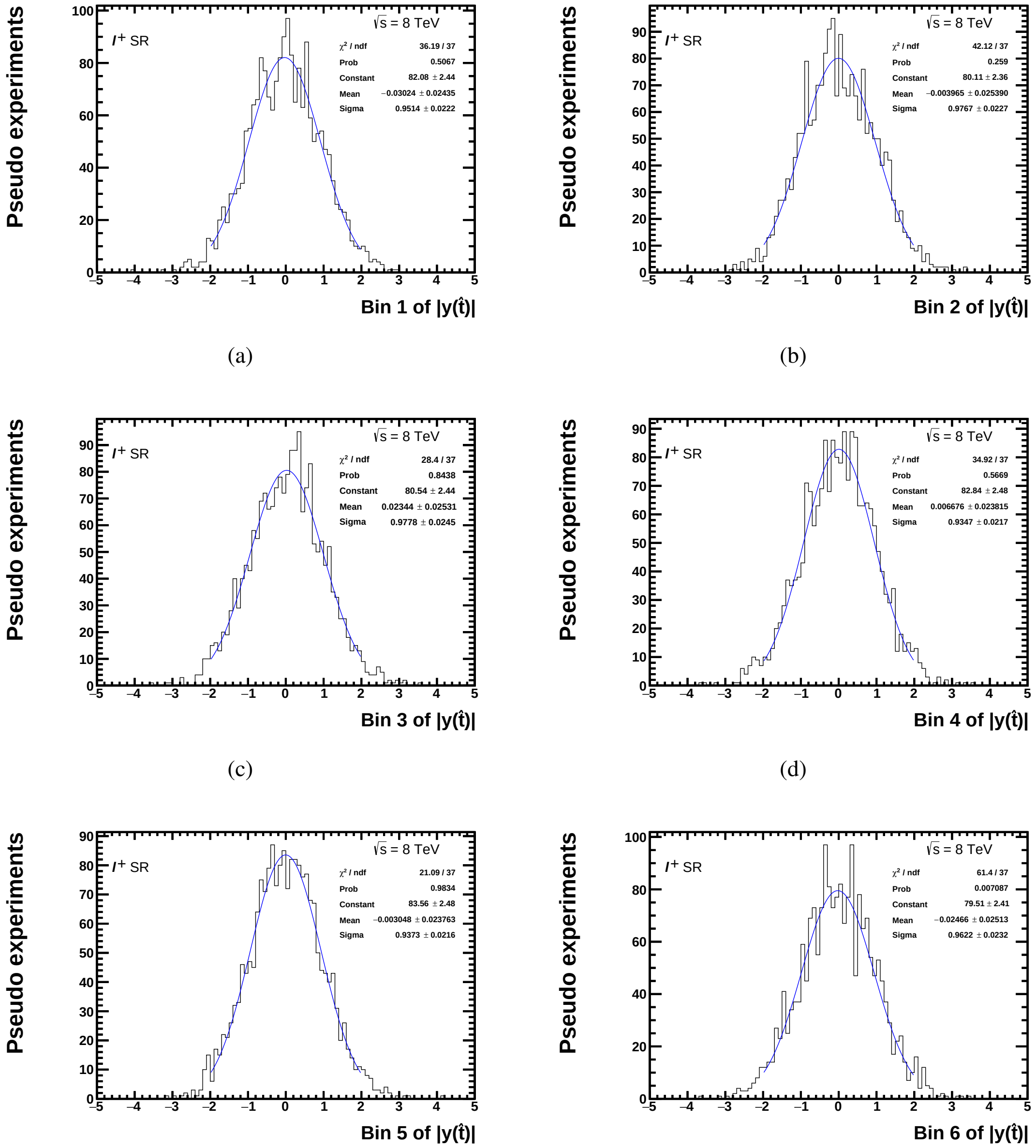

(a) (b)

(c) (d)

(e) (f)

Figure 9.12: Pull distributions of 2000 pseudo experiments for all bins of the $|y^{tq}(\hat{t})|$ variable used to unfold to particle level.

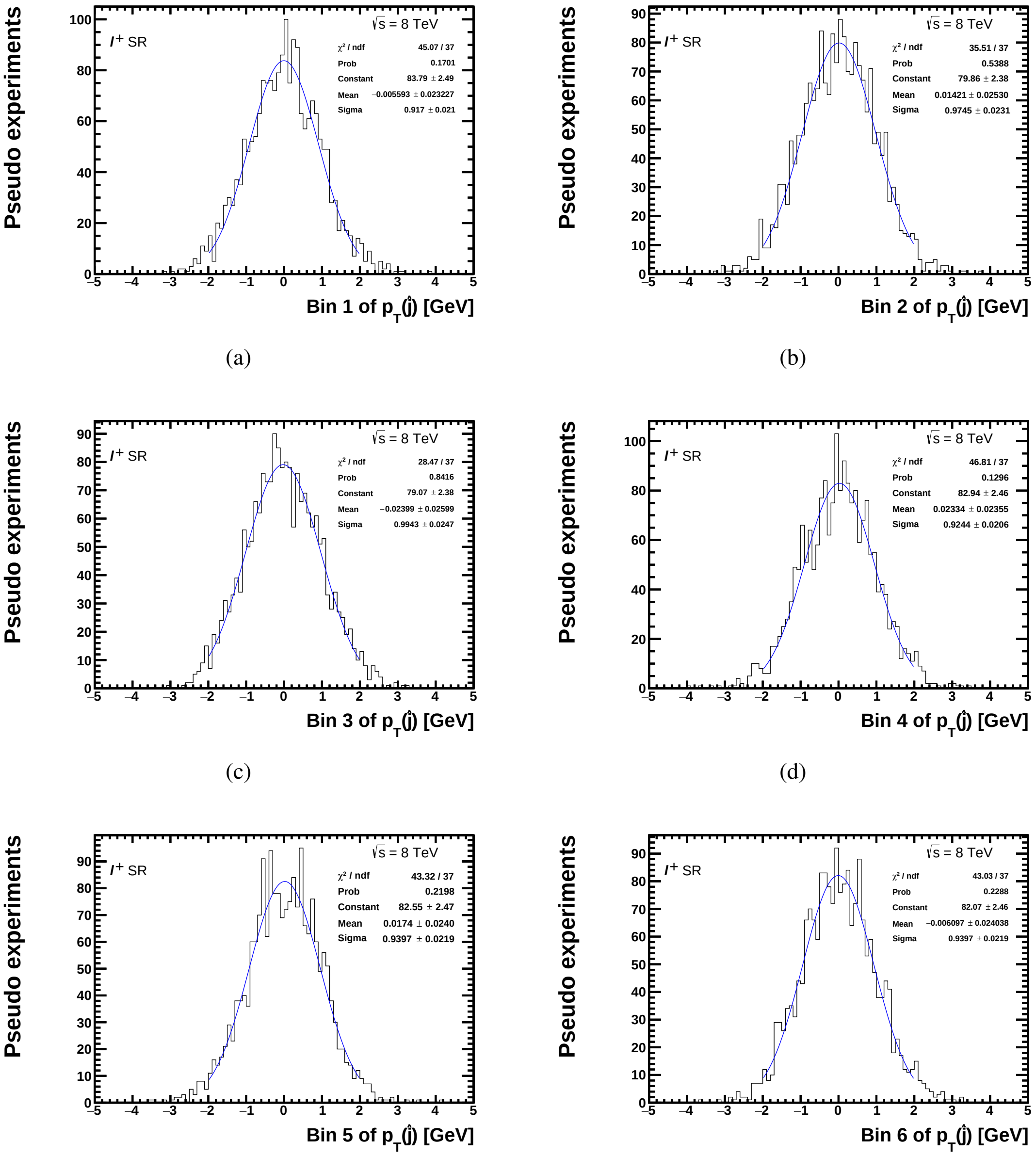

(a) (b)

(c) (d)

(e) (f)

Figure 9.13: Pull distributions of 2000 pseudo experiments for all bins of the $p_{\mathrm{T}}^{tq}(\hat{j})$ variable used to unfold to particle level.

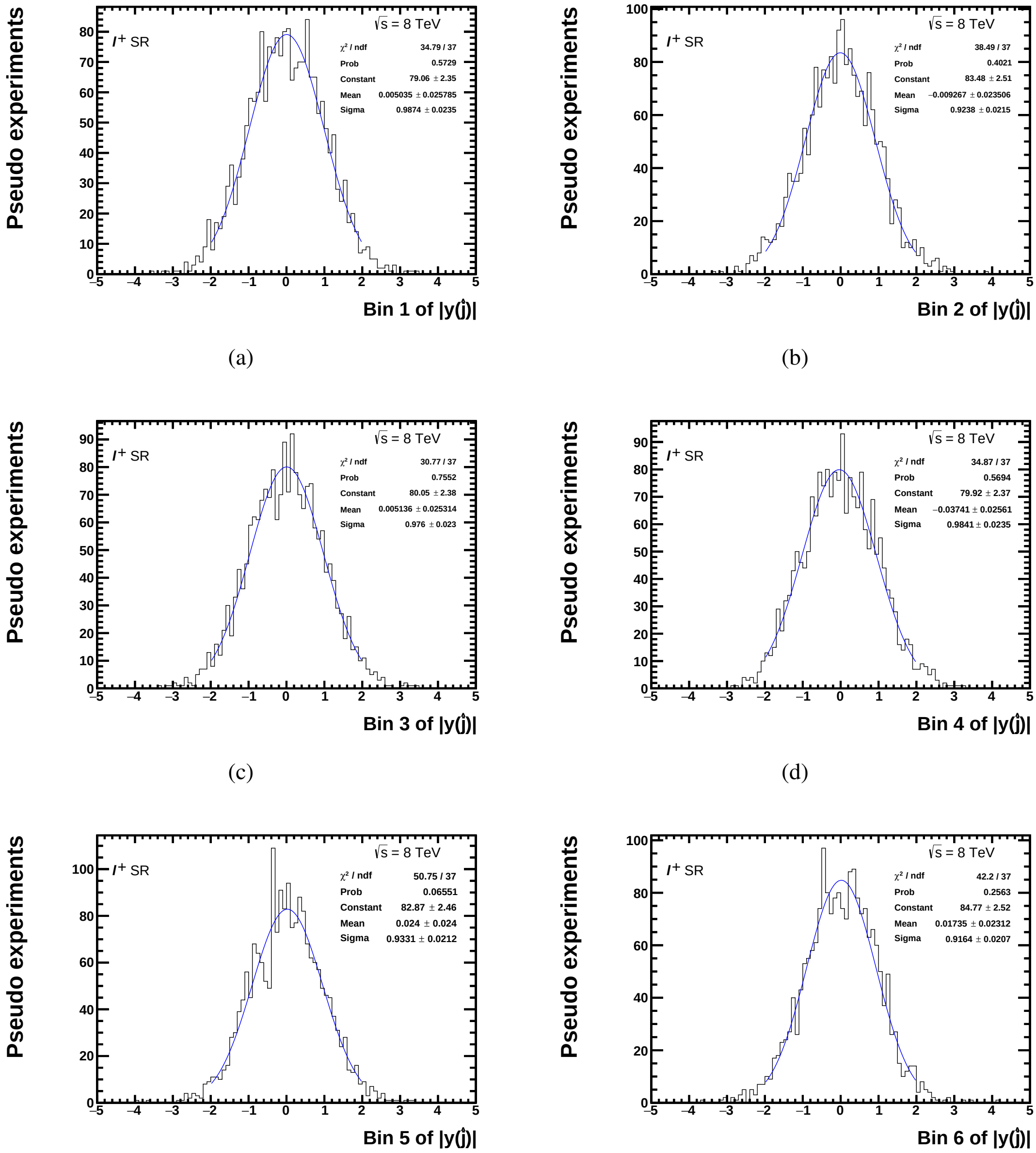

(a) (b) (c) (d) (e) (f)

Figure 9.14: Pull distributions of 2000 pseudo experiments for all bins of the $|y^{tq}(\hat{j})|$ variable used to unfold to particle level.

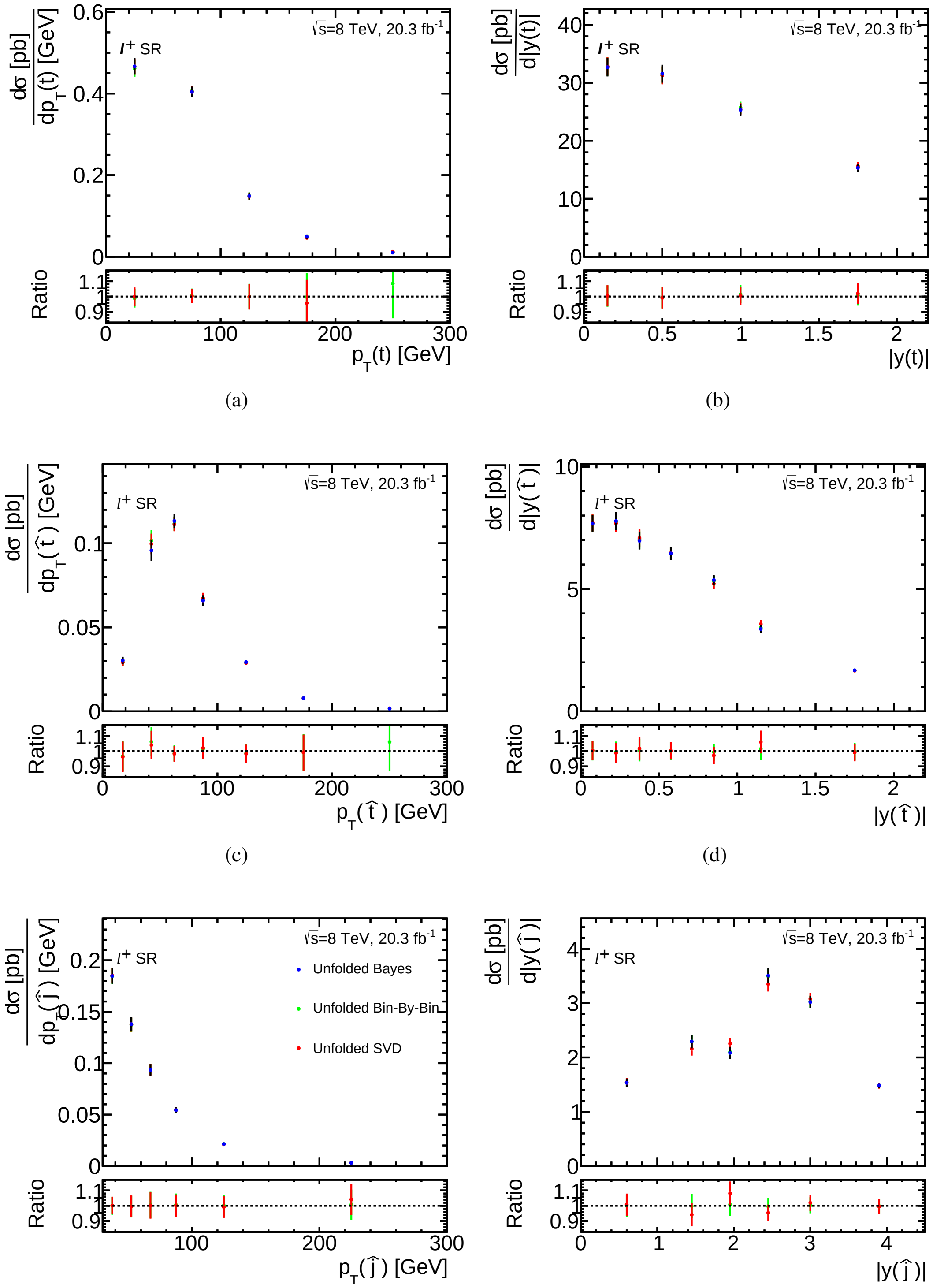

(a) (b)

(c) (d)

(e) (f)

Figure 9.15: Comparison between the three unfolding methods: Bayesian, bin-by-bin and SVD, for (a) $p_T^{tq}(t)$, (b) $|y^{tq}(t)|$, (c) $p_T^{tq}(\hat{j})$, (d) $|y^{tq}(\hat{t})|$, (e) $p_T^{tq}(\hat{j})$ and (f) $|y^{tq}(\hat{j})|$. The error bar represents the uncertainty due to data statistics. The ratio is calculated with respect to the unfolded Bayesian result shown in the bottom plot.

CHAPTER 10

Estimation of uncertainties

The propagation of the statistical and systematic uncertainties in the measured differential cross-sections is described in this chapter. The impact of each source is evaluated individually and separately for signal and background processes, taking all correlations into account. An uncertainty due to the unfolding procedure is also assigned. The quadratic sum of all uncertainties in each bin yields the total uncertainty.

10.1 Statistical uncertainties

The statistical uncertainty on the unfolded result is estimated by running over an ensemble of pseudo experiments. The statistical uncertainty due to the background-subtracted data is determined by drawing a random number from a Poisson distribution whose mean is equal to the bin content in the background-subtracted data distribution. In case of the backgrounds, the sum of all simulated backgrounds is randomised according to a Gaussian distribution with a width corresponding to the bin error (square root of the number of entries after luminosity scaling). This background fluctuation is then subtracted from the data distribution. Each pseudo experiment is unfolded. The root mean square (RMS) of the spread of unfolded results in each bin is taken as the measure of the statistical uncertainty. These two statistical uncertainties are added in quadrature to obtain the total statistical uncertainty on the unfolded result.

For the uncertainty due to the size of the simulated signal sample, the migration matrix and efficiency are fluctuated in pseudo experiments with a Gaussian function whose spread corresponds to the number of MC events in the sample. The unfolding is performed using this variation. The RMS of the spread of unfolded results in each bin is taken as the uncertainty.

10.2 Systematic uncertainties

The unfolded distributions can be influenced by several sources of systematic uncertainties due to detector resolution, object reconstruction, and modelling of both signal and background processes. The systematic uncertainties cause variations in the background yield. The expected background is subtracted from the data distribution resulting a change in the input to the unfolding procedure. The systematic uncertainties also affect the migration matrix and efficiency determined using the simulated signal sample.

In the following, the evaluation of systematics on the signal is discussed first and the background afterwards. Different uncertainties need to be treated in different ways in the unfolding procedure. If an uncertainty is correlated between signal and background, the effects are added linearly in order to take the correlation into account. For the uncertainties due to the MC modelling of the signal process, the bias, introduced in Section 9.5, is taken as the uncertainty. This is because the bias can tell how well the unfolding procedure with alternative ingredients can recover its generator-level distribution. The bias is determined from the difference between the unfolded cross-section using the simulated signal sample with POWHEG-BOX + PYTHIA 6 – nominal signal sample – as an input for unfolding and its generator-level cross-section, usually using an alternative sample for the migration matrix and efficiency. Details of considered systematic uncertainties and their definition are listed in Section 7.2.

Reconstruction uncertainties affecting the signal

The simulated signal samples are used for evaluating the effects of the uncertainties due to the reconstructed objects in the simulation. The varied simulated signal samples are unfolded with the migration matrix and efficiencies obtained from the nominal signal sample. The difference from the unfolded distribution using the nominal signal sample as an input is taken as the systematic uncertainty. Rate and shape uncertainties are taken into account simultaneously.

In case of the uncertainties in the $b\bar{b}$ efficiency affecting the signal, the difference of 0.94% is assigned as the uncertainty over all bins for all absolute differential cross-sections.

Generator uncertainties affecting the signal

The uncertainty due to the NLO matching scheme for the t-channel production is evaluated by unfolding the nominal signal distribution with a migration matrix and efficiencies obtained using either the simulated signal sample of MADGRAPH5_aMC@NLO + HERWIG or the simulated signal sample of POWHEG-BOX + HERWIG. The full difference between the bias of MADGRAPH5_aMC@NLO + HERWIG and the bias of POWHEG-BOX + HERWIG is taken as the systematic uncertainty.

To estimate the uncertainty associated with the modelling of the parton shower and the hadronisation, the nominal signal distribution is unfolded with a migration matrix and efficiencies determined using either the simulated signal sample of POWHEG-BOX + PYTHIA 6 or the simulated signal sample of POWHEG-BOX + HERWIG. The full difference between the bias of POWHEG-BOX + PYTHIA 6 and the bias of POWHEG-BOX + HERWIG is taken as the systematic uncertainty.

For the uncertainty due to the choice of factorisation scale and renormalisation scale, the nominal signal distribution is unfolded with a migration matrix and efficiencies obtained using either the simulated signal sample of the up or down scale choice with POWHEG-BOX + PYTHIA 6. The bias of the up and down scale choices is taken as the uncertainty due to the scale variations.

Parton-distribution-function uncertainties affecting the signal

The uncertainty due to different PDFs for the t-channel process is determined by unfolding the nominal signal distribution with a migration matrix and efficiencies obtained from the simulated signal sample either with the CT10 PDF set or with the PDF4LHC15_NLO PDF set. By comparing the bias of these two PDF sets, the largest difference in the bias is assigned as both the negative and positive PDF uncertainty bin-by-bin. The bias of each eigenvector of the PDF4LHC15_NLO is compared to the bias of the central PDF4LHC15_NLO and the difference is assigned as an additional uncertainty.

Uncertainties in normalisation of backgrounds

An estimation of the normalisation uncertainties of all background processes is taken from the total cross-section measurements discussed in Section 7.3. Table 10.1 lists these uncertainties. The normalisation uncertainties in the sum of all backgrounds need to be evaluated since this sum is subtracted from the

Process	$\Delta N/N$ [%]
$t\bar{t}, Wt, t\bar{b}$	7.5
W^+ + jets	7.1
W^- + jets	7.3
Z, VV + jets	20
Multijets	16

Table 10.1: Uncertainties in the normalisations of the different backgrounds for all processes, as derived from the total cross-section measurement. [2]

data. The normalisation uncertainty in this sum is determined with pseudo experiments used to evaluate the uncertainties on the total cross-sections. For each pseudo experiment, the β value is calculated with:

$$\beta_{\text{fit}}^{\text{corr}} = \frac{\sum\limits_{b\in\text{all background}} \nu_{\text{fit}}}{\sum\limits_{b\in\text{all background}} \nu_{\text{gen}}} - 1\,, \tag{10.1}$$

where ν_{gen} is the expectation value used for the generation of the pseudo experiment and ν_{fit} is the estimator for the ν_{gen} obtained after the fit. With this addition, correlations between all background processes are taken into account

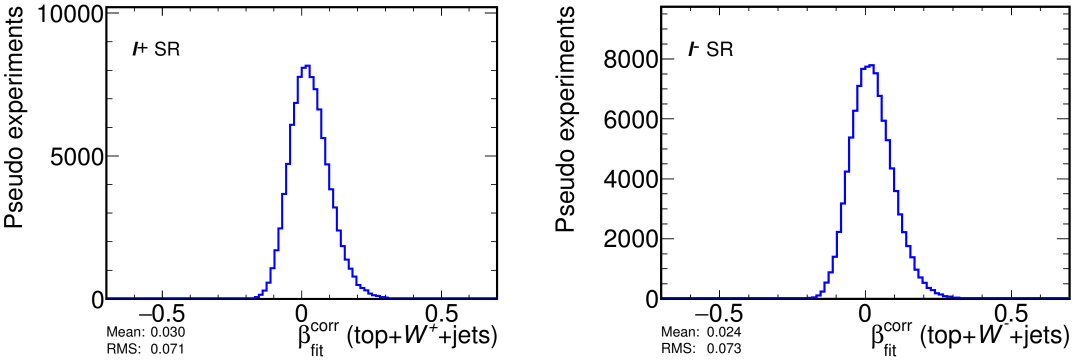

(a) (b)

Figure 10.1: Distribution of the β-values for the sum of all backgrounds for the (a) ℓ^+ and (b) ℓ^- channels, created with the pseudo experiments used to estimate the uncertainties of the total cross-sections. All correlations between the uncertainties and backgrounds are taken into account.

Figure 10.1 visualises the β distribution for the ℓ^+ and ℓ^- channels. The information of the combined top-background and W+jets processes is used in this estimation, as the other backgrounds are fixed in the fitting process because their contribution is very small. The normalisation uncertainty is estimated to be 7.1% for the ℓ^+ channel and 7.3% for the ℓ^- channel. To cross-check, the β value for the sum of all background processes is investigated bin-by-bin in the distributions that are unfolded – see Appendix G. The β values are consistent over all bins. As a result of this study, it is decided that the normalisation uncertainties on the sum of all background processes from the global fit can be used.

The background sum is shifted up and down by this estimated amount. The modified background-subtracted data is unfolded with the migration matrix and efficiencies obtained with the nominal signal sample. The difference from the final cross-section in each bin is assigned as the background normalisation uncertainty.

Uncertainties in shape of backgrounds

The systematic uncertainties can affect the shape of the distribution that is unfolded for all background contributions. Some uncertainties have an insignificant impact in the shape on the analysis. Therefore, the shifts due to the systematic variations are compared to the MC statistical error in each bin of each distribution for each background process in order to avoid counting statistical fluctuations as a shape uncertainty. The uncertainties are considered significant in the shape for each background if the change in the bin content (|nominal - systematic|) in at least two bins is larger than the MC statistical error in those bins. These significant uncertainties are taken into account in the analysis. Tables 10.2 and 10.3 show the list of included/excluded uncertainties in the shape for all variables used in parton-level and particle-level unfolding, respectively. The shifted backgrounds are subtracted from the data and the resulting distribution is unfolded using the migration matrix and efficiencies obtained with the nominal signal sample.

For the uncertainty due to the NLO matching, the full difference between the unfolded distributions using the simulated top-background samples with the MC@NLO + Herwig and with Powheg-Box + Herwig is assigned as the uncertainty. In case of the uncertainty due to the parton shower and hadronisation modelling, the full difference between the unfolded distributions with Powheg-Box + Pythia 6 and with Powheg-Box + Herwig is taken as the uncertainty. For the PDF uncertainty, the full difference between the unfolded distributions with the PDF4LHC15_NLO PDF set and with the CT10 PDF set is taken as the uncertainty. The additional PDF uncertainties due to different eigenvalues are also considered. For all other uncertainties, the difference from the final cross-section is taken as the background shape uncertainty.

The modelling of the top-background processes is the major source to the background shape uncertainty.

Systematic	Included in the analysis			
	$p_{\mathrm{T}}^{tq}(t)$	$p_{\mathrm{T}}^{\bar{t}q}(t)$	$\lvert y^{tq}(t)\rvert$	$\lvert y^{\bar{t}q}(t)\rvert$
b-jet energy scale	×	×	×	×
JES punch-through	×	×	×	×
JES single particle	×	×	×	×
JES pile-up μ	×	×	×	×
JES pile-up n_{vtx}	×	×	×	×
JES pile-up Pt	×	×	×	×
JES pile-up ρ	×	✓	×	×
JES flavour composition	×	×	×	×
JES flavour response	×	×	×	×
Jet vertex fraction	×	×	×	×
$E_{\mathrm{T}}^{\mathrm{miss}}$ CellOut+SoftJet resolution	✓	✓	×	×
$E_{\mathrm{T}}^{\mathrm{miss}}$ CellOut+SoftJet scale	×	×	×	×
Jet reconstruction efficiency	×	×	×	×
JER	✓	✓	✓	✓
JES η intercalibration model	×	×	×	×
JES η intercalibration statistical	×	×	×	×
JES detector 1	×	×	×	×
JES detector 2	×	×	×	×
JES detector 3	×	×	×	×

Systematic	Included in the analysis			
	$p_{\mathrm{T}}^{tq}(t)$	$p_{\mathrm{T}}^{\bar{t}q}(t)$	$\lvert y^{tq}(t) \rvert$	$\lvert y^{\bar{t}q}(t) \rvert$
JES mixed detector and modelling 1	×	×	×	×
JES mixed detector and modelling 2	×	×	×	×
JES mixed detector and modelling 3	×	×	×	×
JES mixed detector and modelling 4	×	×	×	×
JES physics modelling 1	×	×	×	×
JES physics modelling 2	×	×	×	×
JES physics modelling 3	×	×	×	×
JES physics modelling 4	×	×	×	×
JES statistical 1	×	×	×	×
JES statistical 2	×	×	×	×
JES statistical 3	×	×	×	×
JES statistical 4	×	×	×	×
Electron energy resolution	×	×	×	×
Electron energy scale	×	×	×	×
Muon energy resolution: inner detector	×	×	×	×
Muon energy resolution: spectrometer	×	×	×	×
Muon energy scale	×	×	×	×
b-tag efficiency C0	×	×	×	×
b-tag efficiency C1	×	×	×	×
b-tag efficiency C2	×	×	×	×
b-tag efficiency C3	×	×	×	×
b-tag efficiency C4	×	×	×	×
b-tag efficiency C5	×	×	×	×
b-tag efficiency C6	×	×	×	×
b-tag efficiency C7	×	×	×	×
b-tag efficiency C8	×	×	×	×
c-tag efficiency C0	×	×	×	×
c-tag efficiency C1	×	×	×	×
c-tag efficiency C2	×	×	×	×
c-tag efficiency C3	×	×	×	×
Mistag efficiency C0	×	×	×	×
Mistag efficiency C1	×	×	×	×
Mistag efficiency C2	×	×	×	×
Mistag efficiency C3	×	×	×	×
Mistag efficiency C4	×	×	×	×
Mistag efficiency C5	×	×	×	×
Mistag efficiency C6	×	×	×	×
Mistag efficiency C7	×	×	×	×
Mistag efficiency C8	×	×	×	×
Mistag efficiency C9	×	×	×	×
Mistag efficiency C10	×	×	×	×
Mistag efficiency C11	×	×	×	×
Lepton trigger SF	×	×	×	✓
Lepton ID SF	×	×	×	✓
Lepton reco SF	×	×	×	×
Lepton charge ID	✓	✓	✓	✓
$t\bar{t}$ NLO matching	✓	✓	✓	✓
$t\bar{t}$ parton shower	✓	✓	✓	✓
$t\bar{t}$ scale variations	✓	✓	✓	✓
PDF background CT10 to PDF4LHC15	✓	✓	✓	✓

Systematic	Included in the analysis			
	$p_{\mathrm{T}}^{tq}(t)$	$p_{\mathrm{T}}^{\bar{t}q}(t)$	$\lvert y^{tq}(t)\rvert$	$\lvert y^{\bar{t}q}(t)\rvert$
PDF background PDF4LHC15 EV1	✓	✓	✓	✓
PDF background PDF4LHC15 EV2	✓	✓	✓	✓
PDF background PDF4LHC15 EV3	✓	✓	✓	✓
PDF background PDF4LHC15 EV4	✓	✓	✓	✓
PDF background PDF4LHC15 EV5	×	✓	✓	×
PDF background PDF4LHC15 EV6	✓	✓	✓	✓
PDF background PDF4LHC15 EV7	✓	✓	✓	✓
PDF background PDF4LHC15 EV8	✓	✓	×	✓
PDF background PDF4LHC15 EV9	✓	✓	✓	✓
PDF background PDF4LHC15 EV10	✓	✓	✓	✓
PDF background PDF4LHC15 EV11	✓	✓	✓	✓
PDF background PDF4LHC15 EV12	×	✓	×	✓
PDF background PDF4LHC15 EV13	×	✓	×	✓
PDF background PDF4LHC15 EV14	✓	✓	✓	✓
PDF background PDF4LHC15 EV15	✓	✓	×	✓
Multijet model	✓	✓	✓	✓
$b\bar{b}$ efficiency	×	×	×	×

Table 10.2: Considered uncertainties in shape of the sum of all background processes (shown with ✓) for all variables used in parton-level unfolding.

Systematic	Included in the analysis							
	$p_{\mathrm{T}}^{tq}(\hat{t})$	$p_{\mathrm{T}}^{\bar{t}q}(\hat{t})$	$\lvert y^{tq}(\hat{t})\rvert$	$\lvert y^{\bar{t}q}(\hat{t})\rvert$	$p_{\mathrm{T}}^{tq}(\hat{j})$	$p_{\mathrm{T}}^{\bar{t}q}(\hat{j})$	$\lvert y^{tq}(\hat{j})\rvert$	$\lvert y^{\bar{t}q}(\hat{j})\rvert$
b-jet energy scale	×	×	×	×	×	×	×	×
JES punch-through	×	×	×	×	×	×	×	×
JES single particle	×	×	×	×	×	×	×	×
JES pile-up μ	×	×	×	×	×	×	×	×
JES pile-up n_{vtx}	×	×	×	×	✓	×	×	×
JES pile-up Pt	×	×	×	×	×	×	×	×
JES pile-up ρ	×	×	×	×	×	✓	×	×
JES flavour composition	×	×	×	×	×	×	×	×
JES flavour response	×	×	×	×	×	×	×	×
Jet vertex fraction	✓	×	×	×	×	×	×	×
$E_{\mathrm{T}}^{\mathrm{miss}}$ CellOut+SoftJet resolution	✓	✓	✓	✓	×	×	×	✓
$E_{\mathrm{T}}^{\mathrm{miss}}$ CellOut+SoftJet scale	×	×	×	×	×	×	×	✓
Jet reconstruction efficiency	×	×	×	×	×	×	×	×
JER	✓	✓	✓	✓	✓	✓	✓	✓
JES η intercalibration model	×	✓	×	✓	×	×	×	✓
JES η intercalibration statistical	×	×	×	×	✓	×	×	✓
JES detector 1	×	×	×	×	×	×	×	×
JES detector 2	×	×	×	×	×	×	×	×
JES detector 3	×	×	×	×	×	×	×	×
JES mixed detector and modelling 1	×	×	×	×	✓	✓	×	×
JES mixed detector and modelling 2	×	×	×	×	×	×	×	×
JES mixed detector and modelling 3	×	×	×	×	×	×	×	×
JES mixed detector and modelling 4	×	×	×	×	×	×	×	×
JES physics modelling 1	×	×	×	×	✓	×	×	×
JES physics modelling 2	×	×	×	×	×	×	×	×

Systematic	Included in the analysis							
	$p_{\mathrm{T}}^{tq}(\hat{t})$	$p_{\mathrm{T}}^{\bar{t}q}(\hat{t})$	$\lvert y^{tq}(\hat{t})\rvert$	$\lvert y^{\bar{t}q}(\hat{t})\rvert$	$p_{\mathrm{T}}^{tq}(\hat{j})$	$p_{\mathrm{T}}^{\bar{t}q}(\hat{j})$	$\lvert y^{tq}(\hat{j})\rvert$	$\lvert y^{\bar{t}q}(\hat{j})\rvert$
JES physics modelling 3	×	×	×	×	×	×	×	×
JES physics modelling 4	×	×	×	×	×	×	×	×
JES statistical 1	×	×	×	×	×	×	×	×
JES statistical 2	×	×	×	×	×	×	×	×
JES statistical 3	×	×	×	×	×	×	×	×
JES statistical 4	×	×	×	×	×	×	×	×
Electron energy resolution	×	×	×	×	×	×	×	×
Electron energy scale	×	×	×	×	×	×	×	×
Muon energy resolution: inner detector	×	×	×	×	×	×	×	×
Muon energy resolution: spectrometer	×	×	×	×	×	×	×	×
Muon energy scale	×	×	×	×	×	×	×	×
b-tag efficiency C0	×	×	×	×	×	×	×	×
b-tag efficiency C1	×	×	×	×	×	×	×	×
b-tag efficiency C2	×	×	×	×	×	×	×	×
b-tag efficiency C3	×	×	×	×	×	×	×	×
b-tag efficiency C4	×	×	×	×	×	×	×	×
b-tag efficiency C5	×	×	×	×	×	×	×	×
b-tag efficiency C6	×	×	×	×	×	×	×	×
b-tag efficiency C7	×	×	×	×	×	×	×	×
b-tag efficiency C8	×	×	×	×	×	×	×	×
c-tag efficiency C0	×	×	×	×	×	×	×	×
c-tag efficiency C1	×	×	×	×	×	×	×	×
c-tag efficiency C2	×	×	×	×	×	×	×	×
c-tag efficiency C3	×	×	×	×	×	×	×	×
Mistag efficiency C0	×	×	×	×	×	×	×	×
Mistag efficiency C1	×	×	×	×	×	×	×	×
Mistag efficiency C2	×	×	×	×	×	×	×	×
Mistag efficiency C3	×	×	×	×	×	×	×	×
Mistag efficiency C4	×	×	×	×	×	×	×	×
Mistag efficiency C5	×	×	×	×	×	×	×	×
Mistag efficiency C6	×	×	×	×	×	×	×	×
Mistag efficiency C7	×	×	×	×	×	×	×	×
Mistag efficiency C8	×	×	×	×	×	×	×	×
Mistag efficiency C9	×	×	×	×	×	×	×	×
Mistag efficiency C10	×	×	×	×	×	×	×	×
Mistag efficiency C11	×	×	×	×	×	×	×	×
Lepton trigger SF	×	×	×	×	×	×	×	×
Lepton ID SF	×	×	×	×	×	×	×	×
Lepton reco SF	×	×	×	×	×	×	×	×
Lepton charge ID	✓	✓	✓	✓	✓	✓	✓	✓
$t\bar{t}$ NLO matching	✓	✓	✓	✓	✓	✓	✓	✓
$t\bar{t}$ parton shower	✓	✓	✓	✓	✓	✓	✓	✓
$t\bar{t}$ scale variations	✓	✓	✓	✓	✓	✓	✓	✓
PDF background CT10 to PDF4LHC15	✓	✓	✓	✓	✓	✓	✓	✓
PDF background PDF4LHC15 EV1	✓	✓	✓	✓	✓	✓	✓	✓
PDF background PDF4LHC15 EV2	✓	✓	✓	✓	✓	✓	✓	✓
PDF background PDF4LHC15 EV3	✓	✓	✓	✓	✓	✓	✓	✓
PDF background PDF4LHC15 EV4	✓	✓	✓	✓	✓	✓	✓	✓
PDF background PDF4LHC15 EV5	×	✓	×	✓	×	✓	✓	✓
PDF background PDF4LHC15 EV6	✓	✓	✓	✓	✓	✓	✓	✓

Systematic	Included in the analysis							
	$p_{\mathrm{T}}^{tq}(\hat{t})$	$p_{\mathrm{T}}^{\bar{t}q}(\hat{t})$	$\lvert y^{tq}(\hat{t})\rvert$	$\lvert y^{\bar{t}q}(\hat{t})\rvert$	$p_{\mathrm{T}}^{tq}(\hat{j})$	$p_{\mathrm{T}}^{\bar{t}q}(\hat{j})$	$\lvert y^{tq}(\hat{j})\rvert$	$\lvert y^{\bar{t}q}(\hat{j})\rvert$
PDF background PDF4LHC15 EV7	✓	✓	✓	✓	✓	✓	✓	✓
PDF background PDF4LHC15 EV8	✓	✓	×	✓	✓	✓	✓	✓
PDF background PDF4LHC15 EV9	✓	✓	✓	✓	✓	✓	✓	✓
PDF background PDF4LHC15 EV10	✓	✓	✓	✓	✓	✓	✓	✓
PDF background PDF4LHC15 EV11	✓	✓	✓	✓	✓	✓	✓	✓
PDF background PDF4LHC15 EV12	×	✓	×	✓	×	✓	✓	✓
PDF background PDF4LHC15 EV13	×	✓	×	✓	×	✓	✓	✓
PDF background PDF4LHC15 EV14	✓	✓	✓	✓	×	✓	✓	✓
PDF background PDF4LHC15 EV15	✓	✓	×	✓	×	✓	×	✓
Multijet model	✓	✓	✓	✓	✓	✓	✓	✓
$b\bar{b}$ efficiency	×	×	×	×	×	×	×	×

Table 10.3: Considered uncertainties in shape of the sum of all background processes (shown with ✓) for all variables used in particle-level unfolding.

Luminosity uncertainties

The uncertainty in the integrated luminosity of 1.9% is assigned as the luminosity uncertainty over all bins for all absolute differential cross-section measurements.

Uncertainties in the unfolding process

The full difference between the unfolded distribution with the simulated signal sample and its generator-level distribution from the closure test as described in Section 9.6.1 is assigned as the uncertainty due to the unfolding method.

A breakdown into the major sources of uncertainty for all differential cross-sections at both parton and particle levels can be found in Appendix H. The main contributions are from the JES calibration and uncertainties associated with the modelling of both the signal and the top-background processes. The background normalisation uncertainty is typically about half of the total systematic uncertainty, while the statistical uncertainty in each bin is similar to the total systematic uncertainty for the absolute cross-section measurements. Uncertainties due to the unfolding are small compared to the total uncertainty. The uncertainties in the last bin of p_{T} of the top antiquark is large because the measurement is less reliable due to large statistical fluctuations.

A summary of the range of the total uncertainty on the absolute and normalised unfolded cross-sections at both parton level and particle level is given in Table 10.4. In general, the total systematic uncertainty for the normalised differential cross-sections is smaller than the uncertainty for the absolute differential cross-sections because many systematic uncertainties are reduced or cancelled for the normalised cross-section measurements.

Variables	Range of total uncertainty [%]			
	Absolute		Normalised	
	tq	$\bar{t}q$	tq	$\bar{t}q$
Parton level				
$p_{\mathrm{T}}(t)$	8 – 23	10 – 39	5 – 22	9 – 37
$\lvert y(t)\rvert$	9 – 10	12 – 20	7 – 9	10 – 16
Particle level				
$p_{\mathrm{T}}(\hat{t})$	8 – 22	9 – 31	7 – 21	6 – 29
$\lvert y(\hat{t})\rvert$	7 – 10	10 – 14	5 – 8	8 – 11
$p_{\mathrm{T}}(\hat{j})$	9 – 11	10 – 25	7 – 10	7 – 25
$\lvert y(\hat{j})\rvert$	6 – 20	9 – 26	6 – 15	9 – 18

Table 10.4: Range of the total uncertainty on the absolute and normalised unfolded differential cross-sections at both parton level and particle level.

CHAPTER 11

Results and discussion

This chapter presents the results of the measurements of absolute and normalised t-channel single top-quark differential cross-sections at both the parton level and the particle level. The differential cross-sections are measured for top-quark and top-antiquark production separately. The results are compared to different Monte Carlo predictions as well as to available fixed-order QCD calculations. Comparisons of the unfolded differential cross-sections are also given.

11.1 Results at parton level

The results for the absolute and normalised unfolded differential cross-sections as a function of $p_{\mathrm{T}}(t)$ and $|y(t)|$ of the top quarks and the top antiquarks at parton level are given numerically in Tables 11.1–11.4. The absolute and normalised cross-sections as a function of $p_{\mathrm{T}}(t)$ are visualised in Figure 11.1, while the measured cross-sections as a function of $|y(t)|$ are visualised in Figure 11.2. The measurements are compared to different MC predictions using the Powheg-Box and MadGraph5_aMC@NLO generators. Separate predictions using Pythia or Herwig interfaced to Powheg-Box are shown. It can be observed that the parton-shower and hadronisation modelling has a very small effect on the predictions. The measured cross-sections are also confronted with NLO QCD predictions calculated using MCFM. A calculation at approximate NNLO QCD is available for the top-quark and top-antiquark p_{T} distributions [123].

All predictions agree well with the unfolded data, with the same tendency for almost all MC predictions to be somewhat harder than the data as a function of $p_{\mathrm{T}}(t)$. The approximate NNLO prediction describes the data better than the MC predictions as a function of $p_{\mathrm{T}}(t)$. The total unfolded cross-sections for $p_{\mathrm{T}}(t)$ and $|y(t)|$ for both tq and $\bar{t}q$ events are summarised in Table 11.5. The number of events in the overflow bin is calculated from the nominal t-channel MC sample. All total unfolded cross-sections are in good agreement within the statistical uncertainty, and they are compatible with the results from total cross-section measurement shown in Section 7.3.2.

In addition, statistical correlation matrices for all differential cross-sections at both parton and particle levels are presented in Appendix I.

$p_{\mathrm{T}}(t)$ [GeV]	$\mathrm{d}\sigma(tq)/\mathrm{d}p_{\mathrm{T}}(t)$ [fb GeV^{-1}]			$(1/\sigma)\mathrm{d}\sigma(tq)/\mathrm{d}p_{\mathrm{T}}(t)$ [10^{-3} GeV^{-1}]		
		stat.	syst.		stat.	syst.
0 – 50	467	±25	+34 / −39	8.57	±0.33	+0.32 / −0.43
50 – 100	404	±15	+28 / −27	7.42	±0.32	+0.47 / −0.40
100 – 150	149	±10	+17 / −18	2.73	±0.18	+0.27 / −0.29
150 – 200	49.2	±6.3	+5.0 / −4.1	0.903	±0.12	+0.080 / −0.070
200 – 300	10.2	±1.9	+1.2 / −1.3	0.187	±0.035	+0.019 / −0.022

Table 11.1: Absolute and normalised unfolded differential tq production cross-section as a function of $p_{\mathrm{T}}(t)$ at *parton level.* [2]

$p_{\mathrm{T}}(t)$ [GeV]	$\mathrm{d}\sigma(\bar{t}q)/\mathrm{d}p_{\mathrm{T}}(t)$ [fb GeV^{-1}]			$(1/\sigma)\mathrm{d}\sigma(\bar{t}q)/\mathrm{d}p_{\mathrm{T}}(t)$ [10^{-3} GeV^{-1}]		
		stat.	syst.		stat.	syst.
0 – 50	310	±21	+36 / −35	9.67	±0.48	+0.77 / −0.76
50 – 100	228	±13	+19 / −20	7.11	±0.47	+0.49 / −0.51
100 – 150	75.7	±8.8	+14 / −14	2.36	±0.27	+0.45 / −0.46
150 – 300	9.12	±1.8	+3.1 / −2.6	0.284	±0.057	+0.089 / −0.076

Table 11.2: Absolute and normalised unfolded differential $\bar{t}q$ production cross-section as a function of $p_{\mathrm{T}}(t)$ at *parton level.* [2]

$\lvert y(t)\rvert$	$\mathrm{d}\sigma(tq)/\mathrm{d}\lvert y(t)\rvert$ [pb]			$(1/\sigma)\mathrm{d}\sigma(tq)/\mathrm{d}\lvert y(t)\rvert$ [10^{-3}]		
		stat.	syst.		stat.	syst.
0.0 – 0.3	32.7	±1.8	+2.5 / −2.1	636	±35	+47 / −39
0.3 – 0.7	31.5	±1.8	+2.2 / −2.4	613	±34	+31 / −33
0.7 – 1.3	25.3	±1.3	+1.9 / −1.9	492	±24	+26 / −27
1.3 – 2.2	15.4	±0.9	+1.2 / −1.2	299	±14	+14 / −15

Table 11.3: Absolute and normalised unfolded differential tq production cross-sections as a function of $\lvert y(t)\rvert$ at *parton level.* [2]

$\lvert y(t)\rvert$	$\mathrm{d}\sigma(\bar{t}q)/\mathrm{d}\lvert y(t)\rvert$ [pb]			$(1/\sigma)\mathrm{d}\sigma(\bar{t}q)/\mathrm{d}\lvert y(t)\rvert$ [10^{-3}]		
		stat.	syst.		stat.	syst.
0.0 – 0.3	21.5	±1.7	+1.8 / −1.9	714	±55	+41 / −46
0.3 – 0.7	18.8	±1.6	+1.7 / −1.7	626	±53	+46 / −46
0.7 – 1.3	16.3	±1.2	+1.6 / −1.6	543	±37	+44 / −43
1.3 – 2.2	7.0	±0.8	+1.2 / −1.1	233	±23	+30 / −29

Table 11.4: Absolute and normalised unfolded differential $\bar{t}q$ production cross-sections as a function of $\lvert y(t)\rvert$ at *parton level.* [2]

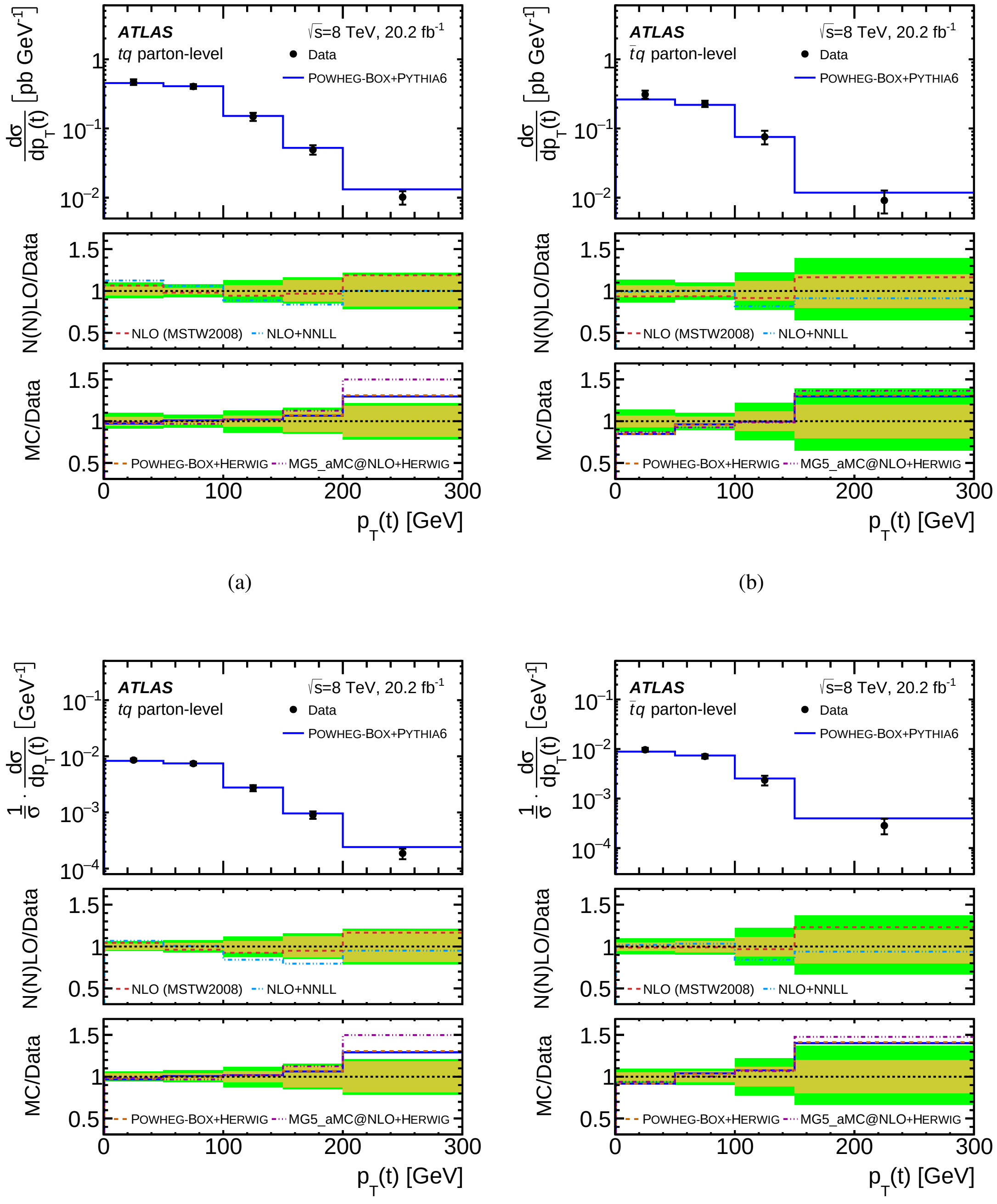

(a) (b)

(c) (d)

Figure 11.1: (a,b) absolute and (c, d) normalised unfolded differential cross-sections as a function of $p_T(t)$ for (a) *top quarks* and (b) *top antiquarks*. The unfolded distributions are compared to QCD N(N)LO calculations and various MC predictions. The vertical error bars on the data points denote the total uncertainty. The dashed (red) line in the central distribution shows the NLO prediction calculated using MCFM. The dash-dot (blue) line is the approximate NNLO prediction [123]. The bottom distribution compares the data with the MC predictions from Powheg-Box (orange dashed line) and MadGraph5_aMC@NLO (purple dash-dotted line). The inner (yellow) band in the bottom part of each figure represents the statistical uncertainty of the measurement, and the outer (green) band the total uncertainty. [2]

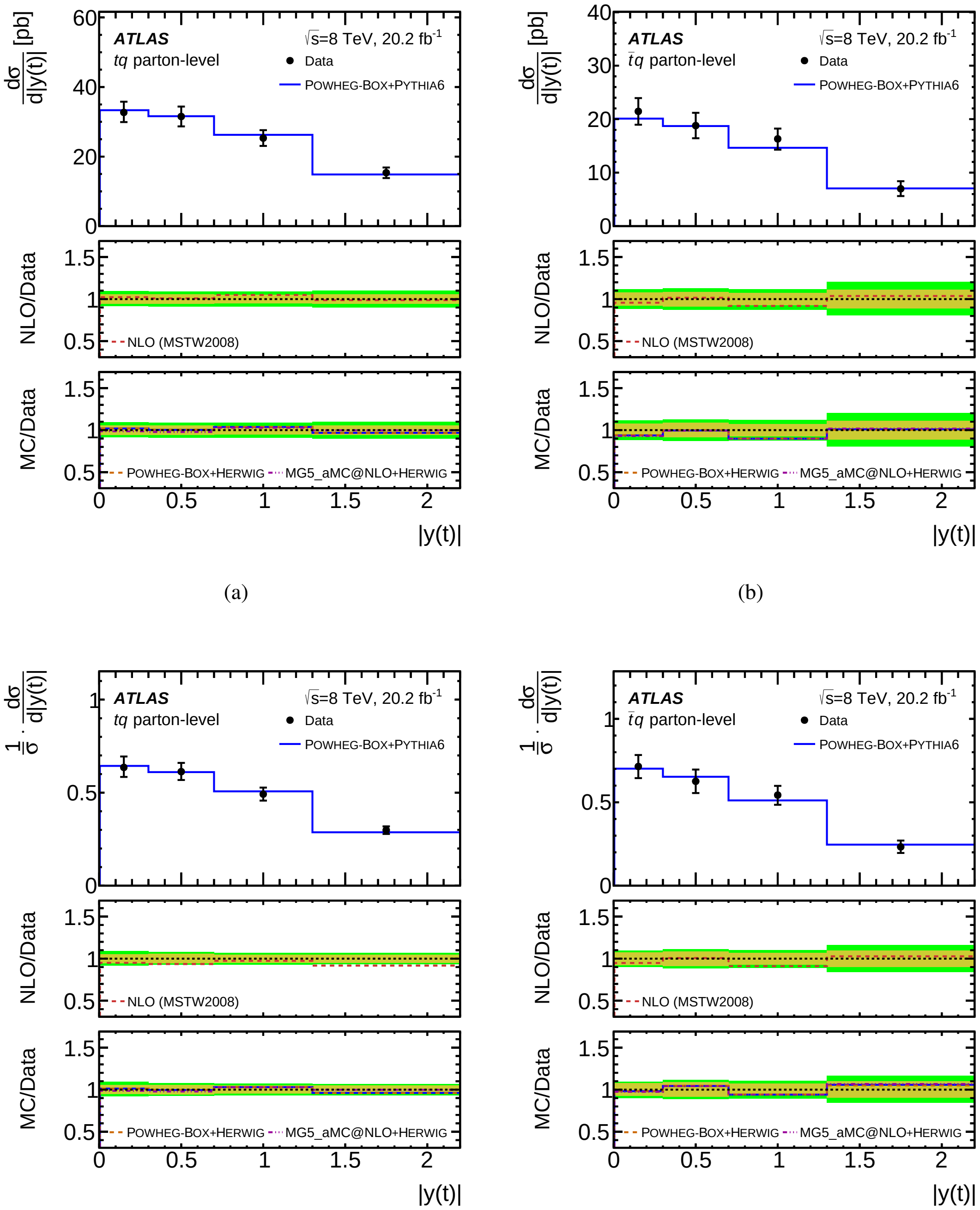

(a) (b)

(c) (d)

Figure 11.2: (a,b) absolute and (c, d) normalised unfolded differential cross-sections as a function of $|y(t)|$ for (a) *top quarks* and (b) *top antiquarks*. The unfolded distributions are compared to a QCD NLO calculation and various MC predictions. The vertical error bars on the data points denote the total uncertainty. The dashed (red) line in the central distribution shows the NLO prediction calculated using MCFM. The bottom distribution compares the data with the MC predictions from Powheg-Box (orange dashed line) and MadGraph5_aMC@NLO (purple dash-dotted line). The inner (yellow) band in the bottom part of each figure represents the statistical uncertainty of the measurement, and the outer (green) band the total uncertainty. [2]

Variables	σ [pb] ± stat. unc.						
	Bin 1	Bin 2	Bin 3	Bin 4	Bin 5	Overflow	Total
$p_\mathrm{T}(t)$							
tq	23.3 ± 1.2	20.2 ± 0.8	7.43 ± 0.51	2.46 ± 0.31	1.02 ± 0.19	0.36	54.8 ± 1.6
$\bar{t}q$	15.5 ± 1.1	11.4 ± 0.7	3.79 ± 0.44	1.37 ± 0.26		0.22	32.3 ± 1.4
$\lvert y(t)\rvert$							
tq	9.81 ± 0.6	12.6 ± 0.7	15.2 ± 0.8	13.8 ± 0.8		3.64	55.1 ± 1.4
$\bar{t}q$	6.44 ± 0.51	7.52 ± 0.66	9.79 ± 0.71	6.29 ± 0.70		1.79	31.8 ± 1.3

Table 11.5: The unfolded tq and $\bar{t}q$ cross-sections with statistical uncertainty for each bin from parton-level unfolding. The number of events in the overflow bin is calculated from the simulated signal sample using Powheg-Box + Pythia 6. The total cross-section with statistical uncertainty for each variable is given in the last column.

11.2 Results at particle level

The absolute and normalised differential cross-sections as a function of p_{T} and $|y|$ of the pseudo-top-quarks, pseudo-top-antiquarks, and untagged jets are performed at particle level for the first time. The default network is used for all measurements, except for the measurement as a function of $|y(\hat{j})|$, where the neural network without $|\eta(j)|$ is exploited.

The values of the absolute and normalised unfolded differential cross-sections as a function of $p_{\mathrm{T}}(\hat{t})$ and $|y(\hat{t})|$ are given in Tables 11.6–11.9. Their distributions are visualised in Figures 11.3 and 11.4. The measured differential cross-sections are compared with the same MC predictions used for the comparison of the parton-level cross-sections. Good agreement between the measured differential cross-sections and the predictions is seen. More measurements (corresponding to the number of bins) can be done at particle level. This is due to better resolution of the particle-level top quarks.

The results of all differential cross-sections as a function of $p_{\mathrm{T}}(\hat{j})$ and $|y(\hat{j})|$ are listed in Tables 11.10–11.13. The absolute and normalised differential cross-sections are pictured in Figures 11.5 and 11.6. All MC predictions again well describe the measured differential cross-sections, even though the predicted spectra tend to be slightly harder than the data as a function of $p_{\mathrm{T}}(\hat{j})$.

The total fiducial unfolded cross-sections with statistical uncertainty for all variables for both tq and $\bar{t}q$ events are summarised in Table 11.14. The number of events in the overflow bin is calculated from the nominal t-channel MC sample. All total fiducial unfolded cross-sections are in good agreement with each other as well as with the results from fiducial cross-section measurement shown in Section 7.3.2.

$p_{\mathrm{T}}(\hat{t})$ [GeV]	$\mathrm{d}\sigma(tq)/\mathrm{d}p_{\mathrm{T}}(\hat{t})$ [fb GeV^{-1}]	stat.	syst.	$(1/\sigma)\mathrm{d}\sigma(tq)/\mathrm{d}p_{\mathrm{T}}(\hat{t})$ [10^{-3} GeV^{-1}]	stat.	syst.
0– 35	38.0	±3.1	+3.3 / −3.4	3.85	±0.29	+0.22 / −0.22
35– 50	121	±8.4	+8.0 / −8.2	12.2	±0.82	+0.61 / −0.59
50– 75	125	±5.3	+7.7 / −7.9	12.7	±0.49	+0.54 / −0.54
75–100	68.1	±3.9	+5.1 / −5.0	6.89	±0.38	+0.36 / −0.34
100–150	27.5	±1.5	+2.1 / −2.1	2.78	±0.15	+0.18 / −0.18
150–200	7.55	±0.76	+0.67 / −0.56	0.765	±0.076	+0.056 / −0.046
200–300	1.50	±0.24	+0.23 / −0.23	0.152	±0.024	+0.022 / −0.022

Table 11.6: Absolute and normalised unfolded differential tq production cross-section as a function of $p_{\mathrm{T}}(\hat{t})$ at *particle level.* [2]

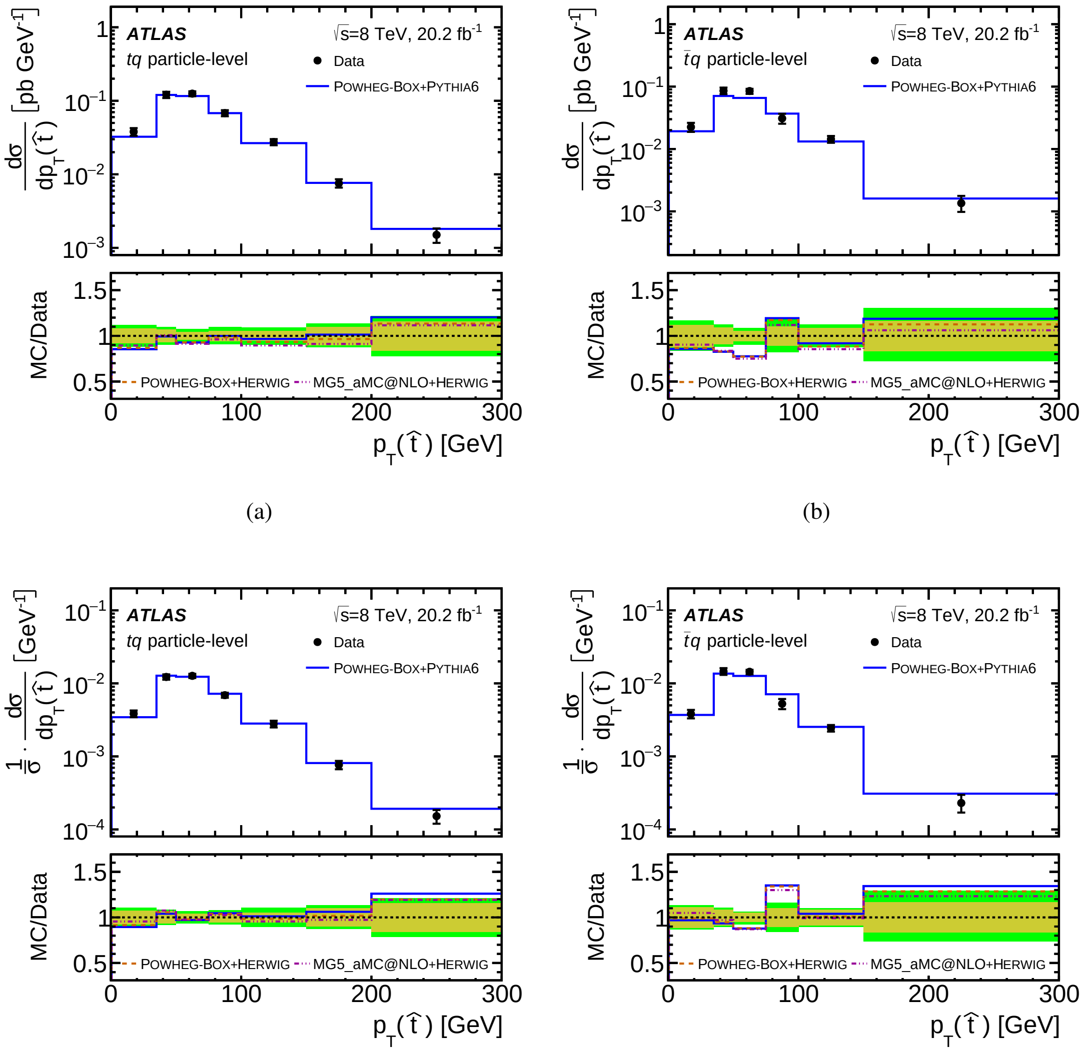

(a)

(b)

(c)

(d)

Figure 11.3: (a,b) absolute and (c, d) normalised unfolded differential cross-sections as a function of $\boldsymbol{p_T(\hat{t})}$ for (a) *top quarks* and (b) *top antiquarks*. The unfolded distributions are compared to various MC predictions. The vertical error bars on the data points denote the total uncertainty. The inner (yellow) band in the bottom part of each figure represents the statistical uncertainty of the measurement, and the outer (green) band the total uncertainty. [2]

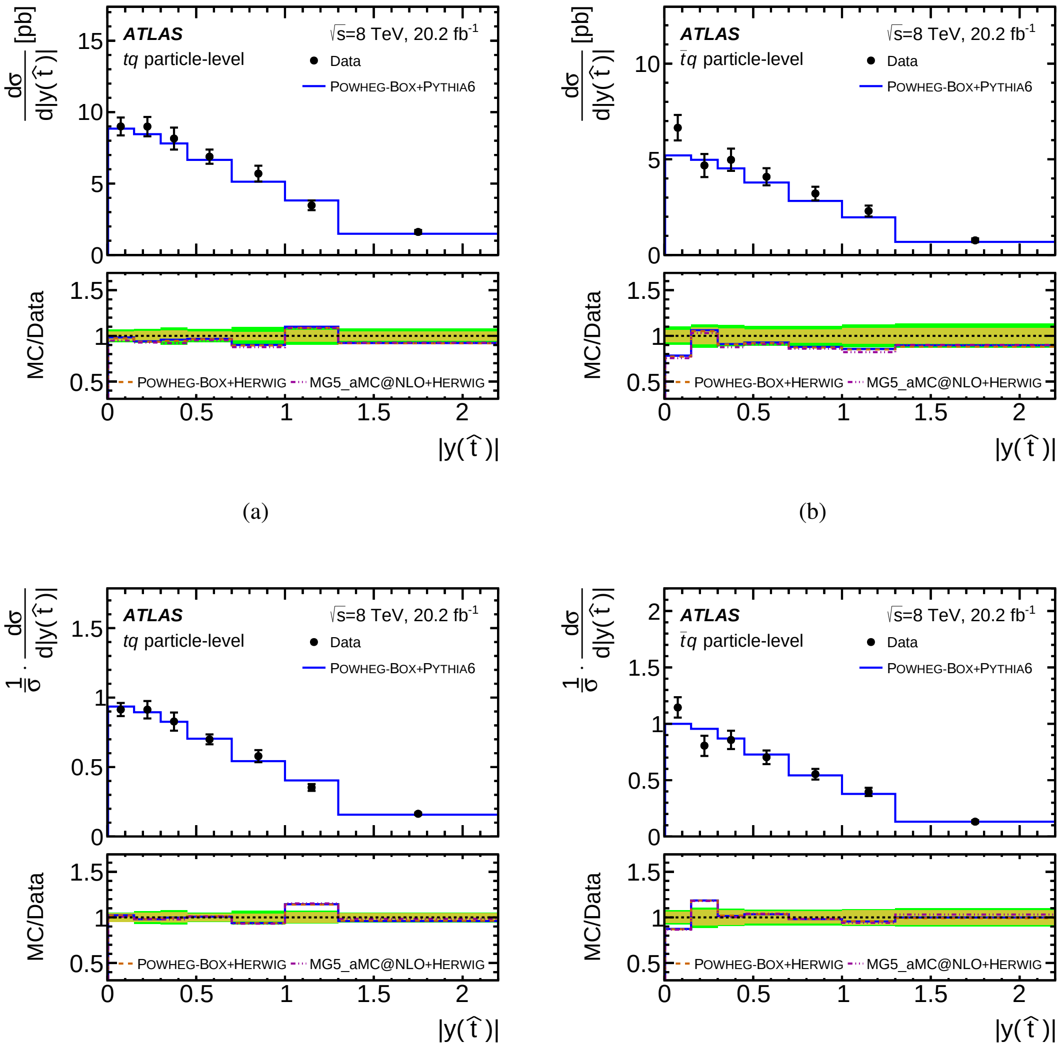

(a)

(b)

(c)

(d)

Figure 11.4: (a,b) absolute and (c, d) normalised unfolded differential cross-sections as a function of $|y(\hat{t})|$ for (a) *top quarks* and (b) *top antiquarks*. The unfolded distributions are compared to various MC predictions. The vertical error bars on the data points denote the total uncertainty. The inner (yellow) band in the bottom part of each figure represents the statistical uncertainty of the measurement, and the outer (green) band the total uncertainty. [2]

$p_{\mathrm{T}}(\hat{t})$ [GeV]	$\mathrm{d}\sigma(\bar{t}q)/\mathrm{d}p_{\mathrm{T}}(\hat{t})$ [fb GeV^{-1}]	stat.	syst.	$(1/\sigma)\mathrm{d}\sigma(\bar{t}q)/\mathrm{d}p_{\mathrm{T}}(\hat{t})$ [10^{-3} GeV^{-1}]	stat.	syst.
0 – 35	22.5	±2.7	+2.5 / −2.4	3.82	±0.44	+0.27 / −0.24
35 – 50	85.6	±7.8	+7.2 / −6.3	14.6	±1.3	+0.98 / −0.79
50 – 75	84.7	±4.7	+5.4 / −6.9	14.4	±0.74	+0.51 / −0.81
75 – 100	30.9	±3.3	+4.6 / −4.4	5.25	±0.54	+0.65 / −0.62
100 – 150	14.4	±1.3	+1.2 / −1.2	2.44	±0.21	+0.13 / −0.13
150 – 300	1.35	±0.23	+0.35 / −0.30	0.230	±0.038	+0.055 / −0.046

Table 11.7: Absolute and normalised unfolded differential $\bar{t}q$ production cross-section as a function of $p_{\mathrm{T}}(\hat{t})$ at *particle level.* [2]

$\lvert y(\hat{t})\rvert$	$\mathrm{d}\sigma(tq)/\mathrm{d}\lvert y(\hat{t})\rvert$ [pb]	stat.	syst.	$(1/\sigma)\mathrm{d}\sigma(tq)/\mathrm{d}\lvert y(\hat{t})\rvert$ [10^{-3}]	stat.	syst.
0.00 – 0.15	9.00	±0.45	+0.43 / −0.43	914	±43	+19 / −18
0.15 – 0.30	8.99	±0.47	+0.47 / −0.49	913	±46	+41 / −43
0.30 – 0.45	8.15	±0.48	+0.59 / −0.60	828	±46	+44 / −46
0.45 – 0.70	6.88	±0.32	+0.38 / −0.37	699	±30	+19 / −17
0.70 – 1.00	5.70	±0.26	+0.49 / −0.48	579	±24	+36 / −36
1.00 – 1.30	3.47	±0.22	+0.26 / −0.25	353	±21	+13 / −11
1.30 – 2.20	1.61	±0.08	+0.11 / −0.11	164	±8	+4 / −4

Table 11.8: Absolute and normalised unfolded differential tq production cross-section as a function of $\lvert y(\hat{t})\rvert$ at *particle level.* [2]

$\lvert y(\hat{t})\rvert$	$\mathrm{d}\sigma(\bar{t}q)/\mathrm{d}\lvert y(\hat{t})\rvert$ [pb]	stat.	syst.	$(1/\sigma)\mathrm{d}\sigma(\bar{t}q)/\mathrm{d}\lvert y(\hat{t})\rvert$ [10^{-3}]	stat.	syst.
0.00 – 0.15	6.65	±0.44	+0.50 / −0.49	1 145	±70	+57 / −55
0.15 – 0.30	4.68	±0.43	+0.41 / −0.43	806	±71	+51 / −57
0.30 – 0.45	4.97	±0.42	+0.40 / −0.39	856	±69	+44 / −40
0.45 – 0.70	4.08	±0.29	+0.34 / −0.33	703	±46	+38 / −39
0.70 – 1.00	3.21	±0.23	+0.27 / −0.27	553	±37	+28 / −30
1.00 – 1.30	2.30	±0.20	+0.20 / −0.21	396	±32	+17 / −17
1.30 – 2.20	0.76	±0.07	+0.08 / −0.07	132	±11	+8 / −7

Table 11.9: Absolute and normalised unfolded differential $\bar{t}q$ production cross-section as a function of $\lvert y(\hat{t})\rvert$ at *particle level.* [2]

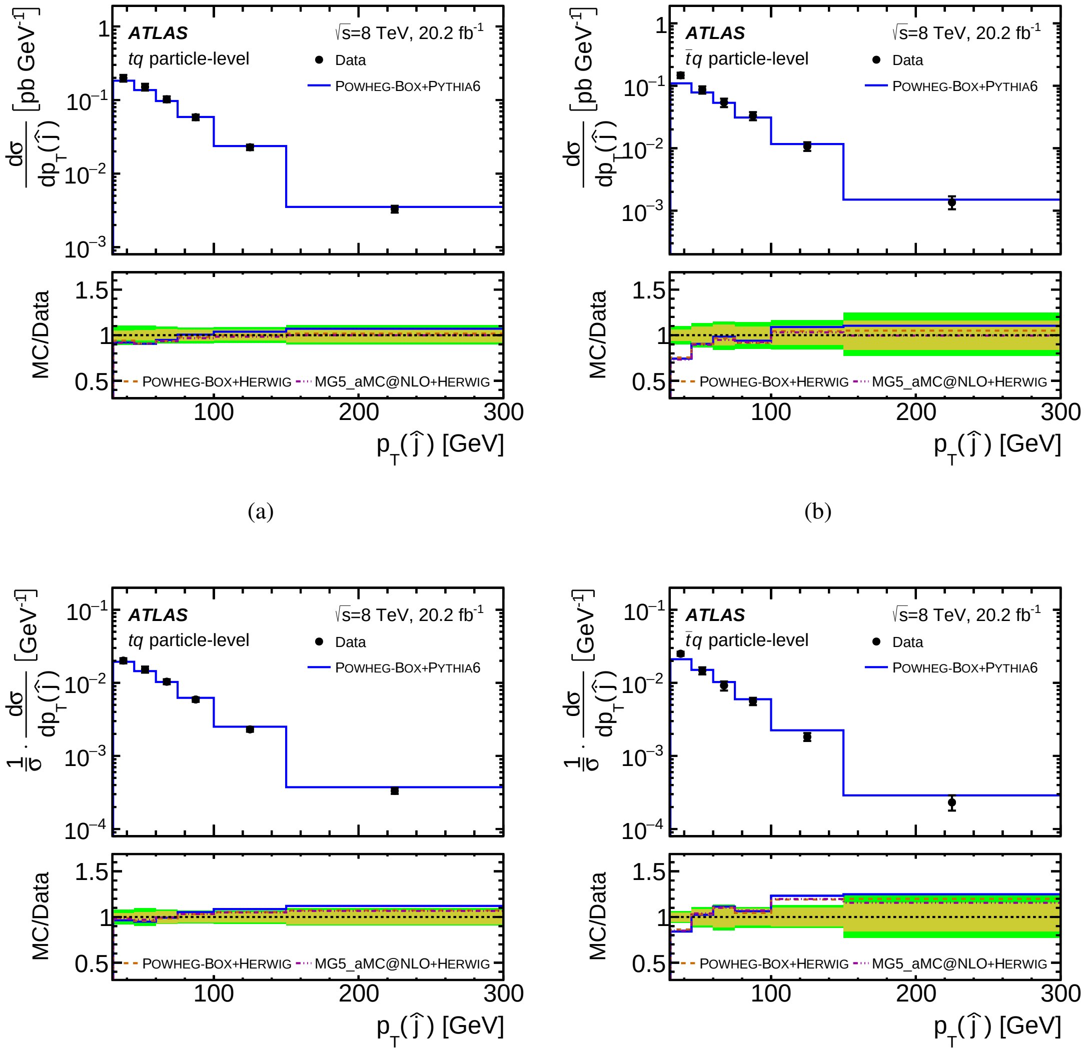

(a)

(b)

(c)

(d)

Figure 11.5: (a,b) absolute and (c, d) normalised unfolded differential cross-sections as a function of $\boldsymbol{p_T(\hat{j})}$ for (a) *top quarks* (b) *top antiquarks*. The unfolded distributions are compared to various MC predictions. The vertical error bars on the data points denote the total uncertainty. The inner (yellow) band in the bottom part of each figure represents the statistical uncertainty of the measurement, and the outer (green) band the total uncertainty. [2]

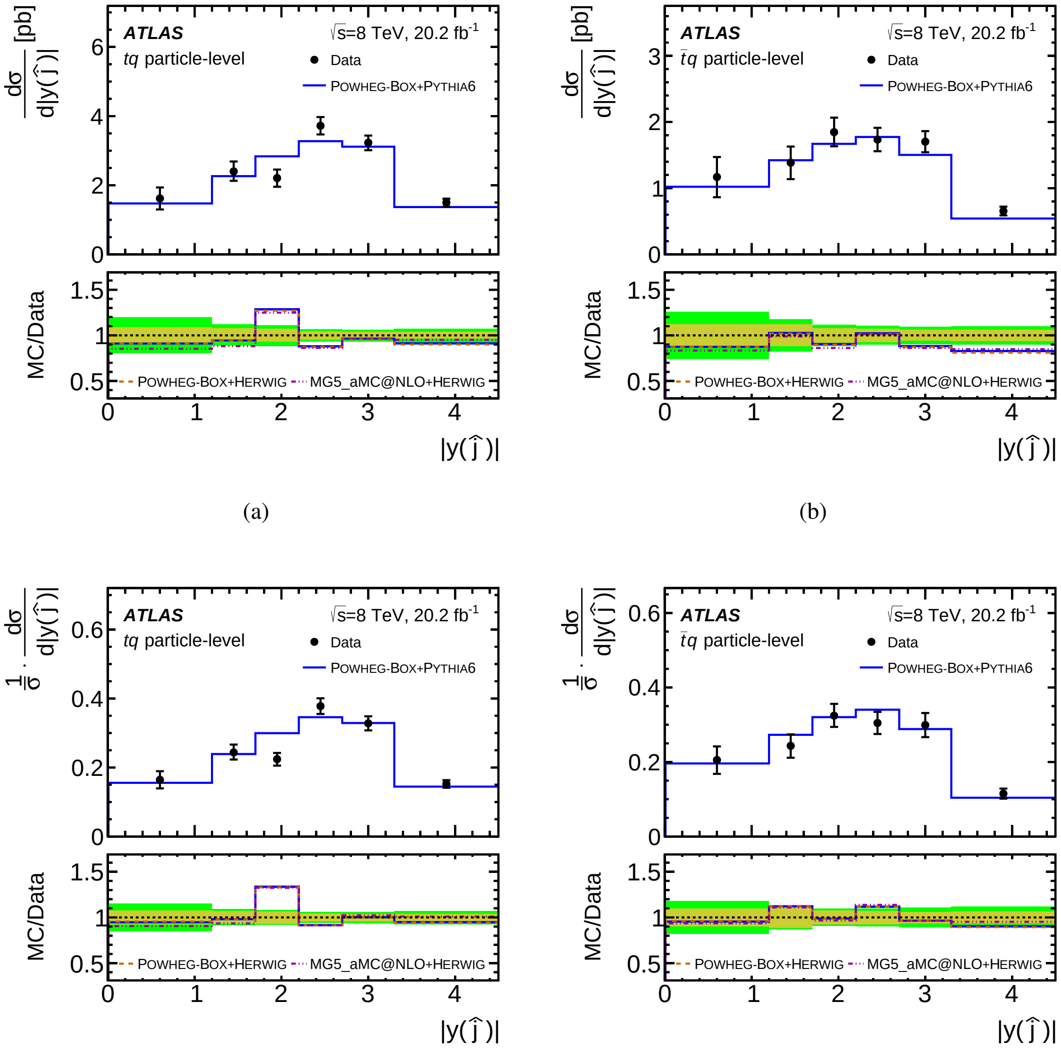

(a) (b)

(c) (d)

Figure 11.6: (a,b) absolute and (c, d) normalised unfolded differential cross-sections as a function of $|y(\hat{j})|$ for (a) *top quarks* and (b) *top antiquarks*. The unfolded distributions are compared to various MC predictions. The vertical error bars on the data points denote the total uncertainty. The inner (yellow) band in the bottom part of each figure represents the statistical uncertainty of the measurement, and the outer (green) band the total uncertainty. [2]

$p_{\mathrm{T}}(\hat{j})$ [GeV]	$\mathrm{d}\sigma(tq)/\mathrm{d}p_{\mathrm{T}}(\hat{j})$ [fb GeV^{-1}]			$(1/\sigma)\mathrm{d}\sigma(tq)/\mathrm{d}p_{\mathrm{T}}(\hat{j})$ [10^{-3} GeV^{-1}]		
		stat.	syst.		stat.	syst.
30 – 45	199	±9.8	+18 / −19	20.1	±0.84	+1.2 / −1.2
45 – 60	151	±8.6	+13 / −14	15.3	±0.85	+0.91 / −0.94
60 – 75	102	±7.0	+6.8 / −5.8	10.4	±0.69	+0.46 / −0.35
75 – 100	58.5	±3.5	+3.5 / −3.9	5.92	±0.35	+0.24 / −0.27
100 – 150	22.8	±1.3	+1.4 / −1.4	2.31	±0.13	+0.11 / −0.11
150 – 300	3.29	±0.26	+0.24 / −0.22	0.333	±0.026	+0.019 / −0.015

Table 11.10: Absolute and normalised unfolded differential $\boldsymbol{tq}$ production cross-section as a function of $\boldsymbol{p_{\mathrm{T}}(\hat{j})}$ at *particle level.* [2]

$p_{\mathrm{T}}(\hat{j})$ [GeV]	$\mathrm{d}\sigma(\bar{t}q)/\mathrm{d}p_{\mathrm{T}}(\hat{j})$ [fb GeV^{-1}]			$(1/\sigma)\mathrm{d}\sigma(\bar{t}q)/\mathrm{d}p_{\mathrm{T}}(\hat{j})$ [10^{-3} GeV^{-1}]		
		stat.	syst.		stat.	syst.
30 – 45	147	±8.9	+12 / −12	25.0	±1.2	+1.1 / −1.0
45 – 60	86.4	±7.8	+8.3 / −8.5	14.7	±1.3	+0.96 / −0.99
60 – 75	54.2	±6.2	+5.1 / −6.0	9.21	±1.0	+0.68 / −0.88
75 – 100	33.0	±3.1	+3.7 / −3.9	5.62	±0.51	+0.36 / −0.41
100 – 150	10.7	±1.1	+1.3 / −1.2	1.82	±0.19	+0.14 / −0.11
150 – 300	1.36	±0.22	+0.26 / −0.22	0.231	±0.036	+0.044 / −0.038

Table 11.11: Absolute and normalised unfolded differential $\boldsymbol{\bar{t}q}$ production cross-section as a function of $\boldsymbol{p_{\mathrm{T}}(\hat{j})}$ at *particle level.* [2]

$\lvert y(\hat{j})\rvert$	$\mathrm{d}\sigma(tq)/\mathrm{d}\lvert y(\hat{j})\rvert$ [pb]			$(1/\sigma)\mathrm{d}\sigma(tq)/\mathrm{d}\lvert y(\hat{j})\rvert$ [10^{-3}]		
		stat.	syst.		stat.	syst.
0.0 – 1.2	1.62	±0.14	+0.28 / −0.28	164	±12	+22 / −22
1.2 – 1.7	2.40	±0.18	+0.22 / −0.20	244	±17	+15 / −11
1.7 – 2.2	2.21	±0.15	+0.19 / −0.20	224	±15	+9.8 / −11
2.2 – 2.7	3.72	±0.16	+0.19 / −0.19	378	±16	+16 / −16
2.7 – 3.3	3.23	±0.13	+0.16 / −0.17	328	±13	+15 / −15
3.3 – 4.5	1.50	±0.056	+0.096 / −0.10	152	±6.0	+9.2 / −9.3

Table 11.12: Absolute and normalised unfolded differential $\boldsymbol{tq}$ production cross-section as a function of $\boldsymbol{\lvert y(\hat{j})\rvert}$ at *particle level.* [2]

$\|y(\hat{j})\|$	$\mathrm{d}\sigma(\bar{t}q)/\mathrm{d}\|y(\hat{j})\|$ [pb]	stat.	syst.	$(1/\sigma)\mathrm{d}\sigma(\bar{t}q)/\mathrm{d}\|y(\hat{j})\|$ $[10^{-3}]$	stat.	syst.
0.0 – 1.2	1.17	±0.14	+0.27 / −0.27	205	±20	+31 / −31
1.2 – 1.7	1.39	±0.17	+0.18 / −0.18	243	±27	+14 / −16
1.7 – 2.2	1.85	±0.14	+0.16 / −0.16	324	±25	+20 / −17
2.2 – 2.7	1.73	±0.13	+0.12 / −0.12	305	±22	+20 / −19
2.7 – 3.3	1.70	±0.10	+0.12 / −0.12	299	±19	+26 / −26
3.3 – 4.5	0.655	±0.040	+0.053 / −0.051	115	±8	+11 / −11

Table 11.13: Absolute and normalised unfolded differential $\bar{t}q$ production cross-section as a function of $|y(\hat{j})|$ at *particle level*. [2]

Variables	σ [pb] ± stat. unc.								
	Bin 1	Bin 2	Bin 3	Bin 4	Bin 5	Bin 6	Bin 7	Overflow	Total
$\boldsymbol{p_{\mathrm{T}}(\hat{t})}$									
tq	1.33 ± 0.11	1.81 ± 0.13	3.13 ± 0.13	1.70 ± 0.10	1.38 ± 0.08	0.378 ± 0.038	0.150 ± 0.024	0.037	9.88 ± 0.25
$\bar{t}q$	0.786 ± 0.096	1.28 ± 0.12	2.12 ± 0.12	0.773 ± 0.082	0.718 ± 0.064	0.203 ± 0.034		0.012	5.88 ± 0.22
$\boldsymbol{\lvert y(\hat{t})\rvert}$									
tq	1.35 ± 0.07	1.35 ± 0.07	1.22 ± 0.07	1.72 ± 0.08	1.71 ± 0.08	1.04 ± 0.07	1.45 ± 0.07	0.016	9.84 ± 0.18
$\bar{t}q$	0.997 ± 0.066	0.702 ± 0.064	0.746 ± 0.063	1.02 ± 0.07	0.964 ± 0.069	0.689 ± 0.059	0.688 ± 0.060	0.006	5.81 ± 0.17
$\boldsymbol{p_{\mathrm{T}}(\hat{j})}$									
tq	2.98 ± 0.15	2.26 ± 0.13	1.53 ± 0.11	1.46 ± 0.09	1.14 ± 0.07	0.493 ± 0.039		0.036	9.88 ± 0.25
$\bar{t}q$	2.21 ± 0.13	1.30 ± 0.12	0.813 ± 0.093	0.826 ± 0.077	0.535 ± 0.057	0.204 ± 0.032		0.012	5.88 ± 0.22
$\boldsymbol{\lvert y(\hat{j})\rvert}$									
tq	1.94 ± 0.17	1.20 ± 0.09	1.10 ± 0.08	1.86 ± 0.08	1.94 ± 0.08	1.80 ± 0.07			9.85 ± 0.25
$\bar{t}q$	1.40 ± 0.17	0.693 ± 0.083	0.923 ± 0.072	0.867 ± 0.064	1.02 ± 0.06	0.786 ± 0.048			5.69 ± 0.23

Table 11.14: The unfolded tq and $\bar{t}q$ cross-sections in the fiducial range with statistical uncertainty for each bin from particle-level unfolding. The number of events in the overflow bin is calculated from the simulated signal sample using Powheg-Box + Pythia 6. The total fiducial cross-section with statistical uncertainty for each variable is given in the last column.

CHAPTER 12

Summary

In this thesis, measurements of differential t-channel single top-quark production cross-sections were presented, using a dataset with an integrated luminosity of 20.2 fb^{-1} recorded by the ATLAS detector in proton–proton collisions at a centre-of-mass energy of 8 TeV. Absolute and normalised differential cross-sections were measured for single top-quark (tq) and top-antiquark ($\bar{t}q$) production over the full kinematic range (referred to as at parton level) as well as within a fiducial phase space (referred to as at particle level). The particle-level differential cross-sections of the t-channel single top-(anti)quark production were measured for the first time. They were extracted as a function of the transverse momentum and the absolute value of the rapidity of the top (anti)quark at both parton level and particle level. In addition, the transverse momentum and rapidity differential cross-sections of the light-quark jet, assumed to be the accompanying jet from the t-channel scattering, were performed at particle level.

Selected events were characterised by one electron or muon with high transverse momentum, a significant magnitude of missing transverse momentum, and two jets with high transverse momentum. One of the jets must be a b-tagged jet. A series of cuts was employed to select signal events and an artificial neural network was exploited to improve the separation power between the signal and the background. These were derived in cooperation with a team from the University of Wuppertal that measured the fiducial and total t-channel single top-quark and top-antiquark cross-sections. The analysis presented in this thesis started with applying an optimised cut on the neural network output in order to achieve a good signal-to-background ratio for both tq production and $\bar{t}q$ production. The binning of each measured distribution was chosen carefully. As the fiducial volume was defined to be as close as possible to the measurement phase space, the kinematic properties of the reconstruction-level top quarks are closer to the particle-level top quarks than the parton-level top quarks. This implies that the resolution of kinematic properties of the particle-level top quark is better than the resolution of the corresponding properties at parton level. As a consequence, more bins are used for the particle-level cross-sections. The measured distributions were then unfolded using an iterative Bayesian method and corrected for the loss in selection efficiency to recover their true distribution at either parton level or particle level. Several tests were performed to ensure that the chosen unfolding method is reliable and can be used for the analysis.

The measurements are at $5-20\%$ precision per bin. The most precise ones are the normalised differential cross-sections at particle level. The precision of the measurements is improved compared to the 7 TeV measurements, whose precision is between $10-30\%$ per bin, due to more statistics of the dataset as well as a better prescription of systematic evaluation. Doing the measurements in the fiducial volume can also reduce systematic uncertainties due to signal modelling. The tq production cross-section was found to be about twice the $\bar{t}q$ production cross-section. This is consistent with the fact that there are two valence u-quarks and one valence d-quark inside the proton. The shape of the measured distributions for the tq production differs from the ones for the $\bar{t}q$ production as they originate from different initial-state light quarks. The measured differential cross-sections at parton level were compared to several Monte Carlo predictions and fixed-order QCD calculations. The particle-level results were compared to the same Monte Carlo predictions as for the parton-level results. Overall, the measured differential cross-sections confirm the Standard Model predictions. No indication of new physics is observed in the presented results. These results not only verify the Standard Model, but also can be used as input for Monte Carlo tuning to improve simulations of these production processes.

Bibliography

[1] P. Tepel, *Measurement of the fiducial and total single top-quark t-channel production cross-sections with the ATLAS detector at* $\sqrt{s} = 8$ *TeV*, thesis in preparation, PhD thesis: Wuppertal U. (cit. on pp. 2, 39, 47, 50, 53, 54, 58).

[2] ATLAS Collaboration, *Fiducial, total and differential cross-section measurements of t-channel single top-quark production in pp collisions at 8 TeV using data collected by the ATLAS detector*, Eur. Phys. J. C **77** (2017) 531, arXiv: `1702.02859 [hep-ex]` (cit. on pp. 2, 40–42, 50, 51, 54–59, 62–64, 67, 71, 72, 74, 76, 95, 104–106, 108–115, 136, 163–192).

[3] S. L. Glashow, *Partial Symmetries of Weak Interactions*, Nucl. Phys. **22** (1961) 579 (cit. on p. 3).

[4] S. Weinberg, *A Model of Leptons*, Phys. Rev. Lett. **19** (21 1967-11) 1264, URL: `https://link.aps.org/doi/10.1103/PhysRevLett.19.1264` (cit. on p. 3).

[5] A. Salam, *Weak and Electromagnetic Interactions*, Conf. Proc. C **680519** (1968) 367 (cit. on p. 3).

[6] Wikipedia, *Standard Model of Elementary Particles*, Visited May 2017, URL: `https://en.wikipedia.org/wiki/Standard_Model#/media/File:Standard_Model_of_Elementary_Particles.svg` (cit. on p. 4).

[7] C. Patrignani et al., *Review of Particle Physics*, Chin. Phys. C **40**.10 (2016) 100001 (cit. on pp. 4, 6, 9).

[8] P. W. Higgs, *Broken Symmetries and the Masses of Gauge Bosons*, Phys. Rev. Lett. **13** (1964) 508 (cit. on p. 5).

[9] F. Englert and R. Brout, *Broken Symmetry and the Mass of Gauge Vector Mesons*, Phys. Rev. Lett. **13** (1964) 321 (cit. on p. 5).

[10] R. P. Feynman, *Space-Time Approach to Quantum Electrodynamics*, Phys. Rev. **76** (6 1949-09) 769, URL: `https://link.aps.org/doi/10.1103/PhysRev.76.769` (cit. on p. 6).

[11] R. P. Feynman, *Very high-energy collisions of hadrons*, Phys. Rev. Lett. **23** (1969) 1415 (cit. on p. 7).

[12] T.-M. Yan and S. D. Drell, *The Parton Model and its Applications*, Int. J. Mod. Phys. A **29** (2014) 0071, arXiv: `1409.0051 [hep-ph]` (cit. on p. 7).

[13] A. D. Martin et al., *Parton distributions for the LHC*, Eur. Phys. J. C **63** (2009) 189, arXiv: `0901.0002 [hep-ph]` (cit. on pp. 7, 8).

[14] J. C. Collins, D. E. Soper and G. F. Sterman, *Factorization of Hard Processes in QCD*, Adv. Ser. Direct. High Energy Phys. **5** (1989) 1, arXiv: `hep-ph/0409313 [hep-ph]` (cit. on p. 7).

[15] M. Kobayashi and T. Maskawa, *CP Violation in the Renormalizable Theory of Weak Interaction*, Prog. Theor. Phys. **49** (1973) 652 (cit. on p. 8).

[16] CDF Collaboration, *Observation of top quark production in $\bar{p}p$ collisions*, Phys. Rev. Lett. **74** (1995) 2626, arXiv: `hep-ex/9503002 [hep-ex]` (cit. on p. 8).

[17] D0 Collaboration, *Observation of the top quark*, Phys. Rev. Lett. **74** (1995) 2632, arXiv: `hep-ex/9503003 [hep-ex]` (cit. on p. 8).

[18] ATLAS, CDF, CMS, D0 Collaborations, *First combination of Tevatron and LHC measurements of the top-quark mass* (2014), arXiv: `1403.4427 [hep-ex]` (cit. on p. 8).

[19] H.-L. Lai et al., *New parton distributions for collider physics*, Phys. Rev. D **82** (2010) 074024, arXiv: `1007.2241 [hep-ph]` (cit. on pp. 10, 35).

[20] R. D. Ball et al., *Parton distributions with LHC data*, Nucl. Phys. B **867** (2013) 244, arXiv: `1207.1303 [hep-ph]` (cit. on p. 10).

[21] M. Czakon, P. Fiedler and A. Mitov, *Total Top-Quark Pair-Production Cross Section at Hadron Colliders Through $O(\alpha\frac{4}{S})$*, Phys. Rev. Lett. **110** (2013) 252004, arXiv: `1303.6254 [hep-ph]` (cit. on p. 10).

[22] M. Cacciari et al., *Top-pair production at hadron colliders with next-to-next-to-leading logarithmic soft-gluon resummation*, Phys. Lett. B **710** (2012) 612, arXiv: `1111.5869 [hep-ph]` (cit. on p. 10).

[23] M. Botje et al., *The PDF4LHC Working Group Interim Recommendations* (2011), arXiv: `1101.0538 [hep-ph]` (cit. on p. 10).

[24] LHC-top-working-group, *Summary of LHC and Tevatron measurements of the top-pair production cross-section*, Visited June 2017, URL: `https://twiki.cern.ch/twiki/bin/view/LHCPhysics/TopPairCrossectionSqrtsHistory` (cit. on pp. 11, 13).

[25] J. M. Campbell et al., *Next-to-Leading-Order Predictions for t-Channel Single-Top Production at Hadron Colliders*, Phys. Rev. Lett. **102** (2009) 182003, arXiv: `0903.0005 [hep-ph]` (cit. on pp. 12, 14).

[26] P. Kant et al., HatHor *for single top-quark production: Updated predictions and uncertainty estimates for single top-quark production in hadronic collisions*, Comput. Phys. Commun. **191** (2015) 74, arXiv: `1406.4403 [hep-ph]` (cit. on pp. 12, 59).

[27] A. Heinson, A. S. Belyaev and E. E. Boos, *Single top quarks at the Fermilab Tevatron*, Phys. Rev. D **56** (1997) 3114, arXiv: `hep-ph/9612424 [hep-ph]` (cit. on p. 12).

[28] N. Kidonakis, *NNLL resummation for s-channel single top quark production*, Phys. Rev. D **81** (2010) 054028, arXiv: `1001.5034 [hep-ph]` (cit. on p. 12).

[29] N. Kidonakis, *Two-loop soft anomalous dimensions for single top quark associated production with a W^- or H^-*, Phys. Rev. D **82** (2010) 054018, arXiv: `1005.4451 [hep-ph]` (cit. on p. 13).

[30] CDF Collaboration, *Observation of Electroweak Single Top-Quark Production*, Phys. Rev. Lett. **103** (9 2009-08) 092002, URL: `https://link.aps.org/doi/10.1103/PhysRevLett.103.092002` (cit. on p. 13).

[31] D0 Collaboration, *Observation of Single Top-Quark Production*, Phys. Rev. Lett. **103** (9 2009-08) 092001, URL: `https://link.aps.org/doi/10.1103/PhysRevLett.103.092001` (cit. on p. 13).

[32] ATLAS Collaboration, *Measurement of the inclusive cross-sections of single top-quark and top-antiquark t-channel production in pp collisions at* $\sqrt{s} = 13$ *TeV with the ATLAS detector*, JHEP **04** (2017) 086, arXiv: `1609.03920 [hep-ex]` (cit. on p. 13).

[33] CMS Collaboration, *Cross section measurement of t-channel single top quark production in pp collisions at* $\sqrt{s} = 13$ *TeV*, Submitted to: Phys. Lett. B (2016), arXiv: `1610.00678 [hep-ex]` (cit. on p. 13).

[34] CDF, D0 Collaborations, *Observation of s-channel production of single top quarks at the Tevatron*, Phys. Rev. Lett. **112** (2014) 231803, arXiv: `1402.5126 [hep-ex]` (cit. on p. 13).

[35] ATLAS Collaboration, *Evidence for single top-quark production in the s-channel in proton–proton collisions at* $\sqrt{s} = 8$ *TeV with the ATLAS detector using the Matrix Element Method*, Phys. Lett. B **756** (2016) 228, arXiv: `1511.05980 [hep-ex]` (cit. on p. 13).

[36] CMS Collaboration, *Observation of the associated production of a single top quark and a W boson in pp collisions at* $\sqrt{s} = 8$ *TeV*, Phys. Rev. Lett. **112**.23 (2014) 231802, arXiv: `1401.2942 [hep-ex]` (cit. on p. 14).

[37] L. Evans and P. Bryant, *LHC Machine*, Journal of Instrumentation **3**.08 (2008) S08001, URL: `http://stacks.iop.org/1748-0221/3/i=08/a=S08001` (cit. on p. 15).

[38] C. Lefèvre, "The CERN accelerator complex. Complexe des accélérateurs du CERN", 2008-12, URL: `http://cds.cern.ch/record/1260465` (cit. on p. 16).

[39] ATLAS Collaboration, *Performance of pile-up mitigation techniques for jets in pp collisions at* $\sqrt{s} = 8$ *TeV using the ATLAS detector*, Eur. Phys. J. C **76** (2016) 581, arXiv: `1510.03823 [hep-ex]` (cit. on p. 16).

[40] ATLAS Collaboration, *Simulation of Pile-up in the ATLAS Experiment*, J. Phys. Conf. Ser. **513** (2014) 022024 (cit. on p. 16).

[41] LHCb Collaboration, *The LHCb Detector at the LHC*, Journal of Instrumentation **3**.08 (2008) S08005, URL: `http://stacks.iop.org/1748-0221/3/i=08/a=S08005` (cit. on p. 16).

[42] ALICE Collaboration, *The ALICE experiment at the CERN LHC*, Journal of Instrumentation **3**.08 (2008) S08002, URL: `http://stacks.iop.org/1748-0221/3/i=08/a=S08002` (cit. on p. 16).

[43] TOTEM Collaboration, *The TOTEM Experiment at the CERN Large Hadron Collider*, Journal of Instrumentation **3**.08 (2008) S08007, URL: `http://stacks.iop.org/1748-0221/3/i=08/a=S08007` (cit. on p. 16).

[44] LHCf Collaboration, *The LHCf detector at the CERN Large Hadron Collider*, Journal of Instrumentation **3**.08 (2008) S08006, URL: `http://stacks.iop.org/1748-0221/3/i=08/a=S08006` (cit. on p. 16).

[45] MoEDAL Collaboration, *Technical Design Report of the MoEDAL Experiment* (2009) (cit. on p. 17).

[46] ATLAS Collaboration, *The Collaboration*, Visited June 2017, URL: `http://atlas.cern/discover/collaboration` (cit. on p. 18).

[47] ATLAS Collaboration, *The ATLAS Experiment at the CERN Large Hadron Collider*, JINST **3** (2008) S08003 (cit. on pp. 18–21).

[48] ATLAS Collaboration, *Performance of the ATLAS Trigger System in 2015*, Eur. Phys. J. C **77** (2017) 317, arXiv: `1611.09661 [hep-ex]` (cit. on p. 22).

[49] ATLAS Collaboration, *Improved luminosity determination in pp collisions at* $\sqrt{s} = 7$ *TeV using the ATLAS detector at the LHC*, Eur. Phys. J. C **73** (2013) 2518, arXiv: `1302.4393 [hep-ex]` (cit. on p. 22).

[50] ATLAS Collaboration, *Luminosity determination in pp collisions at* $\sqrt{s} = 8$ *TeV using the ATLAS detector at the LHC*, Eur. Phys. J. C **76** (2016) 653, arXiv: `1608.03953 [hep-ex]` (cit. on pp. 22, 54).

[51] S. van der Meer, *Calibration of the effective beam height in the ISR*, tech. rep. CERN-ISR-PO-68-31. ISR-PO-68-31, CERN, 1968, URL: `https://cds.cern.ch/record/296752` (cit. on p. 23).

[52] C. Rubbia, *Measurement of the luminosity of* $p-\overline{p}$ *collider with a (generalized) Van der Meer Method*, tech. rep. CERN-$p\overline{p}$-Note-38, CERN, 1977-11, URL: `https://cds.cern.ch/record/1025746` (cit. on p. 23).

[53] ATLAS Collaboration, *Expected performance of the ATLAS experiment: detector, trigger and physics*, Geneva: CERN, 2009, URL: `https://cds.cern.ch/record/1125884` (cit. on p. 25).

[54] M. Limper, S. Bentvelsen and A. P. Colijn, *Track and vertex reconstruction in the ATLAS inner detector*, Presented on 12 Oct 2009, 2009, URL: `https://cds.cern.ch/record/1202457` (cit. on p. 26).

[55] T. Cornelissen et al., *The new ATLAS track reconstruction (NEWT)*, Journal of Physics: Conference Series **119**.3 (2008) 032014, URL: `http://stacks.iop.org/1742-6596/119/i=3/a=032014` (cit. on p. 25).

[56] ATLAS Collaboration, *Performance of the ATLAS Inner Detector Track and Vertex Reconstruction in High Pile-Up LHC Environment*, tech. rep., 2012, URL: `https://cds.cern.ch/record/1435196` (cit. on p. 25).

[57] R. E. Kalman, *A New Approach to Linear Filtering And Prediction Problems*, ASME Journal of Basic Engineering (1960) (cit. on p. 25).

[58] R. Fruhwirth, *Application of Kalman filtering to track and vertex fitting*, Nucl. Instrum. Meth. A **262** (1987) 444 (cit. on p. 25).

[59] G. Piacquadio, K. Prokofiev and A. Wildauer, *Primary vertex reconstruction in the ATLAS experiment at LHC*, J. Phys.: Conf. Ser. **119** (2008) 032033, URL: `https://cds.cern.ch/record/1177127` (cit. on p. 26).

[60] ATLAS Collaboration, *Topological cell clustering in the ATLAS calorimeters and its performance in LHC Run 1* (2016), arXiv: `1603.02934 [hep-ex]` (cit. on p. 26).

[61] ATLAS Collaboration,
Jet energy measurement with the ATLAS detector in proton–proton collisions at $\sqrt{s} = 7$ *TeV*,
Eur. Phys. J. C **73** (2013) 2304, arXiv: `1112.6426 [hep-ex]` (cit. on pp. 26, 39).

[62] M. Cacciari, G. P. Salam and G. Soyez, *The anti-*k_t *jet clustering algorithm*, JHEP **04** (2008) 063, arXiv: `0802.1189 [hep-ph]`, URL: `http://fastjet.fr` (cit. on p. 26).

[63] ATLAS Collaboration, *Data-driven determination of the energy scale and resolution of jets reconstructed in the ATLAS calorimeters using dijet and multijet events at* $\sqrt{s} = 8$ *TeV*,
tech. rep., 2015, URL: `https://cds.cern.ch/record/2008678` (cit. on p. 27).

[64] ATLAS Collaboration,
Selection of jets produced in proton–proton collisions with the ATLAS detector using 2011 data,
tech. rep., 2012, URL: `https://cds.cern.ch/record/1430034` (cit. on p. 27).

[65] ATLAS Collaboration, *Pile-up subtraction and suppression for jets in ATLAS*, tech. rep., 2013,
URL: `https://cds.cern.ch/record/1570994` (cit. on p. 27).

[66] A. B. Galtieri, F. Margaroli and I. Volobouev,
Precision measurements of the top quark mass from the Tevatron in the pre-LHC era,
Rept. Prog. Phys. **75** (2012) 056201, arXiv: `1109.2163 [hep-ex]` (cit. on p. 28).

[67] ATLAS collaboration,
Expected Performance of the ATLAS Experiment - Detector, Trigger and Physics (2009),
URL: `https://cds.cern.ch/record/1125884` (cit. on p. 28).

[68] ATLAS Collaboration, *Performance of b-jet identification in the ATLAS experiment*,
JINST **11** (2016) P04008, arXiv: `1512.01094 [hep-ex]` (cit. on p. 28).

[69] ATLAS Collaboration,
Calibration of the performance of b-tagging for c and light-flavour jets in the 2012 ATLAS data,
tech. rep., 2014, URL: `https://cds.cern.ch/record/1741020` (cit. on p. 28).

[70] ATLAS Collaboration, *Measurement of the b-tag Efficiency in a Sample of Jets Containing Muons with* $5\,fb^{-1}$ *of data from the ATLAS detector*, tech. rep., 2012,
URL: `https://cds.cern.ch/record/1435197` (cit. on p. 28).

[71] ATLAS Collaboration, *Expected electron performance in the ATLAS experiment* (2011),
URL: `https://cds.cern.ch/record/1345327` (cit. on p. 29).

[72] ATLAS Collaboration, *Electron performance measurements with the ATLAS detector using the 2010 LHC proton–proton collision data*, Eur. Phys. J. C **72** (2012) 1909,
arXiv: `1110.3174 [hep-ex]` (cit. on pp. 29, 40).

[73] ATLAS Collaboration, *Object selection and calibration, background estimations and MC samples for top quark analyses using the full 2012 data set*,
tech. rep. ATL-COM-PHYS-2013-1016, CERN, 2013-07,
URL: `https://cds.cern.ch/record/1563201` (cit. on pp. 29, 31).

[74] ATLAS Collaboration, *Electron efficiency measurements with the ATLAS detector using 2012 LHC proton–proton collision data*, Eur. Phys. J. C **77** (2017) 195,
arXiv: `1612.01456 [hep-ex]` (cit. on p. 29).

[75] ATLAS Collaboration,
Electron and photon energy calibration with the ATLAS detector using LHC Run 1 data,
Eur. Phys. J. C **74** (2014) 3071, arXiv: `1407.5063 [hep-ex]` (cit. on pp. 30, 51).

[76] ATLAS Collaboration, *Measurement of the muon reconstruction performance of the ATLAS detector using 2011 and 2012 LHC proton–proton collision data*, Eur. Phys. J. C **74** (2014) 3130, arXiv: `1407.3935 [hep-ex]` (cit. on pp. 30, 51).

[77] K. Rehermann and B. Tweedie, *Efficient Identification of Boosted Semileptonic Top Quarks at the LHC*, JHEP **03** (2011) 059, arXiv: `1007.2221 [hep-ph]` (cit. on p. 30).

[78] ATLAS Collaboration, *Performance of missing transverse momentum reconstruction in proton–proton collisions at* $\sqrt{s} = 7$ *TeV with ATLAS*, Eur. Phys. J. C **72** (2012) 1844, arXiv: `1108.5602 [hep-ex]` (cit. on p. 31).

[79] T. Chwalek, *Measurement of the W boson helicity in top-antitop quark events with the CDF II experiment*, PhD thesis: Karlsruhe U., EKP, 2006, URL: `http://lss.fnal.gov/cgi-bin/find_paper.pl?masters-2006-04` (cit. on p. 32).

[80] P. Sturm and W. Wagner, *Measurement of the t-Channel Single Top-Quark Production Cross-Section with the ATLAS Detector at* $\sqrt{s} = 7$ *TeV*, Presented 01 Jun 2012, PhD thesis: Wuppertal U., 2012-11, URL: `https://cds.cern.ch/record/1501083` (cit. on pp. 32, 54).

[81] ATLAS Collaboration, *Performance of the ATLAS Trigger System in 2010*, Eur. Phys. J. C **72** (2012) 1849, arXiv: `1110.1530 [hep-ex]` (cit. on p. 33).

[82] ATLAS Collaboration, *Performance of the ATLAS muon trigger in pp collisions at* $\sqrt{s} = 8$ *TeV*, Eur. Phys. J. C **75** (2015) 120, arXiv: `1408.3179 [hep-ex]` (cit. on p. 33).

[83] T. Golling et al., *The ATLAS Data Quality Defect Database System*, Eur. Phys. J. C **72** (2012) 1960, arXiv: `1110.6119 [physics.ins-det]` (cit. on p. 33).

[84] S. Mergelmeyer, *Measurement of the Associated Production of a Single Top Quark and a W Boson in Single-Lepton Events with the ATLAS Detector*, PhD thesis: Rheinische Friedrich-Wilhelms-Universität Bonn, 2016, URL: `http://hss.ulb.uni-bonn.de/2016/4394/4394.pdf` (cit. on p. 34).

[85] M. A. Dobbs et al., “Les Houches guidebook to Monte Carlo generators for hadron collider physics”, *Physics at TeV colliders. Proceedings, Workshop, Les Houches, France, May 26-June 3, 2003*, 2004 411, arXiv: `hep-ph/0403045 [hep-ph]`, URL: `http://lss.fnal.gov/cgi-bin/find_paper.pl?conf-04-183` (cit. on p. 35).

[86] S. Agostinelli et al., *GEANT4: A Simulation toolkit*, Nucl. Instrum. Methods Phys. Res., A **506**.CERN-IT-2002-003. SLAC-PUB-9350. 3 (2002-07) 250, URL: `https://cds.cern.ch/record/602040` (cit. on p. 34).

[87] T. Sjostrand, S. Mrenna and P. Z. Skands, *A Brief Introduction to PYTHIA 8.1*, Comput. Phys. Commun. **178** (2008) 852, arXiv: `0710.3820 [hep-ph]` (cit. on pp. 34, 56).

[88] ATLAS Collaboration, *The ATLAS Simulation Infrastructure*, Eur. Phys. J. C **70** (2010) 823, arXiv: `1005.4568 [hep-ex]` (cit. on p. 34).

[89] R. Frederix, E. Re and P. Torrielli, *Single-top t-channel hadroproduction in the four-flavour scheme with POWHEG and aMC@NLO*, JHEP **09** (2012) 130, arXiv: `1207.5391 [hep-ph]` (cit. on p. 34).

[90] J. Alwall et al., *The automated computation of tree-level and next-to-leading order differential cross sections, and their matching to parton shower simulations*, JHEP **07** (2014) 079, arXiv: `1405.0301 [hep-ph]` (cit. on pp. 34, 35).

[91] B. P. Kersevan and E. Richter-Was, *The Monte Carlo event generator AcerMC versions 2.0 to 3.8 with interfaces to PYTHIA 6.4, HERWIG 6.5 and ARIADNE 4.1*, Comput. Phys. Commun. **184** (2013) 919, arXiv: `hep-ph/0405247 [hep-ph]` (cit. on p. 35).

[92] J. Pumplin et al., *New generation of parton distributions with uncertainties from global QCD analysis*, JHEP **07** (2002) 012, arXiv: `hep-ph/0201195 [hep-ph]` (cit. on p. 35).

[93] B. P. Kersevan and I. Hinchliffe, *A Consistent prescription for the production involving massive quarks in hadron collisions*, JHEP **09** (2006) 033, arXiv: `hep-ph/0603068 [hep-ph]` (cit. on p. 35).

[94] ATLAS Collaboration, *Measurement of the Inclusive and Fiducial Cross-Section of Single Top-Quark t-Channel Events in pp Collisions at* $\sqrt{s} = 8$ *TeV*, tech. rep., 2014, URL: `https://cds.cern.ch/record/1668960` (cit. on p. 35).

[95] T. Sjostrand, S. Mrenna and P. Z. Skands, *PYTHIA 6.4 Physics and Manual*, JHEP **05** (2006) 026, arXiv: `hep-ph/0603175 [hep-ph]` (cit. on p. 35).

[96] J. M. Butterworth, J. R. Forshaw and M. H. Seymour, *Multiparton interactions in photoproduction at HERA*, Z. Phys. C **72** (1996) 637, arXiv: `hep-ph/9601371 [hep-ph]` (cit. on p. 35).

[97] P. Z. Skands, *Tuning Monte Carlo Generators: The Perugia Tunes*, Phys. Rev. D **82** (2010) 074018, arXiv: `1005.3457 [hep-ph]` (cit. on p. 35).

[98] ATLAS Collaboration, *New ATLAS event generator tunes to 2010 data*, tech. rep., 2011, URL: `https://cds.cern.ch/record/1345343` (cit. on p. 35).

[99] S. Frixione and B. R. Webber, *Matching NLO QCD computations and parton shower simulations*, JHEP **06** (2002) 029, arXiv: `hep-ph/0204244 [hep-ph]` (cit. on p. 36).

[100] T. Gleisberg et al., *Event generation with SHERPA 1.1*, JHEP **02** (2009) 007, arXiv: `0811.4622 [hep-ph]` (cit. on p. 36).

[101] R. Gavin et al., *FEWZ 2.0: A code for hadronic Z production at next-to-next-to-leading order*, Comput. Phys. Commun. **182** (2011) 2388, arXiv: `1011.3540 [hep-ph]` (cit. on p. 36).

[102] R. Gavin et al., *W Physics at the LHC with FEWZ 2.1*, Comput. Phys. Commun. **184** (2013) 208, arXiv: `1201.5896 [hep-ph]` (cit. on p. 36).

[103] J. M. Campbell, R. K. Ellis and C. Williams, *Vector boson pair production at the LHC*, JHEP **07** (2011) 018, arXiv: `1105.0020 [hep-ph]` (cit. on p. 37).

[104] ATLAS Collaboration, *Estimation of non-prompt and fake lepton backgrounds in final states with top quarks produced in proton–proton collisions at* $\sqrt{s} = 8$ *TeV with the ATLAS Detector*, tech. rep., 2014, URL: `https://cds.cern.ch/record/1951336` (cit. on pp. 40, 52).

[105] *Particle-level objects and pseudo-top-quark definitions*, 2016, URL: `https://twiki.cern.ch/twiki/bin/view/LHCPhysics/ParticleLevelTopDefinitions` (cit. on p. 44).

[106] M. Cacciari, G. P. Salam and G. Soyez, *The Catchment Area of Jets*, JHEP **04** (2008) 005, arXiv: `0802.1188 [hep-ph]` (cit. on p. 45).

[107] ATLAS Collaboration, *Differential top-antitop cross-section measurements as a function of observables constructed from final-state particles using pp collisions at $\sqrt{s} = 7$ TeV in the ATLAS detector*, JHEP **06** (2015) 100, arXiv: `1502.05923 [hep-ex]` (cit. on p. 45).

[108] M. Feindt, *A Neural Bayesian Estimator for Conditional Probability Densities* (2004-02), arXiv: `physics/0402093` (cit. on pp. 47, 49).

[109] M. Feindt and U. Kerzel, *The NeuroBayes neural network package*, Nucl. Instrum. Meth. A **559** (2006) 190 (cit. on p. 47).

[110] C. d. Boor, *A practical guide to splines, Applied Mathematical Sciences* **27**, Springer, 1978 (cit. on p. 48).

[111] Y. LeCun et al., *Efficient BackProp, Neural Networks: tricks of the trade*, Springer, 1998 9 (cit. on p. 48).

[112] D. E. Rumelhart, G. E. Hinton and R. J. Williams, "Neurocomputing: Foundations of Research", ed. by J. A. Anderson and E. Rosenfeld, Cambridge, MA, USA: MIT Press, 1988, chap. Learning Representations by Back-propagating Errors 696, ISBN: 0-262-01097-6, URL: `http://dl.acm.org/citation.cfm?id=65669.104451` (cit. on p. 49).

[113] ATLAS Collaboration, *Jet energy measurement and its systematic uncertainty in proton–proton collisions at $\sqrt{s} = 7$ TeV with the ATLAS detector*, Eur. Phys. J. C **75** (2015) 17, arXiv: `1406.0076 [hep-ex]` (cit. on p. 51).

[114] ATLAS Collaboration, *Jet Energy Resolution and Selection Efficiency Relative to Track Jets from In-situ Techniques with the ATLAS Detector Using Proton–Proton Collisions at a Center of Mass Energy $\sqrt{s} = 7$ TeV*, tech. rep., 2010, URL: `https://cds.cern.ch/record/1281311` (cit. on p. 51).

[115] J. Butterworth et al., *PDF4LHC recommendations for LHC Run II*, J. Phys. G **43** (2016) 023001, arXiv: `1510.03865 [hep-ph]` (cit. on p. 53).

[116] F. James and M. Roos, *Minuit: A System for Function Minimization and Analysis of the Parameter Errors and Correlations*, Comput. Phys. Commun. **10** (1975) 343 (cit. on p. 55).

[117] ATLAS Collaboration, *Comprehensive measurements of t-channel single top-quark production cross sections at $\sqrt{s} = 7$ TeV with the ATLAS detector*, Phys. Rev. D **90** (2014) 112006, arXiv: `1406.7844 [hep-ex]` (cit. on p. 56).

[118] J. Bellm et al., *Herwig 7.0/Herwig++ 3.0 release note*, Eur. Phys. J. C **76**.4 (2016) 196, arXiv: `1512.01178 [hep-ph]` (cit. on p. 56).

[119] M. Brucherseifer, F. Caola and K. Melnikov, *On the NNLO QCD corrections to single-top production at the LHC*, Phys. Lett. B **736** (2014) 58, arXiv: `1404.7116 [hep-ph]` (cit. on p. 59).

[120] G. D'Agostini, *A multidimensional unfolding method based on Bayes' theorem*, Nucl. Instrum. Meth. A **362**.2-3 (1995) 487 (cit. on p. 78).

[121] T. Adye, *Unfolding algorithms and tests using RooUnfold* (2011), arXiv: `1105.1160 [physics.data-an]` (cit. on p. 78).

[122] A. Höcker and V. Kartvelishvili, *SVD approach to data unfolding*, Nucl. Instrum. Meth. A **372** (1996) 469, arXiv: `hep-ph/9509307 [hep-ph]` (cit. on p. 79).

[123] N. Kidonakis, *Top-quark transverse-momentum distributions in t-channel single-top production*, Phys. Rev. D **88**.3 (2013) 031504, arXiv: `1306.3592 [hep-ph]` (cit. on pp. 103, 105).

APPENDIX A

Simulated samples

Sample	Dataset ID	$\sigma \times \mathcal{B}$ [pb]	k-factor	Generator	Events
tq (ℓ+jets)	110070	17.5	1.05	POWHEG-BOX +PYTHIA 6	5M
$\bar{t}q$ (ℓ+jets)	110071	9.4	1.06	POWHEG-BOX +PYTHIA 6	5M
tq (ℓ+jets), radLo	110242	15.9	1.16	POWHEG-BOX +PYTHIA 6	2M
$\bar{t}q$ (ℓ+jets), radLo	110052	8.5	1.17	POWHEG-BOX +PYTHIA 6	2M
tq (ℓ+jets), radHi	110250	17.9	1.03	POWHEG-BOX +PYTHIA 6	2M
$\bar{t}q$ (ℓ+jets), radHi	110060	9.7	1.03	POWHEG-BOX +PYTHIA 6	2M
tq (ℓ+jets)	110086	17.5	1.05	POWHEG-BOX +HERWIG	5M
$\bar{t}q$ (ℓ+jets)	110087	9.4	1.06	POWHEG-BOX +HERWIG	5M
$tq + \bar{t}q$ (ℓ+jets)	110121	26.6	1.07	MADGRAPH5_aMC@NLO +HERWIG	10M
$tq + \bar{t}q$ (ℓ+jets), $\mu = 115$ GeV	110069	27.3	1.04	ACERMC +PYTHIA 6	15M

Table A.1: Monte Carlo samples for signal process used in this analysis.

Sample	Dataset ID	$\sigma \times \mathcal{B}$ [pb]	k-factor	Generator	Events
$t\bar{b}$ (ℓ+jets)	110119	1.6	1.11	Powheg-Box +Pythia 6	6M
$t\bar{b}$ (ℓ+jets), radLo	110045	1.7	1.07	Powheg-Box +Pythia 6	1M
$t\bar{b}$ (ℓ+jets), radHi	110040	1.7	1.07	Powheg-Box +Pythia 6	1M
$t\bar{b}$ (e+jets)	108343	0.6	1.08	MC@NLO +Herwig	1M
$t\bar{b}$ (μ+jets)	108344	0.6	1.08	MC@NLO +Herwig	1M
$t\bar{b}$ (τ+jets)	108345	0.6	1.08	MC@NLO +Herwig	1M
Wt (all decays)	110140	20.5	1.09	Powheg-Box +Pythia 6	20M
Wt (all decays), radLo	110051	21.2	1.06	Powheg-Box +Pythia 6	1M
Wt (all decays), radHi	110046	20.1	1.11	Powheg-Box +Pythia 6	1M
Wt (all decays)	110144	20.5	1.09	Powheg-Box +Herwig	10M
Wt (all decays)	108346	20.6	1.08	MC@NLO +Herwig	5M
$t\bar{t}$ (no all had.), $h_{\text{damp}} = m_{\text{t}}$	110404	114	1.20	Powheg-Box +Pythia 6	100M
$t\bar{t}$ (no all had.), $h_{\text{damp}} = \infty$	110401	114	1.20	Powheg-Box +Pythia 6	15M
$t\bar{t}$ (no all had.), $h_{\text{damp}} = m_{\text{t}}$, radLo	110407	137	1.00	Powheg-Box +Pythia 6	15M
$t\bar{t}$ (no all had.), $h_{\text{damp}} = 2 * m_{\text{t}}$, radHi	110408	137	1.00	Powheg-Box +Pythia 6	15M
$t\bar{t}$ (no all had.), $h_{\text{damp}} = \infty$	105860	115.6	1.19	Powheg-Box +Herwig	30M
$t\bar{t}$ (no all had.)	105200	112.9	1.22	MC@NLO +Herwig	30M

Table A.2: Monte Carlo samples for top-quark background processes used in this analysis.

Sample	Dataset ID	$\sigma \times \mathcal{B}$ [pb]	k-factor	Generator	Events
$W \to e\nu$	167742	10295	1.10	Sherpa	50M
$W \to e\nu$ b-filtered	167740	140	1.10	Sherpa	15M
$W \to e\nu$ c-filtered	167741	538	1.10	Sherpa	10M
$W \to \mu\nu$	167745	10368	1.10	Sherpa	50M
$W \to \mu\nu$ b-filtered	167741	140	1.10	Sherpa	15M
$W \to \mu\nu$ c-filtered	167744	466	1.10	Sherpa	10M
$W \to \tau\nu$	167748	10327	1.10	Sherpa	50M
$W \to \tau\nu$ b-filtered	167742	140	1.10	Sherpa	15M
$W \to \tau\nu$ c-filtered	167747	506	1.10	Sherpa	10M
$Z \to e^+e^-$	167751	764	1.12	Sherpa	1M
$Z \to e^+e^-$ b-filtered	167749	31	1.12	Sherpa	4M
$Z \to e^+e^-$ c-filtered	167750	314	1.12	Sherpa	3M
$Z \to \mu^+\mu^-$	167754	764	1.12	Sherpa	1M
$Z \to \mu^+\mu^-$ b-filtered	167752	31	1.12	Sherpa	4M
$Z \to \mu^+\mu^-$ c-filtered	167753	314	1.12	Sherpa	3M
$Z \to \tau^+\tau^-$	167757	764	1.12	Sherpa	1M
$Z \to \tau^+\tau^-$ b-filtered	167755	31	1.12	Sherpa	4M
$Z \to \tau^+\tau^-$ c-filtered	167756	314	1.12	Sherpa	3M
$WW \to e\nu q\bar{q}$	183734	7	1.06	Sherpa	3.2M
$WW \to \mu\nu q\bar{q}$	183736	7	1.06	Sherpa	3.2M
$WW \to \tau\nu q\bar{q}$	183738	7	1.06	Sherpa	3.2M
$ZZ \to e^+e^-q\bar{q}$	183586	0.2	1.00	Sherpa	120K
$ZZ \to \mu^+\mu^-q\bar{q}$	183588	0.2	1.00	Sherpa	120K
$WZ \to e\nu q\bar{q}$	183735	2	1.05	Sherpa	840K
$WZ \to \mu\nu q\bar{q}$	183737	2	1.05	Sherpa	840K
$WZ \to \tau\nu q\bar{q}$	183739	2	1.05	Sherpa	840K
$ZW \to e^+e^-q\bar{q}$	183585	1.5	1.05	Sherpa	700K
$ZW \to \mu^+\mu^-q\bar{q}$	183587	1.5	1.05	Sherpa	700K
JF17 (dijet $p_{\mathrm{T}} > 17\,\mathrm{GeV}$)	129160	93,052,540	1.00	Pythia 8	110M

Table A.3: Monte Carlo samples for W+jets, Z+jets, VV and multijet processes used in this analysis.

APPENDIX B

Optimisation of the cut on the neural network discriminant

The cut on the neural network discriminant at $O_{\text{NN}} > 0.8$ is investigated to ensure that it is optimal. This is done by comparing the uncertainties for all absolute differential cross-sections to the ones done with different O_{NN} cuts. Two different cuts, one is below and the other one is above the current cut, are checked. A cut of $O_{\text{NN}} > 0.7$ and of $O_{\text{NN}} > 0.9$ are chosen. This optimisation is performed at particle level only for both networks. $p_{\text{T}}(\hat{t})$, $y(\hat{t})$ and $p_{\text{T}}(\hat{j})$ are with the default neural network, while $|y(\hat{j})|$ is with the neural network without $|\eta(j)|$.

Figures 8.1 and 8.6 show the signal-to-background ratios for top (anti)quark events with the default network and the network without $|\eta(j)|$, respectively. For the default neural network, $S/B \sim 1.1$ is obtained with $O_{\text{NN}} > 0.7$, $S/B \sim 1.7$ with $O_{\text{NN}} > 0.8$ and $S/B \sim 3.3$ with $O_{\text{NN}} > 0.9$. For the neural network without $|\eta(j)|$, $S/B \sim 0.8$ is achieved with $O_{\text{NN}} > 0.7$, $S/B \sim 1.3$ with $O_{\text{NN}} > 0.8$ and $S/B \sim 3.6$ with $O_{\text{NN}} > 0.9$.

Table B.1 summarises the total uncertainty for $p_{\text{T}}(\hat{t})$ for the three different O_{NN} cuts, Table B.2 for $y(\hat{t})$, Table B.3 for $p_{\text{T}}(\hat{j})$ and Table B.4 for $|y(\hat{j})|$. The total uncertainties with $O_{\text{NN}} > 0.9$ are highest over all variables; that is mainly due to low statistics. Comparing $O_{\text{NN}} > 0.7$ to $O_{\text{NN}} > 0.8$, total uncertainties are overall smaller with $O_{\text{NN}} > 0.8$. The uncertainty due to data statistics is smaller with $O_{\text{NN}} > 0.7$. On the other hand some systematic uncertainties become more significant. In conclusion, the $O_{\text{NN}} > 0.8$ performs better.

The PDF uncertainty on the signal sample is evaluated by comparing the bias of different PDF MC signal sets: CT10, MSTW2008nlo and NNPDF2.3. The largest difference is set as both the negative and positive PDF uncertainty bin-by-bin. For the PDF uncertainty on the background processes, the unfolded cross-section with the CT10 PDF set is compared to the result with the MSTW2008nl PDF set and to the one with the NNPDF2.3 PDF set. The largest difference is also taken as both the negative and positive PDF uncertainty bin-by-bin. The PDF uncertainties using the PDF4LHC15 PDF set are smaller, due to better prescription. Hence, the quoted total uncertainties with $O_{\text{NN}} > 0.8$ are larger than the final total uncertainties shown in Section 11.2.

	Total uncertainty [%]						
	Bin 1 [%]	Bin 2 [%]	Bin 3 [%]	Bin 4 [%]	Bin 5 [%]	Bin 6 [%]	Bin 7 [%]
$O_{\mathrm{NN}} > 0.7$							
tq	+13/-17	±12	+8/-9	±10	±10	+16/-15	+29/-34
$\bar{t}q$	±20	+13/-12	±12	±15	+14/-15	±24	
$O_{\mathrm{NN}} > 0.8$							
tq	±13	±11	±9	+11/-10	±10	±14	+23/-22
$\bar{t}q$	±18	±13	±10	±19	±13	+29/-28	
$O_{\mathrm{NN}} > 0.9$							
tq	+18/-23	+20/-19	+13/-11	+13/-12	+14/-13	+28/-34	+39/-38
$\bar{t}q$	±29	±15	±11	±19	±19	±21	

Table B.1: Total uncertainty for absolute differential cross-section for $p_{\mathrm{T}}(\hat{t})$ with the 3 different cuts on O_{NN} for tq and $\bar{t}q$ events.

	Total uncertainty [%]						
	Bin 1 [%]	Bin 2 [%]	Bin 3 [%]	Bin 4 [%]	Bin 5 [%]	Bin 6 [%]	Bin 7 [%]
$O_{\mathrm{NN}} > 0.7$							
tq	±9	±10	±10	±8	±10	±12	±10
$\bar{t}q$	±11	±13	±13	±12	±12	±16	±16
$O_{\mathrm{NN}} > 0.8$							
tq	±8	+9/-8	±10	±8	±10	±11	±10
$\bar{t}q$	±10	±12	±12	±11	±11	±12	±14
$O_{\mathrm{NN}} > 0.9$							
tq	±9	±12	±14	+9/-10	±15	±16	+12/-13
$\bar{t}q$	+15/-14	+16/-15	±16	±13	±11	+18/-12	+18/-12

Table B.2: Total uncertainty for absolute differential cross-section for $|y(\hat{t})|$ with the 3 different cuts on O_{NN} for tq and $\bar{t}q$ events

	Total uncertainty [%]					
	Bin 1 [%]	Bin 2 [%]	Bin 3 [%]	Bin 4 [%]	Bin 5 [%]	Bin 6 [%]
$O_{\mathrm{NN}} > 0.7$						
tq	+13/-12	±11	±10	±11	+9/-10	±12
$\bar{t}q$	±13	±17	+16/-17	±15	±16	+25/-29
$O_{\mathrm{NN}} > 0.8$						
tq	+12/-11	±12	+11/-10	±10	±10	+12/-11
$\bar{t}q$	±11	+13/-14	±17	±15	+15/-14	+25/-22
$O_{\mathrm{NN}} > 0.9$						
tq	±11	+15/-16	+18/-15	+16/-15	±15	±17
$\bar{t}q$	±12	+16/-15	+21/-20	+22/-21	+18/-17	+28/-27

Table B.3: Total uncertainty for absolute differential cross-section for $p_{\mathrm{T}}(\hat{j})$ with the 3 different cuts on O_{NN} for tq and $\bar{t}q$ events

	Total uncertainty [%]					
	Bin 1 [%]	Bin 2 [%]	Bin 3 [%]	Bin 4 [%]	Bin 5 [%]	Bin 6 [%]
$O_{\mathrm{NN2}} > 0.7$						
tq	±23	+17/-16	±11	±8	±7	±9
$\bar{t}q$	±36	±20	±11	±14	±9	±11
$O_{\mathrm{NN2}} > 0.8$						
tq	±20	+13/-11	±11	±7	±7	±9
$\bar{t}q$	±25	±18	+11/-12	±11	±9	±11
$O_{\mathrm{NN2}} > 0.9$						
tq	+44/-39	+38/-36	+33/-34	±19	±17	+18/-19
$\bar{t}q$	+126/-128	+29/-28	±21	±21	+22/-21	+25/-24

Table B.4: Total uncertainty for absolute differential cross-section for $|y(\hat{j})|$ with the 3 different cuts on O_{NN2} for tq and $\bar{t}q$ events

APPENDIX C

Distributions of the input variables after cutting on the O_{NN2} discriminant

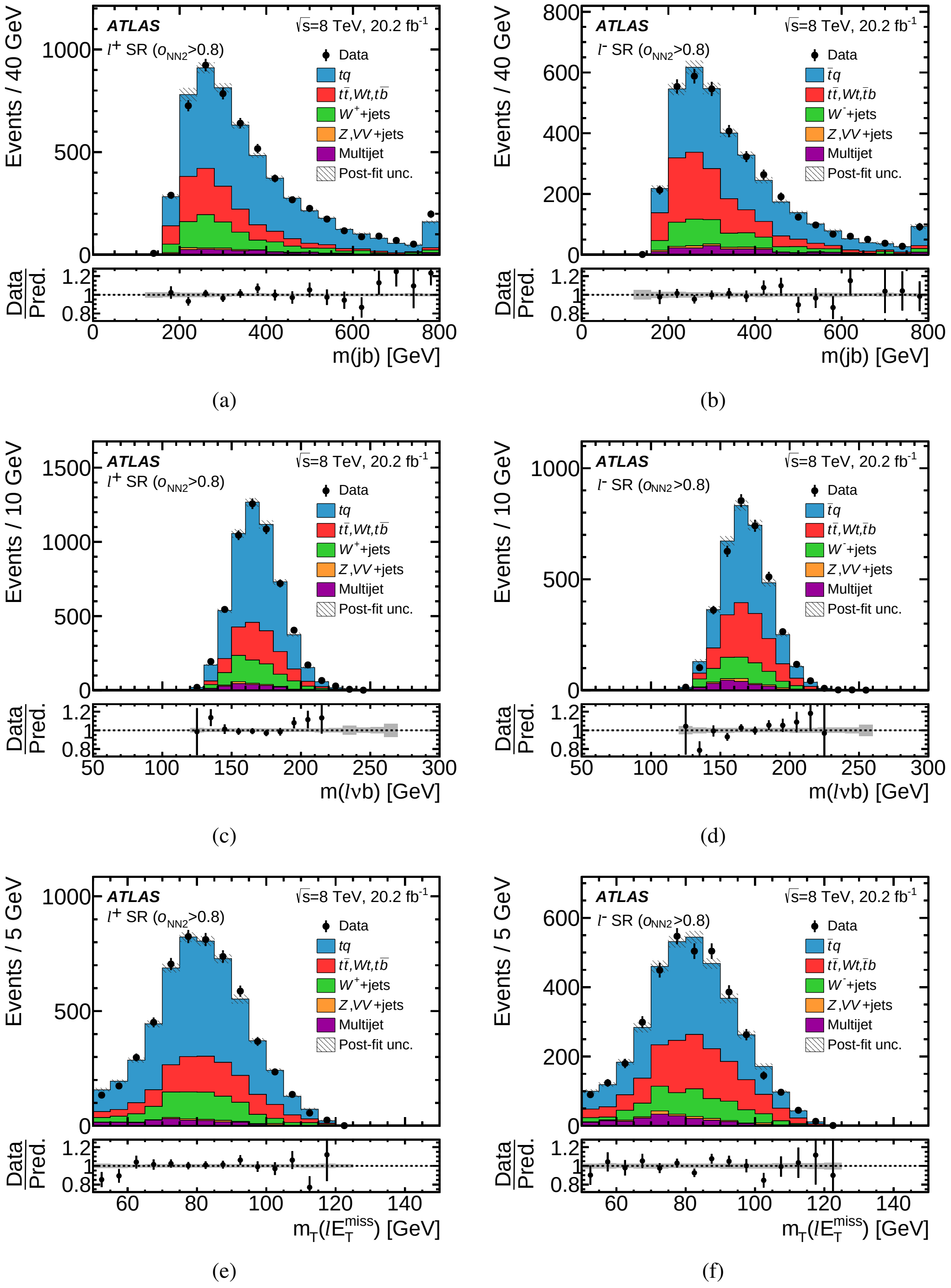

(a) (b) (c) (d) (e) (f)

Figure C.1: Observed distributions of the first three input variables to the neural network without $|\eta(j)|$ in the signal region (SR), after a cut of $O_{\mathrm{NN2}} > 0.8$ on the network output. The distributions are compared to the model obtained from simulated events. The simulated distributions are normalised to the event rates obtained by the fit to the discriminants. The definitions of the variables can be found in Table 7.1. The hatched uncertainty band represents the total uncertainty in the rates of all processes after the fit and the bin-by-bin MC statistical uncertainty, added in quadrature. Events beyond the x-axis range in (a) and (b) are included in the last bin. The lower panels show the ratio between the observed and the expected number of events in each bin. [2]

APPENDIX D

Global selection efficiency and resolution

The chosen binning of each variable is discussed in Section 8.2. This appendix shows its ingredients, used to determine the suitable binning. They are the selection efficiencies and profile of residuals plotted against the corresponding parton(particle)-level variable. The efficiency is defined in Equation 9.3 for parton level and Equation 9.7 for particle level.

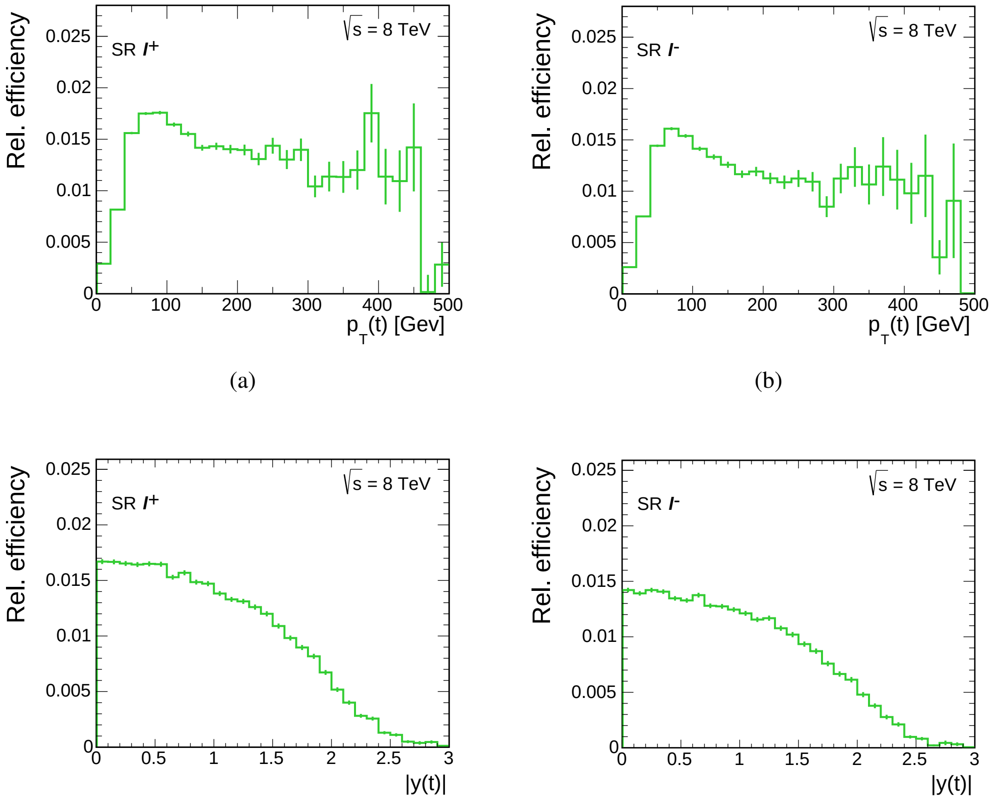

(a) (b)

(c) (d)

Figure D.1: Selection efficiencies of (a,b) $p_{\mathrm{T}}(t)$ and (c,d) $|y(t)|$ for the (a,c) ℓ^{+} and (b,d) ℓ^{-} channels for parton level.

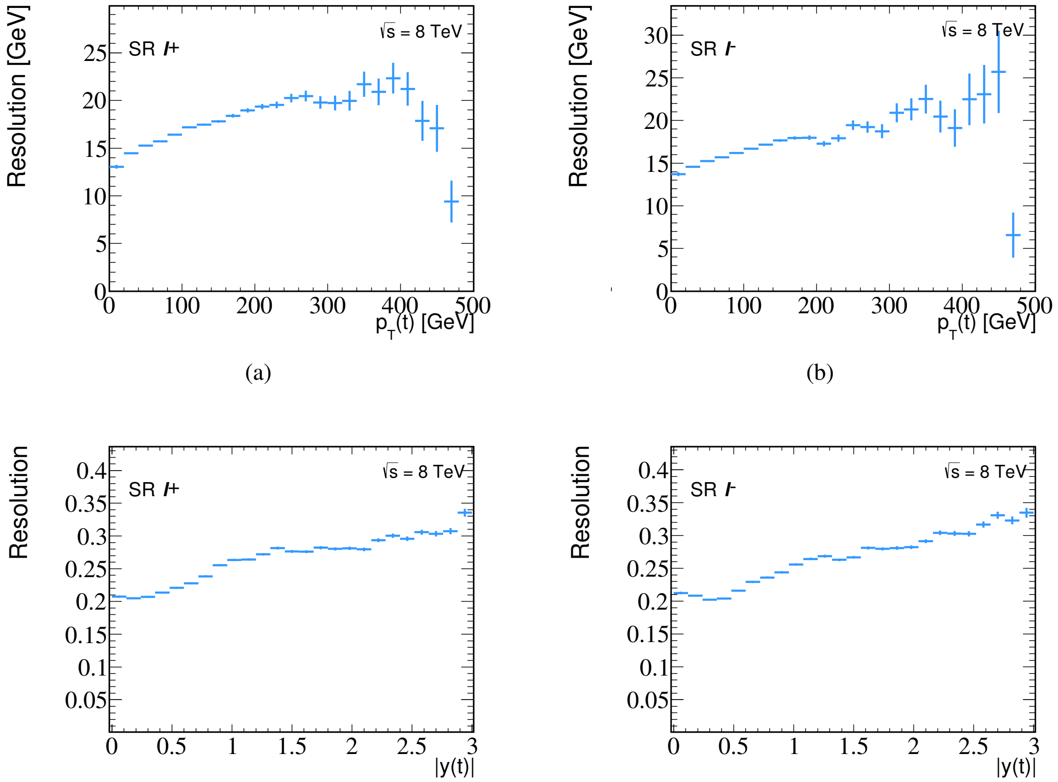

(a)

(b)

(c)

(d)

Figure D.2: Resolution (width of Gaussian fit) of (a,b) $p_{\mathrm{T}}(t)$ and (c,d) $|y(t)|$ for the (a,c) ℓ^{+} and (b,d) ℓ^{-} channels for parton level.

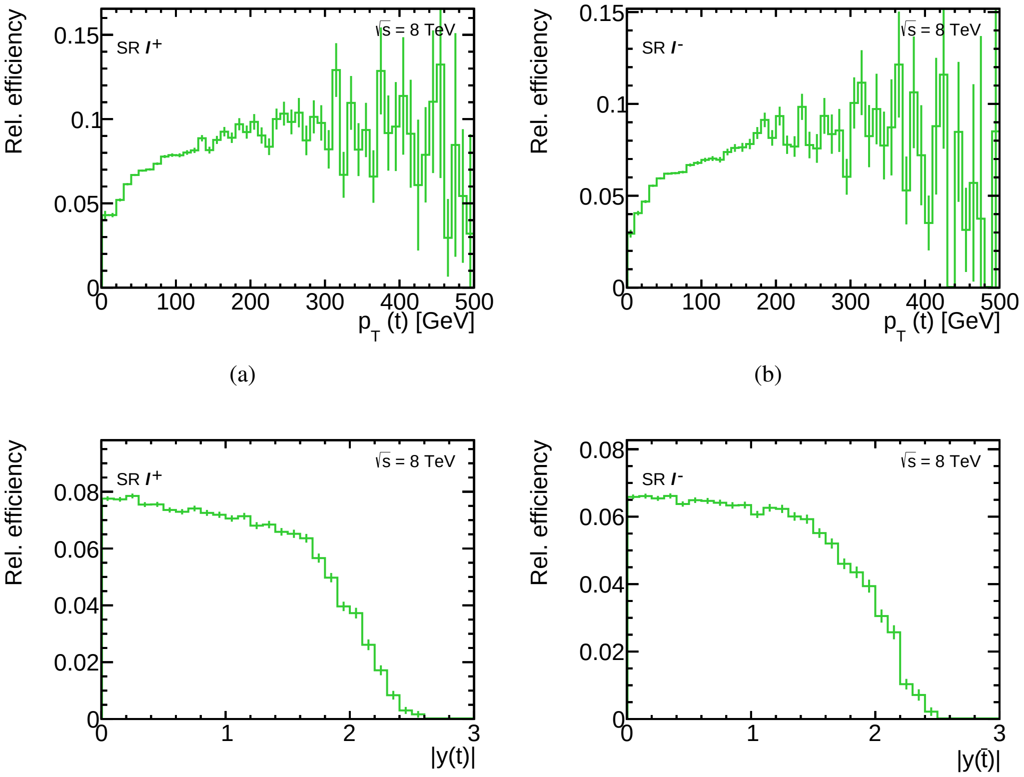

(a) (b) (c) (d)

Figure D.3: Selection efficiencies of (a,b) $p_{\mathrm{T}}(\hat{t})$ and (c,d) $|y(\hat{t})|$ for the (a,c) ℓ^+ and (b,d) ℓ^- channels for particle level.

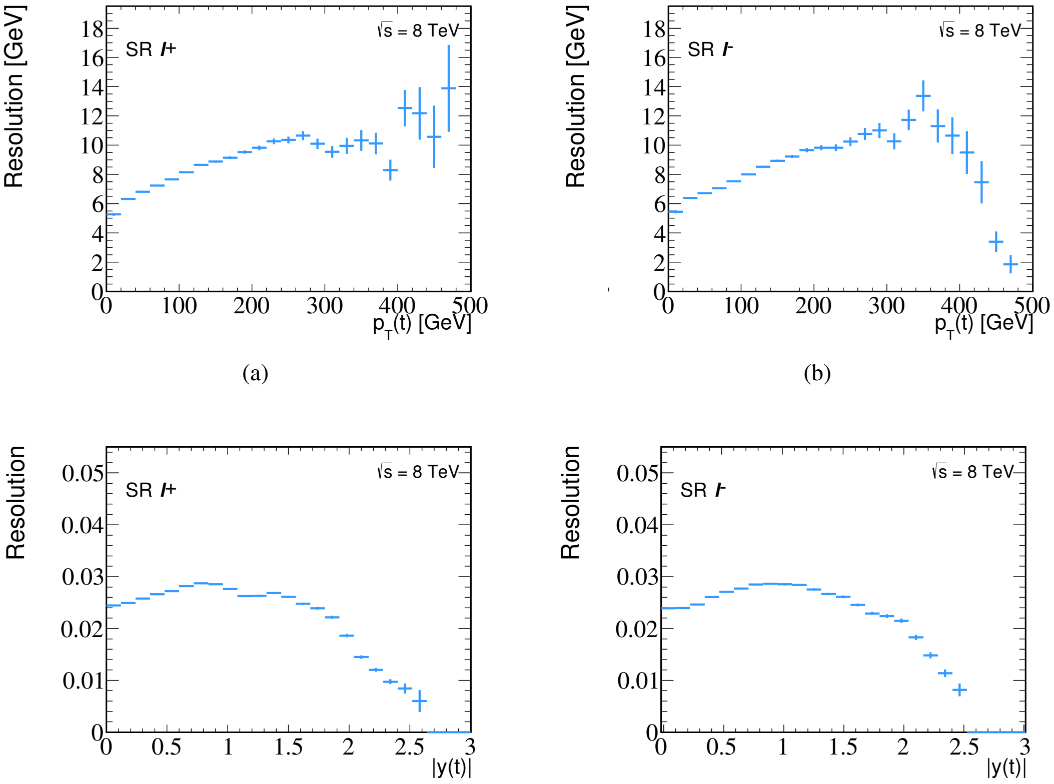

(a) (b)

(c) (d)

Figure D.4: Resolution (width of Gaussian fit) of (a,b) $p_T(\hat{t})$ and (c,d) $|y(\hat{t})|$ for the (a,c) ℓ^+ and (b,d) ℓ^- channels for particle level.

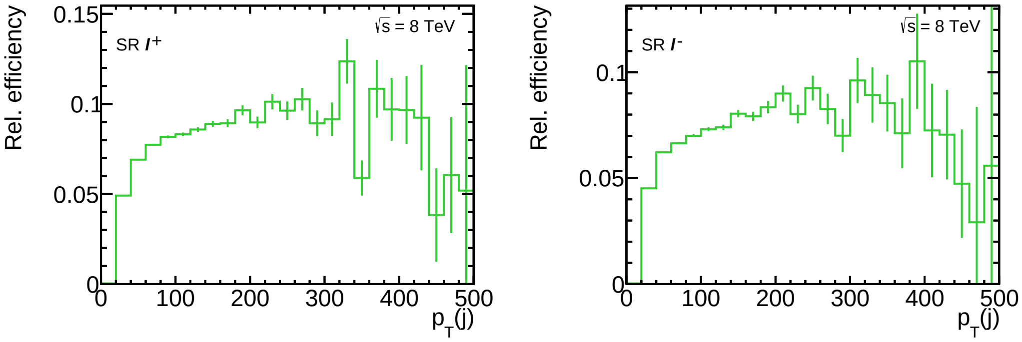

(a) (b)

Figure D.5: Selection efficiencies of $p_T(\hat{j})$ for the (a) ℓ^+ and (b) ℓ^- channels for particle level.

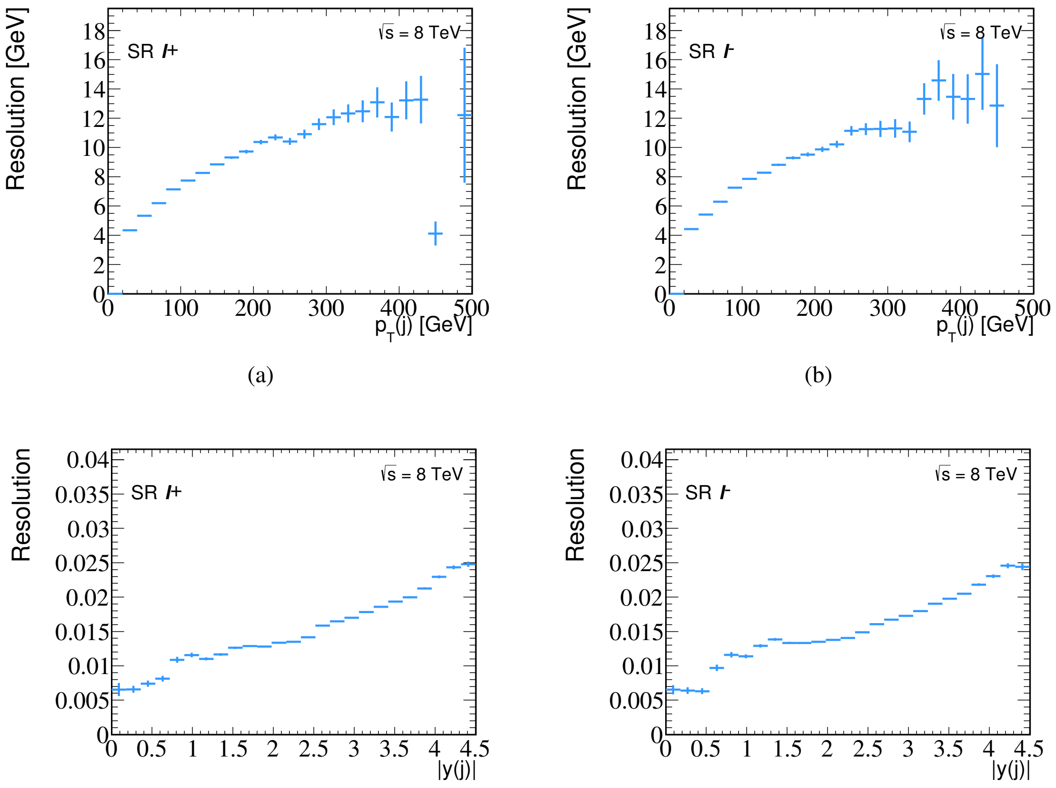

(a)

(b)

(c)

(d)

Figure D.6: Resolution (width of Gaussian fit) of (a,b) $p_{\mathrm{T}}(\hat{j})$ and (c,d) $|y(\hat{j})|$ for the (a,c) ℓ^{+} and (b,d) ℓ^{-} channels for particle level.

APPENDIX E

Distributions for ℓ^- channel from Chapter 9

E.1 Particle-level migration matrices and correction factors

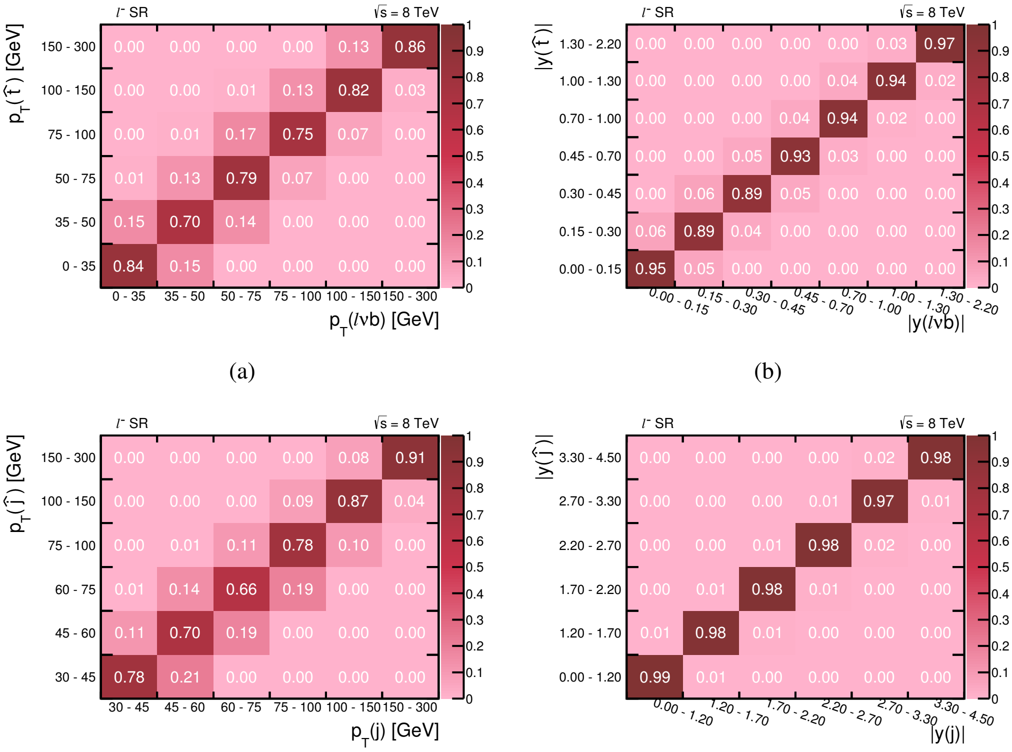

(a) (b)

(c) (d)

Figure E.1: Migration matrix for (a) $p_{\mathrm{T}}^{\bar{t}q}(\hat{t})$, (b) $|y^{\bar{t}q}(\hat{t})|$ (c) $p_{\mathrm{T}}^{\bar{t}q}(\hat{j})$ and (d) $|y^{\bar{t}q}(\hat{j})|$ for particle level. The particle-level variable is shown on the y-axis and the reconstruction-level variable is shown on the x-axis.

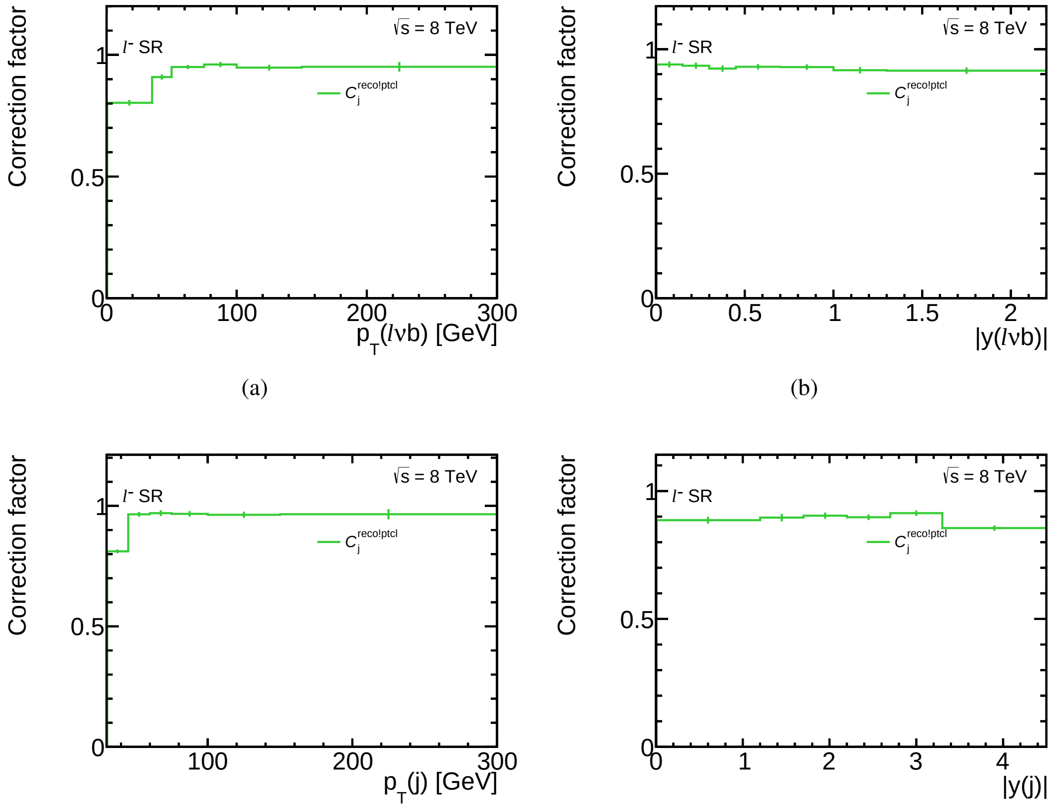

(a) (b)

(c) (d)

Figure E.2: Correction factor $C_j^{\mathrm{reco!ptcl}}$ for (a) $p_{\mathrm{T}}(\ell\nu b)$, (b) $|y(\ell\nu b)|$, (c) $p_{\mathrm{T}}(j)$ and (d) $|y(j)|$ at reconstruction level for $\bar{t}q$ events.

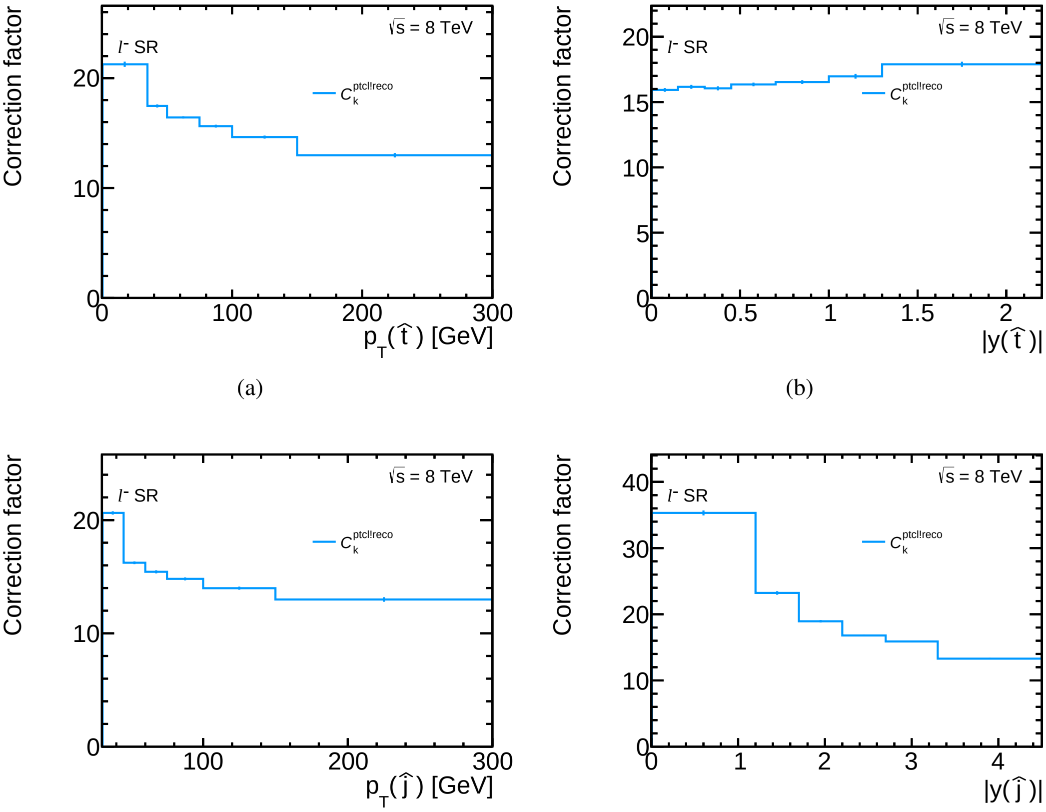

(a)

(b)

(c)

(d)

Figure E.3: Correction factor $C_k^{\text{ptcl!reco}}$ for (a) $p_\text{T}(\hat{t})$, (b) $|y(\hat{t})|$, (c) $p_\text{T}(\hat{j})$ and (d) $|y(\hat{j})|$ for $\bar{t}q$ events.

E.2 Bias of the unfolded cross-section as a function of number of iterations

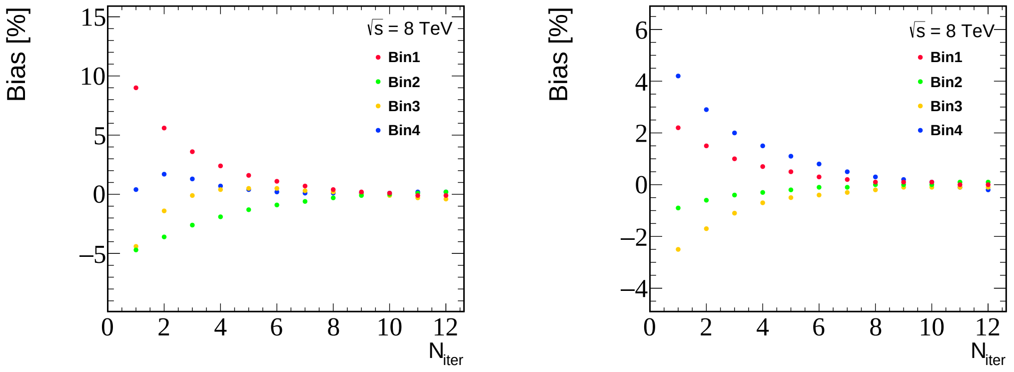

(a) $p_{\mathrm{T}}^{\bar{t}q}(t)$ (b) $|y^{\bar{t}q}(t)|$

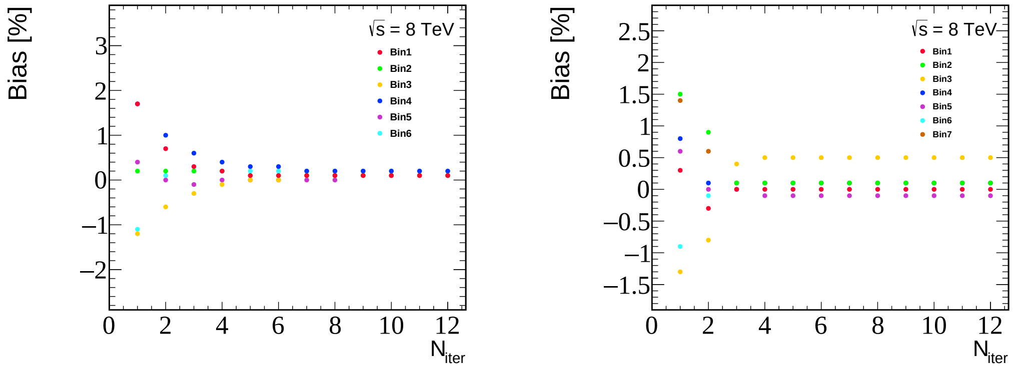

(c) $p_{\mathrm{T}}^{\bar{t}q}(\hat{t})$ (d) $|y^{\bar{t}q}(\hat{t})|$

Figure E.4: Bias of the unfolded cross-section after each iteration for each bin in %, scanning the number of iterations from 1 to 12 for (a) $p_{\mathrm{T}}^{\bar{t}q}(t)$, (b) $|y^{\bar{t}q}(t)|$, (c) $p_{\mathrm{T}}^{\bar{t}q}(\hat{t})$ and (d) $|y^{\bar{t}q}(\hat{t})|$.

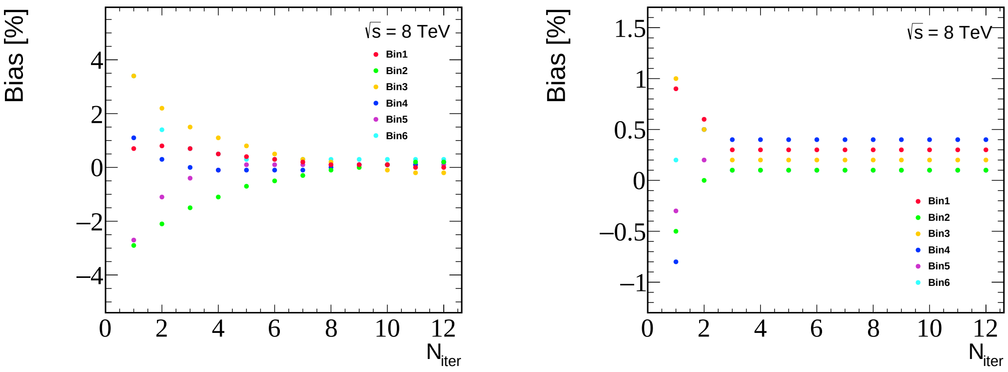

(a) $p_{\mathrm{T}}^{\bar{t}q}(\hat{j})$ (b) $|y^{\bar{t}q}(\hat{j})|$

Figure E.5: Bias of the unfolded cross-section after each iteration for each bin in %, scanning the number of iterations from 1 to 12 for (a) $p_{\mathrm{T}}^{\bar{t}q}(\hat{j})$ and (b) $|y^{\bar{t}q}(\hat{j})|$.

E.3 Tests of the unfolding procedure

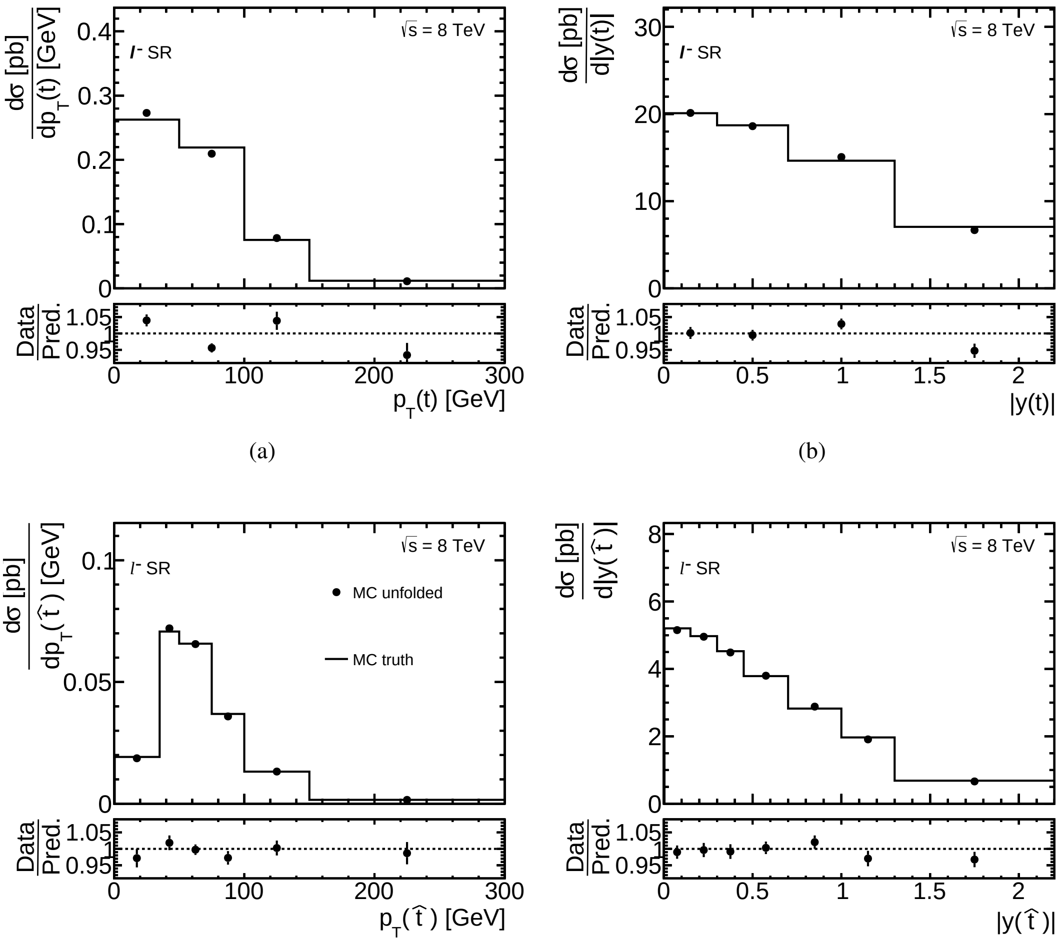

(a) (b)

(c) (d)

Figure E.6: Closure of the unfolding procedure by unfolding one half of the signal MC sample with the migration matrix and efficiency built with the other half. Closure is shown for (a) $p_{\mathrm{T}}^{\bar{t}q}(t)$, (b) $|y^{\bar{t}q}(t)|$, (c) $p_{\mathrm{T}}^{\bar{t}q}(\hat{t})$ and (d) $|y^{\bar{t}q}(\hat{t})|$. The error bar represents the uncertainty due to the size of the signal MC sample. The ratio is the unfolded distribution over the generated distribution shown in the bottom plot.

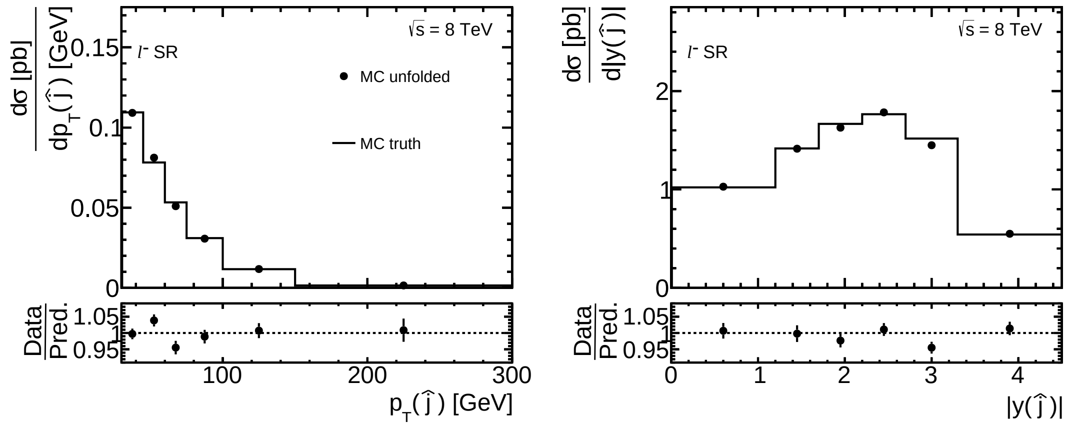

(a)

(b)

Figure E.7: Closure of the unfolding procedure by unfolding one half of the signal MC sample with the migration matrix and efficiency built with the other half. Closure is shown for (a) $p_{\mathrm{T}}^{\bar{t}q}(\hat{j})$ and (b) $|y^{\bar{t}q}(\hat{j})|$. The error bar represents the uncertainty due to the size of the signal MC sample. The ratio is the unfolded distribution over the generated distribution shown in the bottom plot.

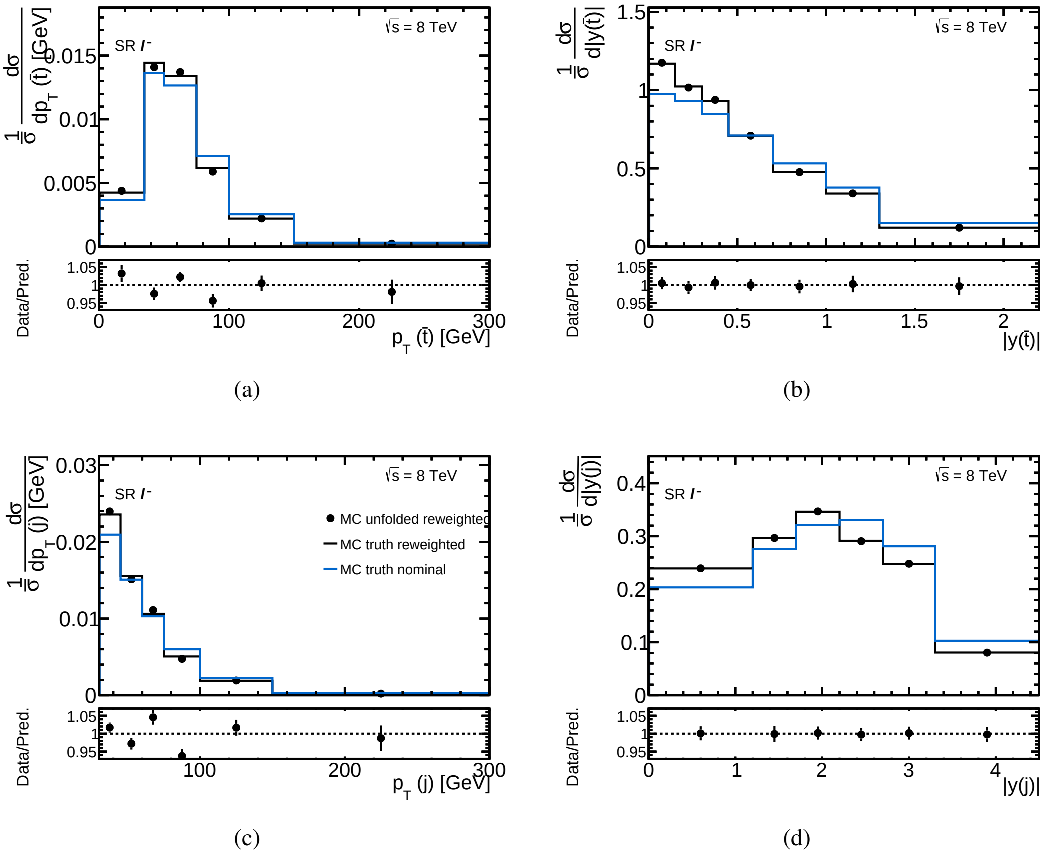

(a) (b)

(c) (d)

Figure E.8: Unfolded distribution of reweighted sample for (a) $p_T^{\bar{t}q}(\hat{t})$, (b) $|y^{\bar{t}q}(\hat{t})|$, (c) $p_T^{\bar{t}q}(\hat{j})$ and (d) $|y^{\bar{t}q}(\hat{j})|$. The unfolded reweighted distribution (black dots) is compared to the reweighted generator-level (black line) and the nominal generator-level (blue line) distribution. The ratio of the unfolded reweighted distribution to the reweighted generator-level distribution is shown in the bottom plot.

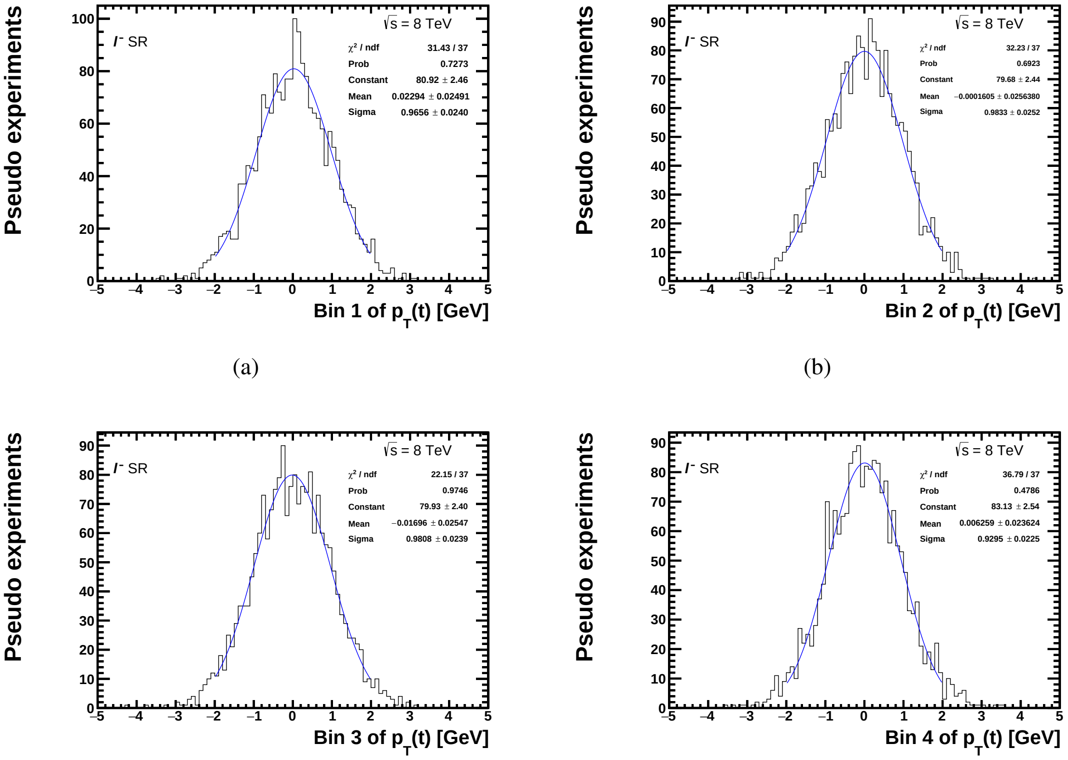

(a) (b)

(c) (d)

Figure E.9: Pull distributions of 2000 pseudo experiments for all bins of the $p_{\mathrm{T}}^{\bar{t}q}(t)$ variable used to unfold to parton level.

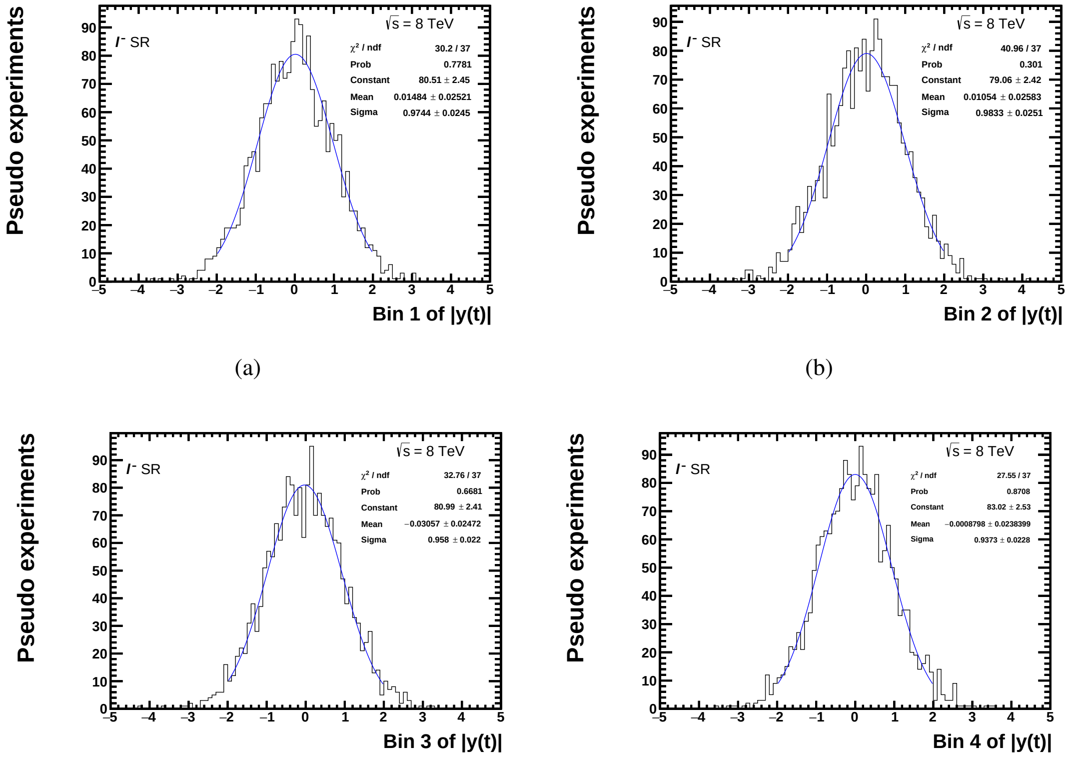

(a)

(b)

(c)

(d)

Figure E.10: Pull distributions of 2000 pseudo experiments for all bins of the $|y^{\bar{t}q}(t)|$ variable used to unfold to parton level.

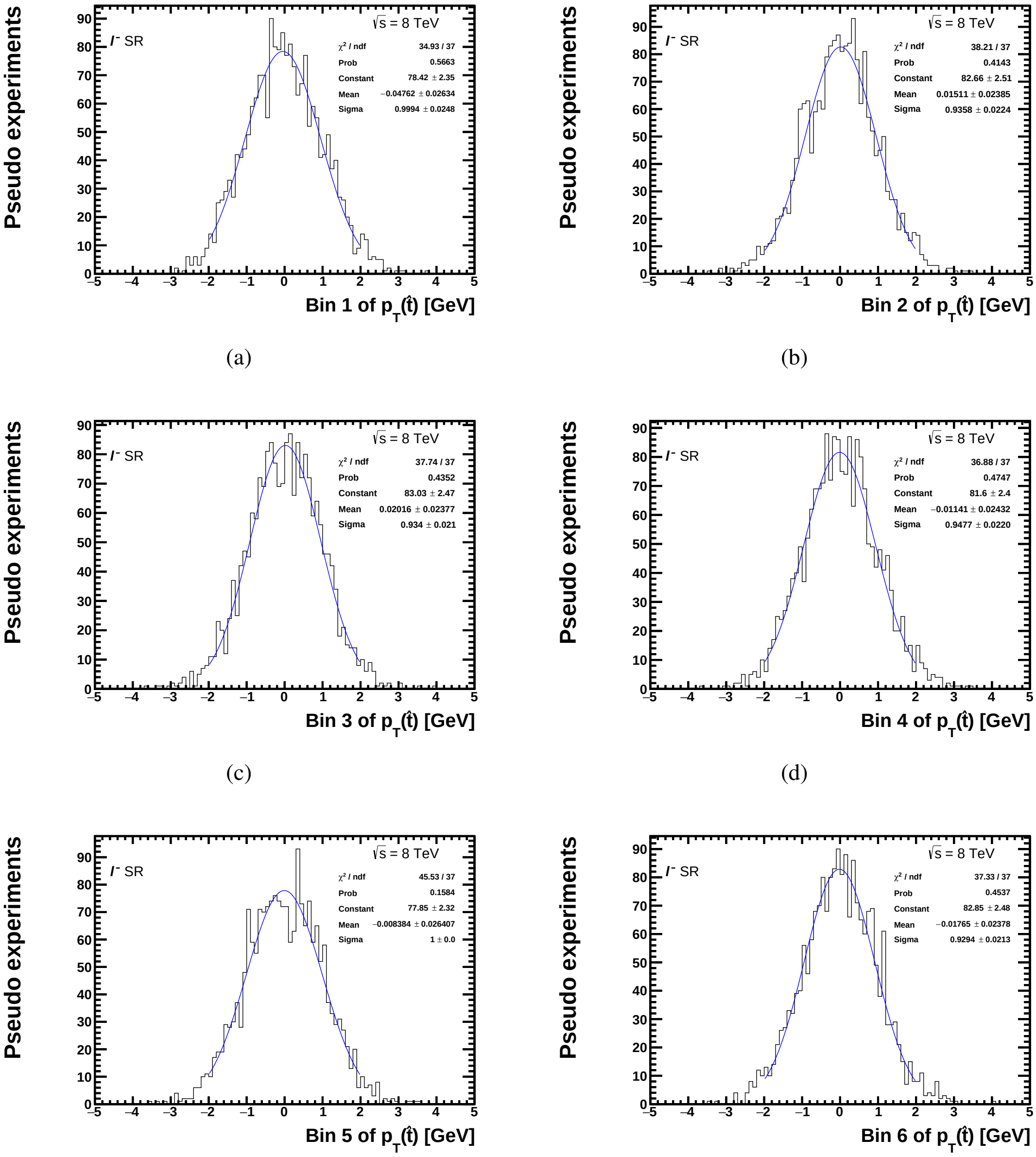

(a)

(b)

(c)

(d)

(e)

(f)

Figure E.11: Pull distributions of 2000 pseudo experiments for all bins of the $p_{\mathrm{T}}^{\bar{t}q}(\hat{t})$ variable used to unfold to particle level.

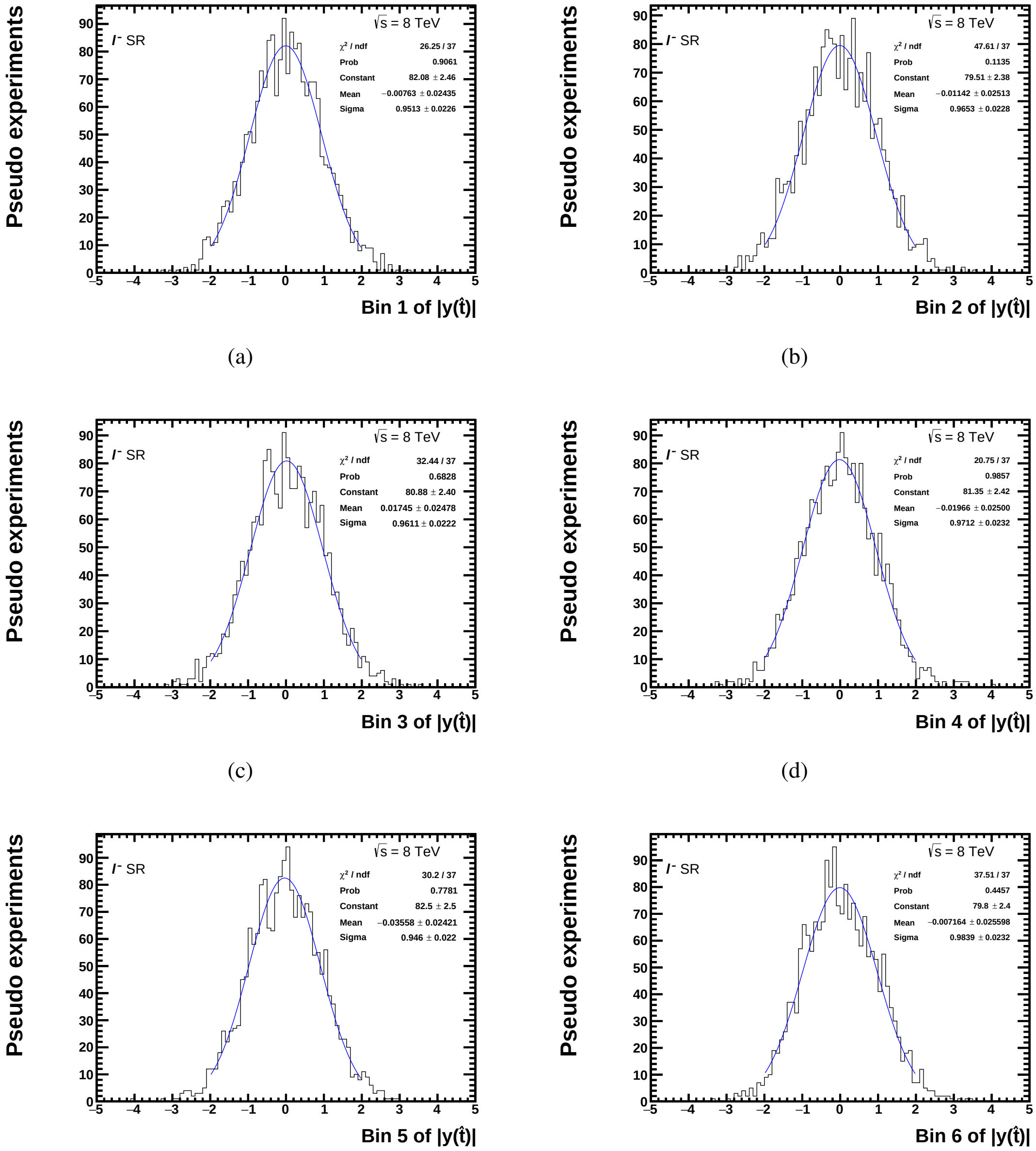

(a) (b)

(c) (d)

(e) (f)

Figure E.12: Pull distributions of 2000 pseudo experiments for all bins of the $|y^{\bar{t}q}(\hat{t})|$ variable used to unfold to particle level.

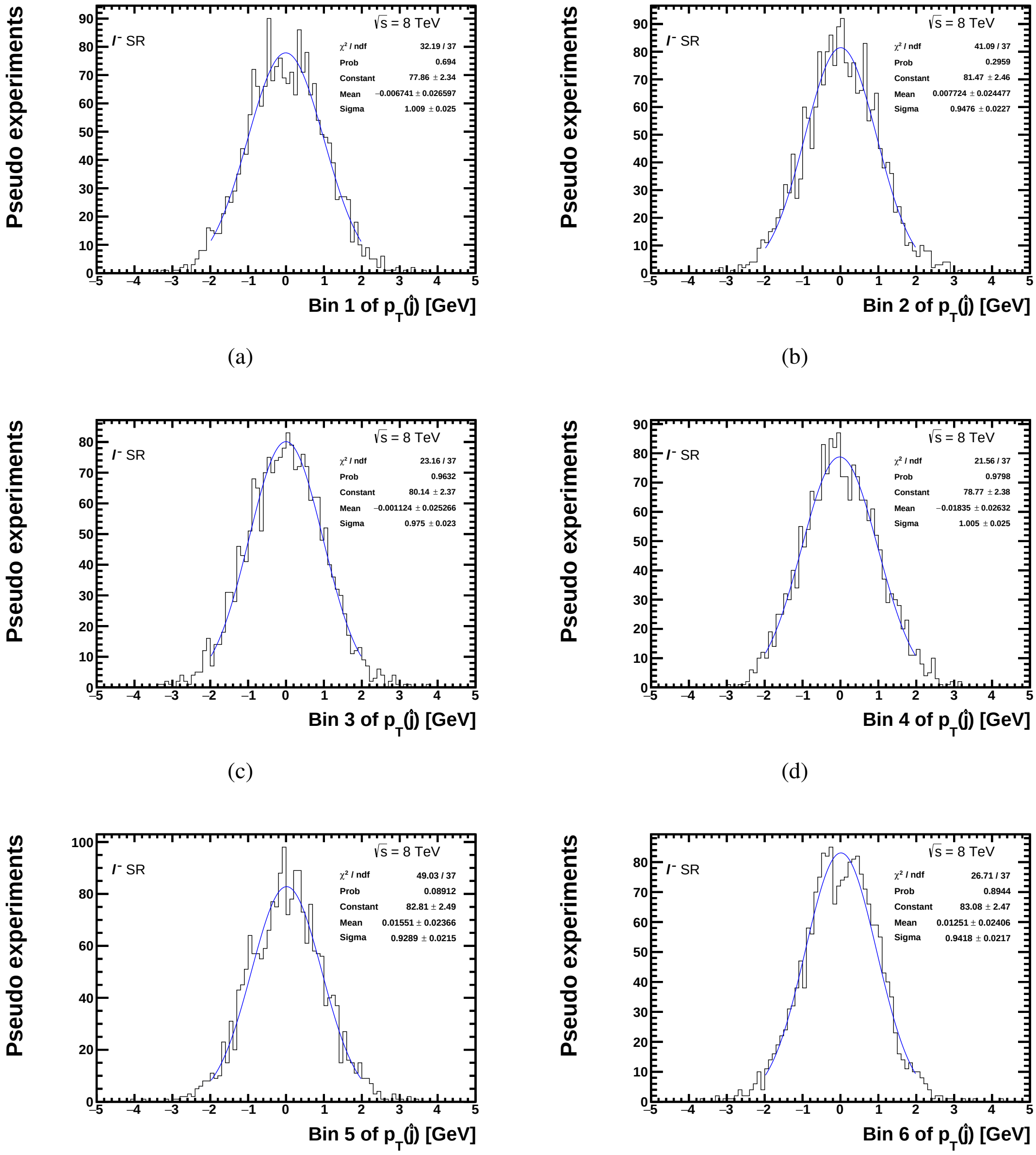

(a) (b) (c) (d) (e) (f)

Figure E.13: Pull distributions of 2000 pseudo experiments for all bins of the $p_T^{\bar{t}q}(\hat{j})$ variable used to unfold to particle level.

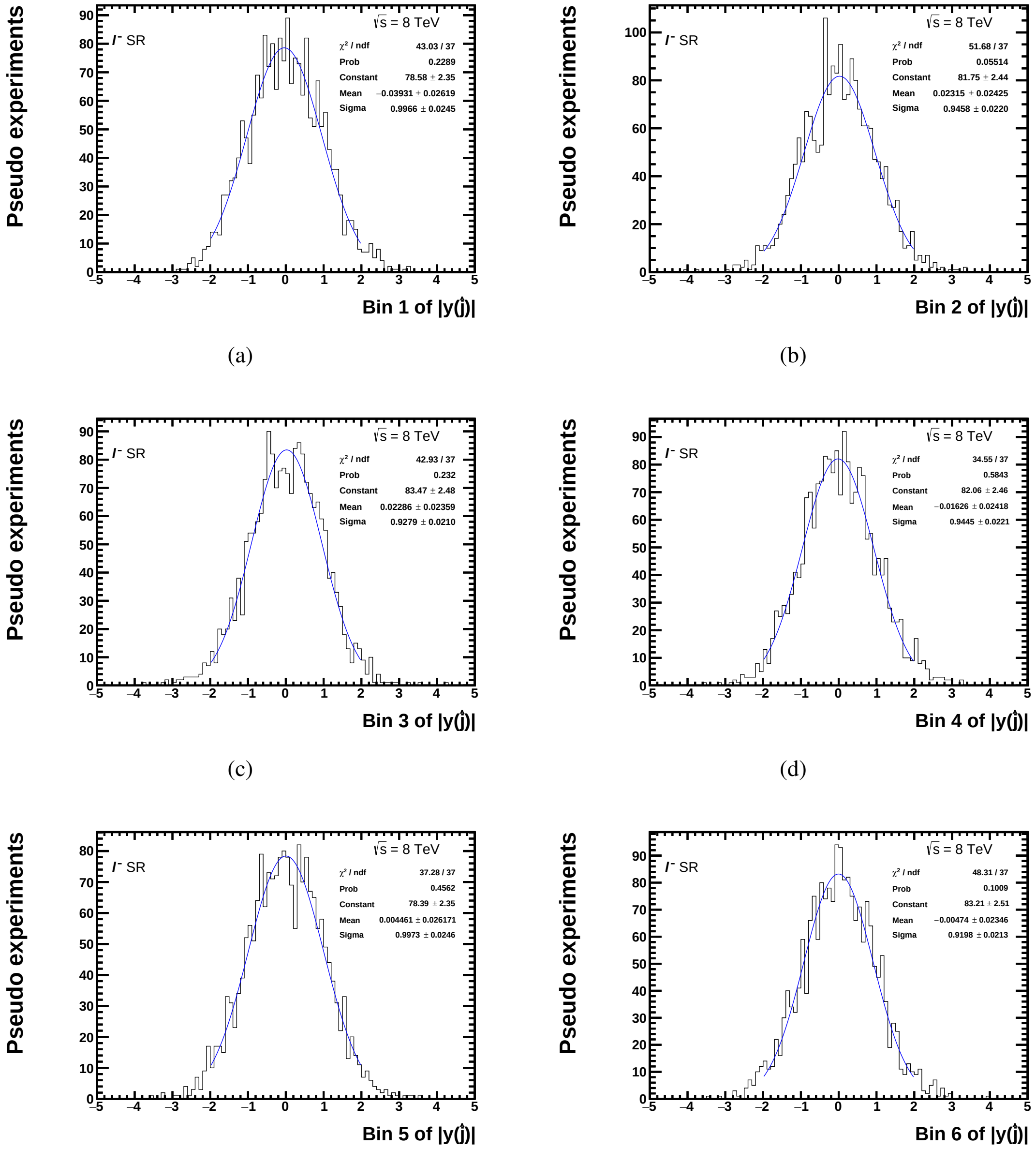

(a)

(b)

(c)

(d)

(e)

(f)

Figure E.14: Pull distributions of 2000 pseudo experiments for all bins of the $|y^{\bar{t}q}(\hat{j})|$ variable used to unfold to particle level.

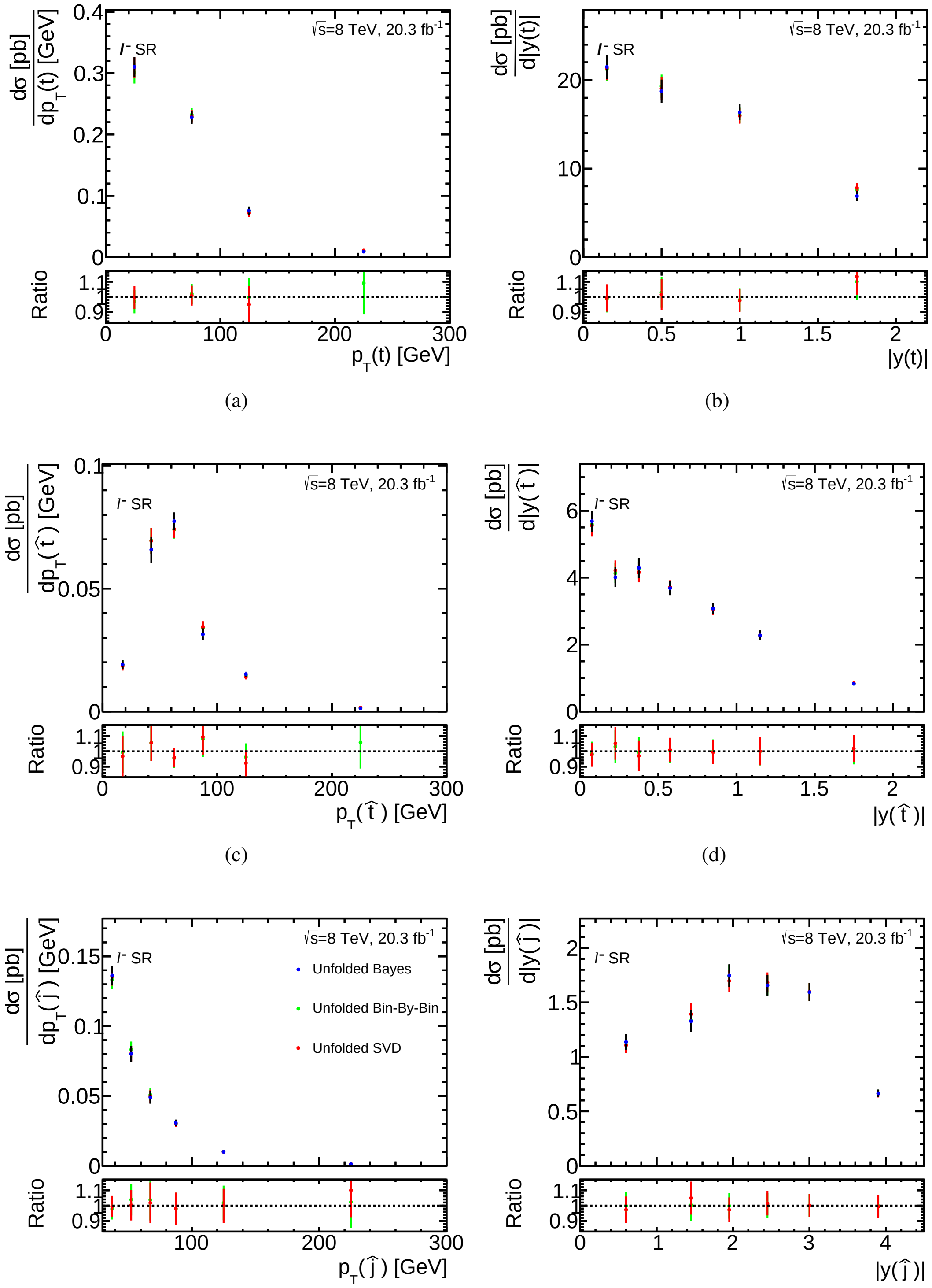

(a) (b) (c) (d) (e) (f)

Figure E.15: Comparison between the three unfolding methods: Bayesian, SVD and bin-by-bin, for (a) $p_{\mathrm{T}}^{\bar{t}q}(t)$, (b) $|y^{\bar{t}q}(t)|$, (c) $p_{\mathrm{T}}^{\bar{t}q}(\hat{t})$, (d) $|y^{\bar{t}q}(\hat{t})|$, (e) $p_{\mathrm{T}}^{\bar{t}q}(\hat{j})$ and (f) $|y^{\bar{t}q}(\hat{j})|$. The error bar represents the uncertainty due to data statistics. The ratio is calculated with respect to the unfolded Bayesian result shown in the bottom plot.

APPENDIX F

Cutflows for the reconstruction-level and particle-level selections

	Reco. level	Particle level
Initial	555800	555800
= 1 lepton	162400	257400
Jet cleaning	160600	"
>= 1 jets	156500	247600
Reco. scale factors	153900	"
>= 2 jets	121300	178400
>= 2 jets [*]	104400	"
= 2 jets [*]	70600	120200
= 1 *b*-jet	32200	99000
Dilepton veto	31600	"
Multijet veto	29500	"
$E_{\mathrm{T}}^{\mathrm{miss}}$ >= 30	22600	"
$m_{\mathrm{T}}(\ell, E_{\mathrm{T}}^{\mathrm{miss}})$ >= 50	18400	"
$m(\ell b) < 160$	17800	96300

Table F.1: Sequential cutflows for the reconstruction-level and particle-level selections applied on the POWHEG-BOX + PYTHIA 6 signal sample. tq and $\bar{t}q$ events are combined. [*] denotes that jets with $2.7 < |\eta| < 3.5$ are required to have $p_{\mathrm{T}} > 35$ GeV for the reconstruction-level selection.

APPENDIX G

Background β value bin-by-bin

The following study is done to see whether the fraction of background varies from bin to bin. The combination of tq and $\bar{t}q$ events is considered, since there is only a small difference between the beta values from the fit and the sum has more statistics. The fit result is investigated bin-by-bin for the four distributions ($p_{\mathrm{T}}(\hat{t})$, $|y(\hat{t})|$, $p_{\mathrm{T}}(\hat{j})$ and $|y(\hat{j})|$) that are unfolded to particle level. The background scale factors are illustrated in Figure G.1 for all four distributions. The background scale factors are consistent

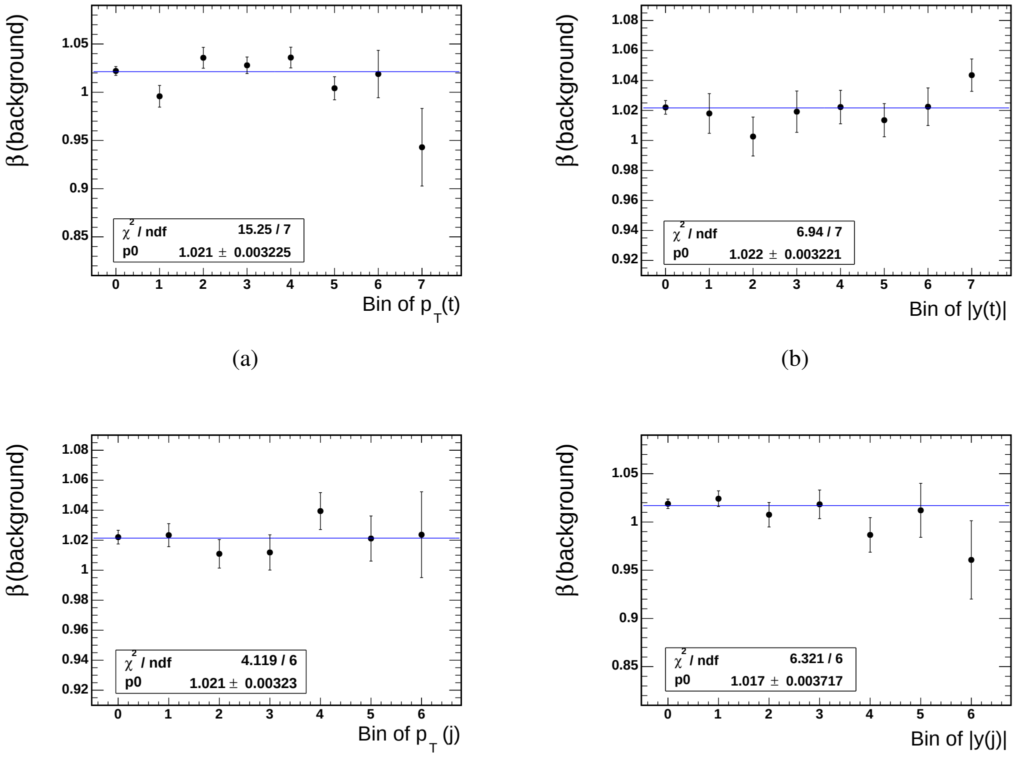

(a) (b)

(c) (d)

Figure G.1: Background scale factors for (a) $p_{\mathrm{T}}(\hat{t})$, (b) $|y(\hat{t})|$, (c) $p_{\mathrm{T}}(\hat{j})$ and (d) $|y(\hat{j})|$.

over the bins. Thus, the normalisation uncertainties on the sum of all background processes from the global fit are used for the differential cross-sections.

APPENDIX H

Uncertainties on the differential cross-sections

	Uncertainties on $\mathrm{d}\sigma(tq)/\mathrm{d}p_{\mathrm{T}}(t)$ at parton level				
Source of uncertainty	Bin 1 [%]	Bin 2 [%]	Bin 3 [%]	Bin 4 [%]	Bin 5 [%]
Data statistics	±5.4	±3.8	±6.8	±13	±19
Monte Carlo statistics	±0.7	±0.5	±0.9	±1.6	±2.4
Unfolding	+2.0/ −2.0	+0.9/ −0.9	+1.5/ −1.5	+0.9/ −0.9	+1.7/ −1.7
Background normalisation	+4.6/ −4.6	+2.6/ −2.6	+3.0/ −3.0	+2.7/ −2.7	+4.0/ −4.0
Background modelling	+0.8/ −0.8	+0.5/ −0.5	+1.0/ −1.0	+1.3/ −1.3	+0.4/ −0.4
Lepton reconstruction	+1.9/ −1.9	+1.9/ −1.9	+2.0/ −1.9	+1.9/ −1.9	+2.0/ −2.1
Jet reconstruction	+1.1/ −1.1	+1.5/ −1.5	+0.8/ −0.8	+0.9/ −0.9	+2.9/ −2.9
Jet energy scale	+2.0/ −1.7	+2.2/ −2.6	+1.9/ −2.2	+6.0/ −2.4	+1.0/ −5.6
Flavour tagging	+1.2/ −1.2	+1.2/ −1.2	+1.2/ −1.2	+1.4/ −1.4	+1.4/ −1.4
$E_{\mathrm{T}}^{\mathrm{miss}}$ modelling	+0.6/ −0.3	+0.2/ −0.2	+0.6/ −1.0	+1.3/ −0.0	+0.0/ −1.9
$b/\bar{b}$ efficiency	±0.9	±0.9	±0.9	±0.9	±0.9
PDF	+0.8/ −0.9	+0.2/ −0.1	+0.4/ −0.4	+1.5/ −1.5	+1.1/ −1.1
tq ($\bar{t}q$) NLO matching	+2.2/ −2.2	+3.7/ −3.7	+8.9/ −8.9	+3.8/ −3.8	+2.8/ −2.8
tq ($\bar{t}q$) parton shower	+0.9/ −0.9	+1.6/ −1.6	+3.1/ −3.1	+0.8/ −0.8	+1.7/ −1.7
tq ($\bar{t}q$) scale variations	+2.0/ −4.9	+2.6/ −0.0	+0.4/ −3.9	+0.0/ −3.6	+3.8/ −1.9
$t\bar{t}$ NLO matching	+0.4/ −0.4	+0.5/ −0.5	+2.3/ −2.3	+3.0/ −3.0	+6.6/ −6.6
$t\bar{t}$ parton shower	+0.1/ −0.1	+0.4/ −0.4	+0.1/ −0.1	+1.6/ −1.6	+4.3/ −4.3
$t\bar{t}$ scale variations	+0.7/ −0.0	+0.0/ −1.4	+1.8/ −0.0	+3.5/ −0.0	+0.0/ −3.4
Luminosity	±1.9	±1.9	±1.9	±1.9	±1.9
Total systematic	+7.2/ −8.4	+6.9/ −6.7	+11 / −12	+10 / −8	+12 / −13
Total (stat. + syst.)	+9.0/ −10.0	+7.9/ −7.7	+13 / −14	+16 / −15	+22 / −23

Table H.1: Uncertainties for the absolute differential tq cross-section as a function of $p_{\mathrm{T}}(t)$ at parton level per bin ($[0, 50, 100, 150, 200, 300]$ GeV) in percent of $\mathrm{d}\sigma(tq)/\mathrm{d}p_{\mathrm{T}}(t)$. [2]

Source of uncertainty	Uncertainties on $(1/\sigma)\mathrm{d}\sigma(tq)/\mathrm{d}p_{\mathrm{T}}(t)$ at parton level Bin 1 [%]	Bin 2 [%]	Bin 3 [%]	Bin 4 [%]	Bin 5 [%]
Data statistics	±3.9	±4.3	±6.7	±13	±19
Monte Carlo statistics	±0.5	±0.5	±0.9	±1.6	±2.4
Unfolding	+1.6 / −1.6	+1.3 / −1.3	+1.9 / −1.9	+0.5 / −0.5	+1.3 / −1.3
Background normalisation	+1.1 / −1.1	+1.0 / −1.0	+0.5 / −0.5	+0.9 / −0.9	+0.5 / −0.5
Background modelling	+0.7 / −0.7	+0.5 / −0.5	+1.1 / −1.1	+1.2 / −1.2	+0.3 / −0.3
Lepton reconstruction	+0.0 / −0.1	+0.1 / −0.2	+0.6 / −0.2	+0.6 / −0.2	+0.3 / −0.8
Jet reconstruction	+0.1 / −0.1	+0.3 / −0.3	+0.4 / −0.4	+0.3 / −0.3	+1.7 / −1.7
Jet energy scale	+1.7 / −1.2	+1.0 / −1.3	+1.4 / −2.3	+4.9 / −2.0	+1.1 / −5.7
Flavour tagging	+0.3 / −0.3	+0.1 / −0.1	+0.5 / −0.5	+0.7 / −0.7	+1.1 / −1.1
$E_{\mathrm{T}}^{\mathrm{miss}}$ modelling	+0.4 / −0.1	+0.1 / −0.1	+0.6 / −1.2	+1.5 / −0.0	+0.0 / −1.8
PDF	+0.6 / −0.7	+0.4 / −0.3	+0.6 / −0.6	+1.7 / −1.7	+1.2 / −1.2
tq ($\bar{t}q$) NLO matching	+1.6 / −1.6	+4.2 / −4.2	+8.4 / −8.4	+4.3 / −4.3	+3.3 / −3.3
tq ($\bar{t}q$) parton shower	+0.7 / −0.7	+1.8 / −1.8	+2.9 / −2.9	+0.6 / −0.6	+1.9 / −1.9
tq ($\bar{t}q$) scale variations	+1.6 / −3.9	+3.7 / −0.0	+1.5 / −4.2	+0.9 / −4.0	+3.5 / −0.8
$t\bar{t}$ NLO matching	+0.4 / −0.4	+0.6 / −0.6	+2.3 / −2.3	+3.0 / −3.0	+6.6 / −6.6
$t\bar{t}$ parton shower	+0.0 / −0.0	+0.5 / −0.5	+0.1 / −0.1	+1.6 / −1.6	+4.3 / −4.3
$t\bar{t}$ scale variations	+0.5 / −0.0	+0.0 / −1.5	+1.7 / −0.0	+3.4 / −0.0	+0.0 / −3.6
Total systematic	+3.7 / −5.0	+6.3 / −5.4	+10 / −11	+8.8 / −7.7	+10 / −12
Total (stat. + syst.)	+5.4 / −6.4	+7.6 / −6.9	+12 / −13	+16 / −15	+21 / −22

Table H.2: Uncertainties for the normalised differential tq cross-section as a function of $p_{\mathrm{T}}(t)$ at parton level per bin ($[0, 50, 100, 150, 200, 300]$ GeV) in percent of $(1/\sigma)\mathrm{d}\sigma(tq)/\mathrm{d}p_{\mathrm{T}}(t)$. [2]

Source of uncertainty	Uncertainties on $\mathrm{d}\sigma(\bar{t}q)/\mathrm{d}p_{\mathrm{T}}(t)$ at parton level			
	Bin 1 [%]	Bin 2 [%]	Bin 3 [%]	Bin 4 [%]
Data statistics	±7.0	±5.8	±12	±20
Monte Carlo statistics	±0.7	±0.6	±1.1	±1.7
Unfolding	+3.9 / −3.9	+4.3 / −4.3	+3.7 / −3.7	+6.5 / −6.5
Background normalisation	+5.8 / −5.8	+4.5 / −4.5	+6.1 / −6.1	+10 / −10
Background modelling	+1.4 / −1.4	+0.6 / −0.6	+3.2 / −3.2	+1.8 / −1.8
Lepton reconstruction	+1.9 / −1.9	+1.9 / −1.9	+2.0 / −2.0	+1.9 / −1.9
Jet reconstruction	+2.3 / −2.3	+3.5 / −3.5	+1.1 / −1.1	+2.1 / −2.1
Jet energy scale	+2.9 / −1.1	+2.0 / −3.1	+3.9 / −2.4	+3.4 / −2.8
Flavour tagging	+1.2 / −1.2	+1.1 / −1.1	+1.3 / −1.3	+1.4 / −1.4
$E_{\mathrm{T}}^{\mathrm{miss}}$ modelling	+0.9 / −0.6	+0.1 / −0.3	+1.0 / −0.3	+0.6 / −0.5
$b/\bar{b}$ efficiency	±0.9	±0.9	±0.9	±0.9
PDF	+2.9 / −2.9	+1.2 / −1.3	+2.8 / −2.8	+2.7 / −2.7
tq ($\bar{t}q$) NLO matching	+6.7 / −6.7	+0.8 / −0.8	+16 / −16	+12 / −12
tq ($\bar{t}q$) parton shower	+1.4 / −1.4	+0.4 / −0.4	+1.5 / −1.5	+1.2 / −1.2
tq ($\bar{t}q$) scale variations	+1.6 / −2.3	+1.4 / −0.7	+0.5 / −0.4	+2.2 / −3.4
$t\bar{t}$ NLO matching	+0.7 / −0.7	+1.4 / −1.4	+1.9 / −1.9	+17 / −17
$t\bar{t}$ parton shower	+1.0 / −1.0	+0.8 / −0.8	+4.2 / −4.2	+15 / −15
$t\bar{t}$ scale variations	+1.2 / −0.0	+0.0 / −1.5	+0.0 / −3.1	+17 / −0
Luminosity	±1.9	±1.9	±1.9	±1.9
Total systematic	+12 / −11	+8.5 / −8.9	+19 / −19	+34 / −29
Total (stat. + syst.)	+14 / −13	+10 / −11	+22 / −22	+39 / −35

Table H.3: Uncertainties for the absolute differential $\bar{t}q$ cross-section as a function of $p_{\mathrm{T}}(t)$ at parton level per bin ($[0, 50, 100, 150, 300]$ GeV) in percent of $\mathrm{d}\sigma(\bar{t}q)/\mathrm{d}p_{\mathrm{T}}(t)$. [2]

Source of uncertainty	Uncertainties on $(1/\sigma)\mathrm{d}\sigma(\bar{t}q)/\mathrm{d}p_{\mathrm{T}}(t)$ at parton level Bin 1 [%]	 Bin 2 [%]	 Bin 3 [%]	 Bin 4 [%]
Data statistics	±5.0	±6.7	±12	±20
Monte Carlo statistics	±0.4	±0.5	±1.1	±1.7
Unfolding	+3.7 / −3.7	+4.5 / −4.5	+3.5 / −3.5	+6.7 / −6.7
Background normalisation	+0.3 / −0.3	+1.1 / −1.1	+0.6 / −0.6	+4.2 / −4.2
Background modelling	+1.3 / −1.3	+0.8 / −0.8	+3.3 / −3.3	+1.6 / −1.6
Lepton reconstruction	+0.3 / −0.1	+0.1 / −0.4	+0.4 / −0.5	+0.6 / −0.3
Jet reconstruction	+2.7 / −2.7	+3.2 / −3.2	+0.8 / −0.8	+1.8 / −1.8
Jet energy scale	+1.6 / −0.6	+0.2 / −1.7	+2.4 / −1.5	+2.5 / −2.5
Flavour tagging	+0.3 / −0.3	+0.2 / −0.2	+0.5 / −0.5	+0.8 / −0.9
$E_{\mathrm{T}}^{\mathrm{miss}}$ modelling	+0.5 / −0.4	+0.0 / −0.2	+1.1 / −0.7	+0.8 / −0.9
PDF	+2.3 / −2.3	+1.8 / −1.9	+3.5 / −3.4	+2.3 / −2.3
tq ($\bar{t}q$) NLO matching	+5.3 / −5.3	+2.2 / −2.2	+17 / −17	+11 / −11
tq ($\bar{t}q$) parton shower	+1.0 / −1.0	+0.8 / −0.8	+1.8 / −1.8	+0.8 / −0.8
tq ($\bar{t}q$) scale variations	+1.3 / −1.9	+1.8 / −1.0	+0.2 / −0.0	+2.7 / −3.7
$t\bar{t}$ NLO matching	+0.8 / −0.8	+1.5 / −1.5	+1.8 / −1.8	+17 / −17
$t\bar{t}$ parton shower	+0.6 / −0.6	+1.1 / −1.1	+4.5 / −4.5	+15 / −15
$t\bar{t}$ scale variations	+0.8 / −0.0	+0.0 / −1.8	+0.0 / −3.4	+17 / −0
Total systematic	+8.0 / −7.9	+6.9 / −7.2	+19 / −19	+31 / −27
Total (stat. + syst.)	+9.4 / −9.4	+10 / −10	+22 / −22	+37 / −33

Table H.4: Uncertainties for the normalised differential $\bar{t}q$ cross-section as a function of $p_{\mathrm{T}}(t)$ at parton level per bin ($[0, 50, 100, 150, 300]$ GeV) in percent of $(1/\sigma)\mathrm{d}\sigma(\bar{t}q)/\mathrm{d}p_{\mathrm{T}}(t)$. [2]

Source of uncertainty	Uncertainties on $\mathrm{d}\sigma(tq)/\mathrm{d}\|y(t)\|$ at parton level Bin 1 [%]	Bin 2 [%]	Bin 3 [%]	Bin 4 [%]
Data statistics	±5.6	±5.6	±5.0	±5.7
Monte Carlo statistics	±0.8	±0.7	±0.6	±0.8
Unfolding	+2.3 / −2.3	+0.8 / −0.8	+0.2 / −0.2	+3.8 / −3.8
Background normalisation	+2.5 / −2.5	+3.0 / −3.0	+3.7 / −3.7	+4.2 / −4.2
Background modelling	+0.0 / −0.0	+0.0 / −0.0	+0.0 / −0.0	+0.0 / −0.0
Lepton reconstruction	+1.9 / −1.9	+1.9 / −1.9	+1.9 / −1.9	+2.0 / −1.9
Jet reconstruction	+1.1 / −1.1	+3.6 / −3.6	+0.2 / −0.2	+2.2 / −2.2
Jet energy scale	+1.0 / −1.7	+2.2 / −2.1	+2.1 / −1.3	+2.8 / −2.9
Flavour tagging	+1.2 / −1.2	+1.2 / −1.2	+1.2 / −1.2	+1.2 / −1.2
$E_{\mathrm{T}}^{\mathrm{miss}}$ modelling	+0.0 / −0.5	+0.5 / −0.0	+0.1 / −0.4	+0.5 / −0.0
$b/\bar{b}$ efficiency	±0.9	±0.9	±0.9	±0.9
PDF	+1.9 / −1.9	+0.5 / −0.6	+2.4 / −2.4	+1.4 / −1.4
tq ($\bar{t}q$) NLO matching	+0.6 / −0.6	+3.2 / −3.2	+4.3 / −4.3	+1.4 / −1.4
tq ($\bar{t}q$) parton shower	+3.4 / −3.4	+0.5 / −0.5	+1.9 / −1.9	+0.9 / −0.9
tq ($\bar{t}q$) scale variations	+4.0 / −0.0	+0.0 / −2.5	+0.0 / −1.8	+0.0 / −1.7
$t\bar{t}$ NLO matching	+0.5 / −0.5	+0.7 / −0.7	+0.6 / −0.6	+1.6 / −1.6
$t\bar{t}$ parton shower	+0.5 / −0.5	+1.4 / −1.4	+0.9 / −0.9	+0.2 / −0.2
$t\bar{t}$ scale variations	+0.0 / −0.3	+0.0 / −0.6	+0.5 / −0.0	+0.5 / −0.6
Luminosity	±1.9	±1.9	±1.9	±1.9
Total systematic	+7.5 / −6.5	+7.1 / −7.5	+7.6 / −7.6	+7.9 / −8.1
Total (stat. + syst.)	+9.3 / −8.6	+9.1 / −9.4	+9.1 / −9.1	+10 / −10

Table H.5: Uncertainties for the absolute differential tq cross-section as a function of $|y(t)|$ at parton level per bin ($[0, 0.3, 0.7, 1.3, 2.2]$) in percent of $\mathrm{d}\sigma(tq)/\mathrm{d}|y(t)|$. [2]

Source of uncertainty	Uncertainties on $(1/\sigma)\mathrm{d}\sigma(tq)/\mathrm{d}|y(t)|$ at parton level Bin 1 [%]	Bin 2 [%]	Bin 3 [%]	Bin 4 [%]
Data statistics	±5.5	±5.5	±4.8	±4.8
Monte Carlo statistics	±0.7	±0.6	±0.6	±0.7
Unfolding	+2.7 / −2.7	+1.2 / −1.2	+0.2 / −0.2	+3.4 / −3.4
Background normalisation	+0.9 / −0.9	+0.5 / −0.5	+0.3 / −0.3	+0.8 / −0.8
Background modelling	+0.0 / −0.0	+0.0 / −0.0	+0.0 / −0.0	+0.0 / −0.0
Lepton reconstruction	+0.3 / −0.2	+0.3 / −0.3	+0.2 / −0.2	+0.5 / −0.4
Jet reconstruction	+2.5 / −2.5	+2.3 / −2.3	+1.1 / −1.1	+0.9 / −0.9
Jet energy scale	+0.8 / −1.6	+1.2 / −0.8	+0.8 / −0.4	+1.2 / −1.1
Flavour tagging	+0.1 / −0.1	+0.0 / −0.0	+0.0 / −0.0	+0.1 / −0.1
$E_{\mathrm{T}}^{\mathrm{miss}}$ modelling	+0.0 / −0.6	+0.5 / −0.0	+0.0 / −0.4	+0.5 / −0.0
PDF	+2.2 / −2.2	+0.6 / −0.6	+2.2 / −2.2	+1.5 / −1.5
tq ($\bar{t}q$) NLO matching	+0.4 / −0.4	+3.5 / −3.5	+4.0 / −4.0	+1.7 / −1.7
tq ($\bar{t}q$) parton shower	+3.7 / −3.7	+0.3 / −0.3	+1.6 / −1.6	+0.7 / −0.7
tq ($\bar{t}q$) scale variations	+4.5 / −0.0	+0.2 / −2.1	+0.0 / −1.4	+0.0 / −1.3
$t\bar{t}$ NLO matching	+0.3 / −0.3	+0.9 / −0.9	+0.8 / −0.8	+1.4 / −1.4
$t\bar{t}$ parton shower	+0.4 / −0.4	+1.5 / −1.5	+0.8 / −0.8	+0.1 / −0.1
$t\bar{t}$ scale variations	+0.0 / −0.3	+0.0 / −0.7	+0.6 / −0.0	+0.4 / −0.5
Total systematic	+7.4 / −6.1	+5.0 / −5.4	+5.2 / −5.4	+4.8 / −4.9
Total (stat. + syst.)	+9.2 / −8.2	+7.4 / −7.7	+7.1 / −7.2	+6.8 / −6.9

Table H.6: Uncertainties for the normalised differential tq cross-section as a function of $|y(t)|$ at parton level per bin ($[0, 0.3, 0.7, 1.3, 2.2]$) in percent of $(1/\sigma)\mathrm{d}\sigma(tq)/\mathrm{d}|y(t)|$. [2]

Source of uncertainty	Uncertainties on $\mathrm{d}\sigma(\bar{t}q)/\mathrm{d}\lvert y(t)\rvert$ at parton level Bin 1 [%]	Bin 2 [%]	Bin 3 [%]	Bin 4 [%]
Data statistics	±7.9	±8.7	±7.2	±11
Monte Carlo statistics	±0.9	±0.8	±0.7	±1.0
Unfolding	+0.1 / −0.1	+0.4 / −0.4	+2.7 / −2.7	+5.1 / −5.1
Background normalisation	+4.1 / −4.1	+5.2 / −5.2	+5.3 / −5.3	+8.7 / −8.7
Background modelling	+0.8 / −0.8	+0.4 / −0.4	+2.0 / −2.0	+3.5 / −3.5
Lepton reconstruction	+1.9 / −1.9	+1.9 / −1.9	+1.9 / −2.0	+1.9 / −1.9
Jet reconstruction	+0.8 / −0.8	+1.1 / −1.1	+1.8 / −1.8	+0.5 / −0.5
Jet energy scale	+2.1 / −2.0	+2.6 / −1.4	+1.8 / −2.7	+4.1 / −2.7
Flavour tagging	+1.2 / −1.2	+1.2 / −1.2	+1.1 / −1.1	+1.2 / −1.2
$E_{\mathrm{T}}^{\mathrm{miss}}$ modelling	+0.5 / −0.1	+0.6 / −0.5	+0.2 / −0.7	+0.9 / −0.0
$b/\bar{b}$ efficiency	±0.9	±0.9	±0.9	±0.9
PDF	+1.2 / −1.2	+3.0 / −3.0	+0.6 / −0.7	+5.8 / −5.8
tq ($\bar{t}q$) NLO matching	+5.8 / −5.8	+3.7 / −3.7	+4.8 / −4.8	+9.2 / −9.2
tq ($\bar{t}q$) parton shower	+0.6 / −0.6	+2.9 / −2.9	+1.6 / −1.6	+0.9 / −0.9
tq ($\bar{t}q$) scale variations	+0.0 / −2.6	+0.1 / −0.0	+3.2 / −0.5	+3.6 / −2.6
$t\bar{t}$ NLO matching	+0.6 / −0.6	+0.9 / −0.9	+1.9 / −1.9	+0.8 / −0.8
$t\bar{t}$ parton shower	+1.5 / −1.5	+3.1 / −3.1	+1.2 / −1.2	+0.9 / −0.9
$t\bar{t}$ scale variations	+0.0 / −0.8	+0.3 / −0.0	+0.0 / −1.5	+4.1 / −0.0
Luminosity	±1.9	±1.9	±1.9	±1.9
Total systematic	+8.4 / −8.8	+9.3 / −9.1	+10 / −10	+17 / −16
Total (stat. + syst.)	+12 / −12	+13 / −13	+12 / −12	+20 / −20

Table H.7: Uncertainties for the absolute differential $\bar{t}q$ cross-section as a function of $\lvert y(t)\rvert$ at parton level per bin ($[0, 0.3, 0.7, 1.3, 2.2]$) in percent of $\mathrm{d}\sigma(\bar{t}q)/\mathrm{d}\lvert y(t)\rvert$. [2]

Source of uncertainty	Uncertainties on $(1/\sigma)\mathrm{d}\sigma(\bar{t}q)/\mathrm{d}\vert y(t)\vert$ at parton level Bin 1 [%]	Bin 2 [%]	Bin 3 [%]	Bin 4 [%]
Data statistics	±7.7	±8.5	±6.9	±10
Monte Carlo statistics	±0.8	±0.7	±0.6	±0.9
Unfolding	+0.5 / −0.5	+0.1 / −0.1	+3.1 / −3.1	+4.7 / −4.7
Background normalisation	+1.7 / −1.7	+0.5 / −0.5	+0.4 / −0.4	+3.1 / −3.1
Background modelling	+0.8 / −0.8	+0.4 / −0.4	+2.0 / −2.0	+3.4 / −3.4
Lepton reconstruction	+0.3 / −0.2	+0.6 / −0.3	+0.2 / −0.4	+0.4 / −0.4
Jet reconstruction	+0.3 / −0.3	+0.1 / −0.1	+0.7 / −0.7	+0.6 / −0.6
Jet energy scale	+0.6 / −0.9	+1.0 / −0.5	+0.1 / −1.3	+1.7 / −0.7
Flavour tagging	+0.0 / −0.0	+0.0 / −0.0	+0.0 / −0.0	+0.1 / −0.1
$E_{\mathrm{T}}^{\mathrm{miss}}$ modelling	+0.3 / −0.0	+0.3 / −0.6	+0.1 / −0.6	+0.9 / −0.0
PDF	+0.9 / −0.9	+3.5 / −3.5	+1.1 / −1.2	+5.2 / −5.2
tq ($\bar{t}q$) NLO matching	+5.0 / −5.0	+4.5 / −4.5	+5.7 / −5.7	+8.4 / −8.4
tq ($\bar{t}q$) parton shower	+0.5 / −0.5	+3.0 / −3.0	+1.6 / −1.6	+0.8 / −0.8
tq ($\bar{t}q$) scale variations	+0.0 / −2.5	+0.2 / −0.5	+3.3 / −1.0	+3.2 / −2.5
$t\bar{t}$ NLO matching	+0.7 / −0.7	+1.0 / −1.0	+1.8 / −1.8	+0.9 / −0.9
$t\bar{t}$ parton shower	+1.4 / −1.4	+3.2 / −3.2	+1.0 / −1.0	+0.8 / −0.8
$t\bar{t}$ scale variations	+0.0 / −0.9	+0.0 / −0.2	+0.0 / −1.9	+3.7 / −0.0
Total systematic	+5.8 / −6.4	+7.4 / −7.4	+8.1 / −7.9	+13 / −12
Total (stat. + syst.)	+10 / −10	+11 / −11	+11 / −10	+16 / −16

Table H.8: Uncertainties for the normalised differential $\bar{t}q$ cross-section as a function of $|y(t)|$ at parton level per bin ($[0, 0.3, 0.7, 1.3, 2.2]$) in percent of $(1/\sigma)\mathrm{d}\sigma(\bar{t}q)/\mathrm{d}|y(t)|$. [2]

Source of uncertainty	Uncertainties on $\mathrm{d}\sigma(tq)/\mathrm{d}p_{\mathrm{T}}(\hat{t})$ at particle level Bin 1 [%]	Bin 2 [%]	Bin 3 [%]	Bin 4 [%]	Bin 5 [%]	Bin 6 [%]	Bin 7 [%]
Data statistics	±8.1	±7.0	±4.2	±5.7	±5.5	±10	±16
Monte Carlo statistics	±1.1	±0.8	±0.6	±0.8	±0.9	±1.6	±2.2
Unfolding	+0.0 / −0.0	+3.1 / −3.1	+1.3 / −1.3	+1.2 / −1.2	+3.2 / −3.2	+3.8 / −3.8	+5.4 / −5.4
Background normalisation	+5.6 / −5.6	+3.3 / −3.3	+2.7 / −2.7	+3.2 / −3.2	+2.9 / −2.9	+2.7 / −2.7	+3.9 / −3.9
Background modelling	+1.3 / −1.3	+0.1 / −0.1	+0.1 / −0.1	+0.6 / −0.6	+0.8 / −0.8	+0.8 / −0.8	+0.5 / −0.5
Lepton reconstruction	+1.9 / −2.0	+2.1 / −1.9	+1.9 / −1.9	+1.9 / −1.9	+1.9 / −1.9	+1.9 / −1.9	+1.9 / −2.0
Jet reconstruction	+0.5 / −0.5	+1.8 / −1.8	+1.0 / −1.0	+1.9 / −1.9	+0.9 / −0.9	+1.0 / −1.0	+2.7 / −2.7
Jet energy scale	+2.6 / −4.1	+2.5 / −0.5	+1.5 / −2.0	+3.2 / −3.1	+1.8 / −1.9	+4.9 / −2.3	+1.1 / −4.9
Flavour tagging	+1.2 / −1.2	+1.3 / −1.3	+1.3 / −1.3	+1.1 / −1.1	+1.2 / −1.2	+1.3 / −1.3	+1.5 / −1.5
$E_{\mathrm{T}}^{\mathrm{miss}}$ modelling	+0.3 / −0.4	+1.0 / −0.4	+0.4 / −0.8	+0.7 / −0.5	+0.4 / −0.7	+1.2 / −0.0	+0.0 / −1.5
$b/\bar{b}$ efficiency	±0.9	±0.9	±0.9	±0.9	±0.9	±0.9	±0.9
PDF	+1.8 / −2.0	+1.0 / −1.0	+1.2 / −1.2	+0.3 / −0.3	+0.3 / −0.2	+2.0 / −2.0	+0.9 / −0.9
tq ($\bar{t}q$) NLO matching	+1.8 / −1.8	+0.3 / −0.3	+2.9 / −2.9	+2.8 / −2.8	+4.5 / −4.5	+1.2 / −1.2	+9.4 / −9.4
tq ($\bar{t}q$) parton shower	+3.2 / −3.2	+1.1 / −1.1	+0.3 / −0.3	+0.4 / −0.4	+1.5 / −1.5	+0.9 / −0.9	+0.6 / −0.6
tq ($\bar{t}q$) scale variations	+2.8 / −0.7	+0.0 / −3.1	+1.8 / −1.1	+0.9 / −0.0	+0.0 / −0.8	+0.0 / −2.3	+5.2 / −0.0
$t\bar{t}$ NLO matching	+0.7 / −0.7	+0.5 / −0.5	+1.6 / −1.6	+3.2 / −3.2	+1.9 / −1.9	+2.0 / −2.0	+5.9 / −5.9
$t\bar{t}$ parton shower	+0.5 / −0.5	+0.3 / −0.3	+0.8 / −0.8	+0.3 / −0.3	+0.0 / −0.0	+1.3 / −1.3	+3.9 / −3.9
$t\bar{t}$ scale variations	+0.5 / −0.2	+0.4 / −0.0	+0.0 / −1.1	+0.9 / −0.9	+1.2 / −0.0	+2.9 / −0.0	+0.0 / −2.3
Luminosity	±1.9	±1.9	±1.9	±1.9	±1.9	±1.9	±1.9
Total systematic	+8.7 / −8.9	+6.7 / −6.8	+6.2 / −6.3	+7.5 / −7.4	+7.8 / −7.8	+9.0 / −7.6	+15 / −15
Total (stat. + syst.)	+12 / −12	+10 / −10	+7.5 / −7.6	+9.4 / −9.3	+10 / −10	+13 / −13	+22 / −22

Table H.9: Uncertainties for the absolute differential tq cross-section as a function of $p_{\mathrm{T}}(\hat{t})$ at particle level per bin ($[0, 35, 50, 75, 100, 150, 200, 300]$ GeV) in percent of $\mathrm{d}\sigma(tq)/\mathrm{d}p_{\mathrm{T}}(\hat{t})$. [2]

Source of uncertainty	Uncertainties on $(1/\sigma)\mathrm{d}\sigma(tq)/\mathrm{d}p_{\mathrm{T}}(\hat{t})$ at particle level						
	Bin 1 [%]	Bin 2 [%]	Bin 3 [%]	Bin 4 [%]	Bin 5 [%]	Bin 6 [%]	Bin 7 [%]
Data statistics	±7.6	±6.7	±3.9	±5.5	±5.3	±10	±16
Monte Carlo statistics	±1.0	±0.7	±0.5	±0.7	±0.8	±1.5	±2.2
Unfolding	+0.1 / −0.1	+3.1 / −3.1	+1.3 / −1.3	+1.2 / −1.2	+3.2 / −3.2	+3.7 / −3.7	+5.4 / −5.4
Background normalisation	+2.3 / −2.3	+0.0 / −0.0	+0.7 / −0.7	+0.1 / −0.1	+0.4 / −0.4	+0.6 / −0.6	+0.5 / −0.5
Background modelling	+1.3 / −1.3	+0.0 / −0.0	+0.0 / −0.0	+0.6 / −0.6	+0.8 / −0.8	+0.8 / −0.8	+0.5 / −0.5
Lepton reconstruction	+0.1 / −0.7	+0.6 / −0.1	+0.0 / −0.2	+0.4 / −0.1	+0.4 / −0.1	+0.4 / −0.1	+0.2 / −0.7
Jet reconstruction	+0.8 / −0.8	+0.5 / −0.5	+0.2 / −0.2	+0.7 / −0.7	+0.3 / −0.3	+0.3 / −0.3	+1.4 / −1.4
Jet energy scale	+1.1 / −2.6	+3.4 / −1.4	+0.6 / −0.8	+1.6 / −1.4	+1.0 / −1.6	+3.7 / −1.6	+1.1 / −4.7
Flavour tagging	+0.4 / −0.4	+0.3 / −0.3	+0.1 / −0.1	+0.1 / −0.1	+0.4 / −0.4	+0.6 / −0.6	+1.1 / −1.1
$E_{\mathrm{T}}^{\mathrm{miss}}$ modelling	+0.4 / −0.5	+0.9 / −0.4	+0.3 / −0.8	+0.8 / −0.5	+0.4 / −0.8	+1.2 / −0.2	+0.0 / −1.4
PDF	+1.7 / −1.9	+1.0 / −1.0	+1.2 / −1.2	+0.3 / −0.3	+0.3 / −0.2	+2.1 / −2.1	+0.9 / −0.9
tq ($\bar{t}q$) NLO matching	+4.8 / −4.8	+0.4 / −0.4	+4.2 / −4.2	+3.8 / −3.8	+7.8 / −7.8	+5.1 / −5.1	+9.0 / −9.0
tq ($\bar{t}q$) parton shower	+3.0 / −3.0	+0.9 / −0.9	+0.4 / −0.4	+0.6 / −0.6	+1.7 / −1.7	+1.1 / −1.1	+0.8 / −0.8
tq ($\bar{t}q$) scale variations	+2.7 / −0.7	+0.0 / −3.0	+1.9 / −1.2	+0.9 / −0.0	+0.0 / −0.8	+0.0 / −2.2	+5.1 / −0.0
$t\bar{t}$ NLO matching	+0.6 / −0.6	+0.5 / −0.5	+1.6 / −1.6	+3.2 / −3.2	+1.8 / −1.8	+2.1 / −2.1	+6.0 / −6.0
$t\bar{t}$ parton shower	+0.6 / −0.6	+0.3 / −0.3	+0.7 / −0.7	+0.4 / −0.4	+0.1 / −0.1	+1.4 / −1.4	+4.0 / −4.0
$t\bar{t}$ scale variations	+0.6 / −0.1	+0.4 / −0.0	+0.0 / −1.0	+1.0 / −0.8	+1.3 / −0.0	+3.1 / −0.0	+0.0 / −2.2
Total systematic	+7.3 / −7.3	+5.1 / −4.9	+5.4 / −5.3	+5.8 / −5.6	+9.1 / −9.1	+9.0 / −7.9	+14 / −14
Total (stat. + syst.)	+11 / −11	+8.4 / −8.3	+6.6 / −6.6	+8.0 / −7.8	+10 / −11	+13 / −13	+21 / −21

Table H.10: Uncertainties for the normalised differential tq cross-section as a function of $p_{\mathrm{T}}(\hat{t})$ at particle level per bin ($[0, 35, 50, 75, 100, 150, 200, 300]$ GeV) in percent of $(1/\sigma)\mathrm{d}\sigma(tq)/\mathrm{d}p_{\mathrm{T}}(\hat{t})$. [2]

	Uncertainties on $\mathrm{d}\sigma(\bar{t}q)/\mathrm{d}p_{\mathrm{T}}(\hat{t})$ at particle level					
Source of uncertainty	Bin 1 [%]	Bin 2 [%]	Bin 3 [%]	Bin 4 [%]	Bin 5 [%]	Bin 6 [%]
Data statistics	±12	±9.1	±5.6	±11	±8.9	±17
Monte Carlo statistics	±1.1	±0.8	±0.6	±0.8	±1.0	±1.5
Unfolding	+2.8 / −2.8	+1.8 / −1.8	+0.3 / −0.3	+2.7 / −2.7	+0.3 / −0.3	+1.3 / −1.3
Background normalisation	+8.0 / −8.0	+4.3 / −4.3	+3.8 / −3.8	+7.1 / −7.1	+5.6 / −5.6	+8.9 / −8.9
Background modelling	+1.3 / −1.3	+2.8 / −2.8	+0.8 / −0.8	+0.1 / −0.1	+2.5 / −2.5	+0.9 / −0.9
Lepton reconstruction	+2.1 / −1.9	+1.9 / −1.9	+1.9 / −1.9	+1.9 / −1.9	+2.0 / −2.0	+1.9 / −1.9
Jet reconstruction	+0.3 / −0.3	+1.2 / −1.2	+2.0 / −2.0	+0.8 / −0.8	+0.8 / −0.8	+0.7 / −0.7
Jet energy scale	+4.0 / −3.1	+2.1 / −0.6	+1.6 / −3.2	+3.1 / −2.5	+3.2 / −2.4	+3.3 / −2.6
Flavour tagging	+1.2 / −1.2	+1.3 / −1.3	+1.2 / −1.2	+1.1 / −1.1	+1.2 / −1.2	+1.4 / −1.4
$E_{\mathrm{T}}^{\mathrm{miss}}$ modelling	+1.1 / −0.5	+1.6 / −1.5	+0.3 / −1.2	+1.1 / −0.2	+0.6 / −0.2	+0.5 / −0.5
$b/\bar{b}$ efficiency	±0.9	±0.9	±0.9	±0.9	±0.9	±0.9
PDF	+3.4 / −3.5	+1.1 / −0.9	+0.8 / −0.9	+1.0 / −0.9	+1.4 / −1.4	+1.4 / −1.3
tq ($\bar{t}q$) NLO matching	+0.6 / −0.6	+1.7 / −1.7	+1.2 / −1.2	+4.6 / −4.6	+1.7 / −1.7	+4.2 / −4.2
tq ($\bar{t}q$) parton shower	+2.7 / −2.7	+0.8 / −0.8	+0.1 / −0.1	+0.3 / −0.3	+1.0 / −1.0	+3.6 / −3.6
tq ($\bar{t}q$) scale variations	+0.8 / −0.0	+3.3 / −0.7	+1.0 / −3.3	+2.3 / −0.7	+0.0 / −0.8	+2.0 / −1.0
$t\bar{t}$ NLO matching	+0.2 / −0.2	+2.3 / −2.3	+2.4 / −2.4	+9.2 / −9.2	+1.9 / −1.9	+14 / −14
$t\bar{t}$ parton shower	+1.6 / −1.6	+0.3 / −0.3	+0.8 / −0.8	+3.8 / −3.8	+2.8 / −2.8	+12 / −12
$t\bar{t}$ scale variations	+2.2 / −0.0	+0.8 / −0.4	+0.0 / −2.4	+4.5 / −3.2	+0.0 / −2.2	+13 / −0
Luminosity	±1.9	±1.9	±1.9	±1.9	±1.9	±1.9
Total systematic	+11 / −11	+8.4 / −7.4	+6.4 / −8.1	+15 / −14	+8.8 / −8.8	+26 / −22
Total (stat. + syst.)	+17 / −16	+12 / −12	+8.5 / −9.9	+18 / −18	+13 / −13	+31 / −28

Table H.11: Uncertainties for the absolute differential $\bar{t}q$ cross-section as a function of $p_{\mathrm{T}}(\hat{t})$ at particle level per bin ($[0, 35, 50, 75, 100, 150, 300]$ GeV) in percent of $\mathrm{d}\sigma(\bar{t}q)/\mathrm{d}p_{\mathrm{T}}(\hat{t})$. [2]

	Uncertainties on $(1/\sigma)\mathrm{d}\sigma(\bar{t}q)/\mathrm{d}p_{\mathrm{T}}(\hat{t})$ at particle level					
Source of uncertainty	Bin 1 [%]	Bin 2 [%]	Bin 3 [%]	Bin 4 [%]	Bin 5 [%]	Bin 6 [%]
Data statistics	±12	±8.7	±5.1	±10	±8.6	±16
Monte Carlo statistics	±1.0	±0.7	±0.5	±0.8	±0.9	±1.5
Unfolding	+2.3 / −2.3	+2.4 / −2.4	+0.3 / −0.3	+2.2 / −2.2	+0.8 / −0.8	+0.7 / −0.7
Background normalisation	+2.9 / −2.9	+1.0 / −1.0	+1.6 / −1.6	+1.9 / −1.9	+0.3 / −0.3	+3.8 / −3.8
Background modelling	+1.2 / −1.2	+2.9 / −2.9	+0.7 / −0.7	+0.2 / −0.2	+2.4 / −2.4	+1.1 / −1.1
Lepton reconstruction	+1.0 / −0.1	+0.2 / −0.4	+0.0 / −0.4	+0.2 / −0.2	+0.2 / −0.3	+0.5 / −0.2
Jet reconstruction	+0.9 / −0.9	+0.1 / −0.1	+0.9 / −0.9	+0.4 / −0.4	+0.4 / −0.4	+0.4 / −0.4
Jet energy scale	+2.0 / −1.3	+2.7 / −1.5	+0.2 / −1.5	+1.1 / −1.0	+1.7 / −1.1	+2.5 / −2.0
Flavour tagging	+0.4 / −0.4	+0.2 / −0.2	+0.1 / −0.1	+0.2 / −0.2	+0.4 / −0.4	+0.7 / −0.7
$E_{\mathrm{T}}^{\mathrm{miss}}$ modelling	+1.1 / −0.7	+1.3 / −1.3	+0.1 / −0.9	+1.2 / −0.4	+0.7 / −0.4	+0.7 / −0.8
PDF	+3.3 / −3.4	+1.0 / −0.8	+1.0 / −1.0	+1.1 / −1.1	+1.5 / −1.5	+1.5 / −1.5
tq ($\bar{t}q$) NLO matching	+0.5 / −0.5	+1.9 / −1.9	+1.4 / −1.4	+4.5 / −4.5	+1.9 / −1.9	+4.1 / −4.1
tq ($\bar{t}q$) parton shower	+2.6 / −2.6	+0.7 / −0.7	+0.2 / −0.2	+0.4 / −0.4	+1.1 / −1.1	+3.8 / −3.8
tq ($\bar{t}q$) scale variations	+0.7 / −0.0	+3.2 / −0.7	+1.0 / −3.4	+2.3 / −0.7	+0.0 / −0.9	+2.0 / −1.1
$t\bar{t}$ NLO matching	+0.3 / −0.3	+2.2 / −2.2	+2.5 / −2.5	+9.0 / −9.0	+2.0 / −2.0	+14 / −14
$t\bar{t}$ parton shower	+1.6 / −1.6	+0.3 / −0.3	+0.8 / −0.8	+3.9 / −3.9	+2.8 / −2.8	+12 / −12
$t\bar{t}$ scale variations	+2.3 / −0.0	+0.9 / −0.3	+0.0 / −2.3	+4.6 / −3.2	+0.0 / −2.1	+13 / −0
Total systematic	+7.1 / −6.4	+6.8 / −5.5	+3.9 / −5.9	+13 / −12	+5.5 / −5.8	+24 / −20
Total (stat. + syst.)	+13 / −13	+11 / −10	+6.4 / −7.8	+16 / −16	+10 / −10	+29 / −26

Table H.12: Uncertainties for the normalised differential $\bar{t}q$ cross-section as a function of $p_{\mathrm{T}}(\hat{t})$ at particle level per bin ($[0, 35, 50, 75, 100, 150, 300]$ GeV) in percent of $(1/\sigma)\mathrm{d}\sigma(\bar{t}q)/\mathrm{d}p_{\mathrm{T}}(\hat{t})$. [2]

	Uncertainties on $\mathrm{d}\sigma(tq)/\mathrm{d}|y(\hat{t})|$ at particle level						
Source of uncertainty	Bin 1 [%]	Bin 2 [%]	Bin 3 [%]	Bin 4 [%]	Bin 5 [%]	Bin 6 [%]	Bin 7 [%]
Data statistics	±5.0	±5.3	±5.9	±4.7	±4.6	±6.4	±5.0
Monte Carlo statistics	±0.9	±0.9	±1.0	±0.8	±0.8	±1.0	±0.9
Unfolding	+0.3 / −0.3	+0.8 / −0.8	+2.6 / −2.6	+0.5 / −0.5	+7.0 / −7.0	+2.0 / −2.0	+1.8 / −1.8
Background normalisation	+2.8 / −2.8	+2.6 / −2.6	+3.4 / −3.4	+2.9 / −2.9	+3.0 / −3.0	+4.6 / −4.6	+3.9 / −3.9
Background modelling	+0.6 / −0.6	+0.2 / −0.2	+0.4 / −0.4	+0.2 / −0.2	+0.5 / −0.5	+1.3 / −1.3	+0.2 / −0.2
Lepton reconstruction	+1.9 / −1.9	+1.9 / −1.9	+1.9 / −1.9	+1.9 / −1.9	+1.9 / −1.9	+1.9 / −1.9	+2.0 / −2.0
Jet reconstruction	+1.0 / −1.0	+1.4 / −1.4	+2.9 / −2.9	+2.2 / −2.2	+0.6 / −0.6	+3.1 / −3.1	+2.2 / −2.2
Jet energy scale	+1.6 / −1.7	+0.6 / −1.7	+2.9 / −2.1	+1.4 / −1.8	+1.7 / −1.4	+2.8 / −1.9	+2.8 / −2.9
Flavour tagging	+1.2 / −1.2	+1.2 / −1.2	+1.2 / −1.2	+1.2 / −1.2	+1.2 / −1.2	+1.2 / −1.2	+1.2 / −1.2
$E_{\mathrm{T}}^{\mathrm{miss}}$ modelling	+0.3 / −0.7	+0.2 / −0.7	+1.7 / −0.0	+0.0 / −0.6	+0.4 / −0.0	+0.0 / −0.7	+0.4 / −0.0
$b/\bar{b}$ efficiency	±0.9	±0.9	±0.9	±0.9	±0.9	±0.9	±0.9
PDF	+0.2 / −0.2	+1.1 / −1.1	+0.9 / −1.0	+0.5 / −0.5	+0.6 / −0.5	+0.7 / −0.6	+0.9 / −1.0
tq ($\bar{t}q$) NLO matching	+0.6 / −0.6	+1.9 / −1.9	+0.7 / −0.7	+1.5 / −1.5	+0.9 / −0.9	+0.4 / −0.4	+0.5 / −0.5
tq ($\bar{t}q$) parton shower	+0.3 / −0.3	+1.0 / −1.0	+1.0 / −1.0	+0.0 / −0.0	+0.1 / −0.1	+0.2 / −0.2	+0.0 / −0.0
tq ($\bar{t}q$) scale variations	+0.9 / −0.0	+1.2 / −0.0	+0.0 / −2.7	+1.5 / −0.0	+0.0 / −0.7	+1.4 / −0.0	+0.0 / −0.8
$t\bar{t}$ NLO matching	+0.1 / −0.1	+0.5 / −0.5	+1.5 / −1.5	+0.2 / −0.2	+0.6 / −0.6	+0.3 / −0.3	+1.3 / −1.3
$t\bar{t}$ parton shower	+0.5 / −0.5	+0.4 / −0.4	+0.8 / −0.8	+0.8 / −0.8	+0.8 / −0.8	+0.3 / −0.3	+0.2 / −0.2
$t\bar{t}$ scale variations	+0.7 / −0.9	+0.5 / −0.9	+0.0 / −0.5	+0.1 / −0.2	+0.5 / −0.1	+1.0 / −0.0	+0.4 / −0.4
Luminosity	±1.9	±1.9	±1.9	±1.9	±1.9	±1.9	±1.9
Total systematic	+4.9 / −4.9	+5.3 / −5.5	+7.3 / −7.4	+5.6 / −5.5	+8.6 / −8.6	+7.7 / −7.2	+6.7 / −6.8
Total (stat. + syst.)	+7.0 / −7.0	+7.5 / −7.6	+9.4 / −9.5	+7.3 / −7.3	+10 / −10	+10 / −10	+8.4 / −8.4

Table H.13: Uncertainties for the absolute differential *tq* cross-section as a function of $|y(\hat{t})|$ at particle level per bin ($[0, 0.15, 0.3, 0.45, 0.7, 1.0, 1.3, 2.2]$) in percent of $\mathrm{d}\sigma(tq)/\mathrm{d}|y(\hat{t})|$. [2]

	Uncertainties on $(1/\sigma)\mathrm{d}\sigma(tq)/\mathrm{d}\lvert y(\hat{t})\rvert$ at particle level						
Source of uncertainty	Bin 1 [%]	Bin 2 [%]	Bin 3 [%]	Bin 4 [%]	Bin 5 [%]	Bin 6 [%]	Bin 7 [%]
Data statistics	±4.7	±5.0	±5.6	±4.3	±4.2	±6.0	±4.6
Monte Carlo statistics	±0.8	±0.8	±0.9	±0.7	±0.8	±0.9	±0.9
Unfolding	+1.0 / −1.0	+2.1 / −2.1	+3.9 / −3.9	+0.8 / −0.8	+5.6 / −5.6	+0.7 / −0.7	+0.5 / −0.5
Background normalisation	+0.5 / −0.5	+0.7 / −0.7	+0.2 / −0.2	+0.4 / −0.4	+0.2 / −0.2	+1.4 / −1.4	+0.7 / −0.7
Background modelling	+0.5 / −0.5	+0.1 / −0.1	+0.3 / −0.3	+0.3 / −0.3	+0.4 / −0.4	+1.4 / −1.4	+0.1 / −0.1
Lepton reconstruction	+0.4 / −0.2	+0.4 / −0.5	+0.3 / −0.4	+0.2 / −0.2	+0.1 / −0.1	+0.3 / −0.2	+0.4 / −0.4
Jet reconstruction	+0.2 / −0.2	+2.6 / −2.6	+1.6 / −1.6	+0.9 / −0.9	+1.9 / −1.9	+1.8 / −1.8	+1.0 / −1.0
Jet energy scale	+0.7 / −0.7	+0.6 / −1.7	+1.7 / −0.6	+0.5 / −0.8	+0.9 / −0.9	+1.2 / −0.7	+1.1 / −1.1
Flavour tagging	+0.0 / −0.0	+0.0 / −0.0	+0.0 / −0.0	+0.0 / −0.0	+0.0 / −0.0	+0.0 / −0.0	+0.1 / −0.1
$E_{\mathrm{T}}^{\mathrm{miss}}$ modelling	+0.2 / −0.6	+0.2 / −0.8	+1.7 / −0.0	+0.0 / −0.7	+0.3 / −0.0	+0.0 / −0.8	+0.4 / −0.0
PDF	+0.2 / −0.2	+1.1 / −1.1	+0.9 / −1.0	+0.5 / −0.5	+0.6 / −0.5	+0.7 / −0.6	+0.9 / −1.0
tq ($\bar{t}q$) NLO matching	+0.6 / −0.6	+1.9 / −1.9	+0.7 / −0.7	+1.5 / −1.5	+0.9 / −0.9	+0.4 / −0.4	+0.6 / −0.6
tq ($\bar{t}q$) parton shower	+0.3 / −0.3	+1.0 / −1.0	+1.0 / −1.0	+0.1 / −0.1	+0.1 / −0.1	+0.2 / −0.2	+0.0 / −0.0
tq ($\bar{t}q$) scale variations	+0.9 / −0.0	+1.2 / −0.0	+0.0 / −2.7	+1.6 / −0.0	+0.0 / −0.7	+1.4 / −0.0	+0.0 / −0.7
$t\bar{t}$ NLO matching	+0.1 / −0.1	+0.5 / −0.5	+1.6 / −1.6	+0.2 / −0.2	+0.6 / −0.6	+0.2 / −0.2	+1.3 / −1.3
$t\bar{t}$ parton shower	+0.5 / −0.5	+0.4 / −0.4	+0.8 / −0.8	+0.8 / −0.8	+0.8 / −0.8	+0.3 / −0.3	+0.2 / −0.2
$t\bar{t}$ scale variations	+0.7 / −0.9	+0.5 / −0.9	+0.0 / −0.5	+0.1 / −0.2	+0.4 / −0.1	+1.1 / −0.0	+0.4 / −0.4
Total systematic	+2.2 / −2.2	+4.6 / −4.8	+5.5 / −5.7	+2.9 / −2.6	+6.2 / −6.3	+3.7 / −3.2	+2.7 / −2.8
Total (stat. + syst.)	+5.2 / −5.2	+6.8 / −6.9	+7.8 / −8.0	+5.2 / −5.0	+7.5 / −7.5	+7.1 / −6.8	+5.3 / −5.4

Table H.14: Uncertainties for the normalised differential tq cross-section as a function of $|y(\hat{t})|$ at particle level per bin ($[0, 0.15, 0.3, 0.45, 0.7, 1.0, 1.3, 2.2]$) in percent of $(1/\sigma)\mathrm{d}\sigma(tq)/\mathrm{d}|y(\hat{t})|$. [2]

	Uncertainties on $\mathrm{d}\sigma(\bar{t}q)/\mathrm{d}|y(\hat{t})|$ at particle level						
Source of uncertainty	Bin 1 [%]	Bin 2 [%]	Bin 3 [%]	Bin 4 [%]	Bin 5 [%]	Bin 6 [%]	Bin 7 [%]
Data statistics	±6.6	±9.2	±8.5	±7.1	±7.2	±8.5	±8.7
Monte Carlo statistics	±0.9	±1.0	±1.0	±0.8	±0.9	±1.1	±1.1
Unfolding	+1.0 / −1.0	+0.4 / −0.4	+0.8 / −0.8	+0.3 / −0.3	+2.0 / −2.0	+3.0 / −3.0	+3.3 / −3.3
Background normalisation	+3.8 / −3.8	+5.2 / −5.2	+4.9 / −4.9	+5.3 / −5.3	+5.4 / −5.4	+5.8 / −5.8	+7.3 / −7.3
Background modelling	+0.9 / −0.9	+0.2 / −0.2	+0.6 / −0.6	+0.2 / −0.2	+1.5 / −1.5	+0.7 / −0.7	+2.5 / −2.5
Lepton reconstruction	+2.0 / −1.9	+1.9 / −1.9	+1.9 / −1.9	+2.0 / −1.9	+1.9 / −1.9	+1.9 / −1.9	+2.0 / −2.0
Jet reconstruction	+2.9 / −2.9	+2.2 / −2.2	+2.3 / −2.3	+0.9 / −0.9	+2.1 / −2.1	+3.3 / −3.3	+0.4 / −0.4
Jet energy scale	+2.1 / −2.1	+2.4 / −1.7	+1.6 / −1.9	+3.0 / −1.5	+1.6 / −1.8	+2.8 / −3.8	+3.7 / −2.7
Flavour tagging	+1.2 / −1.2	+1.2 / −1.2	+1.2 / −1.2	+1.2 / −1.2	+1.2 / −1.2	+1.2 / −1.2	+1.2 / −1.2
$E_{\mathrm{T}}^{\mathrm{miss}}$ modelling	+0.1 / −0.4	+0.8 / −0.0	+0.2 / −0.2	+0.6 / −0.5	+0.7 / −0.6	+0.0 / −0.7	+0.7 / −0.0
$b/\bar{b}$ efficiency	±0.9	±0.9	±0.9	±0.9	±0.9	±0.9	±0.9
PDF	+0.9 / −0.9	+1.2 / −1.3	+0.8 / −0.8	+1.1 / −1.0	+0.7 / −0.7	+0.8 / −0.9	+1.9 / −1.9
tq ($\bar{t}q$) NLO matching	+1.1 / −1.1	+1.8 / −1.8	+3.1 / −3.1	+3.9 / −3.9	+1.6 / −1.6	+0.6 / −0.6	+0.4 / −0.4
tq ($\bar{t}q$) parton shower	+0.9 / −0.9	+1.0 / −1.0	+0.5 / −0.5	+0.3 / −0.3	+0.3 / −0.3	+0.0 / −0.0	+0.4 / −0.4
tq ($\bar{t}q$) scale variations	+0.0 / −0.7	+1.2 / −0.0	+0.5 / −0.6	+0.0 / −0.4	+0.4 / −0.4	+0.5 / −0.5	+1.0 / −0.5
$t\bar{t}$ NLO matching	+3.3 / −3.3	+3.6 / −3.6	+1.7 / −1.7	+1.9 / −1.9	+3.0 / −3.0	+0.9 / −0.9	+0.4 / −0.4
$t\bar{t}$ parton shower	+1.1 / −1.1	+3.0 / −3.0	+2.1 / −2.1	+1.5 / −1.5	+1.9 / −1.9	+0.5 / −0.5	+0.8 / −0.8
$t\bar{t}$ scale variations	+1.8 / −0.1	+0.0 / −3.5	+2.4 / −0.0	+0.0 / −1.6	+0.0 / −1.7	+2.3 / −0.4	+3.0 / −0.0
Luminosity	±1.9	±1.9	±1.9	±1.9	±1.9	±1.9	±1.9
Total systematic	+7.6 / −7.4	+8.8 / −9.2	+8.2 / −7.9	+8.4 / −8.2	+8.3 / −8.5	+9.0 / −9.1	+11 / −10
Total (stat. + syst.)	+10 / −10	+13 / −13	+12 / −12	+11 / −11	+11 / −11	+12 / −12	+14 / −13

Table H.15: Uncertainties for the absolute differential $\bar{t}q$ cross-section as a function of $|y(\hat{t})|$ at particle level per bin ($[0, 0.15, 0.3, 0.45, 0.7, 1.0, 1.3, 2.2]$) in percent of $\mathrm{d}\sigma(\bar{t}q)/\mathrm{d}|y(\hat{t})|$. [2]

	Uncertainties on $(1/\sigma)\mathrm{d}\sigma(\bar{t}q)/\mathrm{d}\lvert y(\hat{t})\rvert$ at particle level						
Source of uncertainty	Bin 1 [%]	Bin 2 [%]	Bin 3 [%]	Bin 4 [%]	Bin 5 [%]	Bin 6 [%]	Bin 7 [%]
Data statistics	±6.1	±8.8	±8.1	±6.6	±6.7	±8.1	±8.1
Monte Carlo statistics	±0.8	±0.9	±0.9	±0.8	±0.8	±1.0	±1.0
Unfolding	+0.4 / −0.4	+0.3 / −0.3	+0.2 / −0.2	+1.0 / −1.0	+2.7 / −2.7	+2.3 / −2.3	+2.6 / −2.6
Background normalisation	+1.6 / −1.6	+0.1 / −0.1	+0.5 / −0.5	+0.0 / −0.0	+0.1 / −0.1	+0.5 / −0.5	+2.1 / −2.1
Background modelling	+0.6 / −0.6	+0.0 / −0.0	+0.3 / −0.3	+0.4 / −0.4	+1.3 / −1.3	+0.5 / −0.5	+2.8 / −2.8
Lepton reconstruction	+0.5 / −0.2	+0.4 / −0.4	+0.3 / −0.4	+0.4 / −0.2	+0.0 / −0.4	+0.4 / −0.4	+0.3 / −0.4
Jet reconstruction	+1.7 / −1.7	+3.3 / −3.3	+1.2 / −1.2	+2.1 / −2.1	+0.9 / −0.9	+2.2 / −2.2	+0.7 / −0.7
Jet energy scale	+0.6 / −1.2	+0.9 / −0.5	+0.6 / −1.2	+0.9 / −0.4	+0.6 / −1.1	+1.0 / −1.9	+1.5 / −0.7
Flavour tagging	+0.0 / −0.0	+0.0 / −0.0	+0.0 / −0.0	+0.0 / −0.0	+0.0 / −0.0	+0.0 / −0.0	+0.1 / −0.1
$E_{\mathrm{T}}^{\mathrm{miss}}$ modelling	+0.0 / −0.3	+0.6 / −0.0	+0.2 / −0.2	+0.4 / −0.6	+0.7 / −0.4	+0.0 / −0.9	+0.6 / −0.0
PDF	+0.8 / −0.8	+1.2 / −1.3	+0.8 / −0.8	+1.1 / −1.0	+0.6 / −0.6	+0.8 / −0.9	+1.9 / −1.9
tq ($\bar{t}q$) NLO matching	+1.1 / −1.1	+1.9 / −1.9	+3.2 / −3.2	+3.8 / −3.8	+1.6 / −1.6	+0.5 / −0.5	+0.3 / −0.3
tq ($\bar{t}q$) parton shower	+0.9 / −0.9	+1.0 / −1.0	+0.5 / −0.5	+0.3 / −0.3	+0.3 / −0.3	+0.0 / −0.0	+0.4 / −0.4
tq ($\bar{t}q$) scale variations	+0.0 / −0.7	+1.2 / −0.0	+0.5 / −0.6	+0.0 / −0.4	+0.4 / −0.4	+0.5 / −0.5	+0.9 / −0.5
$t\bar{t}$ NLO matching	+3.4 / −3.4	+3.5 / −3.5	+1.6 / −1.6	+2.0 / −2.0	+2.9 / −2.9	+1.0 / −1.0	+0.5 / −0.5
$t\bar{t}$ parton shower	+1.1 / −1.1	+3.0 / −3.0	+2.1 / −2.1	+1.5 / −1.5	+1.9 / −1.9	+0.5 / −0.5	+0.8 / −0.8
$t\bar{t}$ scale variations	+1.7 / −0.1	+0.0 / −3.5	+2.3 / −0.0	+0.0 / −1.7	+0.0 / −1.6	+2.3 / −0.4	+3.0 / −0.0
Total systematic	+5.1 / −4.9	+6.5 / −7.2	+5.2 / −4.8	+5.4 / −5.6	+5.2 / −5.4	+4.5 / −4.3	+6.1 / −5.1
Total (stat. + syst.)	+7.9 / −7.8	+11 / −11	+10 / −9	+8.5 / −8.7	+8.5 / −8.6	+9.3 / −9.2	+10 / −10

Table H.16: Uncertainties for the normalised differential $\bar{t}q$ cross-section as a function of $\lvert y(\hat{t})\rvert$ at particle level per bin ($[0, 0.15, 0.3, 0.45, 0.7, 1.0, 1.3, 2.2]$) in percent of $(1/\sigma)\mathrm{d}\sigma(\bar{t}q)/\mathrm{d}\lvert y(\hat{t})\rvert$. [2]

	Uncertainties on $\mathrm{d}\sigma(tq)/\mathrm{d}p_{\mathrm{T}}(\hat{j})$ at particle level					
Source of uncertainty	Bin 1 [%]	Bin 2 [%]	Bin 3 [%]	Bin 4 [%]	Bin 5 [%]	Bin 6 [%]
Data statistics	±4.9	±5.7	±6.8	±6.0	±5.8	±7.9
Monte Carlo statistics	±0.7	±0.7	±0.8	±0.8	±0.9	±1.3
Unfolding	+2.4 / −2.4	+2.4 / −2.4	+2.2 / −2.2	+0.7 / −0.7	+2.1 / −2.1	+0.3 / −0.3
Background normalisation	+5.0 / −5.0	+2.2 / −2.2	+2.8 / −2.8	+2.7 / −2.7	+2.9 / −2.9	+3.0 / −3.0
Background modelling	+0.4 / −0.4	+0.0 / −0.0	+1.0 / −1.0	+0.1 / −0.1	+0.5 / −0.5	+0.7 / −0.7
Lepton reconstruction	+1.9 / −1.9	+1.9 / −1.9	+1.9 / −1.9	+1.9 / −1.9	+1.9 / −1.9	+1.9 / −1.9
Jet reconstruction	+2.0 / −2.0	+1.1 / −1.1	+0.5 / −0.5	+2.1 / −2.1	+0.4 / −0.4	+0.8 / −0.8
Jet energy scale	+1.8 / −1.3	+2.6 / −4.7	+3.4 / −0.9	+3.0 / −4.3	+3.1 / −2.7	+3.1 / −3.0
Flavour tagging	+1.2 / −1.2	+1.2 / −1.2	+1.2 / −1.2	+1.2 / −1.2	+1.3 / −1.3	+1.4 / −1.4
$E_{\mathrm{T}}^{\mathrm{miss}}$ modelling	+0.3 / −0.2	+0.1 / −0.2	+0.5 / −0.2	+0.3 / −0.4	+0.3 / −0.1	+0.4 / −0.5
$b/\bar{b}$ efficiency	±0.9	±0.9	±0.9	±0.9	±0.9	±0.9
PDF	+1.5 / −1.5	+1.6 / −1.6	+0.5 / −0.4	+0.7 / −0.7	+0.8 / −0.8	+0.5 / −0.5
tq ($\bar{t}q$) NLO matching	+3.7 / −3.7	+4.8 / −4.8	+2.1 / −2.1	+0.9 / −0.9	+0.3 / −0.3	+0.5 / −0.5
tq ($\bar{t}q$) parton shower	+3.6 / −3.6	+3.5 / −3.5	+0.1 / −0.1	+1.0 / −1.0	+0.7 / −0.7	+0.3 / −0.3
tq ($\bar{t}q$) scale variations	+0.4 / −2.9	+2.5 / −0.0	+1.8 / −1.6	+1.1 / −0.9	+1.0 / −2.5	+1.8 / −0.0
$t\bar{t}$ NLO matching	+1.0 / −1.0	+0.2 / −0.2	+0.7 / −0.7	+0.6 / −0.6	+0.4 / −0.4	+3.0 / −3.0
$t\bar{t}$ parton shower	+1.3 / −1.3	+0.6 / −0.6	+0.2 / −0.2	+0.3 / −0.3	+0.3 / −0.3	+2.2 / −2.2
$t\bar{t}$ scale variations	+0.0 / −1.3	+0.0 / −0.5	+0.2 / −0.1	+1.1 / −0.0	+1.8 / −1.1	+2.7 / −0.1
Luminosity	±1.9	±1.9	±1.9	±1.9	±1.9	±1.9
Total systematic	+8.9 / −9.4	+8.5 / −9.1	+6.7 / −5.7	+6.0 / −6.7	+6.3 / −6.3	+7.5 / −6.7
Total (stat. + syst.)	+10 / −11	+10 / −11	+10 / −9	+8.5 / −9.0	+8.5 / −8.6	+11 / −10

Table H.17: Uncertainties for the absolute differential tq cross-section as a function of $p_{\mathrm{T}}(\hat{j})$ at particle level per bin ($[30, 45, 60, 75, 100, 150, 300]$ GeV) in percent of $\mathrm{d}\sigma(tq)/p_{\mathrm{T}}(\hat{j})$. [2]

Source of uncertainty	Uncertainties on $(1/\sigma)\mathrm{d}\sigma(tq)/\mathrm{d}p_{\mathrm{T}}(\hat{j})$ at particle level Bin 1 [%]	Bin 2 [%]	Bin 3 [%]	Bin 4 [%]	Bin 5 [%]	Bin 6 [%]
Data statistics	±4.2	±5.6	±6.7	±5.9	±5.6	±7.8
Monte Carlo statistics	±0.6	±0.6	±0.8	±0.8	±0.8	±1.3
Unfolding	+2.3/ −2.3	+2.6/ −2.6	+2.1/ −2.1	+0.9/ −0.9	+2.3/ −2.3	+0.1/ −0.1
Background normalisation	+1.7/ −1.7	+1.2/ −1.2	+0.5/ −0.5	+0.7/ −0.7	+0.5/ −0.5	+0.3/ −0.3
Background modelling	+0.2/ −0.2	+0.2/ −0.2	+0.9/ −0.9	+0.3/ −0.3	+0.6/ −0.6	+0.9/ −0.9
Lepton reconstruction	+0.1/ −0.1	+0.1/ −0.2	+0.3/ −0.3	+0.1/ −0.0	+0.3/ −0.1	+0.1/ −0.2
Jet reconstruction	+0.6/ −0.6	+0.3/ −0.3	+0.8/ −0.8	+0.8/ −0.8	+0.9/ −0.9	+0.6/ −0.6
Jet energy scale	+2.9/ −2.2	+1.2/ −3.3	+2.7/ −0.4	+1.8/ −3.1	+2.3/ −1.9	+2.4/ −2.2
Flavour tagging	+0.2/ −0.2	+0.2/ −0.2	+0.1/ −0.1	+0.2/ −0.2	+0.4/ −0.4	+0.7/ −0.7
$E_{\mathrm{T}}^{\mathrm{miss}}$ modelling	+0.2/ −0.2	+0.1/ −0.4	+0.4/ −0.1	+0.3/ −0.5	+0.2/ −0.1	+0.3/ −0.5
PDF	+1.4/ −1.4	+1.7/ −1.7	+0.5/ −0.4	+0.7/ −0.7	+0.8/ −0.8	+0.5/ −0.5
tq ($\bar{t}q$) NLO matching	+3.5/ −3.5	+5.0/ −5.0	+1.8/ −1.8	+1.2/ −1.2	+0.1/ −0.1	+0.8/ −0.8
tq ($\bar{t}q$) parton shower	+3.3/ −3.3	+3.8/ −3.8	+0.1/ −0.1	+1.2/ −1.2	+0.4/ −0.4	+0.0/ −0.0
tq ($\bar{t}q$) scale variations	+0.4/ −2.6	+2.7/ −0.0	+1.7/ −1.4	+1.4/ −1.0	+1.3/ −2.5	+1.7/ −0.0
$t\bar{t}$ NLO matching	+1.0/ −1.0	+0.1/ −0.1	+0.7/ −0.7	+0.7/ −0.7	+0.4/ −0.4	+3.1/ −3.1
$t\bar{t}$ parton shower	+1.2/ −1.2	+0.7/ −0.7	+0.1/ −0.1	+0.4/ −0.4	+0.4/ −0.4	+2.3/ −2.3
$t\bar{t}$ scale variations	+0.0/ −1.1	+0.0/ −0.5	+0.4/ −0.0	+1.1/ −0.0	+2.0/ −1.1	+2.8/ −0.0
Total systematic	+6.7/ −7.0	+7.8/ −7.9	+4.6/ −3.6	+3.6/ −4.2	+4.5/ −4.4	+6.0/ −4.9
Total (stat. + syst.)	+7.9/ −8.2	+10 / −10	+8.1/ −7.6	+6.9/ −7.2	+7.2/ −7.1	+10 / −9

Table H.18: Uncertainties for the normalised differential tq cross-section as a function of $p_{\mathrm{T}}(\hat{j})$ at particle level per bin ($[30, 45, 60, 75, 100, 150, 300]$ GeV) in percent of $(1/\sigma)\mathrm{d}\sigma(tq)/p_{\mathrm{T}}(\hat{j})$. [2]

Source of uncertainty	Uncertainties on $\mathrm{d}\sigma(\bar{t}q)/\mathrm{d}p_{\mathrm{T}}(\hat{j})$ at particle level Bin 1 [%]	Bin 2 [%]	Bin 3 [%]	Bin 4 [%]	Bin 5 [%]	Bin 6 [%]
Data statistics	±6.0	±9.1	±12	±9.4	±11	±16
Monte Carlo statistics	±0.7	±0.8	±0.9	±0.9	±1.0	±1.6
Unfolding	+0.3 / −0.3	+3.8 / −3.8	+4.4 / −4.4	+1.1 / −1.1	+0.7 / −0.7	+0.9 / −0.9
Background normalisation	+5.8 / −5.8	+4.6 / −4.6	+4.7 / −4.7	+4.7 / −4.7	+6.6 / −6.6	+7.5 / −7.5
Background modelling	+0.0 / −0.0	+0.0 / −0.0	+0.0 / −0.0	+0.0 / −0.0	+0.0 / −0.0	+0.0 / −0.0
Lepton reconstruction	+1.9 / −1.9	+1.9 / −1.9	+1.9 / −1.9	+1.9 / −2.0	+1.9 / −1.9	+1.9 / −1.9
Jet reconstruction	+0.9 / −0.9	+2.8 / −2.8	+0.4 / −0.4	+2.0 / −2.0	+0.1 / −0.1	+1.0 / −1.0
Jet energy scale	+2.1 / −1.1	+3.0 / −3.5	+2.7 / −2.0	+3.8 / −4.1	+3.7 / −3.1	+3.5 / −1.9
Flavour tagging	+1.2 / −1.2	+1.2 / −1.2	+1.1 / −1.1	+1.2 / −1.2	+1.3 / −1.3	+1.4 / −1.4
$E_{\mathrm{T}}^{\mathrm{miss}}$ modelling	+0.5 / −0.3	+0.3 / −0.3	+0.2 / −0.2	+0.4 / −0.3	+0.4 / −0.1	+0.3 / −0.2
$b/\bar{b}$ efficiency	±0.9	±0.9	±0.9	±0.9	±0.9	±0.9
PDF	+1.6 / −1.6	+2.3 / −2.3	+2.7 / −2.8	+3.3 / −3.3	+1.2 / −1.0	+3.3 / −3.3
tq ($\bar{t}q$) NLO matching	+1.8 / −1.8	+3.0 / −3.0	+1.7 / −1.7	+6.3 / −6.3	+6.5 / −6.5	+6.1 / −6.1
tq ($\bar{t}q$) parton shower	+3.3 / −3.3	+3.5 / −3.5	+0.6 / −0.6	+0.2 / −0.2	+1.0 / −1.0	+0.9 / −0.9
tq ($\bar{t}q$) scale variations	+0.8 / −0.1	+0.4 / −0.0	+0.0 / −5.1	+2.7 / −0.0	+1.6 / −0.0	+0.0 / −2.6
$t\bar{t}$ NLO matching	+0.0 / −0.0	+0.4 / −0.4	+1.3 / −1.3	+3.1 / −3.1	+4.2 / −4.2	+9.1 / −9.1
$t\bar{t}$ parton shower	+0.3 / −0.3	+1.8 / −1.8	+1.6 / −1.6	+1.9 / −1.9	+0.6 / −0.6	+6.9 / −6.9
$t\bar{t}$ scale variations	+0.4 / −0.0	+0.0 / −1.2	+3.7 / −5.0	+0.0 / −4.2	+4.7 / −0.0	+10 / −0
Luminosity	±1.9	±1.9	±1.9	±1.9	±1.9	±1.9
Total systematic	+8.2 / −7.9	+10 / −10	+9.3 / −11.0	+11 / −12	+12 / −11	+19 / −16
Total (stat. + syst.)	+10 / −10	+13 / −13	+15 / −16	+15 / −15	+16 / −15	+25 / −23

Table H.19: Uncertainties for the absolute differential $\bar{t}q$ cross-section as a function of $p_{\mathrm{T}}(\hat{j})$ at particle level per bin ($[30, 45, 60, 75, 100, 150, 300]$ GeV) in percent of $\mathrm{d}\sigma(\bar{t}q)/\mathrm{d}p_{\mathrm{T}}(\hat{j})$. [2]

Source of uncertainty	Bin 1 [%]	Bin 2 [%]	Bin 3 [%]	Bin 4 [%]	Bin 5 [%]	Bin 6 [%]
	Uncertainties on $(1/\sigma)\mathrm{d}\sigma(\bar{t}q)/\mathrm{d}p_{\mathrm{T}}(\hat{j})$ at particle level					
Data statistics	±5.0	±8.8	±11	±9.1	±10	±16
Monte Carlo statistics	±0.5	±0.7	±0.8	±0.8	±1.0	±1.6
Unfolding	+0.3 / −0.3	+3.8 / −3.8	+4.5 / −4.5	+1.2 / −1.2	+0.7 / −0.7	+0.8 / −0.8
Background normalisation	+0.4 / −0.4	+0.8 / −0.8	+0.7 / −0.7	+0.7 / −0.7	+1.4 / −1.4	+2.3 / −2.3
Background modelling	+0.0 / −0.0	+0.0 / −0.0	+0.0 / −0.0	+0.0 / −0.0	+0.0 / −0.0	+0.0 / −0.0
Lepton reconstruction	+0.2 / −0.0	+0.2 / −0.2	+0.5 / −0.3	+0.2 / −0.5	+0.1 / −0.4	+0.5 / −0.2
Jet reconstruction	+0.2 / −0.2	+1.6 / −1.6	+1.6 / −1.6	+0.8 / −0.8	+1.1 / −1.1	+0.2 / −0.2
Jet energy scale	+1.9 / −1.2	+1.5 / −1.8	+1.2 / −1.2	+2.2 / −2.6	+2.1 / −2.0	+3.3 / −1.8
Flavour tagging	+0.2 / −0.2	+0.1 / −0.1	+0.1 / −0.1	+0.2 / −0.2	+0.4 / −0.4	+0.8 / −0.8
$E_{\mathrm{T}}^{\mathrm{miss}}$ modelling	+0.2 / −0.1	+0.0 / −0.2	+0.4 / −0.4	+0.2 / −0.2	+0.2 / −0.1	+0.4 / −0.5
PDF	+1.5 / −1.5	+2.3 / −2.3	+2.6 / −2.7	+3.4 / −3.4	+1.1 / −0.9	+3.2 / −3.2
tq ($\bar{t}q$) NLO matching	+1.6 / −1.6	+0.3 / −0.3	+2.1 / −2.1	+0.6 / −0.6	+2.7 / −2.7	+11 / −11
tq ($\bar{t}q$) parton shower	+3.1 / −3.1	+3.8 / −3.8	+0.4 / −0.4	+0.4 / −0.4	+1.2 / −1.2	+0.7 / −0.7
tq ($\bar{t}q$) scale variations	+0.7 / −0.1	+0.3 / −0.0	+0.0 / −5.2	+2.6 / −0.0	+1.5 / −0.0	+0.0 / −2.6
$t\bar{t}$ NLO matching	+0.0 / −0.0	+0.4 / −0.4	+1.3 / −1.3	+3.1 / −3.1	+4.2 / −4.2	+9.1 / −9.1
$t\bar{t}$ parton shower	+0.3 / −0.3	+1.8 / −1.8	+1.6 / −1.6	+1.9 / −1.9	+0.5 / −0.5	+7.0 / −7.0
$t\bar{t}$ scale variations	+0.6 / −0.0	+0.0 / −1.1	+3.7 / −4.8	+0.0 / −4.2	+4.9 / −0.0	+10 / −0
Total systematic	+4.4 / −4.1	+6.6 / −6.8	+7.4 / −9.6	+6.4 / −7.3	+8.0 / −6.0	+19 / −17
Total (stat. + syst.)	+6.7 / −6.5	+11 / −11	+13 / −15	+11 / −12	+13 / −12	+25 / −23

Table H.20: Uncertainties for the normalised differential $\bar{t}q$ cross-section as a function of $p_{\mathrm{T}}(\hat{j})$ at particle level per bin ($[30, 45, 60, 75, 100, 150, 300]$ GeV) in percent of $(1/\sigma)\mathrm{d}\sigma(\bar{t}q)/\mathrm{d}p_{\mathrm{T}}(\hat{j})$. [2]

Source of uncertainty	Uncertainties on $\mathrm{d}\sigma(tq)/\mathrm{d}\lvert y(\hat{j})\rvert$ at particle level Bin 1 [%]	Bin 2 [%]	Bin 3 [%]	Bin 4 [%]	Bin 5 [%]	Bin 6 [%]
Data statistics	±8.9	±7.6	±7.0	±4.4	±4.0	±3.8
Monte Carlo statistics	±1.2	±1.2	±1.0	±0.9	±0.8	±0.8
Unfolding	+5.1 / −5.1	+2.2 / −2.2	+2.4 / −2.4	+2.6 / −2.6	+1.1 / −1.1	+2.7 / −2.7
Background normalisation	+15 / −15	+6.6 / −6.6	+5.7 / −5.7	+2.6 / −2.6	+2.0 / −2.0	+1.5 / −1.5
Background modelling	+1.8 / −1.8	+0.6 / −0.6	+0.4 / −0.4	+0.1 / −0.1	+0.5 / −0.5	+0.2 / −0.2
Lepton reconstruction	+2.0 / −1.9	+1.9 / −1.8	+1.9 / −1.9	+1.9 / −1.9	+1.9 / −1.9	+1.9 / −1.9
Jet reconstruction	+0.6 / −0.6	+0.1 / −0.1	+4.9 / −4.9	+0.4 / −0.4	+2.0 / −2.0	+1.1 / −1.1
Jet energy scale	+0.9 / −1.1	+1.2 / −0.8	+0.2 / −0.8	+1.2 / −1.1	+1.3 / −2.4	+4.5 / −5.0
Flavour tagging	+1.3 / −1.3	+1.2 / −1.2	+1.2 / −1.2	+1.3 / −1.3	+1.2 / −1.2	+1.2 / −1.2
$E_{\mathrm{T}}^{\mathrm{miss}}$ modelling	+0.4 / −0.8	+0.2 / −0.0	+0.3 / −0.4	+0.0 / −0.2	+0.0 / −0.7	+0.1 / −0.2
$b/\bar{b}$ efficiency	±0.9	±0.9	±0.9	±0.9	±0.9	±0.9
PDF	+2.5 / −2.5	+0.9 / −0.8	+0.2 / −0.2	+0.4 / −0.4	+0.7 / −0.7	+0.5 / −0.6
tq ($\bar{t}q$) NLO matching	+0.1 / −0.1	+0.1 / −0.1	+0.0 / −0.0	+0.1 / −0.1	+0.0 / −0.0	+0.1 / −0.1
tq ($\bar{t}q$) parton shower	+0.0 / −0.0	+0.0 / −0.0	+0.0 / −0.0	+0.1 / −0.1	+0.0 / −0.0	+0.0 / −0.0
tq ($\bar{t}q$) scale variations	+0.1 / −0.1	+0.1 / −0.2	+0.1 / −0.0	+0.0 / −0.1	+0.0 / −0.0	+0.0 / −0.0
$t\bar{t}$ NLO matching	+5.0 / −5.0	+2.1 / −2.1	+1.4 / −1.4	+0.0 / −0.0	+1.3 / −1.3	+0.8 / −0.8
$t\bar{t}$ parton shower	+3.4 / −3.4	+2.2 / −2.2	+0.7 / −0.7	+0.1 / −0.1	+0.9 / −0.9	+0.0 / −0.0
$t\bar{t}$ scale variations	+0.0 / −0.4	+4.0 / −0.0	+0.0 / −2.1	+0.0 / −0.7	+0.6 / −0.0	+0.0 / −0.3
Luminosity	±1.9	±1.9	±1.9	±1.9	±1.9	±1.9
Total systematic	+18 / −18	+9.3 / −8.4	+8.7 / −9.0	+5.1 / −5.1	+4.9 / −5.4	+6.5 / −6.8
Total (stat. + syst.)	+20 / −20	+12 / −11	+11 / −11	+6.7 / −6.7	+6.4 / −6.7	+7.5 / −7.8

Table H.21: Uncertainties for the absolute differential tq cross-section as a function of $|y(\hat{j})|$ at particle level per bin ($[30, 45, 60, 75, 100, 150, 300]$ GeV) in percent of $\mathrm{d}\sigma(tq)/|y(\hat{j})|$. [2]

Source of uncertainty	Uncertainties on $(1/\sigma)\mathrm{d}\sigma(tq)/\mathrm{d}\lvert y(\hat{j})\rvert$ at particle level Bin 1 [%]	Bin 2 [%]	Bin 3 [%]	Bin 4 [%]	Bin 5 [%]	Bin 6 [%]
Data statistics	±7.4	±7.1	±6.7	±4.3	±4.1	±3.9
Monte Carlo statistics	±1.0	±1.1	±0.9	±0.8	±0.7	±0.7
Unfolding	+5.8 / −5.8	+1.4 / −1.4	+1.6 / −1.6	+1.8 / −1.8	+0.3 / −0.3	+1.8 / −1.8
Background normalisation	+10 / −10	+1.1 / −1.1	+0.2 / −0.2	+3.1 / −3.1	+3.8 / −3.8	+4.3 / −4.3
Background modelling	+1.7 / −1.7	+0.7 / −0.7	+0.5 / −0.5	+0.2 / −0.2	+0.6 / −0.6	+0.3 / −0.3
Lepton reconstruction	+0.3 / −0.2	+0.3 / −0.1	+0.1 / −0.2	+0.3 / −0.1	+0.1 / −0.2	+0.1 / −0.2
Jet reconstruction	+0.6 / −0.6	+1.1 / −1.1	+3.7 / −3.7	+1.6 / −1.6	+0.8 / −0.8	+0.2 / −0.2
Jet energy scale	+1.9 / −1.4	+1.8 / −1.4	+1.1 / −1.5	+0.8 / −0.4	+0.1 / −0.9	+3.4 / −3.5
Flavour tagging	+0.3 / −0.3	+0.2 / −0.2	+0.0 / −0.0	+0.0 / −0.0	+0.2 / −0.2	+0.3 / −0.3
$E_{\mathrm{T}}^{\mathrm{miss}}$ modelling	+0.2 / −0.4	+0.5 / −0.0	+0.4 / −0.1	+0.2 / −0.2	+0.0 / −0.5	+0.2 / −0.1
PDF	+2.2 / −2.2	+0.6 / −0.5	+0.4 / −0.4	+0.7 / −0.7	+1.0 / −1.0	+0.8 / −0.8
tq ($\bar{t}q$) NLO matching	+0.0 / −0.0	+0.1 / −0.1	+0.0 / −0.0	+0.1 / −0.1	+0.0 / −0.0	+0.1 / −0.1
tq ($\bar{t}q$) parton shower	+0.0 / −0.0	+0.0 / −0.0	+0.0 / −0.0	+0.1 / −0.1	+0.1 / −0.1	+0.0 / −0.0
tq ($\bar{t}q$) scale variations	+0.1 / −0.0	+0.1 / −0.2	+0.1 / −0.0	+0.0 / −0.1	+0.0 / −0.0	+0.0 / −0.0
$t\bar{t}$ NLO matching	+4.6 / −4.6	+2.5 / −2.5	+0.9 / −0.9	+0.5 / −0.5	+1.8 / −1.8	+1.3 / −1.3
$t\bar{t}$ parton shower	+3.1 / −3.1	+2.5 / −2.5	+0.4 / −0.4	+0.4 / −0.4	+1.2 / −1.2	+0.3 / −0.3
$t\bar{t}$ scale variations	+0.0 / −0.4	+3.9 / −0.0	+0.0 / −2.2	+0.0 / −0.7	+0.5 / −0.1	+0.0 / −0.4
Total systematic	+13 / −13	+6.1 / −4.6	+4.5 / −5.1	+4.2 / −4.2	+4.7 / −4.8	+6.0 / −6.1
Total (stat. + syst.)	+15 / −15	+9.4 / −8.5	+8.0 / −8.4	+6.0 / −6.0	+6.2 / −6.3	+7.2 / −7.3

Table H.22: Uncertainties for the normalised differential tq cross-section as a function of $|y(\hat{j})|$ at particle level per bin ($[30, 45, 60, 75, 100, 150, 300]$ GeV) in percent of $(1/\sigma)\mathrm{d}\sigma(tq)/|y(\hat{j})|$. [2]

Source of uncertainty	Uncertainties on $\mathrm{d}\sigma(\bar{t}q)/\mathrm{d}|y(\hat{j})|$ at particle level Bin 1 [%]	Bin 2 [%]	Bin 3 [%]	Bin 4 [%]	Bin 5 [%]	Bin 6 [%]
Data statistics	±12	±12	±7.8	±7.3	±6.0	±6.1
Monte Carlo statistics	±1.1	±1.2	±1.0	±0.9	±0.8	±0.9
Unfolding	+0.7 / −0.7	+0.2 / −0.2	+2.3 / −2.3	+1.1 / −1.1	+4.5 / −4.5	+1.4 / −1.4
Background normalisation	+21 / −21	+12 / −12	+5.8 / −5.8	+5.1 / −5.1	+2.8 / −2.8	+2.8 / −2.8
Background modelling	+1.5 / −1.5	+0.1 / −0.1	+0.2 / −0.2	+0.4 / −0.4	+1.9 / −1.9	+0.8 / −0.8
Lepton reconstruction	+1.9 / −1.9	+2.0 / −1.8	+2.0 / −2.0	+1.9 / −1.9	+2.0 / −1.8	+1.9 / −1.9
Jet reconstruction	+1.4 / −1.4	+2.5 / −2.5	+1.3 / −1.3	+0.8 / −0.8	+1.5 / −1.5	+0.1 / −0.1
Jet energy scale	+1.5 / −0.9	+1.0 / −0.6	+1.5 / −1.2	+1.5 / −1.1	+1.5 / −1.9	+5.7 / −5.5
Flavour tagging	+1.3 / −1.3	+1.3 / −1.3	+1.3 / −1.3	+1.2 / −1.2	+1.2 / −1.2	+1.2 / −1.2
$E_{\mathrm{T}}^{\mathrm{miss}}$ modelling	+1.0 / −0.3	+0.4 / −0.5	+0.6 / −0.4	+0.1 / −0.3	+0.1 / −0.8	+0.5 / −0.0
$b/\bar{b}$ efficiency	±0.9	±0.9	±0.9	±0.9	±0.9	±0.9
PDF	+4.9 / −4.8	+0.8 / −0.8	+0.3 / −0.2	+1.9 / −1.9	+1.1 / −1.1	+0.8 / −0.8
tq ($\bar{t}q$) NLO matching	+0.2 / −0.2	+0.2 / −0.2	+0.1 / −0.1	+0.0 / −0.0	+0.1 / −0.1	+0.6 / −0.6
tq ($\bar{t}q$) parton shower	+0.0 / −0.0	+0.0 / −0.0	+0.0 / −0.0	+0.0 / −0.0	+0.1 / −0.1	+0.0 / −0.0
tq ($\bar{t}q$) scale variations	+0.0 / −0.1	+0.1 / −0.0	+0.1 / −0.0	+0.0 / −0.1	+0.0 / −0.0	+0.0 / −0.0
$t\bar{t}$ NLO matching	+6.5 / −6.5	+2.1 / −2.1	+4.2 / −4.2	+2.3 / −2.3	+1.6 / −1.6	+2.9 / −2.9
$t\bar{t}$ parton shower	+2.9 / −2.9	+3.0 / −3.0	+0.7 / −0.7	+0.2 / −0.2	+0.3 / −0.3	+1.0 / −1.0
$t\bar{t}$ scale variations	+0.0 / −4.1	+0.0 / −3.8	+2.7 / −0.0	+1.0 / −0.7	+0.9 / −0.5	+1.3 / −0.0
Luminosity	±1.9	±1.9	±1.9	±1.9	±1.9	±1.9
Total systematic	+23 / −23	+13 / −13	+8.9 / −8.4	+7.1 / −7.0	+7.2 / −7.2	+8.1 / −7.8
Total (stat. + syst.)	+26 / −26	+18 / −18	+12 / −11	+10 / −10	+9.3 / −9.4	+10 / −10

Table H.23: Uncertainties for the absolute differential $\bar{t}q$ cross-section as a function of $|y(\hat{j})|$ at particle level per bin ($[30, 45, 60, 75, 100, 150, 300]$ GeV) in percent of $\mathrm{d}\sigma(\bar{t}q)/\mathrm{d}|y(\hat{j})|$. [2]

Source of uncertainty	Uncertainties on $(1/\sigma)\mathrm{d}\sigma(\bar{t}q)/\mathrm{d}\lvert y(\hat{j})\rvert$ at particle level Bin 1 [%]	Bin 2 [%]	Bin 3 [%]	Bin 4 [%]	Bin 5 [%]	Bin 6 [%]
Data statistics	±10	±11	±7.6	±7.3	±6.2	±6.6
Monte Carlo statistics	±0.9	±1.1	±0.9	±0.8	±0.8	±0.9
Unfolding	+1.4 / −1.4	+0.5 / −0.5	+1.7 / −1.7	+1.7 / −1.7	+3.8 / −3.8	+2.1 / −2.1
Background normalisation	+13 / −13	+2.6 / −2.6	+3.6 / −3.6	+4.4 / −4.4	+6.9 / −6.9	+6.9 / −6.9
Background modelling	+1.5 / −1.5	+0.2 / −0.2	+0.2 / −0.2	+0.4 / −0.4	+1.9 / −1.9	+0.7 / −0.7
Lepton reconstruction	+0.2 / −0.1	+0.2 / −0.4	+0.1 / −0.3	+0.4 / −0.2	+0.4 / −0.2	+0.2 / −0.1
Jet reconstruction	+0.1 / −0.1	+1.3 / −1.3	+0.1 / −0.1	+0.4 / −0.4	+0.2 / −0.2	+1.4 / −1.4
Jet energy scale	+1.7 / −1.7	+1.6 / −1.5	+0.5 / −0.3	+0.6 / −0.4	+0.2 / −0.8	+4.4 / −4.4
Flavour tagging	+0.3 / −0.3	+0.1 / −0.1	+0.0 / −0.0	+0.0 / −0.0	+0.2 / −0.2	+0.3 / −0.3
$E_{\mathrm{T}}^{\mathrm{miss}}$ modelling	+0.6 / −0.0	+0.1 / −0.4	+0.4 / −0.2	+0.1 / −0.3	+0.0 / −0.7	+0.5 / −0.1
PDF	+4.1 / −4.1	+0.4 / −0.4	+0.8 / −0.8	+2.5 / −2.5	+1.9 / −1.9	+1.5 / −1.5
tq ($\bar{t}q$) NLO matching	+0.1 / −0.1	+0.3 / −0.3	+0.0 / −0.0	+0.1 / −0.1	+0.1 / −0.1	+0.2 / −0.2
tq ($\bar{t}q$) parton shower	+0.0 / −0.0	+0.0 / −0.0	+0.0 / −0.0	+0.0 / −0.0	+0.1 / −0.1	+0.0 / −0.0
tq ($\bar{t}q$) scale variations	+0.0 / −0.1	+0.1 / −0.0	+0.1 / −0.0	+0.0 / −0.1	+0.0 / −0.0	+0.0 / −0.0
$t\bar{t}$ NLO matching	+5.5 / −5.5	+3.1 / −3.1	+3.2 / −3.2	+3.3 / −3.3	+2.6 / −2.6	+3.9 / −3.9
$t\bar{t}$ parton shower	+2.6 / −2.6	+3.3 / −3.3	+0.3 / −0.3	+0.6 / −0.6	+0.0 / −0.0	+1.4 / −1.4
$t\bar{t}$ scale variations	+0.0 / −3.6	+0.1 / −3.6	+3.2 / −0.0	+1.5 / −0.4	+1.1 / −0.0	+1.6 / −0.0
Total systematic	+15 / −15	+5.8 / −6.8	+6.2 / −5.3	+6.6 / −6.4	+8.8 / −8.8	+10 / −10
Total (stat. + syst.)	+18 / −18	+13 / −13	+10 / −9	+10 / −10	+11 / −11	+12 / −12

Table H.24: Uncertainties for the normalised differential $\bar{t}q$ cross-section as a function of $\lvert y(\hat{j})\rvert$ at particle level per bin ($[30, 45, 60, 75, 100, 150, 300]$ GeV) in percent of $(1/\sigma)\mathrm{d}\sigma(\bar{t}q)/\mathrm{d}\lvert y(\hat{j})\rvert$. [2]

APPENDIX I

Statistical correlation matrices

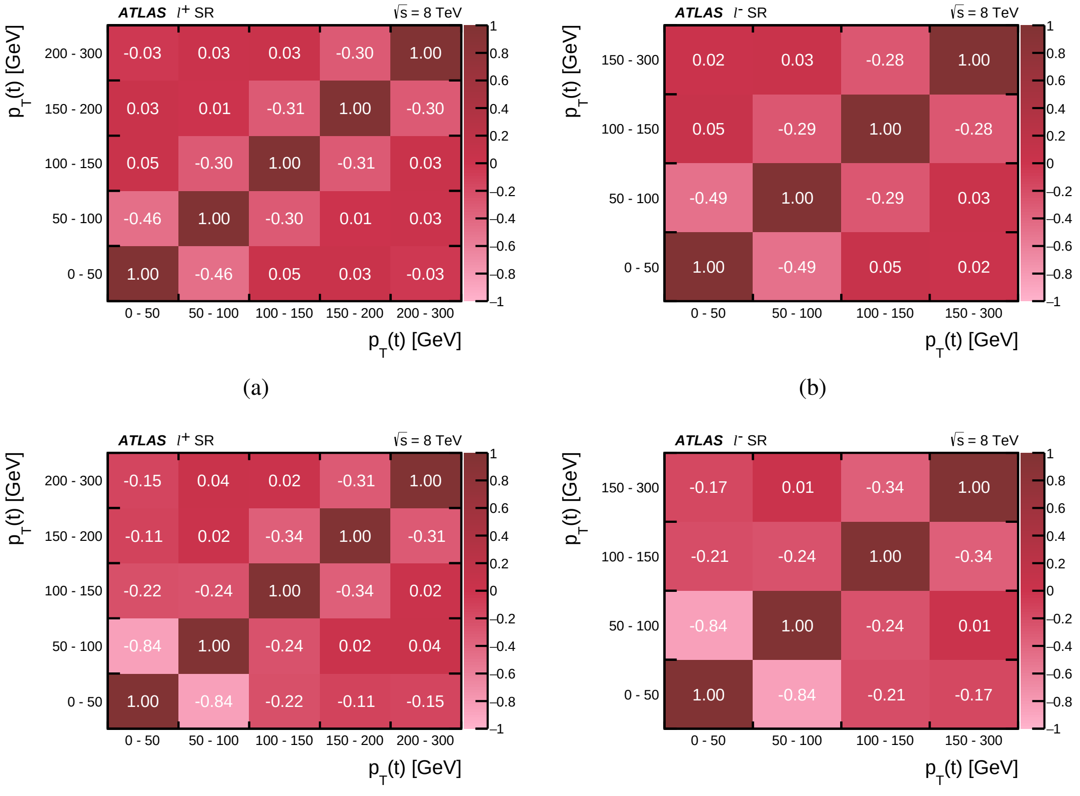

(a)

	0 - 50	50 - 100	100 - 150	150 - 200	200 - 300
200 - 300	-0.03	0.03	0.03	-0.30	1.00
150 - 200	0.03	0.01	-0.31	1.00	-0.30
100 - 150	0.05	-0.30	1.00	-0.31	0.03
50 - 100	-0.46	1.00	-0.30	0.01	0.03
0 - 50	1.00	-0.46	0.05	0.03	-0.03

(b)

	0 - 50	50 - 100	100 - 150	150 - 300
150 - 300	0.02	0.03	-0.28	1.00
100 - 150	0.05	-0.29	1.00	-0.28
50 - 100	-0.49	1.00	-0.29	0.03
0 - 50	1.00	-0.49	0.05	0.02

(c)

	0 - 50	50 - 100	100 - 150	150 - 200	200 - 300
200 - 300	-0.15	0.04	0.02	-0.31	1.00
150 - 200	-0.11	0.02	-0.34	1.00	-0.31
100 - 150	-0.22	-0.24	1.00	-0.34	0.02
50 - 100	-0.84	1.00	-0.24	0.02	0.04
0 - 50	1.00	-0.84	-0.22	-0.11	-0.15

(d)

	0 - 50	50 - 100	100 - 150	150 - 300
150 - 300	-0.17	0.01	-0.34	1.00
100 - 150	-0.21	-0.24	1.00	-0.34
50 - 100	-0.84	1.00	-0.24	0.01
0 - 50	1.00	-0.84	-0.21	-0.17

Figure I.1: Statistical correlation matrix for the absolute differential cross-sections as a function of $p_{\mathrm{T}}(t)$ for (a) tq and (b) $\bar{t}q$ events as well as for the normalised differential cross-sections for (c) tq and (d) $\bar{t}q$ events. It includes the statistical uncertainty due to the number of data events and MC statistics. [2]

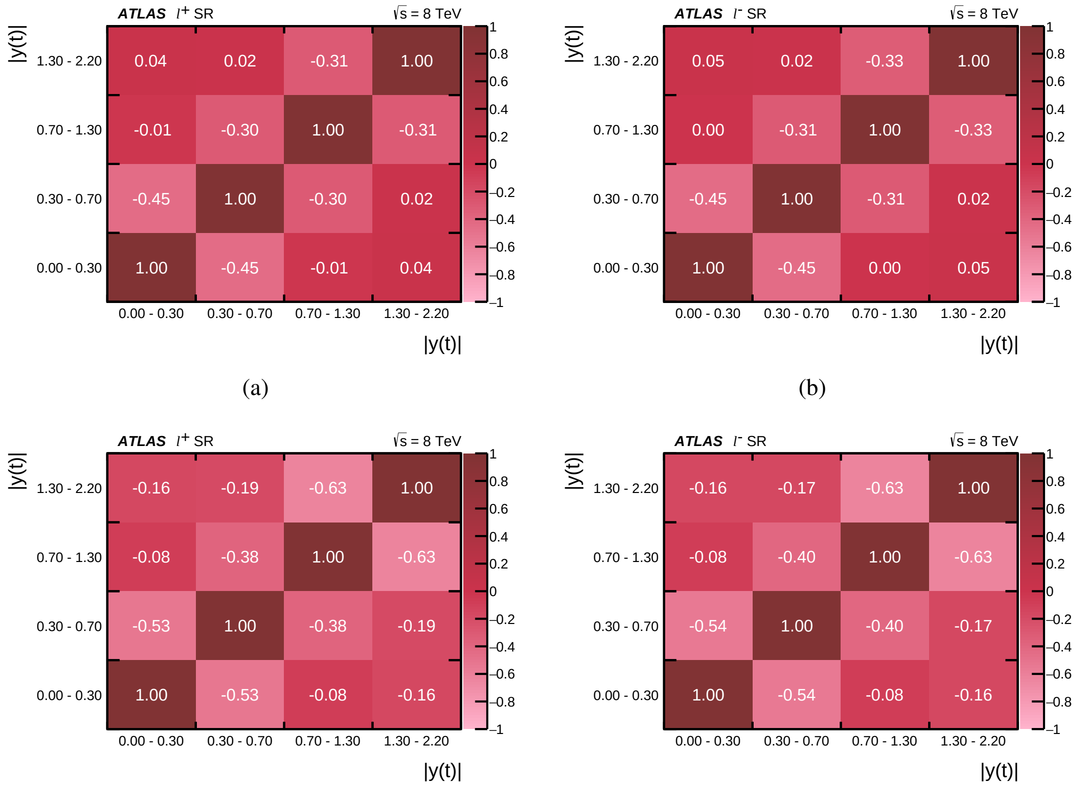

|y(t)|	0.00 - 0.30	0.30 - 0.70	0.70 - 1.30	1.30 - 2.20
1.30 - 2.20	0.04	0.02	-0.31	1.00
0.70 - 1.30	-0.01	-0.30	1.00	-0.31
0.30 - 0.70	-0.45	1.00	-0.30	0.02
0.00 - 0.30	1.00	-0.45	-0.01	0.04

(a)

|y(t)|	0.00 - 0.30	0.30 - 0.70	0.70 - 1.30	1.30 - 2.20
1.30 - 2.20	0.05	0.02	-0.33	1.00
0.70 - 1.30	0.00	-0.31	1.00	-0.33
0.30 - 0.70	-0.45	1.00	-0.31	0.02
0.00 - 0.30	1.00	-0.45	0.00	0.05

(b)

|y(t)|	0.00 - 0.30	0.30 - 0.70	0.70 - 1.30	1.30 - 2.20
1.30 - 2.20	-0.16	-0.19	-0.63	1.00
0.70 - 1.30	-0.08	-0.38	1.00	-0.63
0.30 - 0.70	-0.53	1.00	-0.38	-0.19
0.00 - 0.30	1.00	-0.53	-0.08	-0.16

(c)

|y(t)|	0.00 - 0.30	0.30 - 0.70	0.70 - 1.30	1.30 - 2.20
1.30 - 2.20	-0.16	-0.17	-0.63	1.00
0.70 - 1.30	-0.08	-0.40	1.00	-0.63
0.30 - 0.70	-0.54	1.00	-0.40	-0.17
0.00 - 0.30	1.00	-0.54	-0.08	-0.16

(d)

Figure I.2: Statistical correlation matrix for the absolute differential cross-sections as a function of $|y(t)|$ for (a) tq and (b) $\bar{t}q$ events as well as for the normalised differential cross-sections for (c) tq and (d) $\bar{t}q$ events. It includes the statistical uncertainty due to the number of data events and MC statistics. [2]

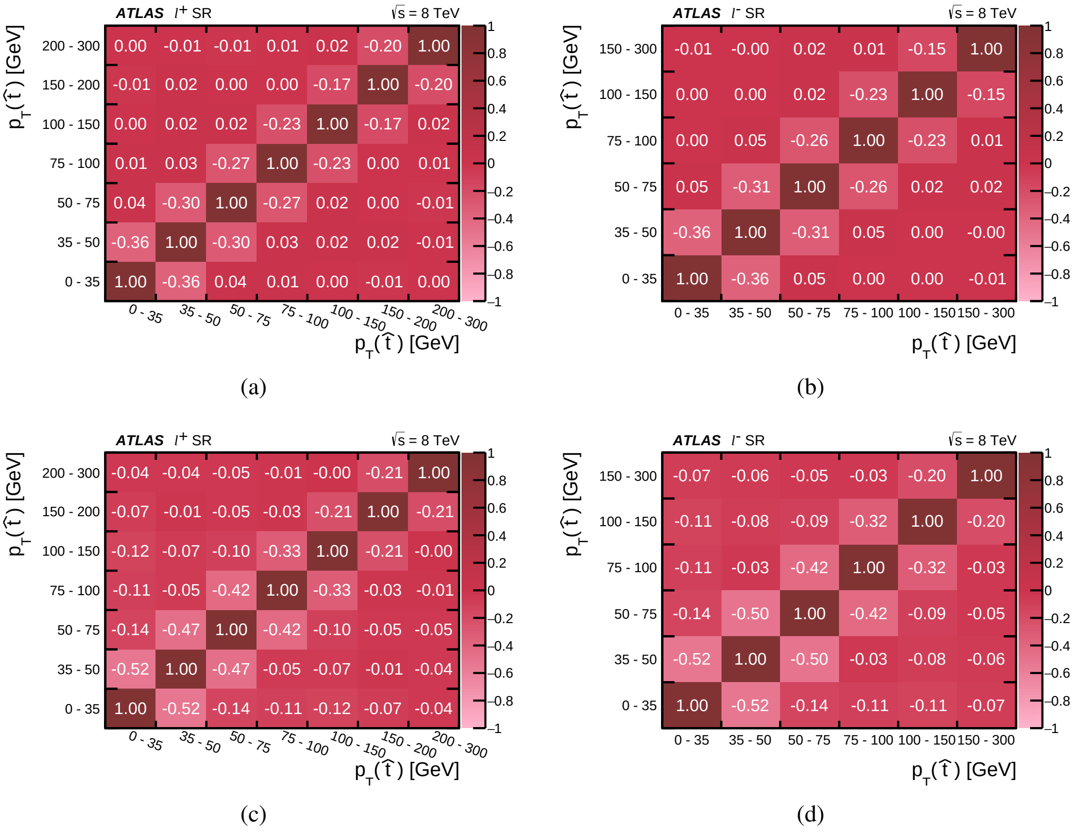

$p_T(\hat{t})$ [GeV]	0 - 35	35 - 50	50 - 75	75 - 100	100 - 150	150 - 200	200 - 300
200 - 300	0.00	-0.01	-0.01	0.01	0.02	-0.20	1.00
150 - 200	-0.01	0.02	0.00	0.00	-0.17	1.00	-0.20
100 - 150	0.00	0.02	0.02	-0.23	1.00	-0.17	0.02
75 - 100	0.01	0.03	-0.27	1.00	-0.23	0.00	0.01
50 - 75	0.04	-0.30	1.00	-0.27	0.02	0.00	-0.01
35 - 50	-0.36	1.00	-0.30	0.03	0.02	0.02	-0.01
0 - 35	1.00	-0.36	0.04	0.01	0.00	-0.01	0.00

(a)

$p_T(\hat{t})$ [GeV]	0 - 35	35 - 50	50 - 75	75 - 100	100 - 150	150 - 300
150 - 300	-0.01	-0.00	0.02	0.01	-0.15	1.00
100 - 150	0.00	0.00	0.02	-0.23	1.00	-0.15
75 - 100	0.00	0.05	-0.26	1.00	-0.23	0.01
50 - 75	0.05	-0.31	1.00	-0.26	0.02	0.02
35 - 50	-0.36	1.00	-0.31	0.05	0.00	-0.00
0 - 35	1.00	-0.36	0.05	0.00	0.00	-0.01

(b)

$p_T(\hat{t})$ [GeV]	0 - 35	35 - 50	50 - 75	75 - 100	100 - 150	150 - 200	200 - 300
200 - 300	-0.04	-0.04	-0.05	-0.01	-0.00	-0.21	1.00
150 - 200	-0.07	-0.01	-0.05	-0.03	-0.21	1.00	-0.21
100 - 150	-0.12	-0.07	-0.10	-0.33	1.00	-0.21	-0.00
75 - 100	-0.11	-0.05	-0.42	1.00	-0.33	-0.03	-0.01
50 - 75	-0.14	-0.47	1.00	-0.42	-0.10	-0.05	-0.05
35 - 50	-0.52	1.00	-0.47	-0.05	-0.07	-0.01	-0.04
0 - 35	1.00	-0.52	-0.14	-0.11	-0.12	-0.07	-0.04

(c)

$p_T(\hat{t})$ [GeV]	0 - 35	35 - 50	50 - 75	75 - 100	100 - 150	150 - 300
150 - 300	-0.07	-0.06	-0.05	-0.03	-0.20	1.00
100 - 150	-0.11	-0.08	-0.09	-0.32	1.00	-0.20
75 - 100	-0.11	-0.03	-0.42	1.00	-0.32	-0.03
50 - 75	-0.14	-0.50	1.00	-0.42	-0.09	-0.05
35 - 50	-0.52	1.00	-0.50	-0.03	-0.08	-0.06
0 - 35	1.00	-0.52	-0.14	-0.11	-0.11	-0.07

(d)

Figure I.3: Statistical correlation matrix for the absolute differential cross-sections as a function of $p_{\mathrm{T}}(\hat{t})$ for (a) tq and (b) $\bar{t}q$ events as well as for the normalised differential cross-sections for (c) tq and (d) $\bar{t}q$ events. It includes the statistical uncertainty due to the number of data events and MC statistics. [2]

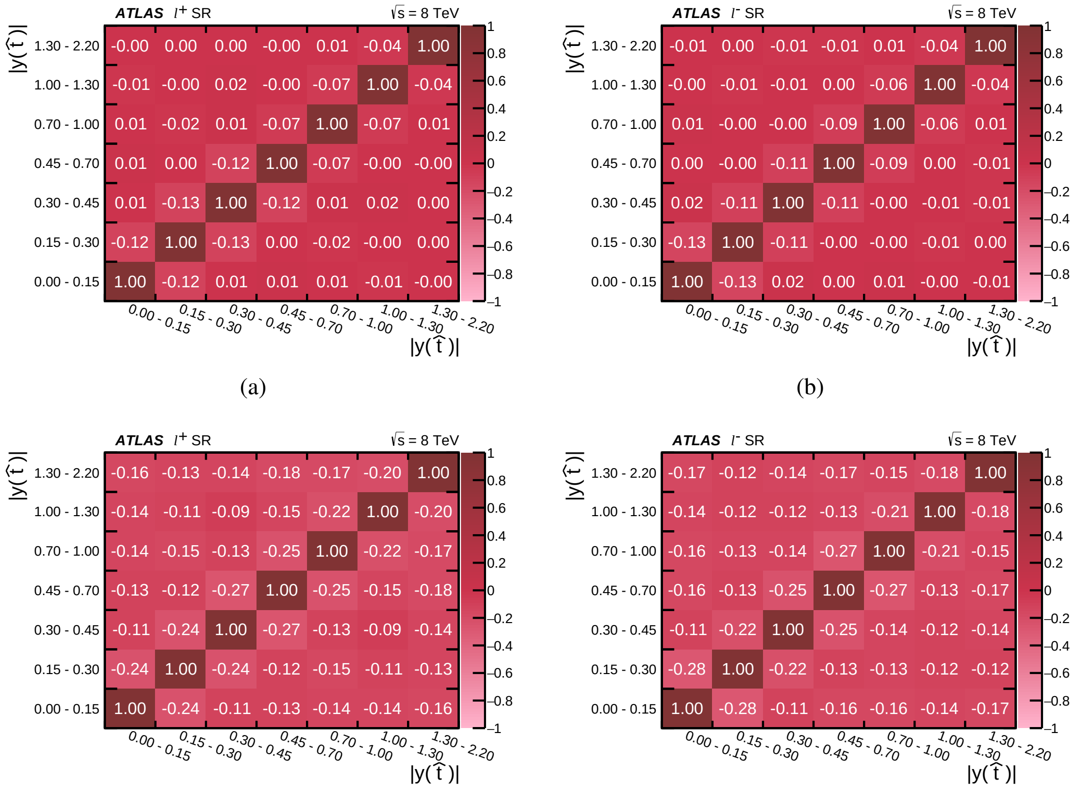

(a)

|y(t̂)|	0.00 - 0.15	0.15 - 0.30	0.30 - 0.45	0.45 - 0.70	0.70 - 1.00	1.00 - 1.30	1.30 - 2.20
1.30 - 2.20	-0.00	0.00	0.00	-0.00	0.01	-0.04	1.00
1.00 - 1.30	-0.01	-0.00	0.02	-0.00	-0.07	1.00	-0.04
0.70 - 1.00	0.01	-0.02	0.01	-0.07	1.00	-0.07	0.01
0.45 - 0.70	0.01	0.00	-0.12	1.00	-0.07	-0.00	-0.00
0.30 - 0.45	0.01	-0.13	1.00	-0.12	0.01	0.02	0.00
0.15 - 0.30	-0.12	1.00	-0.13	0.00	-0.02	-0.00	0.00
0.00 - 0.15	1.00	-0.12	0.01	0.01	0.01	-0.01	-0.00

(b)

|y(t̂)|	0.00 - 0.15	0.15 - 0.30	0.30 - 0.45	0.45 - 0.70	0.70 - 1.00	1.00 - 1.30	1.30 - 2.20
1.30 - 2.20	-0.01	0.00	-0.01	-0.01	0.01	-0.04	1.00
1.00 - 1.30	-0.00	-0.01	-0.01	0.00	-0.06	1.00	-0.04
0.70 - 1.00	0.01	-0.00	-0.00	-0.09	1.00	-0.06	0.01
0.45 - 0.70	0.00	-0.00	-0.11	1.00	-0.09	0.00	-0.01
0.30 - 0.45	0.02	-0.11	1.00	-0.11	-0.00	-0.01	-0.01
0.15 - 0.30	-0.13	1.00	-0.11	-0.00	-0.00	-0.01	0.00
0.00 - 0.15	1.00	-0.13	0.02	0.00	0.01	-0.00	-0.01

(c)

|y(t̂)|	0.00 - 0.15	0.15 - 0.30	0.30 - 0.45	0.45 - 0.70	0.70 - 1.00	1.00 - 1.30	1.30 - 2.20
1.30 - 2.20	-0.16	-0.13	-0.14	-0.18	-0.17	-0.20	1.00
1.00 - 1.30	-0.14	-0.11	-0.09	-0.15	-0.22	1.00	-0.20
0.70 - 1.00	-0.14	-0.15	-0.13	-0.25	1.00	-0.22	-0.17
0.45 - 0.70	-0.13	-0.12	-0.27	1.00	-0.25	-0.15	-0.18
0.30 - 0.45	-0.11	-0.24	1.00	-0.27	-0.13	-0.09	-0.14
0.15 - 0.30	-0.24	1.00	-0.24	-0.12	-0.15	-0.11	-0.13
0.00 - 0.15	1.00	-0.24	-0.11	-0.13	-0.14	-0.14	-0.16

(d)

|y(t̂)|	0.00 - 0.15	0.15 - 0.30	0.30 - 0.45	0.45 - 0.70	0.70 - 1.00	1.00 - 1.30	1.30 - 2.20
1.30 - 2.20	-0.17	-0.12	-0.14	-0.17	-0.15	-0.18	1.00
1.00 - 1.30	-0.14	-0.12	-0.12	-0.13	-0.21	1.00	-0.18
0.70 - 1.00	-0.16	-0.13	-0.14	-0.27	1.00	-0.21	-0.15
0.45 - 0.70	-0.16	-0.13	-0.25	1.00	-0.27	-0.13	-0.17
0.30 - 0.45	-0.11	-0.22	1.00	-0.25	-0.14	-0.12	-0.14
0.15 - 0.30	-0.28	1.00	-0.22	-0.13	-0.13	-0.12	-0.12
0.00 - 0.15	1.00	-0.28	-0.11	-0.16	-0.16	-0.14	-0.17

Figure I.4: Statistical correlation matrix for the absolute differential cross-sections as a function of $|y(\hat{t})|$ for (a) tq and (b) $\bar{t}q$ events as well as for the normalised differential cross-sections for (c) tq and (d) $\bar{t}q$ events. It includes the statistical uncertainty due to the number of data events and MC statistics. [2]

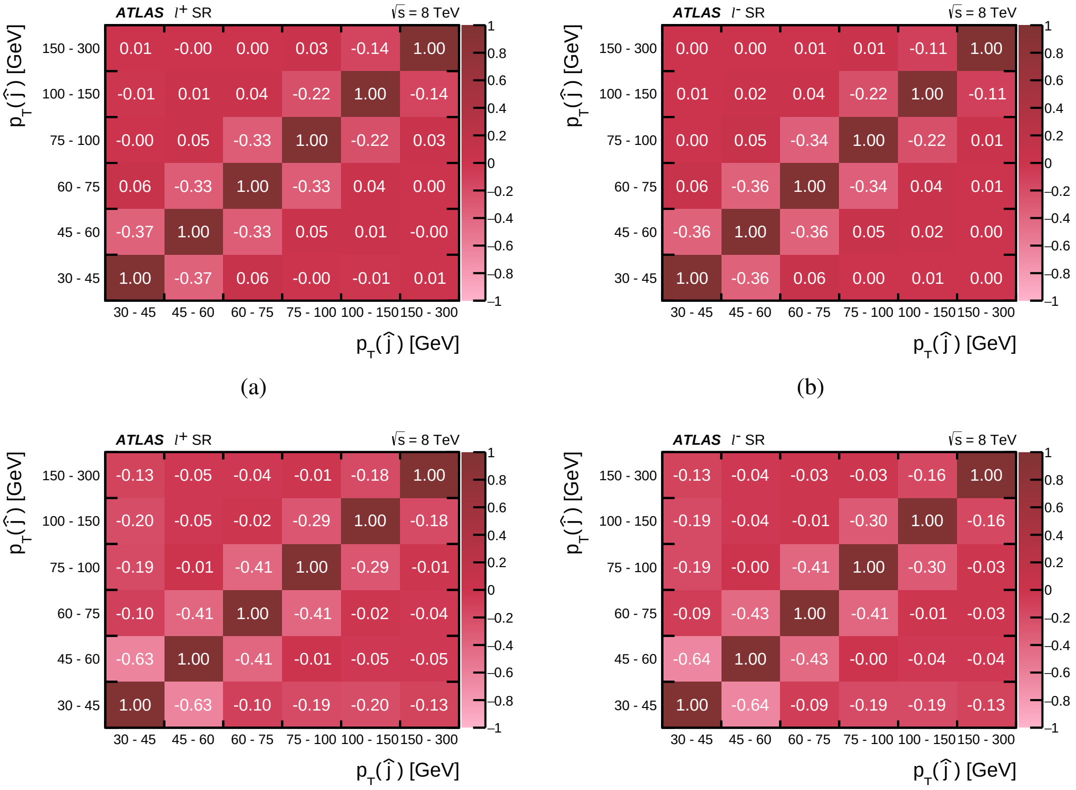

(a)

$p_T(\hat{j})$ [GeV]	30 - 45	45 - 60	60 - 75	75 - 100	100 - 150	150 - 300
150 - 300	0.01	-0.00	0.00	0.03	-0.14	1.00
100 - 150	-0.01	0.01	0.04	-0.22	1.00	-0.14
75 - 100	-0.00	0.05	-0.33	1.00	-0.22	0.03
60 - 75	0.06	-0.33	1.00	-0.33	0.04	0.00
45 - 60	-0.37	1.00	-0.33	0.05	0.01	-0.00
30 - 45	1.00	-0.37	0.06	-0.00	-0.01	0.01

(b)

$p_T(\hat{j})$ [GeV]	30 - 45	45 - 60	60 - 75	75 - 100	100 - 150	150 - 300
150 - 300	0.00	0.00	0.01	0.01	-0.11	1.00
100 - 150	0.01	0.02	0.04	-0.22	1.00	-0.11
75 - 100	0.00	0.05	-0.34	1.00	-0.22	0.01
60 - 75	0.06	-0.36	1.00	-0.34	0.04	0.01
45 - 60	-0.36	1.00	-0.36	0.05	0.02	0.00
30 - 45	1.00	-0.36	0.06	0.00	0.01	0.00

(c)

$p_T(\hat{j})$ [GeV]	30 - 45	45 - 60	60 - 75	75 - 100	100 - 150	150 - 300
150 - 300	-0.13	-0.05	-0.04	-0.01	-0.18	1.00
100 - 150	-0.20	-0.05	-0.02	-0.29	1.00	-0.18
75 - 100	-0.19	-0.01	-0.41	1.00	-0.29	-0.01
60 - 75	-0.10	-0.41	1.00	-0.41	-0.02	-0.04
45 - 60	-0.63	1.00	-0.41	-0.01	-0.05	-0.05
30 - 45	1.00	-0.63	-0.10	-0.19	-0.20	-0.13

(d)

$p_T(\hat{j})$ [GeV]	30 - 45	45 - 60	60 - 75	75 - 100	100 - 150	150 - 300
150 - 300	-0.13	-0.04	-0.03	-0.03	-0.16	1.00
100 - 150	-0.19	-0.04	-0.01	-0.30	1.00	-0.16
75 - 100	-0.19	-0.00	-0.41	1.00	-0.30	-0.03
60 - 75	-0.09	-0.43	1.00	-0.41	-0.01	-0.03
45 - 60	-0.64	1.00	-0.43	-0.00	-0.04	-0.04
30 - 45	1.00	-0.64	-0.09	-0.19	-0.19	-0.13

Figure I.5: Statistical correlation matrix for the absolute differential cross-sections as a function of $p_{\mathrm{T}}(\hat{j})$ for (a) tq and (b) $\bar{t}q$ events as well as for the normalised differential cross-sections for (c) tq and (d) $\bar{t}q$ events. It includes the statistical uncertainty due to the number of data events and MC statistics. [2]

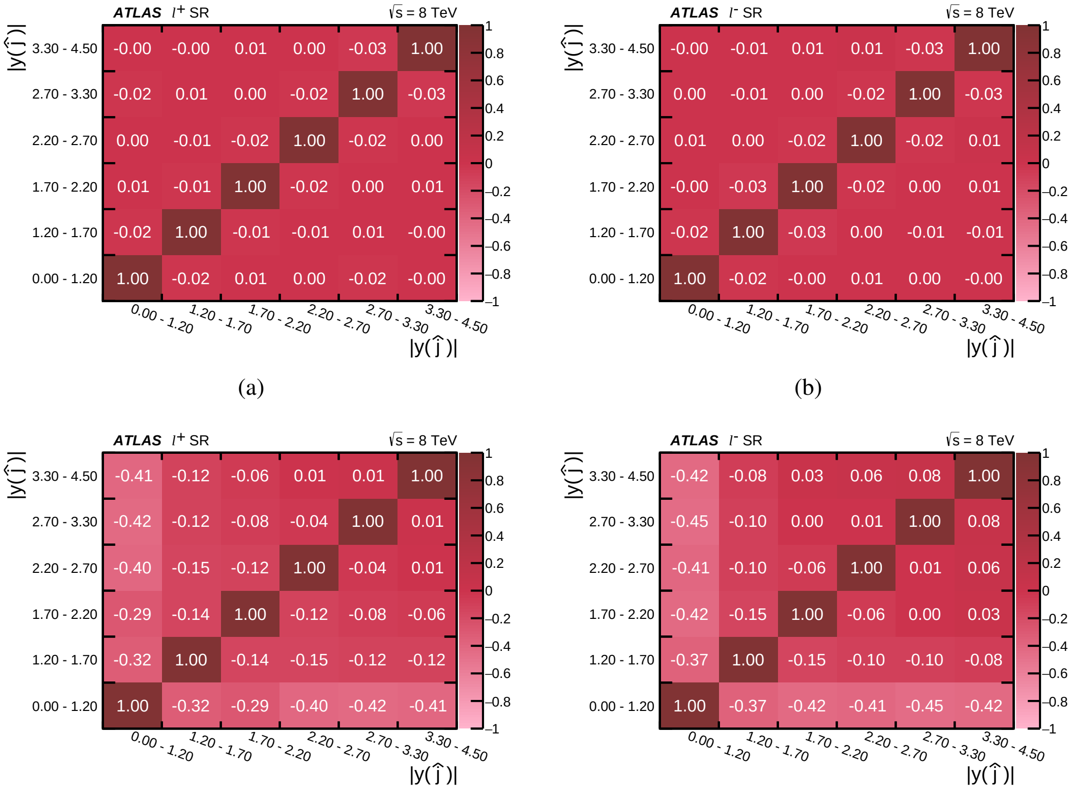

(a)

	0.00 - 1.20	1.20 - 1.70	1.70 - 2.20	2.20 - 2.70	2.70 - 3.30	3.30 - 4.50
3.30 - 4.50	-0.00	-0.00	0.01	0.00	-0.03	1.00
2.70 - 3.30	-0.02	0.01	0.00	-0.02	1.00	-0.03
2.20 - 2.70	0.00	-0.01	-0.02	1.00	-0.02	0.00
1.70 - 2.20	0.01	-0.01	1.00	-0.02	0.00	0.01
1.20 - 1.70	-0.02	1.00	-0.01	-0.01	0.01	-0.00
0.00 - 1.20	1.00	-0.02	0.01	0.00	-0.02	-0.00

(b)

	0.00 - 1.20	1.20 - 1.70	1.70 - 2.20	2.20 - 2.70	2.70 - 3.30	3.30 - 4.50
3.30 - 4.50	-0.00	-0.01	0.01	0.01	-0.03	1.00
2.70 - 3.30	0.00	-0.01	0.00	-0.02	1.00	-0.03
2.20 - 2.70	0.01	0.00	-0.02	1.00	-0.02	0.01
1.70 - 2.20	-0.00	-0.03	1.00	-0.02	0.00	0.01
1.20 - 1.70	-0.02	1.00	-0.03	0.00	-0.01	-0.01
0.00 - 1.20	1.00	-0.02	-0.00	0.01	0.00	-0.00

(c)

	0.00 - 1.20	1.20 - 1.70	1.70 - 2.20	2.20 - 2.70	2.70 - 3.30	3.30 - 4.50
3.30 - 4.50	-0.41	-0.12	-0.06	0.01	0.01	1.00
2.70 - 3.30	-0.42	-0.12	-0.08	-0.04	1.00	0.01
2.20 - 2.70	-0.40	-0.15	-0.12	1.00	-0.04	0.01
1.70 - 2.20	-0.29	-0.14	1.00	-0.12	-0.08	-0.06
1.20 - 1.70	-0.32	1.00	-0.14	-0.15	-0.12	-0.12
0.00 - 1.20	1.00	-0.32	-0.29	-0.40	-0.42	-0.41

(d)

	0.00 - 1.20	1.20 - 1.70	1.70 - 2.20	2.20 - 2.70	2.70 - 3.30	3.30 - 4.50
3.30 - 4.50	-0.42	-0.08	0.03	0.06	0.08	1.00
2.70 - 3.30	-0.45	-0.10	0.00	0.01	1.00	0.08
2.20 - 2.70	-0.41	-0.10	-0.06	1.00	0.01	0.06
1.70 - 2.20	-0.42	-0.15	1.00	-0.06	0.00	0.03
1.20 - 1.70	-0.37	1.00	-0.15	-0.10	-0.10	-0.08
0.00 - 1.20	1.00	-0.37	-0.42	-0.41	-0.45	-0.42

Figure I.6: Statistical correlation matrix for the absolute differential cross-sections as a function of $|y(\hat{j})|$ for (a) tq and (b) $\bar{t}q$ events as well as for the normalised differential cross-sections for (c) tq and (d) $\bar{t}q$ events. It includes the statistical uncertainty due to the number of data events and MC statistics. [2]

Acknowledgements

The thesis would not be in this good shape without the support of many people both inside and outside the physics community. A big thank you to all of you!

First, I would like to express my deep gratitude to my supervisor, Prof. Dr. Ian C. Brock, for giving me the opportunity to enter the world of particle physics and for his continuous support and guidance. He gave me a lot of freedom to pursue my research and allowed me to participate in a variety of conferences. I also thank him for his writing tips. My big thank goes to the other members of examining committee, Prof. Dr. Klaus Desch, Prof. Dr. Ulf-G. Meißner and Prof. Dr. Klaus Willecke for reviewing the thesis and the fruitful discussions.

I am thankful to all my colleagues from Bonn for being good colleagues and friends at all time. Jan Stillings, Thomas Velz and Sebastian Mergelmeyer, thank you all for guiding me throughout my Master thesis studies and for all useful chats and ideas during my PhD studies. With Jan, PI computing infrastructure was running just fine every time when I had to deliver some results. I acknowledge Sebastian for his careful proofreading this thesis. I want to thank Irina Cioară, Regina Moles-Valls and Maike Hansen for the lovely conversation on various topics. It would have been less fun in the office without, Rui Zhang, Anjishnu Bandyopadhyay, Ozan Arslan, Peter Falke, Elena Zarkh and Marius Blaut. I recognise Muhammad Alhroob for his help in a variety of ways when I was working at CERN.

I would like to thank the t-channel single toppers from the University of Wuppertal for the close collaboration. My special thank goes to Prof. Dr. Wolfgang Wagner for proposing me to work on the differential t-channel single top-quark cross-sections. He provided a lot of good comments and productive discussions that made us move forward. I am grateful to Dominic Hirschbühl for his extraordinary tips and for his support. Phillipp Tepel and I worked very closely during publication procedure. Thanks for all of your hard work and friendship. I am thankful to Kathrin Becker for sharing her knowledge about the 7 TeV differential cross-section measurements.

I am grateful for all comments, suggestions and discussions on the analysis provided by all of the members of the ATLAS collaboration, especially the ATLAS single top group.

Finally, I would like to express my deepest gratefulness to my parents, Pramoun and Somjai, in Thailand for their unconditional love and constant support. With their power of love all my dreams always become true. I am extremely lucky to have a special man, my beloved husband, Sebastian. There are no words to express my feelings for you. Thanks for all of your unlimited support, understanding and taking care our lovely son, Max, in particular during my thesis writing. I am pleased with my son for his existence and for being a strong reason for finishing up this thesis. I would like to thank my parents in law, Heinz and Marianne, for all of their help. The food was very tasty. I also cannot forget the other members of my family and my friends who always share a part of my soul. My very special thank must go to the solar eclipse in 1995 for inspiring me to study physics and for keeping me on my toes.